Development of a Stable and Efficient Electron Cyclotron Resonance Thruster with Magnetic Nozzle

Simon Peterschmitt

INSTITUT POLYTECHNIQUE DE PARIS

NNT : 2020IPPAX053

Thèse de doctorat

Development of a Stable and Efficient Electron Cyclotron Resonance Thruster with Magnetic Nozzle

Thèse de doctorat de l'Institut Polytechnique de Paris
préparée à l'Ecole Polytechnique

École doctorale n°626 Ecole Doctorale de l'Institut Polytechnique de Paris (ED IP Paris)

Spécialité de doctorat: Optique, laser et plasma

Thèse présentée et soutenue à Palaiseau, le 1er octobre 2020, par

Simon Peterschmitt

Composition du Jury :

Sophie Kazamias Professeure, Université Paris-Saclay	Présidente
Jean-Pierre Bœuf Directeur de Recherche, CNRS	Rapporteur
Daniele Pavarin Associate Professor, University of Padova	Rapporteur
Amnon Fruchtman Professor, Holon Institute of Technology	Examinateur
Benjamin Jorns Assistant Professor, University of Michigan	Examinateur
Yevgeny Raitses Professor, Princeton University	Examinateur
Sedina Tsikata Chargée de recherche, CNRS	Examinatrice
Denis Packan Chercheur, ONERA	Co-Directeur de thèse (invité)
Jean-Marcel Rax Professeur, Ecole Polytechnique	Directeur de thèse

Titre : Développement d'un propulseur stable et efficace à résonance cyclotron électronique et muni d'une tuyère magnétique

Mots clés : electron-cyclotron, tuyère magnétique, propulseur plasma, micro-propulsion, chauffage résonant

Résumé: Les propulseurs plasmas sont le sujet d'un intérêt grandissant pour équiper de petits satellites. Des miniaturisations de technologies matures ont été proposées ainsi que des concepts innovants, tels le propulseur à résonance cyclotron électronique muni d'une tuyère magnétique (ECRT). Ce propulseur pourrait réaliser une rupture technologique car il est sans grilles, sans neutraliseur et n'a besoin que d'un seul générateur. Le présent travail consiste à développer un ECRT accompagné du dispositif expérimental nécessaire, capable de démontrer avec précision une grande efficacité durant un fonctionnement prolongé en régime permanent. Les précédentes études sur l'ECRT étaient limitées par un manque de précision sur des mesures clés, en raison du dispositif et des technologies nécessaires à l'étude de ce propulseur. La procédure et le dispositif expérimentaux sont donc largement améliorés pour augmenter la précision des mesures. Toutefois, des spécificités dues à la tuyère magnétique compliquent l'interprétation des mesures de densité de courant d'ion. Notre analyse s'appuie donc principalement sur des mesures de poussées obtenues avec une balance. Par ailleurs, nous montrons que les performances du propulseur augmentent significativement quand on diminue la pression dans le caisson de test jusqu'à 10^{-7} mbar Xénon. En outre, d'éventuels effets de caisson sont explorés en testant le propulseur à l'ONERA (Palaiseau, France) et à JLU (Giessen, Allemagne). En prenant en considération ces difficultés expérimentales, nous étudions l'efficacité du propulseur en fonction de la géométrie de l'injection de gaz neutre, de la topologie du champ magnétique, et des conditions aux limites de la tuyère magnétique. De plus, nous abordons la question de l'érosion du propulseur, de deux manières : premièrement par une modification des matériaux et deuxièmement par une modification de la structure de couplage (coaxiale, ou guide d'onde circulaire). Le couplage de type guide d'onde produit des ions à des énergies trop faibles pour les exigences de la propulsion spatiale ; en revanche, une structure de couplage coaxiale usinée en graphite semble diminuer substantiellement l'érosion sans compromettre l'efficacité. Ces résultats permettent de concevoir et de tester un propulseur ~ 30 W et un propulseur ~ 200 W dont les performances sont répétables dans le temps. L'efficacité et la durée de vie sont considérablement augmentées : une première campagne de test indique une efficacité allant jusqu'à ~ 50% et une durée de vie estimée de un à quelques milliers d'heures. Pour éclairer les résultats expérimentaux, nous proposons une nouvelle démarche de modélisation, fondée sur l'étude des trajectoires des électrons et sur une approche du chauffage électronique au moyen d'une équation de Fokker-Planck. Cette démarche débouche sur le calcul de la fonction de distribution en énergie des électrons dans le propulseur ; celle-ci détermine le courant d'ions extrait et l'énergie des ions.

Title : Development of a Stable and Efficient Electron Cyclotron Resonance Thruster with Magnetic Nozzle

Keywords : electron-cyclotron, magnetic nozzle, plasma thruster, micro-propulsion, resonant heating

Abstract: Plasma thrusters are the subject of growing interest as a means for small satellite propulsion. Miniaturizations of mature technologies as well as innovative concepts have been proposed such as the electron-cyclotron resonance thruster with magnetic nozzle (ECRT). This thruster appears as a potentially disruptive technology because it is gridless, neutralizerless, and only requires one power supply. The present work consists in the development of an ECRT and its accompanying experimental test set-up, able to accurately demonstrate high thruster efficiency during prolonged steady state operation. Previous studies on the ECRT were limited by a significant lack of accuracy on key measurements, due to the specific setups and technologies needed for this thruster. The experimental procedure and the setup are thus heavily upgraded to improve the accuracy of the experimental data. However, peculiarities due to the magnetic nozzle complicate the interpretation of the ion current density measurements. Our analysis of performance thus mainly rests on thrust balance measurements. Besides, thruster performance is shown to significantly increase when decreasing vacuum tank pressure down to 10^{-7} mbar Xenon, and facility effects are investigated by testing the thruster both at ONERA (Palaiseau, France) and at JLU (Giessen, Germany). Well aware of these experimental difficulties, we study the efficiency of the thruster as a function of the neutral gas injection geometry, the magnetic field topology, and the boundary conditions of the magnetic nozzle. Furthermore, we address erosion issues in two ways: first by a change of materials, and second by a change of coupling structure (coaxial, or circular waveguide). Waveguide coupling yields insufficient ion energies for space propulsion requirements but manufacturing the coaxial coupling structure with graphite appears to substantially mitigate erosion without compromising the efficiency. These results enable to design and test a ~ 30 W thruster and a ~ 200 W thruster consistently performing in time. They achieve large improvements in efficiency and lifetime: a first test campaign reports up to ~ 50% efficiency and one to a few thousand hours of estimated lifetime. In order to shed light on the experimental outcomes, a new modelling approach is proposed based on the study of the electron trajectories and on a Fokker-Planck heating model. This approach leads to the calculation of the electron energy distribution function in the thruster which determines the extracted ion current and the ion energy

Institut Polytechnique de Paris
91120 Palaiseau, France

Acknowledgements

Ce travail de thèse, je l'ai parfois vécu comme une aventure bien solitaire. Comment aurait-il pu en être autrement alors que je m'efforçais de tourner mes pensées et mes actions vers un sujet aussi particulier et aussi éloigné de la vie en commun ? Indépendamment de cette impression je veux souligner la contribution de nombreuses personnes à cette thèse, de manière plus ou moins apparente. Mais avant tout je veux exprimer ma reconnaissance pour ces années de vie et de travail ; j'apprends petit à petit à ne rien prendre pour acquis.

Je remercie les membres du jury pour leur temps, leurs encouragements et les échanges scientifiques que nous avons eu lors de la soutenance ; j'espère que ce moment aura été fertile pour la compréhension de la physique du propulseur ECR. Je pense plus particulièrement aux rapporteurs de ce mémoire : si j'ose volontiers espérer qu'il fut une lecture intéressante, je suis sûr que la lecture complète a représenté un effort pour lequel je leur suis obligé.

Le déroulement de la thèse a été ponctué de rendez-vous avec Jean-Marcel Rax et pour lesquels je le remercie vivement. Toujours formateurs, les échanges couvraient un large champ incluant même parfois la physique du propulseur ! Je suis reconnaissant envers Denis Packan pour l'opportunité de travailler à l'ONERA, pour son aide au laboratoire, ses conseils de présentation et d'écriture, et bien d'autres coups de pouce distillés au cours de notre collaboration. Par-dessous tout j'ai particulièrement apprécié son esprit positif en entreprenant. C'est avec plaisir que je repense aux échanges et à la collaboration avec Paul-Quentin, Julien, ainsi que Victor ; et c'est avec amitié et plein d'espoir que je le vois prendre la suite de mon travail. Bien entendu, je prendrai de temps en temps des nouvelles du propulseur !

Je suis songeur et plein de gratitude quand je pense à la fortune qui a voulu que je partage un bureau avec Jean. Nos échanges quotidiens ont été d'une valeur inestimable. Je pense également avec amitié à Fabrice et Vincent avec qui j'ai partagé l'aventure initiatique de la thèse, et je remercie l'ensemble de l'équipe FPA.

C'est avec Théo que j'ai découvert le laboratoire de propulsion électrique. Bien qu'il terminât sa thèse avant moi, il a continué à habiter le laboratoire par les retentissantes vibrations d'Amorphis – pas le moindre de ses héritages... Il n'y a de science que du général et d'existence que du particulier ; c'est finalement contre cette maxime aristotélicienne que nous avons ferraillé ensemble, essayant de voir de l'ordre dans la réalité souvent inextricable du propulseur, lui-même soumis à de nombreuses perturbations qu'il s'agissait de traquer âprement. Merci donc à Théo, mais aussi à Jana, mes compagnons de laboratoire, pour leur humour et leur soutien.

Je remercie également mes parents, mais comment choisir un élément plutôt qu'un autre quand je leur dois tant ? Peut-être l'environnement stimulant qu'ils m'ont offert depuis un jeune âge, mais aussi leur soutien pendant les trois ans de la thèse.

En terminant cette thèse je pense aussi à mes amis Khoa et Yvon, avec qui j'ai cultivé une tenace envie de comprendre les choses, ainsi que le plaisir et l'art de mener cette quête. Je pense aussi à Alejandro, Camille, Quentin et Victor, pour le chemin parcouru pendant la thèse et pour une stimulation déterminante sur ma manière de penser des choses comme le monde académique, la connaissance, ou l'enseignement. Je n'oublierai pas les copains et les lumineuses semaines d'été à Lou Clapas qui ont entrecoupé le travail.

J’ai écrit les premières et les dernières lignes de ce mémoire pendant le premier et le deuxième confinement de l’année 2020. Je remercie Lucie pour l’opportunité de rédiger une large part du mémoire dans un cadre exceptionnel et propice au travail, mais surtout en étant remarquablement entouré : merci à Lucie, Pierre, Khoa et Madeleine. En songeant à la dernière année de la thèse je pense en particulier à Madeleine, pour de grandes joies partagées, des moments magiques, et pour un soutien régulier.

Table of content

Table of figures

Table of tables

1. Introduction

Plasma physics can be understood as a corpus of knowledge shared by three active research communities: the natural plasma community, the fusion community, and the industrial plasma community. These communities deal with a remarkable diversity of phenomena resulting from the behavior of ionized gases that vary by more than ten orders of magnitude in density, and several orders of magnitudes in temperature. In spite of that diversity, the essence of the concept of plasma may be defined following Chen [1] as the collective behavior exhibited by a gas of charged and neutral particles. Collective behavior stems from long range electric, magnetic and electromagnetic interactions: the positions and velocities of the set of considered charged particles determine the forces that apply on each charged particle. This collective behavior implies tremendous complexity as compared to the case of a neutral gas in which the forces imparted on each particle depend mostly on neighboring particles.

The plasma thruster community, often presented as a part of the industrial plasma community, aims at the development of electric plasma thrusters for space propulsion applications. From an application standpoint, the mission statement of the plasma thruster community could be expressed as follows: *to develop devices able to efficiently produce thrust through ion acceleration, during an extended period of time and in a controllable way, using electrical power as primary source of power.* We will elaborate on this statement in the next chapter. A variety of thruster concepts were envisioned from the early years of the plasma thruster community, in the 1960's. Among those, a few led to presently mature technologies, some were discarded, and others are still presently in development.

History of the electron cyclotron resonance thruster development

In the 1930's, the experimental discovery of waveguides [2], as well as the early work on the propagation of radio waves in the ionosphere (e.g., APPLETON, 1932 [3]), marked the inception of two related fields: microwave engineering and the study of waves in magnetized plasmas. These fields flourished in the following decades because of radar and telecommunication applications. They established theoretical grounds as well as techniques that allowed imagining electric thrusters using radio frequencies or microwaves. Several such thruster concepts were proposed. For example, microwave operation of existing lower-frequency pulsed plasma thrusters [4], accelerator using the ponderomotive force [5], or much more recently the helicon plasma thruster derived from industrial plasma systems [6]. Among

those microwave plasma accelerators is the electron-cyclotron resonance plasma thruster with magnetic nozzle.

The concept of electron-cyclotron resonance plasma thruster with magnetic nozzle (ECRT) was first publicly described by MILLER ET AL. (1962) [7]. They conducted a preliminary theoretical study of this thruster concept and pointed out three main phenomena expected to play a key role in that thruster's acceleration process.

1. Energy transfer from the electric field to the electrons, achieved at cyclotron frequency through resonant coupling of a right-hand circularly polarized (RHCP) wave to a plasma immersed in a static magnetic field.

2. Conversion of electronic motion from transverse to longitudinal (to the magnetic field), by a static magnetic field gradient.

3. Subsequent acceleration of ions, by a charge separation static electric field.

MILLER ET AL. (1962) also mentioned the Doppler broadening of resonance, provided the cold plasma dispersion relation for the RHCP wave, and discussed a strategy to minimize wave reflection at the plasma interface. However, no experimental tests were conducted, for it was only the very beginning of a research program carried out for NASA Lewis Research Center by the General Electric Space Science Laboratory between 1962 and 1967. In later documents, this program is called CYCLOPS, for CYCLOtron resonance Propulsion System. A number of reports and communications stem from this program [7]–[17], which is the framework for the efforts described in the next four paragraphs.

MILLER AND GIBBONS (1964) [11] is the first journal publication reporting experimental results. The authors experimented with an Argon plasma excited with a continuous 2.45 GHz linearly polarized wave. A mass flow of ~ 0.01mg/s was coupled to ~ 320W of microwave power in a section of a RG48/U rectangular waveguide. A pendulum-calorimeter was scanned perpendicularly to the thrust axis to obtain the power in the jet (through temperature measurement) and the thrust (through pendulum deflection measurement). This experiment demonstrated the thrust-producing ability of the device as well as the possibility to efficiently couple microwave power to the plasma: indeed, 260 µN of thrust and 80-90% coupling were reported. The total efficiency was estimated to be 1%. However, there were a number of limitations to this preliminary study, including: the absence of direct thrust measurement, the calorimeter too close to the thruster (13 cm), short runs (<90s), a background operating pressure as high as 10^{-4} mbar, and no ion energy measurement.

Extensive unpublished experimental efforts were conducted in the framework of the CYCLOPS program in the 1960s. They are presented in this paragraph based on the analysis of the final report of the contract [16]. Injection optimization and geometry optimization were performed on a set of 5 different thrusters. The effect of propellant species (Argon, Krypton, Xenon, and Mercury), magnetic field, pulsed or continuous power, and propellant flow were studied on the selected configuration. It consisted in a 29 mm diameter and 25 mm long circular waveguide used as coupling structure. It was operated with a (partially) circularly polarized wave at 8.35 GHz in the power range 300 W – 3 kW. The diagnostics included a retarding potential analyzer (RPA), a Langmuir probe, an ion current mapping, a diamagnetic loop, radio frequency probes, a calorimeter, and a thrust balance. This study concluded that the total thruster efficiency was below 10%, and the ion energy between 25 and 70 eV, which is well below the expected value. Low electron energy was identified as the cause of low performance rather than poor conversion of electron energy into thrust (i.e., perpendicular electron temperature was in agreement with ion energy). Major experimental issues were identified, such as background pressure

effect (responsible for mass utilization efficiencies above 1), thermal drift of the thrust balance and mechanical perturbation by the pumps, outgassing of the thruster, non-repeatability, and thermal management issues limiting the duration of the runs to 10 min. Although clearly described, those issues were not tackled. In addition, considerable uncertainties as well as a large dispersion cloud the interpretation of the results.

By the end of the program, KOSMAHL ET AL. (1967) [14],[15], proposed a collisionless model of particle trajectories in a diverging magnetic field (nozzle), with a self-consistent calculation of a two dimensional axis-symmetric electrostatic potential. A few relevant measurements were selected to compare with numerical results. The comparison exhibited good agreement about the electrostatic potential shape and the beam divergence. Measurement and modelling agreed that particles do not follow field lines (i.e., detachment takes place) and that beam divergence is independent from ion mass and particle energy. However, the model strongly over-estimated the potential drop across the acceleration region. Collisions, partial circular polarization of the wave, and excitation processes were suggested as unmodelled phenomena responsible for the discrepancy.

The doctoral work of CRIMI (1967) [17] consisted in measurements similar to those of the CYCLOPS program, as well as an analysis of the phenomena playing a substantial role in the physics of the thruster. He estimated the power lost through three radiative channels (in increasing order of importance: cyclotron bremsstrahlung, free-bound, de-excitation), the characteristic times for collisions, the dispersion relation for a hot plasma, the required breakdown field, and the diffusion coefficient across the magnetic field. This modelling work allowed for the computation of a detailed integrated power balance. However, it was only a global model that did not provide solutions for relevant quantities in one or more dimensions. The measured electron energy and ion energy remained unexplained and the global power balance was not understood. The existence of multiply charged ions and radiation fluxes stronger than expected were suggested as an explanation. These hypotheses were not tested by means of experimental measurements.

A Princeton team conducted a similar experiment to that of the General Electric Space Science Laboratory yielding similar results (HENDEL, 1963 [18] and AHMED AND HENDEL, 1964 [19]). They reported 30% of total efficiency and up to 150 eV of ion energy. Such total efficiency is certainly chargeable to unwanted background gas ingestion, which is the consequence of an insufficient pumping speed. During the course of the CYCLOPS program, total efficiency above 40% was claimed [13] and later disproved [16].

Simultaneously, experiments were conducted at Tokyo University by NAGATOMO [20]–[22]. NAGATOMO (1967) [20] studied an ECRT prototype using coaxial coupling. He worked with an Argon plasma excited with about 400 W of microwave power at 2.45 GHz. He studied the effects of mass flow and magnetic field strength on electron temperature, ion energy, and microwave coupling to the plasma. The electrostatic potential was measured along a segment parallel to the thrust axis. The diagnostics included a thrust balance, a RPA, and a hot Langmuir probe. In addition, a one electron model for ECR energy gain, and a one dimensional flow model for a hot plasma in a diverging nozzle were proposed. The existence of an optimal magnetic field achieving 80% coupling was demonstrated experimentally. Ion energies up to 120 eV were measured at the lowest mass flow of 0.07 mg/s. This value is well below the prediction of the model at 0.07 mg/s. Nevertheless the predictions of the model are in line with experiments for higher mass flows. At 0.2 mg/s of Argon and 400W, the thrust balance measurements indicated 250μN of thrust applied on the coil generating the static magnetic field. Total efficiency is below 8%. Regrettably, the results of this very comprehensive study on coaxial coupling are limited

because the thruster was only run continuously for less than 5 min and the background operating pressure was as high as 10^{-4} mbar.

Although not propulsion oriented, the work of Bardet, Consoli, and Geller on ECR plasma acceleration should be acknowledged here. BARDET ET AL. (1964) measured the ion energy obtained with an ECR accelerator consisting of a TE111 cavity at 2.76 GHz immersed in a magnetic field gradient. The reported chamber pressure is about 10^{-5} mbar. For 400 W of deposited microwave power and a neutral Argon flow of 2.6 10^{16} atom/s (0.06 sccm), they measured a total flux of 7,2 10^{15} ion/s at 6 keV. Using electric propulsion performance indicators, this translates into 28% mass utilization efficiency and 1.7% power efficiency. This experiment demonstrates the possibility to achieve ion acceleration at levels that are largely sufficient for propulsion purposes. Therefore the important question, as later emphasized by SERCEL (1993) [23], is "*at what efficiency and at what power level can these devices be made to work for propulsion application ?"* For reference, at 400 W (the power deposited in this experiment) mature propulsion systems typically claim a total efficiency of 40% (see VIALIS (2018), figure 29 [24]).

In the late 1960's, while pulsed plasma thrusters as well as gridded ion thrusters had already flown in space and the development of Hall effect thrusters was well-advanced, the development efforts carried out on the ECRT did not demonstrate sufficient potential for the research to be continued. It revived briefly in the late 1980's, at the California Institute of Technology with Sercel's doctoral work [23], [25], [5] and a contract with the Air Force Office of Scientific Research [26]. Three reasons reportedly motivated this new feasibility study. Advancements in superconductor technology (for magnetic field generation), advancements in microwave technology, and advancements in ECR plasma physics, driven by two active areas of research: nuclear fusion and semiconductor etching.

SERCEL (1993) [23] designed and solved a first comprehensive quasi-1D flow model of the acceleration in the diverging magnetic field of an ECRT. He included Bohm diffusion, and argued that previous power balances may be wrong because of the use of classical diffusion. He studied the performance of a thruster using a circular waveguide as coupling structure, with 12 cm in diameter 6 cm in length. The prototype was operated with Argon and excited with a supposedly circularly polarized wave at 2.115 GHz. The input power was between 0.4 kW and 7 kW and the background pressure during operation was 2-5 10^{-5} mbar. The effect of background pressure was studied both numerically and experimentally. Sercel identified that high background pressure widens the ion energy distribution (and also causes unwanted background gas ingestion, as previously noticed). The best total efficiency was below 2%, which was attributed to low electron temperature rather than poor conversion of electron energy into ion directed kinetic energy, in agreement with the 1960's work. The model failed to predict performance, which implies that the inclusion of Bohm diffusion in the power balance is insufficient. The author concluded that an unidentified loss mechanism decreased electron temperature in the experiments. There are several limitations to this work: coupling from microwave power to the plasma was poorly measured, background pressure influenced the experimental results, and no thrust balance measurement was performed.

This disappointing performance caused the interruption of the research for the following two decades until a revival of the technology with a patent by Larigladie [27] at ONERA, France, and the follow-up studies in the plasma team leading to the doctoral work of CANNAT (2015) [28]–[31] in the early 2010's at ONERA. He evaluated the performance of a coaxial ECRT configuration with electrostatic probe measurements, using cryogenic pumping. The best performing prototype had a coaxial coupling structure of 29 mm in diameter and a variable length. It was operated at 2.45 GHz. The effect of magnetic field strength and propellant (Argon and Xenon) was studied. A model comprising a one dimensional discharge region followed by a two dimensional axis-symmetric flow region (the magnetic nozzle) was

adapted from LAFLEUR (2014) [32]. The experimental measurements unveiled the potential of the technology: at 8 10^{-6} mbar, 1 mN of thrust for 0.1 mg/s of Xenon and 30 W was claimed, corresponding to 16% total efficiency. This performance is in line with mature technologies ([24], figure 29). Xenon propellant proved better than Argon. The global power balance proposed by the model was in agreement with experimental measurements. Besides, it successfully predicted the thrust at 0.4 mg/s. Nevertheless, the model failed for lower mass flows (which are the mass flows of interest), only three geometrical configurations were tested, and no thrust balance measurement was performed to corroborate electrostatic probe estimates of thrust.

The doctoral work of VIALIS (2018) [24], [33]–[35] addressed both these experimental limitations. He performed reliable thrust balance measurements (meeting the challenges identified in the 1960's [16]) on a number of geometric configurations derived from that of Cannat, except for the use of a permanent magnet. Ion energy, jet divergence, and thrust were measured as a function of background pressure. Magnetic thrust and pressure thrust contributions were separately measured. Among several geometric configurations, this work identified the one maximizing total efficiency measured with the thrust balance: 12.5% for 0.06 mg/s of Xenon and 40 W. The author showed that the contributions of magnetic thrust and pressure thrust are primarily dependent on mass flow, rather than deposited power. Magnetic thrust is 70% of the total for 0.1 mg/s of Xenon and deposited power between 20 and 60 W. Thrust increased by a factor 2.7 when decreasing background operating pressure from 9.10^{-5} mbar down to 8.10^{-6} mbar. Ion energy, total current and divergence efficiency increased considerably. No asymptote was observed, which allows expecting better performance in space vacuum. However, the dispersion of experimental measurement was not addressed, only one injection was tested, the erosion of the inner conductor of the coaxial structure was insufficiently studied, and the thruster was usually operated during runs of 5 min only.

Summary of ECRT development and motivation for this study

The narrative of early research presented above intends to pay a tribute to the considerable effort directed at accurate performance measurements, identification of challenges, and identification of key phenomena driving the system. However, little quantitative information can be inferred from experiments before 2010, for at least three combined reasons: dispersion of measurements blurs the results, experimental difficulties often make the interpretation of results delicate if not impossible, and background operating pressure in the facility was too high. Therefore, early experiments seem to have missed the potential of the ECRT because of technical reasons. Since then however, the works on a coaxial configuration led by Vialis and Cannat with the plasma team at ONERA demonstrated performance commensurate with other technologies at the same power level.

In addition, the ECRT intrinsically bears significant advantages with respect to other propulsion systems which could lead to a device combining simplicity, robustness and easy operation. It is gridless, neutralizerless, and only requires one power supply as identified by the MINOTOR project [36]. The combination of these advantages with standard total thruster efficiency could lead to a very competitive propulsion system.

Nevertheless, the capacity to sustain prolonged efficient operation is still to be proved: we need to verify whether thrust will be stable and whether erosion of the inner conductor will limit the lifetime of the device. In addition, to strengthen existing measurements and advance on solid grounds, dispersion of measurements must be addressed.

This is the motivation for the present study. It consists in the development of an electron-cyclotron resonance thruster with magnetic nozzle and its accompanying experimental test set-up, able to accurately demonstrate high thruster efficiency during prolonged steady state operation.

Outline of the dissertation

Chapter 2 presents elements of the technological and scientific state of the art, as well as useful background knowledge. The preceding introduction is development-oriented and is intended for a reader having some familiarity with the field already. In contrast, chapter 2 intends to provide the necessary physical background and to present some key concepts of the field in a more didactical way. The first section is about microwave engineering. It provides the necessary framework and tools that were used throughout the experimental work. The second section deals with electric propulsion, presented from an application standpoint. It aims at situating the electron-cyclotron resonance thruster in the market of satellite propulsion. The third section considers the electron cyclotron resonance thruster from a plasma physics standpoint. It aims at giving a picture of how we presently understand the thruster.

Chapters 3 to 7 of this dissertation report the contribution of the doctoral work to the subject.

In chapter 3, the goal is to be able to accurately control the neutral gas feed and the deposited microwave power. Indeed, as previously reported and extensively observed at the beginning of our study, the variance of the measured data was so large that it precluded from comparison between different thruster configurations. In order to eliminate external perturbations and in order to make more accurate measurements, the experimental setup and measurement procedure were redesigned.

In chapter 4 the goal is to assess the accuracy of the plasma measurements, in particular the ion current measurement and the thrust balance measurement. To this end, we focus on the coherence between measurements: first, between diagnostics available at ONERA; second, between measurements made in two different vacuum facilities: the B61 facility at ONERA and the Jumbo facility at Justus Liebig University (JLU), Giessen.

In chapter 5, the goal is to further the coaxial ECRT experimental characterization, equipped with a better understanding of the diagnostics and operating conditions. First we focus on the 5 hour start-up transient as a possible explanation for a time-drift of measurements observed in the course of the previous chapter. Second, we address the crucial issue of inner conductor erosion, by measuring erosion for several materials. Third, we study the effect of neutral gas injection geometry and magnetic field topology. These three studies pave the way for the design and test of a larger ~ 200 W thruster promising greater efficiencies; preliminary results are presented.

In chapter 6, the goal is to explore waveguide-coupling instead of coaxial-coupling, as more radical solution to the erosion of the inner conductor, although promising results are obtained to mitigate inner conductor erosion. To this end, a waveguide-coupled thruster is designed and built. The coaxial and the waveguide thrusters, differing only by the coupling, are then experimentally characterized and compared using ion current angular density, ion energy, and thrust balance measurement. They are observed to yield very distinct results.

In chapter 7, the goal is to propose a global kinetic model of the thruster that calculates the formation of the electron energy distribution function. This goal is motivated by the experimental results of the previous chapters. We first study the trajectory of confined electrons in the thruster. From this analysis,

we propose a Fokker-Planck equation to model electron heating, and a simple way to account for losses. A parametric study is discussed.

Chapter 8 is the conclusion.

2. State of the art

The work presented in this document draws on results from different fields of knowledge and from a variety of experimental practices. This chapter presents some of the existing knowledge and knowhow in which this work takes its roots. It can be read as a complement to the introduction, in order to put in perspective the work described in the following chapters (this concerns mainly section 2.2 and 2.3). It may also be skipped and consulted when necessary, as it was meant as a practical toolbox for the reader (mainly section 0). As such, and contrary to all the following chapters, the subsections sometimes bear no connection with the adjoining subsections. The following chapters will frequently refer to the material presented here.

The first section is about microwave engineering. It provides the necessary framework and tools used throughout the experimental work. The second section deals with electric propulsion, presented from an application standpoint. It aims at situating the electron-cyclotron resonance thruster with magnetic nozzle in the market of satellite propulsion. The third section considers the electron cyclotron resonance thruster from a plasma physics standpoint. It aims at giving a picture of how we presently understand the thruster.

2.1 Elements of microwave engineering

Outline of the approach. Microwave engineering tools were used throughout this study: to design a robust transmission line in vacuum, to design a custom solution for mechanically decoupled microwave power transmission to the balance, to improve the accuracy of microwave power measurement, and to design a waveguide-coupled thruster. These tasks together constitute a considerable fraction of the work, for which we somewhat self-trained as microwave engineers. We wish that these efforts can benefit to future ECRT developments, hence the perhaps surprising length of this part for a plasma physics thesis.

Content

2.1.1 Maxwell equations

The Maxwell equations for sources in vacuum are the following [37].

$$\nabla \cdot \boldsymbol{E} = \frac{\rho}{\epsilon_0} \quad (1)$$

$$\nabla \cdot \boldsymbol{B} = 0 \quad (2)$$

$$\boldsymbol{\nabla} \times \boldsymbol{E} = -\frac{\partial \boldsymbol{B}}{\partial t} \quad (3)$$

$$\boldsymbol{\nabla} \times \boldsymbol{B} = \mu_0 \boldsymbol{J} + \mu_0 \epsilon_0 \frac{\partial \boldsymbol{E}}{\partial t} \quad (4)$$

$\boldsymbol{E}$ is the electric field and $\boldsymbol{B}$ the magnetic field or magnetic flux density, depending on the communities. Whatever their names, $\boldsymbol{E}$ and $\boldsymbol{B}$ are the quantities such that Lorentz force equation writes:

$$\mathbf{F} = \mathrm{q}(\boldsymbol{E} + \boldsymbol{v} \times \boldsymbol{B}). \quad (5)$$

Maxwell equations 1-4, so called "for sources in vacuum" or "for free sources" can also be thought of as microscopic Maxwell equations for any medium, for the fields everywhere in space down to the atomic scale. However, for the study of filled waveguides (resp. plasmas), the calculation of $\boldsymbol{E}$ and $\boldsymbol{B}$ everywhere at the atomic scale (resp. sub-Debye-length scale), is both irrelevant and intractable. It would require the knowledge of the source terms ρ and $\boldsymbol{J}$ at the same microscopic length-scale and consume huge computing power.

In these situations, among others, the knowledge of $\boldsymbol{E}$ and $\boldsymbol{B}$ averaged at some macroscopic length-scale is sufficient. Nevertheless, the knowledge of the source terms at this scale length is insufficient in general

to calculate $\boldsymbol{E}$ and $\boldsymbol{B}$ from equation 1-4. It is therefore relevant to break down the source terms into the contribution of free source on the one hand and bounded source on the other hand, the former having variations on the macroscopic scale length of interest and the latter having variations at the atomic scale.

$$\begin{aligned} \rho &= \rho_{bounded} + \rho_{free} \\ \mathbf{J} &= \mathbf{J}_{bounded} + \mathbf{J}_{free} \end{aligned} \quad (6)$$

Let's introduce the quantity $\boldsymbol{P}$ such that $\nabla \cdot \boldsymbol{P} = -\rho_{bounded}$ and $\nabla \cdot \boldsymbol{D} = \epsilon_0 \boldsymbol{E} + \boldsymbol{P}$. Then, equation 1 becomes

$$\nabla \cdot \boldsymbol{D} = \rho_{free}. \quad (7)$$

Similarly, introducing $\boldsymbol{M}$ such that $\boldsymbol{\nabla} \times \boldsymbol{M} + \frac{\partial \boldsymbol{P}}{\partial t} = \boldsymbol{J}_{bounded}$ and $\mathbf{H} = \frac{\boldsymbol{B}}{\mu_0} - \boldsymbol{M}$ equation 3 becomes

$$\boldsymbol{\nabla} \times \boldsymbol{H} = \frac{\partial \boldsymbol{D}}{\partial t} + \boldsymbol{J}_{free}. \quad (8)$$

Equations 2 and 3 are unchanged since this modification is about taking into account the source terms in a more convenient way and no source terms appear in these equations. Equations 1-4 then write

$$\nabla \cdot \boldsymbol{D} = \rho_{free} \quad (9)$$

$$\nabla \cdot \boldsymbol{B} = 0 \quad (10)$$

$$\boldsymbol{\nabla} \times \boldsymbol{E} = -\frac{\partial \boldsymbol{B}}{\partial t} \quad (11)$$

$$\boldsymbol{\nabla} \times \boldsymbol{H} = \frac{\partial \boldsymbol{D}}{\partial t} + \boldsymbol{J}_{free}. \quad (12)$$

A more detailed derivation of these "Maxwell equations in macroscopic media" can be found in JACKSON, section 6.7 [37]. In the process, the additional variables $\boldsymbol{P}$ and $\boldsymbol{M}$ have been introduced. To solve the equations, relations between $\boldsymbol{D}$ and $\boldsymbol{E}$ as well as between $\boldsymbol{H}$ and $\boldsymbol{B}$ are used. They express a modelling of the microscopic behavior of the medium.

2.1.2 Fields in a closed waveguide

In this section the electromagnetic field inside an infinite perfectly conducting waveguide are analyzed, following JACKSON chapter 8 [37] and POZAR chapter 3 [38]. In the more general meaning of the term a waveguide is a device guiding the propagation of electromagnetic waves (in particular at microwave frequencies) in a preferential direction. Constant section as well as uniform isotropic dielectric filling is assumed in the following. Exact detailed solutions are derived for a coaxial section (here thought of as a particular type of waveguide) and a circular section. These waveguides will be extensively used in this study.

2.1.2.1 Analysis for an arbitrary section

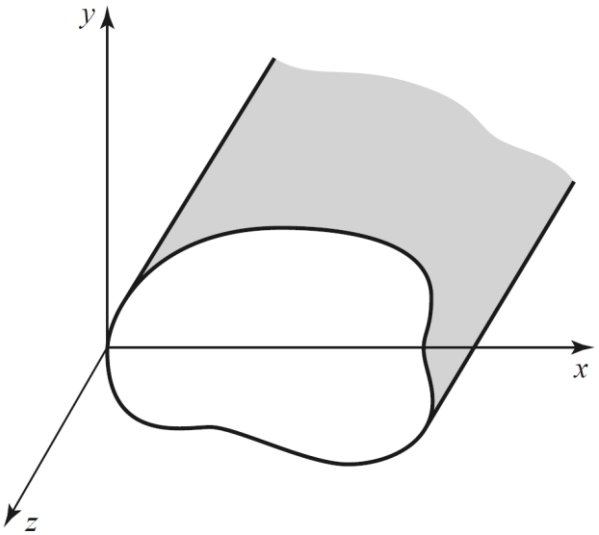

Figure 1. Arbitrary closed constant section of a waveguide [38]

For a uniform isotropic dielectric filling of the waveguide, $\boldsymbol{B} = \mu \boldsymbol{H}$ and $\boldsymbol{D} = \epsilon \boldsymbol{E}$, with μ and ϵ constant complex scalars. Besides, $\rho_{free} = 0$ and $\boldsymbol{J}_{free} = 0$. Then, we have (from 11 and 12)

$$\boldsymbol{\nabla} \times \boldsymbol{E} = -\mu \frac{\partial \boldsymbol{H}}{\partial t} \quad (13)$$

$$\boldsymbol{\nabla} \times \boldsymbol{H} = \epsilon \frac{\partial \boldsymbol{E}}{\partial t}. \quad (14)$$

Since the physical problem is invariant through translation in time and along z we may assume that the fields are periodic in t and z. They are then decomposed on a Fourier basis, each term of the decomposition being solution of the problem, for it is a linear problem. A given element of the decomposition writes

$$\boldsymbol{E}(x, y, z, t) = \boldsymbol{E}'(x, y) e^{-j(\omega t - \beta z)} \quad (15)$$

$$\boldsymbol{H}(x, y, z, t) = \boldsymbol{H}'(x, y) e^{-j(\omega t - \beta z)} \quad (16)$$

where ω is a radian frequency and β is a propagation constant, or wave number. By the choice of signs in the exponential we have chosen to proceed the analysis with the wave propagating in the $+z$ direction only. Then,

$$\boldsymbol{\nabla} \times \boldsymbol{E} = -j\omega\mu \boldsymbol{H} \quad (17)$$

$$\boldsymbol{\nabla} \times \boldsymbol{H} = j\omega\epsilon \boldsymbol{E}. \quad (18)$$

The full electromagnetic field can be derived from E_z and $\mathrm{H_z}$. Indeed, rearrangement of the components of equations 17 and 18 imply

$$\mathrm{H_x} = \frac{\mathrm{j}}{\mathrm{k_c^2}} \left(\omega\epsilon \frac{\partial \mathrm{E_z}}{\partial \mathrm{y}} - \beta \frac{\partial \mathrm{H_z}}{\partial \mathrm{x}} \right) \quad (19)$$

$$\mathrm{H_y} = \frac{-j}{k_c^2}\left(\omega\epsilon\frac{\partial E_z}{\partial x} + \beta\frac{\partial H_z}{\partial y}\right) \quad (20)$$

$$\mathrm{E_x} = \frac{-j}{k_c^2}\left(\beta\frac{\partial E_z}{\partial x} + \omega\mu\frac{\partial H_z}{\partial y}\right) \quad (21)$$

$$\mathrm{E_y} = \frac{j}{k_c^2}\left(-\beta\frac{\partial E_z}{\partial y} + \omega\mu\frac{\partial H_z}{\partial x}\right) \quad (22)$$

where $k_c^2 = k^2 - \beta^2$ and $\mathrm{k} = \omega\sqrt{\mu\epsilon}$. Let's start by determining the longitudinal fields, for which the presence of perfectly conducting walls forces the following constraints, on the surface S of the walls.

$$E_z|_S = 0 \quad (23)$$

$$\left.\frac{\partial \mathrm{H_z}}{\partial \mathrm{n}}\right|_{\mathrm{S}} = 0 \quad (24)$$

where $\frac{\partial}{\partial n}$ is the normal derivative at a point on the surface.

To do so, let's start again with equations 17 and 18. The second can be injected in the rotational of first and vice versa to yield

$$(\nabla^2 + \mu\epsilon\omega^2)\begin{Bmatrix}\boldsymbol{E}\\ \boldsymbol{H}\end{Bmatrix} = 0. \quad (25)$$

Given the z dependence that was assumed,

$$(\nabla_\mathrm{t}^2 + \mu\epsilon\omega^2 - \beta^2)\begin{Bmatrix}\mathbf{E}\\ \mathbf{H}\end{Bmatrix} = 0 \quad (26)$$

where ∇_t^2 is the transverse part of the Laplacian operator $\nabla_t^2 = \nabla^2 - \frac{\partial^2}{\partial z^2}$.

The third (resp. sixth) component of equation 26 specifies an eigenvalue problem for the operator $[\nabla_\mathrm{t}^2 + \mu\epsilon\omega^2]$ in the space of E_z (resp. $\mathrm{H_z}$) functions such that 23 (resp. 24) is satisfied. Since the conditions 23 and 24 are different, there is no reason a priori that the same eigenvalues be found for both problems. Yet, the same wavenumber (eigenvalue) was assumed for $\boldsymbol{E}$ and $\boldsymbol{H}$, to represent an electromagnetic wave field. Therefore E_z and $\mathrm{H_z}$ cannot both be non-zero for the same wavenumber. Three cases are then distinguished that together cover all the solutions to the problem.

4. **<u>TEM mode.</u>** $E_z = 0$ and $\mathrm{H_z} = 0$ is a solution of the problem. In this case, we see from equations 19-22 that a non-zero electromagnetic field is obtained if $k_c = 0$. This "transverse electromagnetic" mode is the same as that propagating in free space: $\boldsymbol{E}$ is orthogonal to $\boldsymbol{\beta}$, $\boldsymbol{H} = \frac{1}{\mu}\frac{\boldsymbol{\beta}\times\boldsymbol{E}}{\omega}$, and $\boldsymbol{\beta} = \omega\sqrt{\mu\epsilon}\boldsymbol{e_z}$ (non-dispersive). The TEM mode is then treated as an electrostatics problem in the plane parallel to the propagation direction. Although $\nabla\times\boldsymbol{E} \neq 0$, for any surface in that plane, $\iint \boldsymbol{\nabla}\times\boldsymbol{E}.\boldsymbol{dS} = 0$ from equation 17, implying that on the closed contour around that surface $\oint \boldsymbol{E}.\boldsymbol{dl} = 0$ therefore $\oint \boldsymbol{E'}.\boldsymbol{dl} = 0$. This justifies the existence of a two-dimensional scalar potential $\Phi(x, y)$ such that $\boldsymbol{E'} = -\boldsymbol{\nabla}\,\Phi$. In the absence of charges (using equation 1), Φ satisfies Laplace equation.

$$\nabla^2\Phi = 0 \quad (27)$$

5. **TE modes.** The "transverse electric modes" or "H waves" are solutions characterized by $E_z = 0$ and $H_z \neq 0$.

6. **TM modes.** The "transverse magnetic modes" or "E waves" are solutions characterized by $E_z \neq 0$ and $H_z = 0$.

2.1.2.2 Electromagnetic solutions for the coaxial line

The coaxial line is a compact, shielded and flexible solution to guide the propagation of microwaves. For those reasons it will be extensively used in this work. It is however a difficult medium in which to fabricate complex microwave components. Equivalent waveguide components may achieve better performance, for example higher directivity in the case of the bidirectional power coupler.

The coaxial line propagates electromagnetic waves in the gap between two coaxial cylindrical conductors (figure 2). It is mainly used to propagate the TEM mode, but also supports TE and TM modes above a certain cutoff frequency.

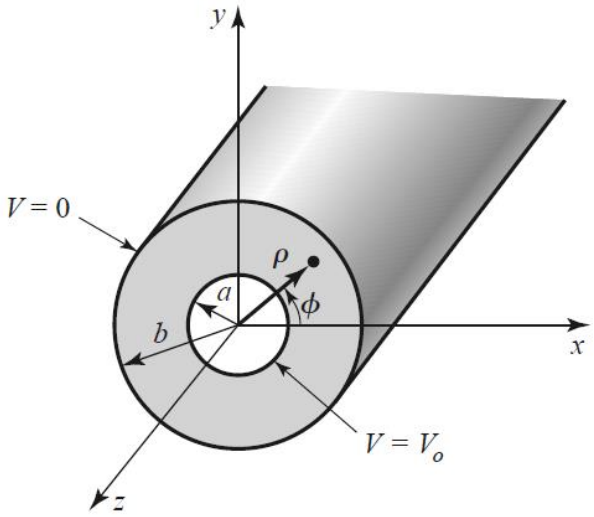

Figure 2. Geometry of a coaxial waveguide [38]

2.1.2.2.1 TEM mode

The two-dimensional Laplace equation 27 for $\Phi(\rho, \phi)$ writes in cylindrical coordinates:

$$\frac{1}{\rho}\frac{\partial}{\partial\rho}\left(\rho\frac{\partial\Phi}{\partial\rho}\right)+\frac{1}{\rho^2}\frac{\partial^2\Phi}{\partial\phi^2}=0. \quad (28)$$

The axis-symmetric boundary conditions imposed by the metallic structure are the reason behind the use of cylindrical coordinates. For any ϕ:

$$\Phi(a,\phi)=V_0 \quad (29)$$

$$\Phi(b,\phi)=0. \quad (30)$$

Assuming $\Phi(\rho,\phi)=R(\rho)P(\phi)$,

$$\frac{\rho}{R}\frac{\partial}{\partial\rho}\left(\rho\frac{\partial R}{\partial\rho}\right)+\frac{1}{P}\frac{\partial^2 P}{\partial\phi^2}=0. \quad (31)$$

Since the first term depends only on ρ and the second term only on ϕ, both must be equal to opposite constants,

$$\frac{\rho}{R}\frac{\partial}{\partial\rho}\left(\rho\frac{\partial R}{\partial\rho}\right) = n^2 \quad (32)$$

$$\frac{1}{P}\frac{\partial^2 P}{\partial\phi^2} = -n^2 \quad (33)$$

where the choice of signs is guided by the fact that we are looking for periodic solutions in ϕ. The general solution to the equation in ϕ is

$$P(\phi) = A\cos n\phi + B\sin n\phi \quad (34)$$

with A and B real constants. The axis-symmetric boundary conditions impose $n = 0$, thus for $\rho \neq 0$

$$\frac{\partial}{\partial\rho}\left(\rho\frac{\partial R}{\partial\rho}\right) = 0 \quad (35)$$

and

$$\Phi(\rho,\phi) = C\ln(\rho) + D. \quad (36)$$

Applying the boundary conditions,

$$\Phi(\rho,\phi) = \frac{V_0 \ln b/\rho}{\ln b/a}. \quad (37)$$

from which the full electromagnetic field can be derived. It is represented in figure 3a and writes

$$\mathbf{E} = -\boldsymbol{\nabla}\Phi = \frac{1}{\rho}\frac{V_0}{\ln b/a}\boldsymbol{e_\rho}$$

$$\boldsymbol{H} = \frac{1}{\mu}\frac{\boldsymbol{\beta}\times\boldsymbol{E}}{\omega} = \sqrt{\frac{\epsilon}{\mu}}\boldsymbol{e_z}\times\boldsymbol{E} = \frac{1}{\rho}\frac{V_0}{\eta\ln b/a}\boldsymbol{e_\theta} \quad (38)$$

where a $e^{-j\omega t\pm j\beta z}$ factor is understood and $\eta = \sqrt{\mu/\epsilon}$ the intrinsic impedance of the dielectric medium.

The TEM mode can propagate at any frequency. It has the dispersion relation of waves in free space $\beta = \omega\sqrt{\mu\epsilon}$ and the wavelength is independent from the sectional guiding geometry. In a coaxial line, the amplitude of the TEM electromagnetic fields is axis-symmetric and inversely proportional to the radius. The electric field is radial and the magnetic field azimuthal.

For an empty coaxial line ($\epsilon_r, \mu_r = 1$), at the usual working frequency for the study, $f_0 = 2.45$ GHz, the wavelength is $\lambda_{TEM}(2.45\ GHz) = 1/(f_0\sqrt{\mu_0\epsilon_0}) = 12.24$ cm.

2.1.2.2.2 TE and TM modes

The coaxial structure do accommodate propagating TE and TM modes above a certain cutoff wave number

$$k_c = \frac{2}{a+b}. \quad (39)$$

The details of the derivation of this limit, as well as calculation of the fields can be found in POZAR section 3.5 [38]. An example is represented in figure 3b. The fields could be derived from the same development that will be detailed for the circular waveguide in the next section. It will not be specifically presented here because the fields are irrelevant to this study since the cutoff frequency for these modes for the coaxial lines used is well above our working frequency.

For the CFP15 coaxial cable that will be used in the microwave line, $a = 2.24$ mm and $b = 5.78$ mm and $\epsilon_r = 1.16$ for the dielectric filling, so the cut of frequency is $f_c = k_c/(2\pi\sqrt{\mu\epsilon}) = 11.0$ GHz. These modes could only have a reactive effect near discontinuities or sources, where they may be excited[1].

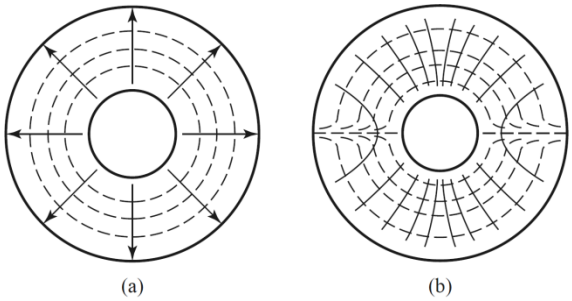

Figure 3. Field lines for the coaxial line, (a) for the TEM mode, and (b) for the TE11 mode. Solid: electric field. Dashed: magnetic field. [38]

2.1.2.3 Electromagnetic solutions for the circular waveguide

We will now focus on the circular waveguide because it is the type of waveguide that will be most used in this study, although the rectangular waveguide is usually presented first (perhaps because its solutions are proportional to the familiar sine and cosine functions). A circular waveguide is a cylindrical pipe that supports TE and TM modes. A well-known application of the circular waveguide is very low loss transmission which is achieved by the TE01 mode, because of some peculiarity in the electric field pattern implying monotonically decreasing conductor losses (see for example POZAR, figure 3.12 [38]). In addition, although a single polarization plane is possible in a rectangular waveguide, for non-axis-symmetric modes of the circular wave guide any polarization plane containing the direction of propagation is allowed. This is the reason for the use of circular waveguides in the ECR thruster work of CRIMI [17] in order to propagate circularly polarized waves, which are the combination of two waveguide modes with perpendicular direction of polarization and a $\pi/2$ phase shift.

Again because this structure imposes axis-symmetric boundary conditions it is convenient to work with the cylindrical coordinates defined in figure 4.

[1] With the dimensions in the example, TE and TM modes are evanescent modes at 2.45 GHz, thus they only carry reactive power ($E \times \bar{H}$ is pure imaginary). They are exponentially decaying for the problem of the infinite coaxial line, thus they may appear only near "a perturbation to this problem", for example a discontinuity or a source.

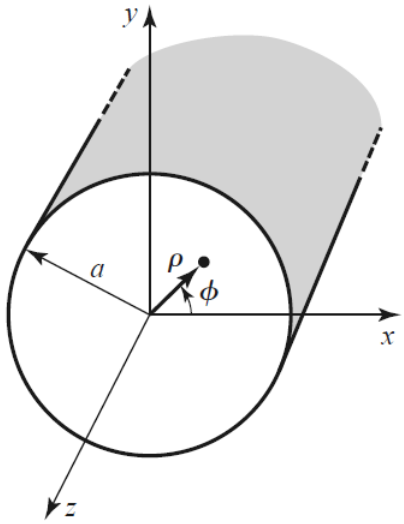

Figure 4. Geometry of a circular waveguide [38]

2.1.2.3.1 Absence of the TEM mode

The same reasoning as that presented in section 2.1.2.2.1 can be applied here up to the derivation of equation 36. However, for the circular waveguide, the solution should be valid up to the limit $\rho \to 0$, so $C = 0$. Therefore the potential Φ is constant and the fields are zero. Two conductors are required to support the TEM mode.

2.1.2.3.2 TE modes

In order to derive the TE modes equations 19-22 can be re-written in cylindrical coordinates as

$$\mathrm{H_\rho} = \frac{\mathrm{j}}{\mathrm{k_c^2}}\left(\frac{\omega\epsilon}{\rho}\frac{\partial \mathrm{E_z}}{\partial \phi} - \beta\frac{\partial \mathrm{H_z}}{\partial \rho}\right) \quad (40)$$

$$\mathrm{H_\phi} = \frac{-j}{k_c^2}\left(\omega\epsilon\frac{\partial E_z}{\partial \rho} + \frac{\beta}{\rho}\frac{\partial H_z}{\partial \phi}\right) \quad (41)$$

$$\mathrm{E_\rho} = \frac{-j}{k_c^2}\left(\beta\frac{\partial E_z}{\partial \rho} + \frac{\omega\mu}{\rho}\frac{\partial H_z}{\partial \phi}\right) \quad (42)$$

$$\mathrm{E_\phi} = \frac{j}{k_c^2}\left(-\frac{\beta}{\rho}\frac{\partial E_z}{\partial \phi} + \omega\mu\frac{\partial H_z}{\partial \rho}\right) \quad (43)$$

where $k_c^2 = k^2 - \beta^2$ and $\mathrm{k} = \omega\sqrt{\mu\epsilon}$. For TE modes, $\mathrm{E_z} = 0$ and $\mathrm{H_z}$ is determined from equation 26

$$(\nabla_\mathrm{t}^2 + \mu\epsilon\omega^2 - \beta^2)\mathrm{H_z} = 0. \quad (44)$$

If $\mathrm{H_z}(\rho, \phi, z) = H'_z(\rho, \phi)e^{-j\beta z}$,

$$\frac{1}{\rho}\frac{\partial}{\partial \rho}\left(\rho\frac{\partial H'_z}{\partial \rho}\right) + \frac{1}{\rho^2}\frac{\partial^2 H'_z}{\partial \phi^2} + k_c^2 H'_z = 0. \quad (45)$$

Assuming that $H'_z(\rho, \phi) = R(\rho)P(\phi)$ we get

$$\frac{\rho}{R}\frac{\partial}{\partial \rho}\left(\rho\frac{\partial \mathrm{R}}{\partial \rho}\right) + \frac{1}{P}\frac{\partial^2 \mathrm{P}}{\partial \phi^2} + \rho^2 k_c^2 = 0. \quad (46)$$

and

$$\frac{\rho^2}{R}\frac{\partial^2 R}{\partial \rho^2}+\frac{\rho}{R}\frac{\partial R}{\partial \rho}+\rho^2 k_c^2=-\frac{1}{P}\frac{\partial^2 \mathrm{P}}{\partial \phi^2} \quad (47)$$

where the right-hand side depends only on ϕ and the left-hand side only on ρ. Thus both sides must be equal to a constant.

$$\frac{\rho^2}{R}\frac{\partial^2 R}{\partial \rho^2}+\frac{\rho}{R}\frac{\partial R}{\partial \rho}+\rho^2 k_c^2=n^2 \quad (48)$$

$$\frac{1}{P}\frac{\partial^2 \mathrm{P}}{\partial \phi^2}=n^2 \quad (49)$$

where the choice of signs is guided by the fact that we are looking for periodic solutions in ϕ. More specifically, we are looking for 2π-periodic solutions in ϕ which implies that n is integer. The general solution to the equation in ϕ is

$$\mathrm{P}(\phi)=A\cos n\phi+B\sin n\phi \quad (50)$$

with A and B real constants. The equation in ρ can be recast as

$$\rho^2\frac{\partial^2 R}{\partial \rho^2}+\rho\frac{\partial R}{\partial \rho}+(\rho^2 k_c^2-n^2)R=0 \quad (51)$$

which is the Bessel differential equation. The solution is

$$\mathrm{R}(\rho)=CJ_n(k_c\rho)+DY_n(k_c\rho), \quad (52)$$

where J_n and Y_n are the Bessel functions of the first and second kinds respectively. Because Y_n tends to infinity when the variable approaches 0, this term is physically unacceptable for a circular waveguide, so $D=0$. The solution for H'_z is

$$H'_z(\rho,\phi)=(A'\cos n\phi+B'\sin n\phi)J_n(k_c\rho) \quad (53)$$

From which the full electromagnetic field is found using relations 40-43 . In order to derive the dispersion relation we enforce the boundary condition

$$\mathrm{E}_\phi(a,\phi)=0\ \ \forall\phi. \quad (54)$$

Since $\mathrm{E_z}$, substituting equation 53 into 43 yields

$$E_\phi(\rho,\phi,z)=\frac{j\omega\mu}{k_c}(A'\cos n\phi+B'\sin n\phi)J'_n(k_c\rho)e^{-j\beta z}. \quad (55)$$

where J_n' is the derivative of the first kind Bessel function of order n. The boundary condition implies

$$J_n'(k_c a)=0, \quad (56)$$

which is satisfied for any m for $k_c a=p'_{nm}$ where p'_{nm} is the m-th root of J_n'.

The TE modes are a discrete set of modes indexed by $n\in\mathbb{N}$ and $m\in\mathbb{N}^*$, where n refers to the periodicity in ϕ and m to the number of radial zeros. The dispersion relation of the $\mathrm{TE_{nm}}$ mode is

$$\beta_{\mathrm{nm}}^{TE} = \sqrt{k^2 - k_{c,nm}^2} = \sqrt{k^2 - \left(\frac{p'_{nm}}{a}\right)^2}. \quad (57)$$

Besides, the cutoff frequency is

$$\mathrm{f_c^{TE}} = \frac{\mathrm{k_c}}{2\pi\sqrt{\mu\epsilon}} = \frac{\mathrm{p'_{nm}}}{2\pi a\sqrt{\mu\epsilon}}, \quad (58)$$

and the wave impedance is

$$\mathrm{Z_w^{TE}} := \frac{E_\rho}{H_\phi} := -\frac{E_\phi}{H_\rho} = \frac{\eta k}{\beta} \quad (59)$$

where $\eta := \sqrt{\mu/\epsilon}$. For non-axis-symmetric modes ($n \neq 0$), each $\mathrm{TE_{nm}}$ mode is in fact a continuous set of modes identified by their ϕ-orientation. The constants A' and B' are determined by the amplitude of the wave and, if relevant, its polarization, meaning its "ϕ-orientation".

2.1.2.3.3 TM modes

Starting with $\mathrm{H_z} = 0$, along with the wave equation

$$(\nabla_\mathrm{t}^2 + \mu\epsilon\omega^2 - \beta^2)\mathrm{E_z} = 0, \quad (60)$$

and the boundary condition

$$\mathrm{E_z}(a, \phi) = 0 \ \ \forall\phi, \quad (61)$$

the same reasoning yields the fields for the $\mathrm{TM_{nm}}$ modes as well as the dispersion relation

$$\beta_{\mathrm{nm}}^{TM} = \sqrt{k^2 - k_{c,nm}^2} = \sqrt{k^2 - \left(\frac{p_{nm}}{a}\right)^2} \quad (62)$$

where p_{nm} is the m-th root of J_n.

Besides the cutoff frequency is

$$\mathrm{f_c^{TM}} = \frac{\mathrm{k_c}}{2\pi\sqrt{\mu\epsilon}} = \frac{\mathrm{p_{nm}}}{2\pi a\sqrt{\mu\epsilon}}, \quad (63)$$

and the wave impedance is

$$\mathrm{Z_w^{TM}} := \frac{E_\rho}{H_\phi} := -\frac{E_\phi}{H_\rho} = \frac{\eta\beta}{k}. \quad (64)$$

The dispersion relation for the three lowest order modes (i.e. having lowest cutoff frequencies) is plotted in figure 5 for an empty circular waveguide with $a = 43$ mm. The linear dispersion relation of the TEM mode is plotted for reference although it does no propagate in a circular waveguide.

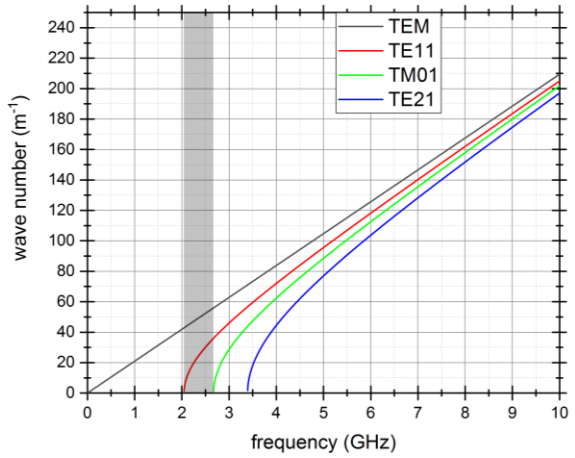

Figure 5. Dispersion relation for three lowest order modes of the circular waveguide. Wavenumber is calculated for a 43 mm-radius empty waveguide. The linear dispersion relation of the TEM mode is plotted for reference. The grey interval indicates the mono-mode frequency-interval of the TE11 mode.

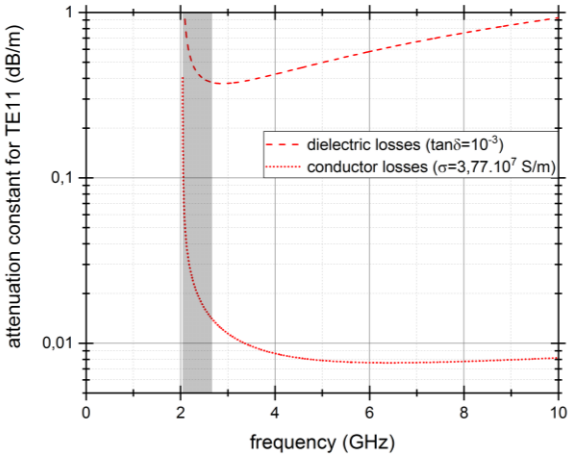

Figure 6. Attenuation constants for a 43 mm-radius aluminum ($\sigma = 3.77.10^7 S/m$) waveguide filled with a dielectric having a loss tangent ($tan\ \delta = 10^{-3}$) constant with frequency. The grey interval indicates the mono-mode frequency-interval of the TE11 mode.

2.1.2.3.4 The TE11 mode

The fundamental mode (i.e. with the lowest cutoff frequency) of the circular waveguide is the TE11 mode. It will be extensively used in this study, both for transmission of the microwave power up to the thruster and for coupling to the plasma in the case of the waveguide coupled thruster. The fields of this mode write (a $e^{-j\omega t - j\beta z}$ factor is understood):

$$\mathrm{H}_\rho = -\frac{j\beta}{k_c} A \sin\phi\ J_1'(k_c\rho) \quad (65)$$

$$\mathrm{H}_\phi = \frac{-j\beta}{k_c^2\rho} A \cos\phi\ J_1(k_c\rho) \quad (66)$$

$$\mathrm{H}_z = A \sin\phi\ J_1(k_c\rho) \quad (67)$$

$$\mathrm{E}_\rho = \frac{-j\omega\mu}{k_c^2\rho} A \cos\phi\ J_1(k_c\rho) \quad (68)$$

$$\mathrm{E}_\phi = \frac{j\omega\mu}{k_c} A \sin\phi\ J_1'(k_c\rho) \quad (69)$$

$$\mathrm{E}_z = 0 \quad (70)$$

It is a non-axis-symmetric mode represented in figure 7. The orientation of the fields in the sectional plane (polarization) is determined by the excitation.

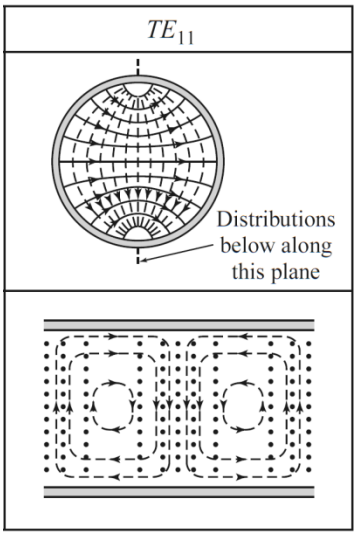

Figure 7. Electromagnetic field lines for the TE11 mode. Solid line: electric field. Dashed line: magnetic field. Dots: electric field lines perpendicular to the figure plane [39]

For an empty circular waveguide ($\epsilon_r, \mu_r = 1$) with radius $a = 43$ mm, at the usual working frequency for the study, $f_0 = 2.45$ GHz, the wavelength is, from relation 57 ,

$$\lambda_{TE11}(2.45\ GHz) = 2\pi\left(k^2 - \left(\frac{p'_{11}}{a}\right)^2\right)^{-1/2} = 2\pi\left(\left(2\pi f_0\sqrt{\mu_0\epsilon_0}\right)^2 - \left(\frac{1.841}{0.043}\right)^2\right)^{-1/2} = 22{,}22 \text{ cm}.$$

Power losses can originate either from the finite conductivity of the walls or from non-zero permittivity of the dielectric filling the waveguide. Both can be analytically calculated following a perturbation method, meaning that we calculate the losses on the field previously derived under the assumption of a perfect conductor and lossless dielectric, instead of recalculating the fields from Maxwell equations under the assumption of finite conductivity and complex permittivity. This approach is valid for sufficiently high conductivity (skin depth $\delta_s = \sqrt{2/\omega\mu\sigma} \ll a$) and sufficient low imaginary part in the permittivity ($\tan\delta \ll 1$) so that the fields of the lossy line are not greatly different from that of the corresponding lossless line. The loss tangent $\tan\delta$ is the ratio of the imaginary part of the permittivity to the real part of the permittivity.

The calculation of the attenuation constant for dielectric losses requires only the knowledge of the wave number and results in the expression

$$\alpha_d = \frac{k^2 \tan\delta}{2\beta}\ Np/m \qquad (71)$$

in neper per meter, meaning that $e^{-\alpha_d z}$ factors the lossless fields. Also, $\alpha_d[dB/m] = 20\log(\exp(\alpha_d[Np/m]))$. On the contrary, the calculation of the attenuation constant for conductor losses necessitates the detailed electromagnetic field. For the TE11 mode of the circular waveguide, the attenuation constant writes

$$\alpha_c = \frac{R_S}{ak\eta\beta}\left(k_c^2 + \frac{k^2}{p_{11}'^2 - 1}\right)\ Np/m \qquad (72)$$

where R_S is the surface conductivity of the walls $R_S := \sqrt{\omega\mu/2\sigma}$ and η is the intrinsic impedance of the dielectric medium $\eta := \sqrt{\mu/\epsilon}$. The derivation of these expressions is in POZAR chapter 3 [38]. They are

plotted in figure 6, for a constant typical loss tangent of a good dielectric microwave material and the conductivity of aluminum. Two interesting properties are apparent on the plot. First, for dense material, dielectric losses dominate conductor losses. (On the contrary for air filled waveguides, dielectric losses are negligible.) Second, the losses steeply increase when approaching the cutoff frequency.

The choice of dimensions of a waveguide operated at a certain frequency is governed by the cutoff frequencies of the desired propagating-modes as well as that of the next higher order mode, attenuation, and voltage breakdown [40]. For most applications, the waveguide dimension is chosen such that only the fundamental mode propagates. If not, imperfection on the line may enable power transfer between modes. In addition it is preferred that the working frequency be significantly higher than the cutoff frequency, for two reasons. First, it avoids distorting signal because the higher the frequency the lower the dispersion (figure 5). Second, it reduces power loss, since, in the mono-mode interval, the higher the frequency the lower the dissipation.

2.1.3 Transmission line theory

Transmission line theory primarily applies to two conductor transmission lines operated in the TEM mode. However, it can be applied to some extent to TE and TM modes. In the literature, the phrase "transmission line" may refer to any structure extending in some direction to guide the propagation of electromagnetic waves. It may also refer specifically to two conductor structures such as the coaxial line, the stripline, the two-wire line or the slotline. Symmetrically, the term "waveguide" may have the former meaning of "transmission line" or may refer specifically to one conductor closed structures such as the rectangular waveguide or circular waveguide.

2.1.3.1 Telegrapher's equation and notion of impedance

There are a number of microwave engineering problems for which the knowledge of the electromagnetic field is dispensable because the phenomena under study can be represented by transmission line theory. Transmission line theory deals with two conductor transmission lines supporting one dimensional voltage and current waves. Instead of considering a three dimensional propagation medium (with dielectric volumes and conducting surfaces) as in the previous sections, the propagating medium is represented by a distributed resistance, conductance, inductance and capacitance. Transmission line theory can therefore be considered as a one-dimensional reduction of electromagnetic theory. It can also be thought of as an extension of lumped-element circuit theory for cases such that the circuit dimensions are not small compared to the wavelength of the signal.

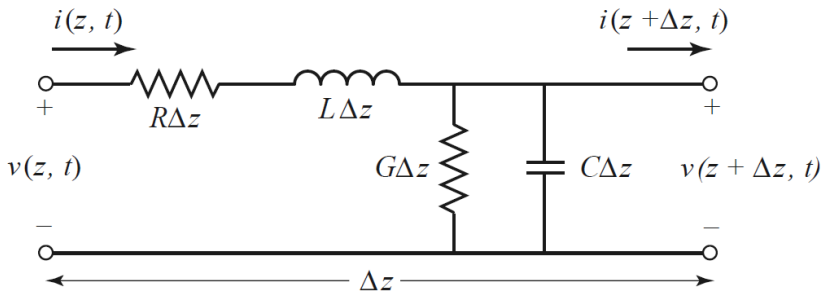

Figure 8. Lumped element equivalent circuit [38]

The transition from lumped-element circuit theory to transmission line theory can be performed by considering a circuit such as that represented in figure 8. Writing Kirchhoff's voltage law and Kirchhoff's current law and taking the limit $\Delta z \rightarrow 0$, the telegrapher's equations are obtained:

$$\frac{\partial \mathrm{v(z,t)}}{\partial \mathrm{z}} = -Ri(z,t) - L\frac{\partial \mathrm{i(z,t)}}{\partial \mathrm{t}} \quad (73)$$

$$\frac{\partial \mathrm{i(z,t)}}{\partial \mathrm{z}} = -G\mathrm{v(z,t)} - C\frac{\partial \mathrm{v(z,t)}}{\partial \mathrm{t}}. \quad (74)$$

For sinusoidal steady state solutions we get

$$\frac{\mathrm{dV(z)}}{\mathrm{dz}} = -(R + j\omega L)I(z) \quad (75)$$

$$\frac{\mathrm{dI(z)}}{\mathrm{dz}} = -(G + \mathrm{j\omega C})\mathrm{V(z)}. \quad (76)$$

that can be combined to yield wave equations for both quantities

$$\frac{\mathrm{d^2V(z)}}{\mathrm{dz^2}} - \beta^2 V(z) = 0 \quad (77)$$

$$\frac{\mathrm{d^2I(z)}}{\mathrm{dz^2}} - \beta^2 I(z) = 0 \quad (78)$$

where $\beta = \sqrt{(R + j\omega L)(G + j\omega C)}$ is the complex wave number, which is a function of frequency. The solutions are

$$V(z) = V_0^+ e^{-\beta z} + V_0^- e^{+\beta z} \quad (79)$$

$$I(z) = I_0^+ e^{-\beta z} + I_0^- e^{+\beta z}. \quad (80)$$

From equation 75, the voltage and current amplitudes are related by a quantity, called characteristic impedance of the line:

$$Z_0 := \frac{V_0^+}{I_0^+} = -\frac{V_0^-}{I_0^-} = \sqrt{\frac{R + j\omega L}{G + j\omega C}}. \quad (81)$$

It is the ratio of voltage and current for a wave travelling in one direction towards an infinite line. The notion of impedance is crucial to transmission line theory. For each type of transmission line, electromagnetic field analysis provides an expression for the characteristic impedance of the line, as a function of geometric and electromagnetic quantities. It is calculated for the TEM mode. For example, for the lossless coaxial line (figure 2):

$$Z_0^{coax} = \sqrt{\frac{\mu}{\epsilon}}\frac{\ln(b/a)}{2\pi}. \quad (82)$$

It is a very convenient definition appearing in many calculations. For example the power flowing through a section of coaxial line can be calculated from the complex fields (definition 38) to be

$$\mathrm{P_{coax}} = \frac{1}{2}\mathrm{Re}\int_S \boldsymbol{E}_+ \times \overline{\boldsymbol{H}_+}\,\boldsymbol{dS} = \frac{1}{2}\int_a^b\int_0^{2\pi} \frac{1}{\eta}\frac{1}{\rho^2}\left(\frac{V_0}{\ln b/a}\right)^2 \rho\rho d\,d\phi = \frac{V_0^2}{2Z_0} = \frac{Z_0 I_0^2}{2}. \quad (83)$$

Three definitions of impedance should be distinguished, although they may coincide in some instances.

1. *Impedance of an electromagnetic mode,* $Z_w := E_t \backslash H_t$, which depends on the geometry of the conductors, on the dielectric material, and for non TEM modes on frequency.

2. *Characteristic impedance of a homogeneous and isotropic medium,* $\eta := \sqrt{\mu/\epsilon}$, which is dependent only on the medium and is equal to the wave impedance of the TEM mode.

3. *Characteristic impedance of a transmission line,* $Z_0 := V_0^+/I_0^+$. We see from relation 82 for example that it is different from the impedance of the TEM mode, the latter being independent of geometric parameters. This concept may be extended to waveguides, although it proves less effective and calls on a less evident definition. Because $\iint \boldsymbol{\nabla} \times \boldsymbol{E}.\boldsymbol{dS} \neq 0$, contrary to TEM transmission lines, there is no well-define electrostatic potential, hence no well-define voltage to build an impedance definition upon.

2.1.3.2 Terminated transmission line

A typical situation of transmission line theory is that of figure 9: a transmission line is terminated by a load impedance imposing $V(0) = Z_L I(0)$.

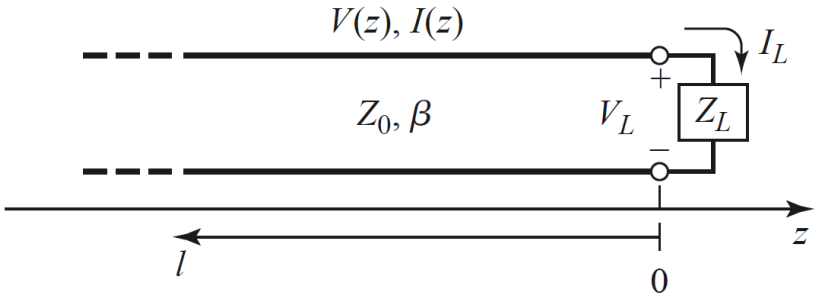

Figure 9. Transmission line terminated by load impedance Z_L [38]

Straightforward calculation show that the satisfaction of this boundary condition requires the existence of a reflected wave with amplitude V_0^- such that

$$\Gamma := \frac{V_0^-}{V_0^+} = \frac{Z_L - Z_0}{Z_L + Z_0}. \quad (84)$$

Γ is the voltage reflection coefficient at $z = 0$. *If* $\mathrm{Z_L} = \mathrm{Z_0}$, *there is no reflected wave and the line is said to be terminated by a matched load or adapted load.* This relation is equivalent to

$$\mathrm{Z_L} = Z_0\frac{1+\Gamma}{1-\Gamma}. \quad (85)$$

The quantity Γ can be defined at any point on the line,

$$\Gamma(z) \coloneqq \frac{V_0^- e^{-j\beta z}}{V_0^+ e^{+j\beta z}} = \Gamma e^{-2j\beta z} \quad (86)$$

meaning that the perceived impedance varies with the position on the line (which is not the case in circuit theory). This justifies the definition of an input impedance "seen by the wave", looking towards the load from z:

$$\mathrm{Z_{in}}(z) = Z_0 \frac{1+\Gamma(z)}{1-\Gamma(z)} = Z_0 \frac{1+\Gamma e^{-2j\beta z}}{1-\Gamma e^{-2j\beta z}}. \quad (87)$$

The first equality is simply the equation 85 written for an arbitrary z location. To obtain the second expression, relation 86 was used. Substituting Γ from 84 yields the following more practical relation.

$$\mathrm{Z_{in}}(z) = Z_0 \frac{Z_L + jZ_0 \tan \beta z}{Z_0 + jZ_L \tan \beta z} \quad (88)$$

2.1.3.3 Junction between two lines

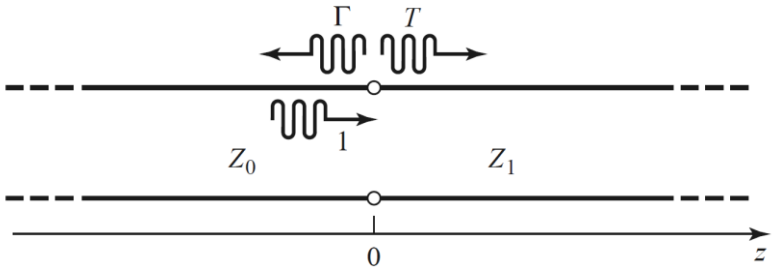

Figure 10. Junction of two lines with different characteristic impedances [38]

Figure 10 is another typical situation of transmission line theory: transmission and reflection at the junction between two lines with different characteristic impedances. If the line on the right is infinite or loaded with $\mathrm{Z_1}$, the impedance seen by the line on the left is $\mathrm{Z_1}$. No wave travelling to the left is considered on the right side. Therefore the voltage reflection coefficient is

$$\Gamma_{01} = \frac{Z_1 - Z_0}{Z_1 + Z_0}. \quad (89)$$

Continuity of voltage at $z = 0$ yields the voltage transmission coefficient:

$$\mathrm{T_{01}} = \frac{2Z_1}{Z_1 + Z_0}. \quad (90)$$

These coefficients point out the analogy between characteristic impedance of a line and the refractive index of a medium. They have the same form as the Fresnel coefficients in amplitude for normal incidence (if 1 and 0 are swapped) and verify the following relations.

$$\mathrm{T_{01}} = 1 + \Gamma_{01}\,,\ \Gamma_{10} = -\Gamma_{01} \quad (91)$$

Analogy with the Fresnel coefficient may save us the calculation of the coefficients in power

$$\Gamma_{01}^{\mathrm{P}} = \Gamma_{01}\overline{\Gamma_{01}}\,,\ \mathrm{T}_{10}^{P} = \frac{Z_0}{Z_1}\mathrm{T_{01}}\overline{\mathrm{T_{01}}} \quad (92)$$

that verify as expected the conservation of power $1 - \Gamma_{01}^{P} - T_{10}^{P} = 0$. The bar denotes complex conjugate.

2.1.3.4 Quarter wave transformer

A more complex situation is that of the succession of three different characteristic impedances. It may challenge our intuition of reflection coefficient, forged by the well-known derivation of Fresnel coefficient (figure 10), for which no wave travelling to the left is considered in the right hand medium. This situation can be treated from an impedance view point using relation 88, but it may be more instructive to analyze it using a multiple reflection view point (figure 11).

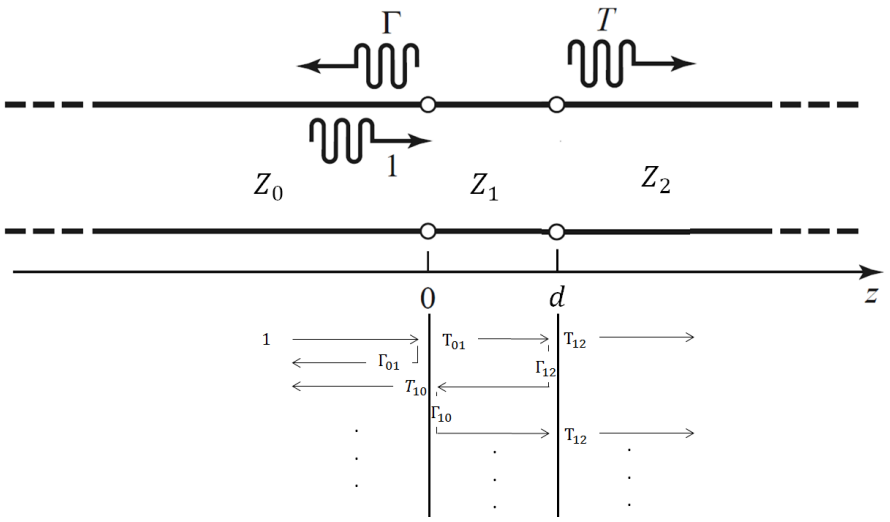

Figure 11. Three successive lines with different characteristic impedances

This approach consists in following the path of a wave front, undergoing a succession of reflections, propagation in line 1, and transmissions. The total reflection coefficient can be calculated as the following sum of complex amplitudes at $z = 0$.

$$\Gamma = \Gamma_{01} + T_{10}e^{j\beta_1 d}\,\Gamma_{12}\,e^{j\beta_1 d}\,T_{01} + T_{10}e^{j\beta_1 d}\,\Gamma_{12}e^{j\beta_1 d}(\Gamma_{10}e^{j\beta_1 d}\,\Gamma_{12}\,e^{j\beta_1 d})\,T_{01} + \cdots \quad (93)$$

Which is the sum of a geometric series.

$$\Gamma = \Gamma_{01} + T_{10}\frac{1}{\Gamma_{10}}\left(\sum_{1}^{\infty}\left(\Gamma_{10}\,\Gamma_{12}e^{2j\beta_1 d}\right)^{n}\right)T_{01} = \Gamma_{01} + \frac{T_{10}T_{01}}{\Gamma_{10}}\,\frac{\Gamma_{12}\Gamma_{10}e^{2j\beta_1 d}}{1 - \Gamma_{12}\Gamma_{10}e^{2j\beta_1 d}} \quad (94)$$

Using relations 91:

$$\Gamma = \frac{\Gamma_{01} + \Gamma_{12}e^{2j\beta_1 d}}{1 + \Gamma_{12}\Gamma_{01}e^{2j\beta_1 d}}. \quad (95)$$

The transmission coefficient at $z = d$ can be calculated similarly:

$$T = T_{01}e^{j\beta_1 d}T_{12} + T_{01}e^{j\beta_1 d}\left(\Gamma_{10}e^{j\beta_1 d}\Gamma_{12}e^{j\beta_1 d}\right)T_{12} + \cdots \quad (96)$$

$$\mathrm{T} = T_{01} e^{j\beta_1 d} \left(\sum_0^{\infty} \left(\Gamma_{10}\, \Gamma_{12} \mathrm{e}^{2\mathrm{j}\beta_1 \mathrm{d}} \right)^n \right) T_{12} = \frac{\mathrm{T}_{01}\mathrm{T}_{12}\, \mathrm{e}^{\mathrm{j}\beta_1 \mathrm{d}}}{1 + \Gamma_{12}\Gamma_{01}\mathrm{e}^{2\mathrm{j}\beta_1 \mathrm{d}}}. \quad (97)$$

These relations are valid even if the propagation constant in line 1 is complex or pure imaginary (evanescent waves). In this latter case, if d does not exceeds a few wavelengths, a fraction of the incident wave from 0 wave can be transmitted to 2 even though 1 only supports evanescent solutions. The same relations apply in optics where this phenomenon is known as frustrated total internal reflection.

The quarter wave transformer is a particular lossless situation where $\mathrm{d} = \lambda_1/4$ and $Z_1 = \sqrt{Z_0 Z_2}$. It follows that $\mathrm{e}^{\mathrm{j}2\beta_1 \mathrm{d}} = -1$ and $\Gamma_{01} = \Gamma_{12}$ (thus $\mathrm{T}_{01} = \mathrm{T}_{12}$). Therefore $\Gamma = 0$ and $\mathrm{T} = \mathrm{j}(1 + \Gamma_{01})/(1 - \Gamma_{01})$. It is a common misconception to expect $\mathrm{T} = 1$, whereas on the contrary the difference in impedances requires $\mathrm{T} \neq 1$ to conserve power flow. Only the transmission coefficient in power T^{P} equals 1, as can be verified from the relations 92:

$$\mathrm{T}^{\mathrm{P}} = \frac{Z_0}{Z_2}\left(\frac{1+\Gamma_{01}}{1-\Gamma_{01}}\right)^2 = \frac{Z_0}{Z_2}\left(\frac{Z_1}{Z_0}\right)^2 = \frac{Z_0 Z_2}{Z_0 Z_2} = 1. \quad (98)$$

The quarter wave transformer is a technical solution to achieve full transmission of power between two lines of different characteristic impedances.

2.1.3.5 Scope of effectivity of the concept of impedance

Even for relatively abrupt transitions on a coaxial line, the prediction of reflection and transmission from the impedance on both sides (relations 89 and 90) proves very effective. However, in general, these relations are valid only for the characteristic impedance of a two conductor transmission line supporting a TEM mode.

Although characteristic impedances for guided TE or TM modes may be proposed (for example RIZZI relations 5-98 and 5-99 [41]) *most results derived in the framework of transmission line theory do not apply with these characteristic impedances.*

To exemplify this statement, let's look at the transition on a circular waveguide represented in figure 12. The proposed characteristic impedance definitions for guided TE and TM waves are all proportional to the wave impedance. Therefore, it is enough to test one, since relations 89 and 90 are left unchanged by application of a multiplicative factor on the characteristic impedance. For the circular waveguide case, wave impedance of the TE11 mode is used as characteristic impedance. The reflected power fractions from transmission line theory as well as from COMSOL simulation are presented in table 1. The coefficient from transmission line theory, calculated with wave impedance, fails to predict the reflected power fraction for the transition on a circular waveguide whereas it succeeds even for an abrupt transition on a coaxial line.

Reference in figure 12	Reflected power ($\|S11\|^2$) from finite element simulation	Reflected power ($\|S11\|^2$) from relation 92
a	26.8%	26.7%
b	86%	28%

Table 1. Reflected power for the junctions in figure 12

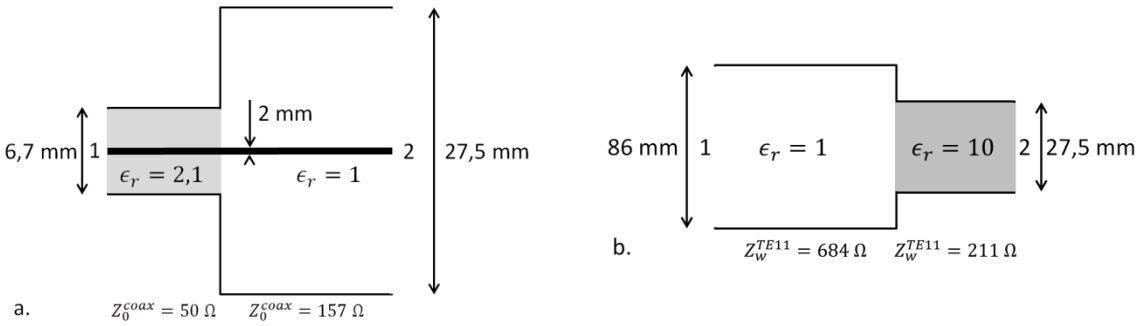

Figure 12. Sectional views of transitions with a change in diameter and dielectric permittivity on (a) a coaxial line and (b) a circular waveguide (for which both portions support a propagating TE11 mode at 2.45 GHz).

2.1.4 The coaxial-to-waveguide transition

A number of different techniques can be used to achieve coupling between transmission lines and waveguides or between different types of waveguides (see for example THOUREL chapter 5 [5]). The coaxial-to-waveguide transition is a way to couple a waveguide to a coaxial line by connecting the outer conductor of the coaxial line to a wall of the waveguide and having the inner conductor extends into the waveguide volume. This type of transition will be useful for the design of the microwave setup as well as waveguide coupling of the thruster.

The most common coaxial-to-waveguide transition geometry is shown in figure 13 for the rectangular waveguide. It excites the TE10 mode. In this study, this type of geometry will rather be used to excite the TE11 mode of the circular waveguide (as described in THOUREL [42] and analyzed in several references, for example [43], [44]). However, for easier analytical manipulation, the following analysis of this coaxial-to-waveguide transition will be carried out for the rectangular waveguide, whose modes are written as circular functions instead of Bessel functions. We follow the approach sketched by problem 8.10 from JACKSON [37].

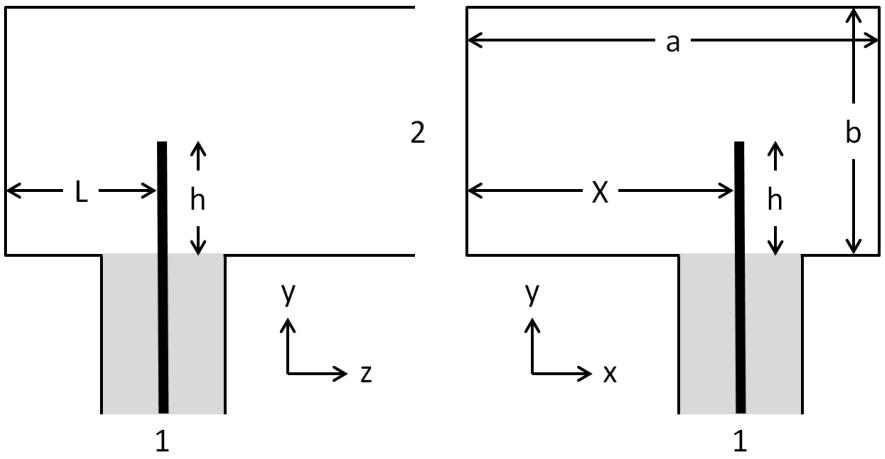

Figure 13. Sectional views of a coaxial to rectangular waveguide transition. The section of the waveguide is in the xy plane and z is the direction of propagation.

The section of the waveguide is assumed to be of such size that only the TE10 mode (lowest mode) propagates. Its electric field is represented in figure 14 and the fields write

$$E_x = E_z = H_y = 0 \qquad (99)$$

$$E_{\pm,y} = -\frac{j\omega\mu a}{\pi} A_{10} \sin\frac{\pi x}{a} e^{\pm j\beta z}$$

$$H_{\pm x} = \frac{j\beta a}{\pi} A_{10} \sin\frac{\pi x}{a} e^{\pm j\beta z}$$

$$H_z = A_{10} \cos\frac{\pi x}{a} e^{\pm j\beta z}$$

with a $e^{-j\omega t}$ dependence.

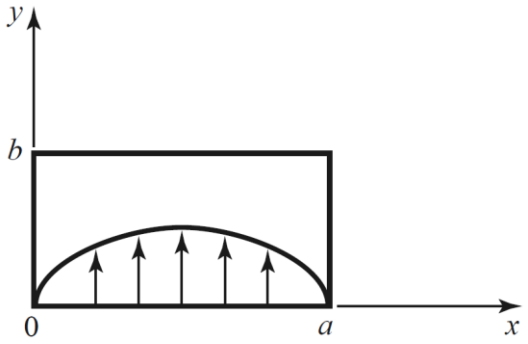

Figure 14. Electric field of the TE10 mode of the rectangular waveguide

The inner conductor extension into the waveguide, thereafter called the probe, will be modelled by the localized source term

$$\boldsymbol{J_{probe}} = \begin{cases} I_0 \sin\big(k(h-y)\big)\,\delta(x-X)\delta(z)\boldsymbol{e_y}, & if\ 0 \le y \le h \\ \mathbf{0}, & otherwise \end{cases} \qquad \textbf{(100)}$$

where we have assumed that the exciting current in the probe has $k = \omega/c$, as in the coaxial line ($\epsilon_r = 1$). In the following we will determine the amplitude of the excited mode as a function of I_0. A perturbation method will be used in the sense that we will take the source-free waveguide modes and examine the power deposited in those modes by the excitation current $\boldsymbol{J_{probe}}$, rather than calculating the fields from the Maxwell equations with the source term $\boldsymbol{J_{probe}}$.

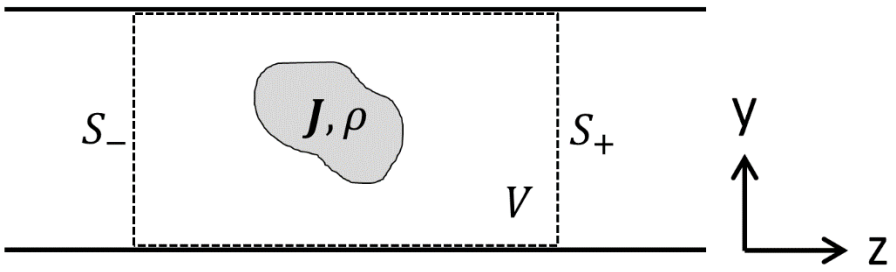

Figure 15. Localized source in a waveguide

As a first step, let's ignore the short circuit of the considered coaxial-to-waveguide transition as well as the particular shape of the exciting probe (figure 13, left). Instead, let's consider the more general problem of an arbitrary source in a waveguide infinite in both directions (figure 15). We which to evaluate the power radiated by the probe in both directions

$$\mathrm{P}_{\mathrm{probe}} = \frac{1}{2} Re \int_{S^+} \boldsymbol{E_+} \times \overline{\boldsymbol{H_+}}\, \boldsymbol{dS} + \frac{1}{2} Re \int_{S^-} \boldsymbol{E_-} \times \overline{\boldsymbol{H_-}}\, \boldsymbol{dS}. \qquad \textbf{(101)}$$

Because of the symmetry of the problem it simplifies to

$$\mathrm{P}_{\mathrm{probe}} = \mathrm{Re}\int_{S^+} \boldsymbol{E}_+ \times \overline{\boldsymbol{H}_+}\, \boldsymbol{dS}. \qquad \textbf{(102)}$$

In the vicinity of the probe, a number of modes, including evanescent modes, are excited. Nevertheless, far enough from the probe, only the finite number of propagating modes remain. Here, we have assumed that TE10 is the only propagating mode. Therefore, there exists a distance from the probe to S^+such that the previous expression reduces the power carried by the TE10 mode:

$$\begin{aligned}\mathrm{P}_{\mathrm{probe}} &= \mathrm{Re}\int_{S^+} -(A_+^{TE10}E_{+,y}^{TE10})\overline{(A_+^{TE10}H_{+,x}^{TE10})}\, dS \\ &= Re\int_{S^+} \frac{1}{Z_w^{TE10}}(A_+^{TE10}E_{+,y}^{TE10})\overline{(A_+^{TE10}E_{+,y}^{TE10})}\, dS.\end{aligned} \qquad \textbf{(103)}$$

where we used that $Z_w^{\beta} := \frac{E_x}{H_y} = -\frac{E_y}{H_x}$ similarly to definition 59. Now the calculation of $\mathrm{P}_{\mathrm{probe}}$ reduces to the evaluation of the amplitude of the TE10 mode excited by the probe, A_+^{TE10}, thereafter defined. Let's accept the result that the modes of the waveguide are a complete set of orthogonal modes, so any electric field respecting the waveguide's boundary conditions can be expanded in the following way, separating propagation towards positive and negative z,

$$\begin{aligned}\boldsymbol{E}_+ &= \sum_{\boldsymbol{\beta}} A_+^{\beta}\boldsymbol{E}_+^{\boldsymbol{\beta}} \\ \boldsymbol{H}_+ &= \sum_{\boldsymbol{\beta}} A_+^{\beta}\boldsymbol{H}_+^{\boldsymbol{\beta}} \\ \boldsymbol{E}_- &= \sum_{\boldsymbol{\beta}} A_-^{\beta}\boldsymbol{E}_-^{\boldsymbol{\beta}} \\ \boldsymbol{H}_- &= \sum_{\boldsymbol{\beta}} A_-^{\beta}\boldsymbol{H}_-^{\boldsymbol{\beta}}\end{aligned} \qquad \textbf{(104)}$$

where the sum is over all TE and TM modes including evanescent modes. They are all treated on an equal footing and indexed by their propagating constant β. The fields for the β mode are written as the sum of transverse and longitudinal components and the direction of propagation are separated.

$$\begin{aligned}\boldsymbol{E}_+^{\boldsymbol{\beta}}(x,y,z) &= \left(\boldsymbol{E}^{\boldsymbol{\beta}}(x,y) + \boldsymbol{E}^{\boldsymbol{z\beta}}(x,y)\right)e^{j\beta z} \\ \boldsymbol{H}_+^{\boldsymbol{\beta}}(x,y,z) &= \left(\boldsymbol{H}^{\boldsymbol{\beta}}(x,y) + \boldsymbol{H}^{\boldsymbol{z\beta}}(x,y)\right)e^{j\beta z} \\ \boldsymbol{E}_-^{\boldsymbol{\beta}}(x,y,z) &= \left(\boldsymbol{E}^{\boldsymbol{\beta}}(x,y) - \boldsymbol{E}^{\boldsymbol{z\beta}}(x,y)\right)e^{-j\beta z} \\ \boldsymbol{H}_-^{\boldsymbol{\beta}}(x,y,z) &= \left(-\boldsymbol{H}^{\boldsymbol{\beta}}(x,y) + \boldsymbol{H}^{\boldsymbol{z\beta}}(x,y)\right)e^{-j\beta z}\end{aligned} \qquad \textbf{(105)}$$

The choice of signs can be understood from the need to satisfy null divergence of the fields for each direction of propagation and positive power flow in the direction of propagation. The transverse fields are normalized such that

$$\int_S \boldsymbol{E^\beta E^\alpha} dS = \delta_{\beta\alpha} \qquad \textbf{(106)}$$

and

$$\int_S \boldsymbol{H^\beta H^\alpha} dS = \frac{\delta_{\beta\alpha}}{Z_w^\beta}. \qquad \textbf{(107)}$$

The time average power flow $\frac{1}{2}\int_S \boldsymbol{E^\beta} \times \boldsymbol{H^\alpha dS}$ is

$$\frac{1}{2}\int_S \left(E_x^\beta H_y^\alpha - E_y^\beta H_x^\alpha\right) dS = \frac{1}{2}\int_S \left(E_x^\beta \frac{E_x^\alpha}{Z_w^\alpha} - E_y^\beta \frac{-E_y^\alpha}{Z_w^\alpha}\right) dS = \frac{\delta_{\beta\alpha}}{Z_w^\beta} \qquad \textbf{(108)}$$

where the first equality uses the definition of the wave impedance and the second uses the normalization relation.

We will take as a starting point the following relation from JACKSON chapter 8 [37],

$$\nabla \cdot \left(\boldsymbol{E} \times \boldsymbol{H_\pm^\beta} - \boldsymbol{E_\pm^\beta} \times \boldsymbol{H}\right) = \boldsymbol{J E_\pm^\beta}, \qquad \textbf{(109)}$$

which follows from the source free Maxwell equations verified by $\boldsymbol{E_\pm^\beta}$ and $\boldsymbol{H_\pm^\beta}$ (by construction) and the Maxwell equations with source satisfied by $\boldsymbol{E}$ and $\boldsymbol{H}$, the fields in the waveguide in the presence of the excitation. Let's integrate this relation over the volume V from figure 15 using the divergence theorem:

$$\int_S \left(\boldsymbol{E} \times \boldsymbol{H_\pm^\beta} - \boldsymbol{E_\pm^\beta} \times \boldsymbol{H}\right) \boldsymbol{dS} = \int_V \boldsymbol{J E_\pm^\beta}\, dV \qquad \textbf{(110)}$$

The volume is chosen as in figure 15. Given the boundary conditions imposed by the perfectly conducting wall, only the surface integrals over S^+ and S^- contribute to the left hand side. For S^+, $\boldsymbol{E}$ and $\boldsymbol{H}$ can be expanded for propagation towards positive z only since propagation is expected outward only:

$$\int_{S^+} \left(\boldsymbol{E} \times \boldsymbol{H_\pm^\beta} - \boldsymbol{E_\pm^\beta} \times \boldsymbol{H}\right) \boldsymbol{dS} = \sum_\alpha A_+^\alpha \int_{S^+} \left(\boldsymbol{E_+^\alpha} \times \boldsymbol{H_\pm^\beta} - \boldsymbol{E_\pm^\beta} \times \boldsymbol{H_+^\alpha}\right) \boldsymbol{dS}. \qquad \textbf{(111)}$$

Only the transverse components yield cross products perpendicular to the surface, therefore, for the upper signs

$$\int_{S^+} \left(\boldsymbol{E} \times \boldsymbol{H_+^\beta} - \boldsymbol{E_+^\beta} \times \boldsymbol{H}\right) \boldsymbol{dS} = \sum_\alpha A_+^\alpha \int_{S^+} \left(\boldsymbol{E^\alpha} \times \boldsymbol{H^\beta} - \boldsymbol{E^\beta} \times \boldsymbol{H^\alpha}\right) \boldsymbol{dS} = 0 \qquad \textbf{(112)}$$

where the definitions 105 have been used for the first equality. For the second equality we see from relation 108 that only the two β terms of the first sum are non-zero, but cancel out. For the lower signs in relation 111:

$$\int_{S^+} \left(\boldsymbol{E} \times \boldsymbol{H_-^\beta} - \boldsymbol{E_-^\beta} \times \boldsymbol{H}\right) \boldsymbol{dS} = \sum_\alpha A_+^\alpha \int_{S^+} \left(\boldsymbol{E^\alpha} \times (-\boldsymbol{H^\beta}) - \boldsymbol{E^\beta} \times \boldsymbol{H^\alpha}\right) \boldsymbol{dS} = -\frac{2A_+^\beta}{Z_w^\beta}. \qquad \textbf{(113)}$$

After similar calculation for S^-, the results can be summarized as:

$$\mathrm{A}_{\mp}^{\beta} = -\frac{Z_w^{\beta}}{2}\int_{\mathrm{V}} \boldsymbol{J}\boldsymbol{E}_{\pm}^{\boldsymbol{\beta}}\, dV \qquad \textbf{(114)}$$

We are now well-equipped to calculate A_{+}^{TE10}. TE10 electric field reduces to its y-component (definition 99) and is normalized according to normalization 106,

$$E_{\pm,y}^{TE10} = \sqrt{\frac{2}{ab}}\sin\frac{\pi x}{a}e^{\pm j\beta z}. \qquad \textbf{(115)}$$

From relation 114 and definitions 105 we have

$$\mathrm{A}_{\mp}^{TE10} = -\frac{Z_w^{\beta}}{2}\int_{\mathrm{V}} \boldsymbol{J}E_y^{TE10}e^{\pm j\beta z}\boldsymbol{e_y}\, dV. \qquad \textbf{(116)}$$

Now going back to the particular situation of the considered coaxial-to-waveguide transition where the source term is $\boldsymbol{J_{probe}}$ we have the following.

$$\mathrm{A}_{\mp}^{TE10} = -\frac{Z_w^{TE10}}{2}\int_0^a\int_0^h\int_{z^-}^{z^+} I_0\sin\left(\frac{\omega}{c}(h-y)\right)\delta(x - X)\delta(z)\sqrt{\frac{2}{ab}}\sin\frac{\pi x}{a}e^{\pm j\beta z}\, dxdydz \qquad \textbf{(117)}$$

Straightforward integration yields

$$\mathrm{A}_{+}^{TE10} = \mathrm{A}_{-}^{TE10} = -\frac{Z_w^{TE10}}{2}I_0\sqrt{\frac{2}{ab}}\sin\left(\frac{\pi X}{a}\right)\frac{c}{\omega}\ 2\sin^2\left(\frac{\omega}{2c}h\right) \qquad \textbf{(118)}$$

and with $Z_w^{TE10} = \frac{k\eta}{\beta^{TE10}} = \frac{\omega\mu}{\beta^{TE10}}$

$$\mathrm{A}_{+}^{TE10} = \mathrm{A}_{-}^{TE10} = -\frac{\omega\mu}{\beta^{TE10}}I_0\sqrt{\frac{2}{ab}}\sin\left(\frac{\pi X}{a}\right)\frac{c}{\omega}\ \sin^2\left(\frac{\omega}{2c}h\right). \qquad \textbf{(119)}$$

From relation 103

$$\mathrm{P}_{\mathrm{probe}} = \frac{{A_+^{TE01}}^2}{Z_w^{TE01}}\int_{S^+} E_{+,y}^{TE10}\overline{E_{+,y}^{TE10}}\, dS. \qquad \textbf{(120)}$$

where with normalization 106 the integral is 1. In the end, the sum of the power radiated in both directions is

$$\mathrm{P}_{\mathrm{probe}} = 2\frac{I_0^2\mu c^2}{\omega\beta^{TE10}ab}\sin^2\frac{\pi X}{a}\sin^4\frac{\omega h}{2c}. \qquad \textbf{(121)}$$

Let's go back to the coaxial-to-waveguide transition of figure 13, having a metallic wall at $z = -L$ instead of an infinite waveguide. No power is radiated through S^- and the power radiated through S^+ writes

$$\mathrm{P'}_{\mathrm{probe}} = \frac{1}{2}\int_{S^+} \boldsymbol{E}_+(1 + e^{i(2\beta^{TE10}L-\pi)}) \times \overline{\boldsymbol{H}_+(1 + e^{\imath(2\beta^{TE10}L-\pi)})}\, \boldsymbol{dS}. \qquad \textbf{(122)}$$

where the factor $e^{i(2\beta^{TE10}L-\pi)}$ accounts for the phase shift between the wave starting from the probe towards positive z and that reflecting on the wall. This phase shift accounts for propagation and reflection. Then, with

$$\left(1 + e^{i(2\beta^{TE10}L-\pi)}\right)\overline{(1 + e^{\imath(2\beta^{TE10}L-\pi)})} = 2(1 - \cos 2\beta^{TE10}L) = 4\sin^2\beta^{TE10}L,$$

$$\begin{aligned}\mathrm{P'}_{\mathrm{probe}} &= \frac{1}{2}4\sin^2\beta^{TE10}L\ \mathrm{P}_{\mathrm{probe}} \\ &= 4\frac{I_0^2\mu c^2}{\omega\beta^{TE10}ab}\sin^2\frac{\pi X}{a}\sin^4\frac{\omega h}{2c}\sin^2\beta^{TE10}L.\end{aligned} \qquad \textbf{(123)}$$

From this relation, it is apparent that for a given I_0 the power transferred to the waveguide is maximized if $X = a/2$, $h = \pi/k$ which is half of the coaxial line wavelength, and $L = \pi/2\beta^{TE10}$, which is a quarter of the waveguide wavelength. This calculation turns out to be correct regarding the choice of X and L but fails for h. It may be caused by three assumptions. First, that $\boldsymbol{J_{probe}}$ varies according to the coaxial dispersion relation. Indeed, $\boldsymbol{J_{probe}}$ must also be strongly dependent on the actual waveguide fields. Second, modelling the probe simply as source term whereas it also imposes additional perfectly conducting boundary conditions (figure 14): in the extreme case where $h = b$, it would short-circuit the y-component of the electric field. Third, ignoring the higher order modes that do have a reactive effect in the vicinity of the probe. It is apparent from figure 16 that the field lines at the closing walls are not that of the TE10 mode, thus raising doubt about the validity of relation 122. Not only electromagnetic coupling but also capacitive coupling takes place between the probe and the closing wall, as indicated by the presence of electric field lines linking both objects (RAX section 7.2 [45]). Nonetheless $L = \pi/2\beta^{TE10}$ is a valid rule of thumb.

Documents on microwave engineering (for example [42], [46], [41]) recommend $h \cong b/2$, and $L \cong \pi/2\beta^{TE10}$. Here, as for many microwave systems, they provide approximate guidelines for the dimensions of but insist that experimental tuning (or numerical simulation) is required.

From relation 83 it seems relevant to define $Z_{waveguide} = \frac{2\mathrm{P'}_{\mathrm{probe}}}{I_0}$, the load impedance seen by the coaxial line, to represent this coaxial-to-waveguide transition in the framework of figure 9.

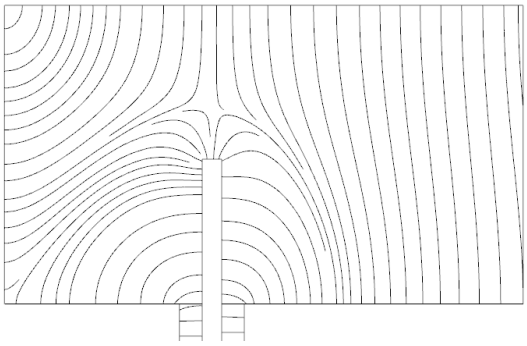

Figure 16. Electric field lines in the y-z plane containing the probe (same plane as figure 13, left) from finite element calculation on COMSOL®.

2.1.5 Experimental microwave measurement

2.1.5.1 Low power measurement: the vector network analyzer

In the laboratory, microwave components and transmission line can be connected to form a microwave network, having several ports establishing connection to external systems. The study and operation of this microwave network may not require the knowledge of the electromagnetic field at any point in the system and at any time. Instead, a steady state input/output relation may often suffice. For simplicity, and because it will be the case in this study, let's assume that the ports are coaxial ports supporting TEM waves. In this case the wave at the coaxial ports can be represented by equivalent voltage and current in each direction. They are complex scalar quantities defined by relations 79 and 80. Defining for each port a sectional plane for which those quantities are measured, the microwave network can be represented as in figure 17.

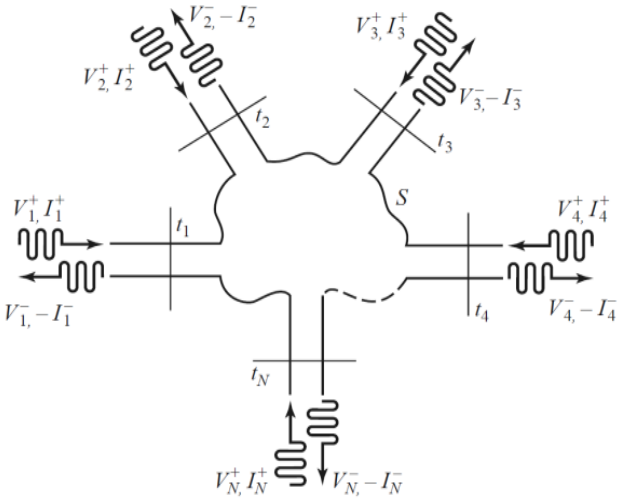

Figure 17. Arbitrary N-port microwave network

The scattering matrix S is a complete description of the network as seen from its N ports. It relates the voltage waves going out the ports to those coming in as follows.

$$\begin{bmatrix} V_1^- \\ V_2^- \\ \vdots \\ V_N^- \end{bmatrix} = \begin{bmatrix} S_{11} & S_{12} & \dots & S_{1N} \\ S_{21} & & & \vdots \\ \vdots & & & \vdots \\ S_{N1} & \dots & \dots & S_{NN} \end{bmatrix} \begin{bmatrix} V_1^+ \\ V_2^+ \\ \vdots \\ V_N^+ \end{bmatrix} \quad (124)$$

This matrix is symmetric for reciprocal network and unitary for lossless network.

Any matrix element, also called S-parameter in the experimental context, writes

$$S_{ij} = \left. \frac{V_i^-}{V_j^+} \right|_{\forall k \neq j, V_k^+ = 0}, \quad (125)$$

meaning that it can be measured by driving port j with an outgoing voltage wave V_j^+ and looking at the incoming voltage wave V_i^- at port i, provided that all ports are terminated by matched loads (defined in section 2.1.3.2).

A vector network analyzer (VNA) is a device able to perform this measurement at microwave frequencies. It most often has two or four ports. A calibration procedure specifies the locations of the

measurement t-planes (figure 17) so that the S-parameters are measured for the microwave network under study, also called DUT (device under test) in some instances, and are free from the effect of connecting cables.

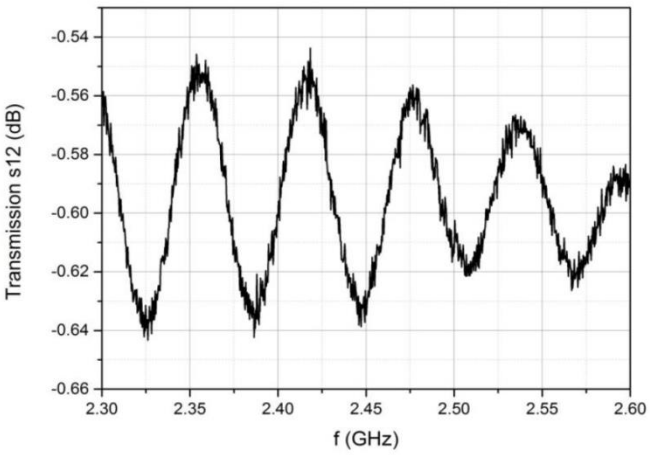

Figure 18. Typical VNA measurement of a coaxial cable (VIALIS III-2.3 [24])

It is noteworthy when making VNA measurements that the plot of S-parameters as a function of frequency often displays small amplitude (~ 0.1dB) oscillations, even for a DUT as simple as a coaxial cable (figure 18). These oscillations come from a number of small interfering reflections typically originating from connectors. In the simplest case, which is that of a cable, reflections appear at both ends of the cable. We see from section 2.1.3.4 that the equivalent voltage of a wave transmitted through two reflective junctions separated by distance D follows a $2D/\lambda$ periodicity. To go through one period of the S-parameter signal, the frequency should be increased so as to fit one more half wavelength in D. As a consequence, we may write that

$$D = \alpha\frac{\lambda}{2} = (\alpha+1)\frac{\lambda+\Delta\lambda}{2} \qquad (126)$$

where α is a real number and $\Delta\lambda$ the increment of wavelength acquired through one S-parameter period. For $\Delta\lambda \ll \lambda$, $\Delta\lambda = -(c/f^2)\,\Delta f$. From the second equality in the above relation, $\alpha = -(\lambda+\Delta\lambda)/\Delta\lambda$, which yields, using the first equality

$$D = \frac{\lambda}{2}\frac{\lambda+\Delta\lambda}{-\Delta\lambda}. \qquad (127)$$

In the case of the measurement shown in figure 18, $\Delta f = 60$ MHz is read. Therefore, taking $f = 2.45$ GHz and $\lambda = c/f = 12.24$ cm we get $D = 2.44$ m: a 2.5 m cable was used for this measurement.

In making measurements, these variations are an issue because it is difficult to discriminate between the contribution of the internal reflections of the DUT and that of the connecting cable. This sets a lower limit for the random error on VNA measurements around 0.1 dB.

2.1.5.2 High power real time measurement: the directional coupler

In order to determine the actual incident and reflected power during the operation of the thruster, a bidirectional coupler is installed on the microwave line ([24], figure 33). A bidirectional coupler is a four-port passive microwave component diverting a small known fraction of the incident and reflected power from the main line to the respective coupled ports [38]. The ratio of the sampled power to the

power flowing in the main line is called the coupling and is typically -30dB. With this quantity known, the power flowing through the main line can be calculated from measurement of the sampled power. However, a fraction of the incident power (typically -50 dB) is coupled to the reflected sampling port and vice versa, creating interferences between microwaves that result in erroneous measurement. This phenomenon is known as directivity error. If the ports are numbered as in figure 19, directivity in dB is defined as $D_I = 20\log|S13/S14|$ for the measurement a wave propagating to the right (incident) and $D_R = 20\log|S24/S23|$ for the measurement a wave propagating to the left (reflected). This source of error was previously over looked. We will deal with that issue in chapter 3.

For a simple bidirectional coupler, port 3 and 4 would be at both ends of the same coupled line. A dual directional coupler (figure 19) avoids possible perturbations by using two separate coupled lines terminated by adapted charges. This type of devices was used in recent ECRT development studies [24], [28].

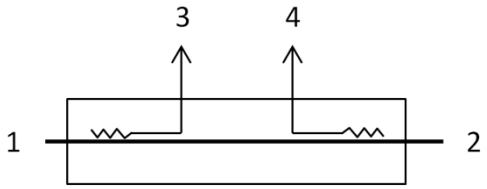

Figure 19. Schematic view of a dual directional coupler. A known fraction of the wave propagating from left to right is measurable at port 3. Ideally, it is isolated from the wave propagating from right to left

2.1.5.3 Recommended laboratory practices

Microwave engineering is founded on the well-established classical electrodynamics theory. Its practice however revealed to be somewhat of an art. A training in microwave engineering therefore cannot be completed without a good deal of laboratory practice. Here are a few very practical remarks that we believe from experience to have a tremendous time-saving potential…

- Connectors must be screwed tightly to achieve efficient and unperturbed transmission.
- Connectors systematically generate reflections (return losses, in microwave jargon) that do not waste a lot of power but complicate measurements. Design should minimize the number of connections. The circuit should be as simple as possible.
- Accuracy better than 0.1 dB (~ 2.3%) should never be expected.
- In-vacuum connectors are prone to discharges. Unless airtight, the air contained inside can be at any pressure, depending on micro leaks. As a solution, a small drilled hole enables pumping of the inside of the connector without perturbing microwave transmission significantly.
- A welded microwave feedthrough is recommended instead of a microwave feedthrough held on flange with a gasket and o-ring. The latter may be difficult to screw tightly and may also transmit forces from the outside cable to the in-vacuum cable (prone to perturb the in vacuum setup).
- Accurate microwave power measurements are difficult. To obtain 10% accuracy, the possibility of non-idealities in microwave components should be considered. In particular, substantial second harmonics production by generators and finite directivity for power couplers may be an issue.
- The behavior of active components such as the continuous wave generator of the VNA varies with temperature. Hence it is not stable until thermal equilibrium is reached.
- The microwave properties of ceramics such as alumina may vary considerably with temperature.

2.2 The ECRT in the context of space propulsion

Outline of the approach. This section deals with electric propulsion, presented from an application standpoint. We zoom in from jet propulsion down to the electron cyclotron resonance thruster, to provide a simple picture of the technological and economical context of this study.

Content

2.2.1 Jet propulsion

Let's first derive and discuss a relation that will be extensively used in the following chapters: the expression of thrust as the product of the mass flow and the average ejection velocity with respect to the vehicle. Considering the system sketched in figure 20, subject to no external forces, conservation of momentum between time t and $t + dt$ writes:

$$M(t)V(t) = M(t+dt)V(t+dt) + \big(M(t) - M(t+dt)\big)v(t+dt). \quad \textbf{(128)}$$

Hence with $v(t+dt) = V(t+dt) - u_e$ we get:

$$M(t)\big(V(t+dt) - V(t)\big) = -u_e(t)\big(M(t+dt) - M(t)\big). \quad \textbf{(129)}$$

Dividing by dt and having $dt \to 0$:

$$M(t)\frac{dV}{dt}(t) = -u_e(t)\frac{dM}{dt}(t). \quad \textbf{(130)}$$

This relation is the justification for the definition of thrust T, that is a *quantity homogeneous to a force and "responsible" for the variation of the vehicle velocity*. Defining the (positive) mass flow $\dot{m} = -dM/dt$ that is ejected at velocity u_e with respect to the vehicle,

$$T \coloneqq -u_e(t)\frac{dM}{dt}(t) = \dot{m}u_e. \quad \textbf{(131)}$$

This is a somewhat specific and propulsion oriented definition of force, that focuses on the variation of velocity. Indeed, T is not equal to the variation of the vehicle momentum, $d(MV)/dt$ but rather to

MdV/dt. Hence it is *not* the expression of the sum of the forces applied to the vehicle due to mass ejection.

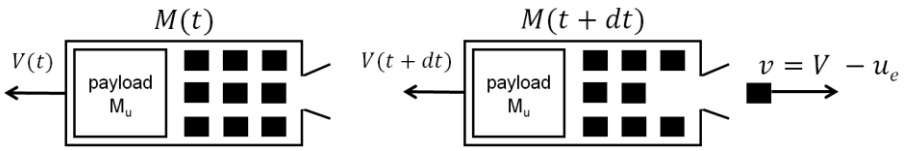

Figure 20. Jet propulsion in a fixed reference frame. u_e is a positive ejection velocity. The direction drawn for v is arbitrary and could be opposite if $u_e < V$.

From the definition of thrust it seems that increasing the ejection velocity u_e or increasing the mass flow $\dot{m}$ are equally good options to increase thrust. However, these two options have very different implication on the mission.

2.2.1.1 Effect of mass flow

To discuss first increase of mass flow let's integrate relation 130 for a constant ejection velocity, taking M_0 as the initial mass, M_u as the final mass, and ΔV the increment of velocity between the initial and final instants. It yields a relation often called the Tsiolkovski (or rocket) equation

$$\Delta V = -u_e \ln \frac{M_u}{M_0} \qquad (132)$$

or

$$M_u = M_0 \exp\left(-\frac{\Delta V}{u_e}\right) \qquad (133)$$

from which we see that imposing a certain velocity increment ΔV to a certain payload M_u, requires a certain initial mass M_0, ($M_0 - M_u$ being ejected mass) and ejection velocity u_e. A small increase in $u_e$will save a considerable quantity of fuel. Besides, *it is necessary to provide* u_e *comparable with* ΔV *if a significant fraction of the original mass is to be brought to the final velocity*, as expressed by JAHN, chapter 1[47].

2.2.1.2 Effect of ejection velocity

Jahn also states that *enthusiasm for high specific impulses* [i.e. high ejection velocities, Isp $\coloneqq T/\dot{m}g_0 \propto u_e$] *must be tempered by considerations of the power plant* […] *needed to drive these engines.* To assess the relevance of high ejection velocity, let's consider the energy balance for the system in figure 20. The variation of kinetic energy between time t and $t + dt$ equals the power delivered by the propulsion system P_T times dt

$$2P_T dt = \left[M(t+dt)V^2(t+dt) + \big(M(t) - M(t+dt)\big)v^2(t+dt)\right] - [M(t)V^2(t)]. \qquad (134)$$

With $v(t+dt) = V(t+dt) - u_e$ it can be recast as

$$2P_T dt = \big(M(t+dt)V^2(t+dt) - M(t)V^2(t)\big) - \big(M(t+dt) - M(t)\big)(V(t+dt) - u_e(t))^2. \qquad (135)$$

Dividing by $2dt$ and having $dt \to 0$,

$$P_T = \underbrace{\frac{d}{dt}\left(\frac{1}{2}MV^2\right)(t)}_{\substack{Variation\ of\ kinetic \\ energy\ of\ the\ vehicle}} \underbrace{-\frac{1}{2}\frac{dM}{dt}(t)(V(t)-u_e(t))^2}_{\substack{Kinetic\ power\ carried \\ by\ the\ jet}}. \quad \textbf{(136)}$$

Expanding the derivative and the second term, and using relation 130 yields

$$P_T = -\frac{1}{2}\frac{dM}{dt}(t)u_e(t), \quad \textbf{(137)}$$

thus

$$P_T = \frac{\dot{m}\,{u_e}^2}{2} = \frac{T^2}{2\dot{m}}. \quad \textbf{(138)}$$

This justifies the above statement from JAHN since the kinetic power delivered by the system is proportional to ${u_e}^2$ but only to $\dot{m}$.

It is noteworthy that only a fraction of this power contributes to the variation of kinetic energy of the vehicle, the rest being carried by the jet (relation 136). The respective fractions depend on the ratio V/u_e; the fraction benefiting to the vehicle's kinetic energy variation is

$$\eta_P = \frac{\frac{d}{dt}\left(\frac{1}{2}MV^2\right)}{-\frac{1}{2}\frac{dM}{dt}u_e} = 1 - \left(\frac{V}{u_e} - 1\right)^2. \quad \textbf{(139)}$$

This quantity is negative for $V > 2u_e$ because then the kinetic energy of the vehicle decreases: the loss of mass dominates the increase in velocity. $\forall V > 2u_e$, $-\frac{1}{2}\frac{dM}{dt}V^2 > MV\frac{dV}{dt}$. However, the fraction η_P is not in fact something we want to maximize because we are interested in increasing velocity of the vehicle rather than increasing its kinetic energy. To this end, the relevant relation is relation 130.

2.2.2 Electric propulsion

Jet propulsion technologies are generally split into three families, presented below in order of increasing ejection velocity.

1. Cold gas thrusters use the expansion of a pressurized gas. The energy source is microscopic kinetic energy stored as pressure. In practice $u_e^{cold\ gas} \leq 1\ km/s$.

2. Chemical thrusters use chemical energy to increase the pressure and temperature of the fuel which is then converted into directed kinetic energy. The available chemical energy per unit mass of fuel and thus the ejection velocity is intrinsically limited. In practice $u_e^{chemical} \leq 4\ km/s$.

3. Electric thrusters use an external electric power supply to ionize and accelerate the propulsive gas. Therefore, regardless of the particular operation of the thruster, the power supply imposes the upper limit on the ejection velocity. In practice $u_e^{electric} \leq 40\ km/s$ [48].

This section will focus on electric thrusters.

2.2.2.1 Example: geostationary transfer

Until recently, geostationary satellites have constituted the vast majority of the satellite-propulsion market [49]. To illustrate the benefit of high ejection velocities associated with electric propulsion, let's

consider geostationary transfer for a telecommunication satellite having a payload of 3000 kg. Launchers do not typically deliver their payload on the geostationary orbit (GEO) but rather on a lower energy geostationary transfer orbit (GTO) from which the satellite performs a stationing manoeuver. This manoeuver aims at stationing the satellite on the desired GEO orbit, that is a circular orbit at 35786 km, with 0° inclination, at the desired phase (longitude). The stationing manoeuver minimizing energy expenses is the Hohmann transfer. It requires a velocity increment $\Delta V^{ch} \approx 1.6$ km/s to circularize the GTO by applying one or a few impulsive velocity increment at the apogee. The GTO orbit is a strongly elliptical orbit on which the satellite is injected by the launcher. The altitude of its apogee is that of the circular GEO orbit. This type of trajectory is achievable only by chemical propulsion because it requires a short high thrust burst, at the end of the Hohmann transfer manoeuver. On contrary, the manoeuvers suited to electric propulsion consist in applying a low thrust continuously (SUTTON AND BIBLARZ, chapter 17 [50]). A number of transfer orbits are possible and the associated stationing manoeuvers typically require a velocity increment $\Delta V^{el} \approx 2.2$ km/s [51], [52]. An additional 0.5 km/s accounts for 10 years of North-South station keeping necessary to cancel out perturbations caused by the Sun and the Moon to the Kepler orbit of the satellite around the Earth. Let's assume the ejection velocities $u_e^{ch} = 3.14$ km/s (Airbus Defence&Space 400-N bipropellant apogee motor, $Isp^{ch} = 320s$) and $u_e^{el} = 16.2$ km/s (Safran PPS-1350 Hall effect thruster, $Isp^{el} = 1650s$)[2]. Numerical application of Tsiolkovski equation (relation 133) yields the launch masses displayed in table 1 below. In this example, electric propulsion saves initial propellant mass by more than a factor 5, which provides a considerable advantage in extending lifetime or reducing launch costs. The satellite may even qualify for a smaller launcher. There is however a substantial associated drawback: as a consequence of high ejection velocity and limited power available, the thrust is low, therefore the duration of the manoeuver is long. Assuming 12 kW of electrical power available, 8 PPS-1350 of 1.5kW can be used simultaneously. They each provide $T^{el} = 90$ mN of thrust. Tsiolkovski equation is re-written for any time t as

$$M_0^{el} - \dot{m}\Delta t^{el} = M_0^{el} \exp\left(-\frac{\Delta V^{el}(t)}{u_e^{el}}\right) \quad \textbf{(140)}$$

thus

$$\Delta t^{el} = \frac{M_0^{el}}{\dot{m}}\left[1 - \exp\left(-\frac{\Delta V^{el}}{u_e^{el}}\right)\right]. \quad \textbf{(141)}$$

With $\dot{m} = 8T^{el}/u_e^{el} = 42.4$ mg/s we find $\Delta t^{el} = 4.1$ month instead of days for a stationing manoeuver with chemical propulsion [50].

GEO transfer of a 3000 kg payload	Transfer manoeuver	Required ΔV (km/s)	Ejection velocity (km/s)	Launch mass M_0 (kg)	Transfer duration
Chemical propulsion	Hohmann	1.6+0.5	3.14	5857	a few hours
Electric propulsion	Spiral	2.2+0.5	16.2	3545	4.1 month

Table 2. Compared geostationary transfers with chemical propulsion and electric propulsion.

Looking at this situation at system level may reveal that the electric propulsion system introduces an additional mass as compared to the chemical propulsion. In practice however this additional mass is small compared to the gain in propellant mass.

[2] Data available on the manufacturer's websites.

2.2.2.2 Propulsion tasks

This example only mentions two of the many propulsion tasks that can be undertaken by electric propulsion. They generally fall into the following categories [50].

1. Station keeping, which mainly includes North-South (and East-West) station keeping and drag compensation for satellites in low Earth orbit (LEO).

2. Orbit changing for earth satellites, which mainly includes orbit raising and end of life deorbiting.

3. Interplanetary travel and deep space probes, missions for which high specific impulse may be of considerable value if a suitable power source is available.

4. Attitude and position control, which includes pointing the satellites instrument in a particular direction or precisely controlling the position relative to other object or satellites (formation flying).

For the first three categories, the key advantage of electric propulsion lies in high specific impulse whereas for attitude and position control, electric propulsion is more often appreciated for the ability to provide small and accurate impulses.

2.2.2.3 A brief history of electric propulsion

A variety of electric propulsion concepts have been proposed from the very beginning of the space programs in the 1950's. In the early 1960's, the USSR and the USA conducted the firsts suborbital in-space electric propulsion tests on pulsed plasma thrusters (PPT) and gridded ion thrusters (GIE) respectively. During the first decades following these tests, development efforts brought five main types of electric propulsion technologies to maturity: GIE, PPT, resistojets, arcjets, and Hall effect thrusters (HET). However, electric propulsion only started to spread out in the mid-1990's, mainly because onboard available electric power increased. Satellites carrying a payload with high power requirement, such as telecommunication satellites, have facilitated the use of electric propulsion. In 1993, the first commercial satellite with an electric propulsion system was launched. Since then, more than 200 GEO satellites have used electric propulsion for station keeping, nonetheless performing orbit raising with chemical propulsion [53]. The first GEO satellite performing both orbit raising and station keeping with electric propulsion (so-called "all-electric satellite") was launched in 2015. As of March 2020, 8 such satellites were launched [54]. Since 1993, 7 interplanetary spacecrafts have used electric propulsion. As of August 2018, Aerojet Rockdyne counted 257 operational spacecrafts with electric propulsion (from any manufacturer) [55]. Most of those spacecrafts are in GEO for now (figure 33). However, the number of LEO satellites using electric propulsion is growing rapidly and will soon exceed the number of GEO satellites using electric propulsion [53], [56], [57].

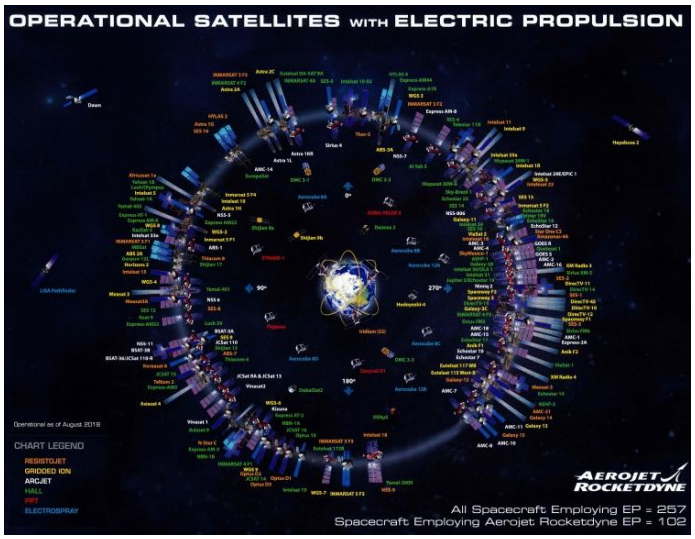

Figure 21. Operational satellites with electric propulsion [55].

2.2.2.4 Micro-propulsion

The possibility to miniaturize and standardize small satellite manufacturing has enabled the use of satellites for applications that previously could not afford manufacturing and launching costs. Therefore strong interest for small satellites has recently appeared. In particular, OneWeb, Starlink, and Kuiper Systems are LEO mega-constellations that would each comprise thousands of satellites. The former two will use Fakel SPT-50M HET and in-house HET respectively. The propulsion solution for Kuiper systems' satellites is undecided. These constellations aim at providing high speed and low latency internet connection everywhere on the planet. They intend to cover lands that are not yet covered by the ground network but their main clients may be in the air transport and maritime transport [58]. Launches of batches of satellites have started in 2019.

In addition to the propulsion requirement for orbit raising and formation flying, propulsion is necessary to deorbit satellites. Indeed, although the natural lifetime on a 300 km orbit is only a few month because of drag, it exponentially increases for higher altitudes reaching hundreds of years before 1000 km [59]. If those orbits are to be used extensively, end-of-life deorbiting must be implemented to avoid pollution.

Therefore, micro-propulsion has been identified has one of the major technological challenges on this rapidly growing market of small satellites [57]. Miniaturizations of existing technologies as well as innovative concepts have been proposed. The Electron Cyclotron Resonance Thruster (ECRT) currently under development in the framework of the H2020 "MINOTOR" project funded by the UE [60] appears as a potentially disruptive technology on this market. This electromagnetic thruster concept could lead to a robust, easy to operate, and low cost propulsion system. The development of this thruster is the object of the present work. The main features and results on the technology will be reviewed in section 2.3. The MINOTOR project (MagnetIc NOzzle thruster with elecTron cyclOtron Resonance), proposed and coordinated by ONERA, involves seven partners from four countries.

2.2.2.5 Basic electric propulsion classifications

In 1968 already, JAHN ([47], chapter 1) proposed to categorize electric thrusters according the following concepts. This classification appears unaltered in modern presentations on electric propulsion [50]. Thrusters mentioned above are given as examples.

1. Electrothermal propulsion, wherein the propellant gas is heated electrically, then expanded in a suitable nozzle. Example: resistojet, arcjet.

2. Electrostatic propulsion, wherein the propellant is accelerated by direct application of electric body forces to ionized particles. Example: GIE.

3. Electromagnetic propulsion, wherein an ionized propellant stream is accelerated by interaction of external and internal magnetic fields with electric currents driven through the streams. Example: PPT, HET, ECRT.

2.2.3 Performance indicators in electric propulsion

In this section, widespread performance indicators are defined and briefly commented. They enable comparison of a technology to others and will be evaluated for the ECRT. The four following definitions provide a precise and quantitative meaning to the mission statement of electric propulsion studies proposed in the introduction. To develop devices able to efficiently *(total thruster efficiency, thrust to weight ratio)* produce thrust through ion acceleration *(specific impulse)*, during an extended period of time *(total impulse)* and in a controllable way, using electrical power as the primary source of power.

Specific impulse Isp (expressed in s) is a measure of ion acceleration and is often considered the main figure of merit of a thruster [49]. It is defined as the ratio of the thrust to the mass rate of propellant consumption. It quantifies the efficiency in the use of propellant mass. The thrust is as if all the propellant were ejected at an average velocity called u_e in the previous sections, with $u_e = Ispg_0$, $g_0 = 9.81\ ms^{-2}$.

$$Isp \coloneqq \frac{T}{\dot{m} g_0} \quad (142)$$

The total thruster efficiency η_T is the ratio of the squared thrust to the squared ideal thrust T_{ideal} for the considered set-point $(\dot{m}, P_e)$. The ideal thrust is achieved when the input electric power P_e is fully converted into kinetic energy, evenly distributed in the input mass flow $\dot{m}$ (i.e. uniform ejection velocity $u_e = \sqrt{2P_e/\dot{m}}$), and the momenta of all particles flow on the same axis. Thus $T_{ideal} = \sqrt{2\dot{m}P_e}$ and

$$\eta_T \coloneqq \frac{T^2}{2\dot{m}P_e}. \quad (143)$$

The fact that we are trying to maximize this second figure of merit expresses the following: a thruster is not only required to accelerate ions to high velocities (i.e. have high Isp), it should also be efficient, with respect to both propellant and power consumption. The input electric power P_e may either be the input electric power to the thruster from the power processing unit (PPU), or the input electric power to the PPU from the available power source on the spacecraft. Since this study is not carried out at system level but rather focuses on plasma acceleration, in the following P_e will be an input microwave power to the thruster.

Total impulse $Itot$ (expressed in N.s) is the integral of thrust over time. It is a measure of the thrust that can be delivered over the lifetime of the thruster. Although it strongly depends on the application, the expected lifetime of an electric thruster should in general be of a few thousand hours. Some thrusters have a lifetime above ten thousand hours (SUTTON AND BIBLARZ table 17-7[50]). The demonstration of sufficient lifetime is one of the main issues in the development of an electric thruster.

Thrust-to-weight ratio quantifies the efficiency with respect to the added weight to the spacecraft because of the propulsive system (except propellant). It may be particularly critical for a small total impulse mission. Some recommend the use of a system level specific impulse $Issp$, using an effective mass rate of propellant defined as $\dot{m}' = \dot{m} + M_{PS,dry}/t_L$, where $M_{PS,dry}$ is the mass of the propulsive system except propellant and t_L the lifetime. It is equivalent to $Issp = Itot/(M_{PS}g_0)$ [61].

Thrust-to-power ratio quantifies the efficiency in the use of input electric power. It is inversely proportional to specific impulse if the total thruster efficiency is kept constant. It is therefore somewhat redundant with indicators already presented above.

$$TTPR \coloneqq \frac{T}{P_e} \quad \textbf{(144)}$$

To analyze in more detail the performance of a thruster, the total efficiency can be broken down into several factors. Let M be the ion mass, e be the elementary charge, $\dot{m}$ the neutral gas mass flow rate, $J_{tot}$the total ion electric current exiting the thruster, and v the average velocity of ions. For simplicity, let's define the ion mass flow $\dot{m}_\iota = (M/e)J_{tot}$, under the assumption of singly charged ions. Thrust may be written as the ion mass flow times the average ion velocity projected on the thrust axis z (constant velocity distribution with angle is assumed).

$$T = \dot{m}_\iota \overline{\boldsymbol{v}\cdot\boldsymbol{e_z}} = \frac{\dot{m}_\iota \overline{\boldsymbol{v}\cdot\boldsymbol{e_z}}}{\dot{m}_\iota \bar{v}} \dot{m}_\iota \bar{v} \quad \textbf{(145)}$$

Now we can construct the total thruster efficiency:

$$\eta_T = \frac{T^2}{2\dot{m}P_e} = \left(\frac{\dot{m}_\iota \overline{\boldsymbol{v}\cdot\boldsymbol{e_z}}}{\dot{m}_\iota \bar{v}}\right)^{\mathbf{2}} (\dot{m}_\iota \bar{v})^2 \frac{1}{2\dot{m}P_e} = \left(\frac{\dot{m}_\iota \overline{\boldsymbol{v}\cdot\boldsymbol{e_z}}}{\dot{m}_\iota \bar{v}}\right)^{\mathbf{2}} \frac{\dot{m}_\iota}{\dot{m}} \frac{\dot{m}_\iota \bar{v}^2}{2P_e}. \quad \textbf{(146)}$$

Thus the total efficiency can be written as the product of three meaningful factors that are respectively the square of the divergence efficiency η_D^2, the mass utilization efficiency η_m, and the power efficiency η_E. These factors can be written as functions of the following measureable quantities: thrust T, total ion electric current J_{tot}, and mean ion energy E_i. The thruster set point $(\dot{m}, P_e)$ is required as well. These partial efficiencies can therefore be evaluated individually from experimental measurements, as is apparent in the following definitions.

The mass utilization efficiency is the ratio of the ion mass flow rate to the input gas mass flow rate. It is assumed that neutral gas come out of the thruster unaccelerated and therefore does not contribute to thrust, and that the ions are singly charged.

$$\eta_m \coloneqq \frac{\frac{M}{e}J_{tot}}{\dot{m}} \quad \textbf{(147)}$$

The power efficiency is the ratio of the ion kinetic power flowing in the jet to the microwave input power P_e.

$$\eta_E \coloneqq \frac{\frac{1}{2}\frac{M}{e}J_{tot}\frac{\overline{E_\iota}}{2M}}{P_e} \quad \textbf{(148)}$$

The divergence efficiency is the ratio of the effective thrust to what it would be if all the current were on the axis.

$$\eta_D \coloneqq \frac{T}{\frac{M}{e} J_{tot} \sqrt{\frac{\overline{E_i}}{2M}}} \quad (149)$$

For a uniform current distribution on the radius lines of a half sphere centered on the thruster, we have $\eta_D = 1/2$.

The total thruster efficiency is

$$\eta_T = \eta_m \eta_E \eta_D^2 = \frac{T^2}{2\dot{m} P_e} \quad (150)$$

2.2.4 Examples of high-TRL products comparable to the ECRT

The available ECRT prototype from VIALIS [24] operates in the power range from 10 to 60 W, corresponding to the "nano-satellite" market. Comparison of the ECRT with propulsion systems aspiring to imminent commercialization is presented in table 3. The Exotrail ExoMG™ - nano is a miniature Hall effect thruster claiming to reduce the time to reach operational orbit in comparison with its competitors. It has moderate power requirement with respect to the produced thrust, at the expense of propellant consumption. The ThrustMe NPT30-Xe is the most advanced electric propulsion product from ThrustMe. It is a gridded ion engine with a neutralizer. This startup is also developing a NPT30 version using iodine and aims at implementing the Neptune concept [62]. The Enpulsion IFM Nano Thruster implements a field emission electric propulsion (FEEP) concept. It is an electrostatic propulsion concept accelerating ions extracted from liquid metal. The Busek BIT-3 is an iodine-fueled gridded ion engine scheduled for launch on two deep-space CubeSat missions aboard NASA's Space Launch System rocket in 2021.

	Development status	Thruster type	Propellant	Power (W)	Thrust (µN)	Isp (s)	Total efficiency	Total impulse (kN.s)
ECRT	under development, TRL3	ECRT	Xenon	40	~ 775	~ 1000	~ 0.1	
Exotrail ExoMG™ - nano	under development	HET	Xenon	50	1500	800	0.12	up to 5
ThrustMe NPT30-Xe	"undergoing industrialization"	GIE	Xenon	40	650			1.7
Enpulsion IFM Nano Thruster	"successfully tested in orbit in 2018"	FEEP	Indium	40	410	3100	0.16	6
Busek BIT-3	scheduled for launch in 2021	GIE	Iodine	55	650	2100	0.12	17

Table 3. Comparison of the ECRT prototype with products aspiring to imminent commercialization. For those, the data is the claim of the manufacturer on their websites. For the ECRT the data is from Vialis [24]. In this case, the power is the deposited microwave power in the plasma rather than the input power of the propulsion system, which is unknown to date. The performance is presented for a given set-point to facilitate comparison; however performance maps would be required to make a more thorough analysis.

We see from this data that the total efficiency of the ECRT is commensurate to the state of the art performance of other comparable technologies. However, the ECRT as a propulsion system is less mature. System level issues are addressed in the framework of the MINOTOR project [60] and the present work focuses on further development and understanding of the thruster itself. In particular, life time is to be assessed; in order to obtain a competitive total impulse, the lifetime of the ECRT should be of a few thousand hours.

2.3 Elements of physics of the ECRT

Outline of the approach. In this section, we present and discuss elements from the state-of-the-art physical understanding of the electron cyclotron resonance thruster (ECRT). It brings together sometimes scattered elements from the literature and from previous experiments at ONERA to shed light on the physics of the thruster. Section 2.3.1 provides a general picture of the plasma through orders of magnitudes estimates of plasma quantities. Sections 2.3.2 and 2.3.3 discuss important phenomena occurring in the coupling structure and in the magnetic nozzle respectively. Finally, section 2.3.4 presents and discusses some particular aspects of ECRT testing. We tried to emphasize on the aspects that differ the most from other electric thrusters.

Note that 1 sccm of Xenon = 97.8 µg/s.

Content

Figure 22 is a schematic view of the ECRT extensively studied in VIALIS (2018) [24]. It consists of a 27.5 mm diameter and 20 mm long semi-open coaxial coupling structure. Xenon gas is injected at a typical flow rate of 1sccm. Typically, 30 W of microwave power at 2.45 GHz is fed through a boron

nitride “backplate”, at the close end of the coaxial structure. It is immersed in a static and divergent magnetic field that is created by an annular permanent magnet. All the necessary power for ionization of the gas and heating of the electrons is provided by the absorption of the microwave. Hot electrons expand in the magnetic nozzle. They create a charge separation electric field accelerating ions. Their motion is guided by magnetic field lines. Additional illustrations are in figure 23 to figure 26.

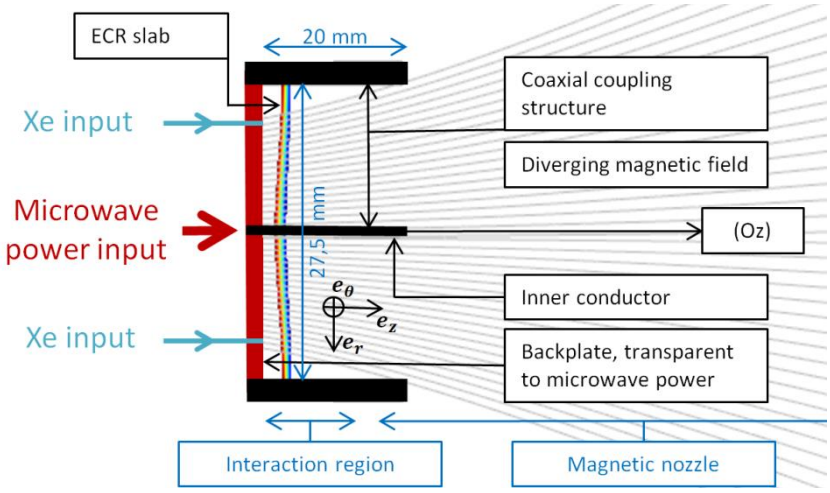

Figure 22. Sectional schematic view of the nominal Vialis ECRT configuration. It is axis-symmetric except for gas injection through a pair of ~ 1 mm holes. Calculated magnetic field lines going through the right end of the coupling structure are represented.

In this chapter and throughout this work we distinguish two regions constituting the plasma volume. *The interaction region* is characterized by the presence of intense electromagnetic field and high neutral gas density, both strongly interacting with the plasma. Also, the static magnetic field in this region is less divergent than in the rest of the plasma volume, that we will term *the magnetic nozzle*. It extends from the upper $z = z_0$ limit of the interaction region towards increasing z, until the plasma is no longer influenced by the magnetic field. In the magnetic nozzle, no electromagnetic field is present, and the plasma is considered collisionless. Although the $z = z_0$ plane limiting the regions is not perfectly well defined, we may have $z_0 \cong 1 - 2$ cm. It may not correspond exactly to the plasma volume inside the coupling structure. Unless otherwise specified the origin of z is taken at the interface between the backplate and the plasma.

The 20 mm length of the outer conductor of the coupling structure is the result of an experimental parametric optimization ([24], section VI – 3.3). The existence of an optimum length may be interpreted a compromise between increasing plasma losses and increasing neutral gas confinement, when the length of the outer conductor is increased. The electromagnetic field is likely absorbed before the $z = 2$ cm.

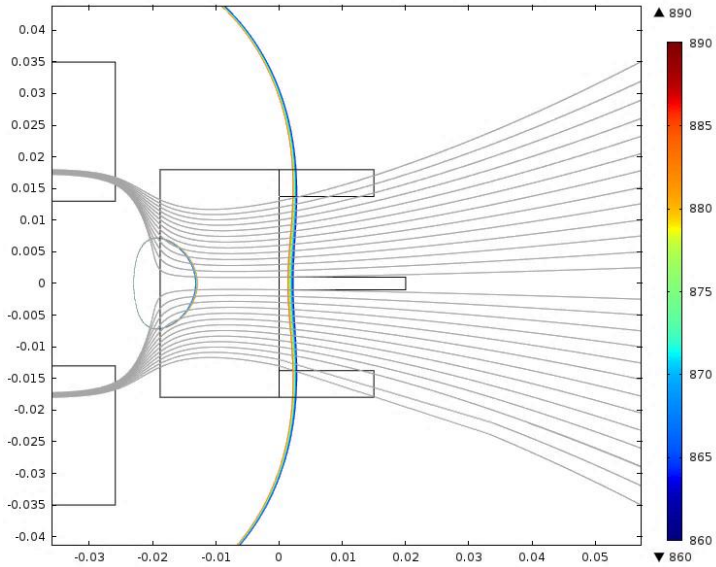

Figure 23. COMSOL simulation of the magnetic field (sectional view). The annular magnet and the general thruster structure are drawn.

Figure 24. Typical implementation of the thruster (from [24]).

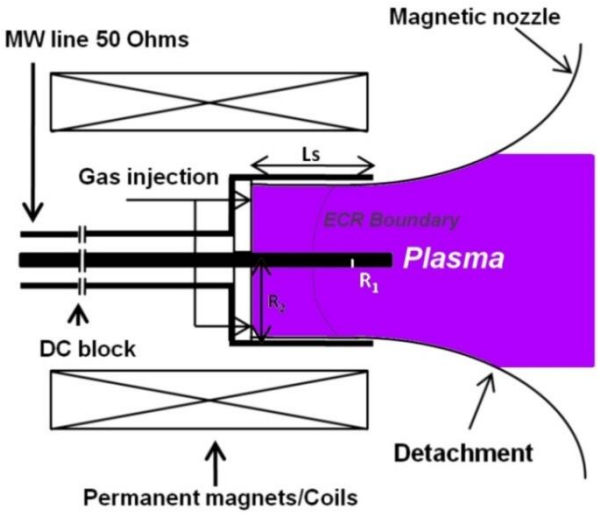

Figure 25. Principle of the ECRT.

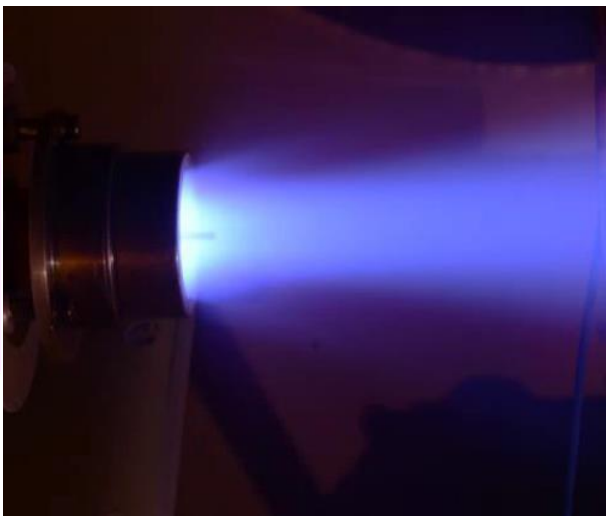

Figure 26. ECRT firing with Xenon.

2.3.1 Orders of magnitude

Table 4 provides a first picture of the ECRT plasma through order of magnitude estimates, mainly based on existing results or very simple modelling. The table is followed by a few lines of justification. For each parameter, a value is proposed at two locations: first, in the plasma slice extending one to two centimeters to the right of the backplate named “the interaction region”; second, in the magnetic nozzle, 25 cm from the exit plane, on thrust axis (Oz). In this section, this location will be simply named “the plume” for simplicity. Note that in the magnetic nozzle plasma parameters vary greatly both in z and r. Therefore the values thereafter given for “the plume” are not representative of the magnetic nozzle as a whole. The distance of 25 cm is approximately that of the Faraday probe scans of Vialis. At this distance,

plasma potential is almost asymptotically flat (figure 34). The magnetic field profile on axis is plotted in figure 27.

Name of the parameter	Symbol or expression in SI units	Expression in practical units	Typical value in the interaction region	Typical value on thrust axis 25 cm from the exit plane
(1) Magnetic flux density	B		875 G	5,2 G
(2) Derivative of the magnetic field	$\left\|\frac{\partial B}{\partial z}\right\|$		$\approx$ 25 G/mm	$\approx$ 0,05 G/mm
(3) Ionic and electronic density	$n_e \gtrsim \frac{\dot{m}\eta_m}{S v_i}$	$n_e[cm^{-3}] \gtrsim 3{,}68.10^{14} \frac{\eta_m\, \dot{m}[sccm]}{S[m^2]\sqrt{\Delta\phi[V]}}$	$\gtrsim 2.10^{11}$ cm^{-3}	$\approx 3.10^{8}$ cm^{-3}
(4) Total ion energy	E_i		$\approx$ 200 eV	$\approx$ 200 eV
(5) Ion kinetic energy	T_i		$\approx$ 2 eV	$\approx$ 150 eV
(6) Mean electron perpendicular kinetic energy	$T_e^{\perp}$		$\approx$ 50 eV	$\approx$ 1 eV
(7) Mean electron parallel kinetic energy	$T_e^{\parallel}$		$\approx$ 4 eV	$\approx$ 1 eV
(8) Xenon gas density	$n_g \lesssim \frac{\dot{m}}{S v_{th}}$	$n_g[cm^{-3}] \lesssim 3{,}43.10^{12}\, \dot{m}[sccm]$	$\lesssim 4.10^{12}$ cm^{-3}	$\approx 4.10^{10}$ cm^{-3}
(9) Electron mean free path	$L_e(v_e) = \frac{1}{\sum_{k,l} n_k \sigma_{k,l}(v_e)}$	$L_e^{50eV/1eV}[m] = \frac{10^{13\ to\ 14}}{n_g[cm^{-3}]}$	$\gtrsim$ 3 m	$\approx$ 17 km
(10) Electron guiding center mean free path	$L_e^{GC} = L_e \frac{v_{\parallel}}{(v_{\parallel}{}^2 + v_{\perp}{}^2)^{1/2}}$	$L_e^{GC} = L_e \sqrt{\frac{T_e^{\parallel}}{T_e^{\parallel} + T_e^{\perp}}}$	$\gtrsim$ 0.8 m	$\approx$ 11 km
(11) Electron mean collision frequency	$\nu_{col} = \frac{\int \frac{1}{L_e}(v_e) f(v_e) v_e dv_e}{\int f(v_e) dv_e}$	$\nu_{col} \approx \frac{5{,}93.10^5 \sqrt{T_e^{\parallel} + T_e^{\perp}}}{L_e}$	$\lesssim$ 5 MHz	$\approx$ 3 kHz
(12) Resonance width (Doppler)	$\Delta z_{res} = \frac{2 v_e^{\parallel}/c}{\frac{1}{B}\left\|\frac{\partial B}{\partial z}\right\|}$		$\approx$ 0,3 mm	
(13) Plasma frequency	$f_{pe} = \frac{1}{2\pi}\sqrt{\frac{e^2 n_e}{\epsilon_0 m_e}}$	$f_{pe}[GHz] = 8{,}98.10^{-6}\sqrt{n_e[cm^{-3}]}$	$\gtrsim$ 4,0 GHz	$\approx$ 0,16 GHz
(14) Debye length	$\lambda_{De} = \sqrt{\frac{\epsilon_0 k_B T_e}{e^2 n_e}}$	$\lambda_{De}[cm] = 743\sqrt{\frac{T_e[eV]}{n_e[cm^{-3}]}}$	$\approx$ 0,01 cm	$\approx$ 0,04 cm
(15) Electron-cyclotron frequency	$f_{ce} = \frac{1}{2\pi}\frac{\lvert eB\rvert}{m_e}$	$f_{ce}[GHz] = 2{,}80.10^{-3}\, B[G]$	2,45 GHz	14,6 MHz
(16) Xe^+-cyclotron frequency	$f_{ci} = \frac{1}{2\pi}\frac{\lvert eB\rvert}{M_i}$	$f_{ce}[kHz] = 1{,}17.10^{-2}\, B[G]$	10.2 kHz	60,8 Hz
(17) Electron Larmor radius	$r_L = \frac{v_e^{\perp}}{\omega_{ce}}$	$r_L[cm] = 3{,}36\frac{\sqrt{T_e^{\perp}[eV]}}{B[G]}$	$\approx$ 0,03 cm	$\approx$ 0,6 cm
(18) Xe^+ Larmor radius	$r_L = \frac{v_{th}}{\omega_{ci}}$	$r_L[cm] = 258\,\frac{1}{B[G]}$	$\approx$ 0,3 cm	$\approx$ 50 cm

Table 4. Orders of magnitude of physical quantities in the Vialis prototype at 1 sccm Xenon and ~ 40 W. Justifications are below.

(3) Given the small fraction of doubly charged ions measured in the plume [63] we may assume equal ionic and electronic density (if averaged at any scale length larger than Debye length). Typical ion density in the interaction region is estimated by conservation of flux, assuming $\eta_m = 0{,}5$ (typical order of magnitude in the experiments) and a potential drop over the interaction region of $\approx$ 2 V (LIF measurements [64]). Typical ion density in the plume is estimated from ion current density (80 µA/cm^2) and ion energy (200 eV, Xenon), from VIALIS (2018) ([24], figure 101 and 104).

(4,5) Ion energy of ≈ 200 eV is typical. Kinetic energy in the interaction region is $\approx$ 1 eV (say half of the $\approx$ 2 V potential drop over the interaction region), whereas the kinetic energy in the plume is ≈ 150 eV since the plasma potential at this location is ≈ 50 eV (figure 34).

(6) Perpendicular electron temperature in the interaction region has not been measured and no mature simulation code is available. Because of resonant heating the electron velocity distribution is likely non-

maxwellian therefore electron temperature should be understood as mean kinetic energy. Langmuir probe measurements revealed an electron temperature of 25 eV, 8 cm down the thruster exit plane (LAFLEUR ET AL. (2015), CORREYERO (2019) [30],[65]). With the expected conversion of the perpendicular temperature into parallel directed kinetic energy performed by the magnetic field (see section 2.3.2.1.2), the value in the interaction region is certainly higher. Besides, a PIC/fluid simulation of the Vialis configuration obtained 50 eV of electron temperature near the inner conductor (SÁNCHEZ-VILLAR [66]). Perpendicular electron temperature in the plume is estimated through conservation of the magnetic moment for electrons having 200 eV of perpendicular kinetic energy in the interaction region. The value of 200eV (rather than mean electron energy for example) is chosen because electrons that reach this location have overcome the static longitudinal potential. They are from the high energy tail of the electron distribution in the interaction region.

(7) A typical value for the electron parallel temperature in the interaction region is taken from the full PIC electromagnetic simulation currently developed by PORTO [67]. The value in the plume is estimated under the assumption that the net (to the right minus to the left) ion and electron fluxes are equal, $\Gamma_e^+ - \Gamma_e^- = \Gamma_i$ (steady state charge conservation). Besides, the Debye length is such that no significant deviation from quasi-neutrality is expected at the scale length of the nozzle and we have negligible fraction of multiply charged ions. Since we measure $\Gamma_e^+ \cong 50\Gamma_i$ we have $(n_0/2)\, v_e^+ \approx 50\, n_0 v_i$. We will elaborate on this rationale in section 4.1.4.

(8) An upper limit for average neutral gas density is obtained through conservation of the flow over the outer conductor section under the assumption of no depletion. Neutral gas density in the plume is roughly the sum of the density attributable to the flow coming from the thruster and of the background density in the tank. The former term is $\approx 4.10^9$ cm^{-3} at 25 cm, estimated by assuming a uniform flow on the front half-sphere and $\eta_m = 0{,}5$. The latter term (background Xenon density) is $\approx 4.10^{10}$ cm^{-3} for 1 sccm Xenon and for a facility achieving 10 000 L/s. Only the dominant background pressure term is presented in the table.

(9,10,11) Given the cross-sections (figure 31) and estimated densities, electron collisional processes are dominated by collisions with the neutrals. These collisions are simply counted by imagining a flux of electrons impinging on fixed neutral targets. This allows for straightforward calculations of mean free path and collision frequency estimates[3]. Electron mean free path is therefore estimated with a total electron-neutral cross section of 10^{-19} m^2 at 50 eV and 10^{-20} m^2 at 1 eV. These figures account for the contributions of ionization, elastic momentum transfer and elastic viscosity. It results that the mean free paths at both locations are large compared with the dimension of the system (coupling structure and magnetic nozzle). The mean free path is also calculated along the guiding center trajectory rather than along the particle trajectory. Again, simple calculation is allowed because we deal with collisions on neutrals. For collisions with charged particles this calculation might be complicated by the Larmor radius being commensurate to the Debye length. The collision frequency is straightforwardly calculated from the mean free path. It is three orders of magnitude below the cyclotron frequency. This is the reason why the coupling to the microwave power is believed to be resonant rather than collisional.

(12) Doppler broadening of resonance was pointed out since the first ECRT publication [7]. Depending on their parallel velocity, electrons perceive the resonance condition at different locations. Hence the distribution in parallel velocities implies the existence of a resonance slab, rather than a resonance plane. The following lines of the table ensue from those already commented.

[3] In contrast, the count of electron-electron collisions for example would require a much more sophisticated approach (GOLDSTON section 11.2 [68], DELCROIX section 13 [69]).

In the following, we discuss first important phenomena occurring first, in the interaction region and second, in the magnetic nozzle.

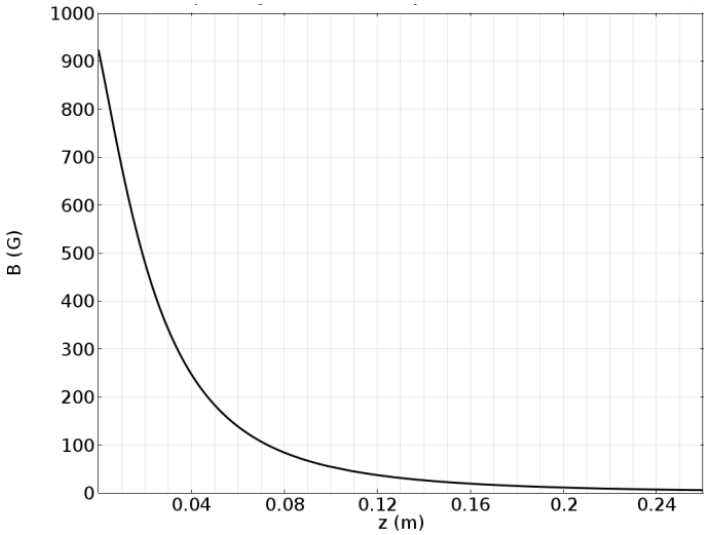

Figure 27. Magnetic field on thrust axis for the nominal Vialis ECRT configuration. The origin is taken at the backplate.

2.3.2 The plasma in the interaction region

In this section we first examine particular motion in static fields. These results are valid, both for the interaction region and the magnetic nozzle. We then move to phenomena that are more specific to the interaction region: electron interaction with the electromagnetic field, particle-particle collisions, and briefly wall interaction.

2.3.2.1 Collisionless particular motion in static fields

One particle motion into static field appears as an essential tool to analyze ECRT physics. A comprehensive analysis of basic charged particle motions is available in BITTENCOURT (2004) [70]. Only fundamental results and cases of particular interest for the ECRT are recalled here.

Ions trajectories are considered to be entirely determined by the static electric field, mainly the longitudinal accelerating field and the field in the sheaths, at the walls of the coupling structure. Given their inertia and the time spent in the magnetic field ($\lesssim 10^{-4}$ s) they trajectories are considered to be independent from the magnetic field (they hardly complete a Larmor radius before being ejected). In the following, only electron trajectories are considered.

2.3.2.1.1 Uniform fields

Exact analytical solutions can be found for uniform fields by solving

$$m\frac{d\boldsymbol{v}}{dt} = q\boldsymbol{E} + q\boldsymbol{v}\times\boldsymbol{B}. \qquad (151)$$

In the following, subscripts ∥ and ⊥ refer to vector components parallel and perpendicular to **B**. The total motion is the sum of three motions.

1. The cyclotron motion, which is a circular motion in the plane perpendicular to $\boldsymbol{B}$ at constant angular velocity $\omega_c = |q\boldsymbol{B}|/m$. The center of that circular trajectory is called the guiding-center

and the radius is called the Larmor radius, $r_L = v_\perp/\omega_c$, where $v_\perp$ is the norm of the (constant) velocity in the plane perpendicular to **B**. Electrons in the thruster have this movement.

2. A translation along **B,** with constant acceleration $(q/m)\boldsymbol{E}_\parallel$. In the ECRT, a longitudinal charge separation electric field creates this type of motion: it accelerates ions in the nozzle and reflects back electrons towards the interaction region.

3. A translation at constant velocity, perpendicular to both $\boldsymbol{E}$ and $\boldsymbol{B}$, called $E \times B$ drift with $\boldsymbol{v_{E\times B}} = \boldsymbol{E} \times \boldsymbol{B}/\boldsymbol{B}.\boldsymbol{B}$ It is independent from mass and charge, therefore does not generate electric currents in a neutral plasma. Such $E \times B$ drift can be expected in the sheaths of the coupling structure walls, along $\boldsymbol{e_\theta}$. It may involve at most a few electron-volts ($v_{E\times B} \approx 10^6$ m/s) for electrons: $B \approx$ 0.1 T and say $E \approx 10^5$ V/m (100 V over 10 Debye length, 100V is the order of magnitude of the difference between ion energy and the coupling structure potential).

The effect of any constant force $\boldsymbol{F}$ can be accounted for by simply substituting $q\boldsymbol{E} + \boldsymbol{F}$ to $q\boldsymbol{E}$ in the preceding, hence a drift velocity

$$\boldsymbol{v_F} = \frac{\boldsymbol{F} \times \boldsymbol{B}}{q\boldsymbol{B}.\boldsymbol{B}}. \qquad (152)$$

2.3.2.1.2 Slightly non-uniform magnetic field

The one particle motion for slightly non-uniform magnetic field without electric field is also well known. Slightly non uniform means that the variation of the magnetic field over a length of order of the Larmor radius is small compared to its total value. Under this assumption a first order perturbation method is used to linearize equation 151. A new force term appears, $q\boldsymbol{v_0} \times ((\boldsymbol{\nabla B}).\boldsymbol{r_0})$, where the subscript 0 denotes the motion described in the previous section. In general, the instantaneous value of that force is irrelevant but rather we are interested in its average over cyclotron motion.

The variations of the magnetic field are described by the matrix $\boldsymbol{\nabla B}$**.** Because the equation is linearized, we can analyze separately the motion implied by each matrix element and reconstitute the full motion as the sum of these motions. Besides, although these matrix elements may be distinguished for the advantage of the analysis, some necessarily coexist in reality since $\nabla.\boldsymbol{B} = 0$, and $\boldsymbol{\nabla} \times \boldsymbol{B} = \boldsymbol{0}$ in a static and current free case. We set apart shear terms, which do not produce first order drifts [70], and concentrate on divergence and gradient terms on the one hand, and curvature terms on the other hand.

Divergence and gradient terms. They comprise, in Cartesian coordinates $\partial_i B_i$ and $\partial_i B_z$, where z is the direction of the zeroth order uniform field. The fact that the magnetic field lines are straight in that case simplifies the calculation because the cyclotron motion stays in xy planes. After some simple calculation (averaging over cyclotron period and use of $\nabla.\boldsymbol{B} = 0$ [70]), the average force reads

$$< \boldsymbol{F_G} >= -|\boldsymbol{\mu}|\boldsymbol{\nabla}\mathrm{B_z} \qquad (153)$$

where $\boldsymbol{\mu} = \frac{mv_\perp^2}{\boldsymbol{B}.\boldsymbol{B}}\mathbf{B}$ is the magnetic moment. It is independent of charge. This force has at least two consequences in the ECRT.

1. The parallel component of the force implies a constant acceleration along magnetic field lines that is considered as the main acceleration mechanism. It is sometimes called diamagnetic force, in reference to the fact that free charged particles are repelled towards regions of lower magnetic field, or equivalently that the movement of the particles create a field opposite to that generating

the movement. That force transforms $v_\perp$ into $v_\parallel$ for a decreasing magnetic field (diverging field lines) and vice-versa for increasing magnetic field (converging filed lines).

2. The perpendicular component of the force implies an azimuthal drift called gradient drift, along $\boldsymbol{e_\theta}$ for electrons (relation 152). It typically involves 10^{-3} eV ($v_{\nabla B \times B} \approx 2.10^4$ m/s) if estimated in a plane 5 cm from the backplate, where the perpendicular gradient is strong.

Curvature terms. They comprise $\partial_z B_x$ and $\partial_z B_y$. The force imparted on the particle is understood as a centrifugal force maintaining the guiding center on a field line

$$\boldsymbol{F_C} = -\frac{m v_\parallel^2}{R}\boldsymbol{n_1} \qquad (154)$$

where $\boldsymbol{n_1}$ is a unit vector, normal to the field line, and pointing "inward" ([70], figure 16). It is by definition a perpendicular force, thus implying a drift, called curvature drift. For the ECRT the drift is estimated to be negligible as compared to the gradient drift (about two orders of magnitude lower in velocity).

2.3.2.1.3 Conservation of adiabatic invariants

Under the assumption of slightly a non-uniform magnetic field, momentum conservation along *z* reads:

$$m\frac{dv_\parallel}{dt} = -|\boldsymbol{\mu}|\partial_\parallel B. \qquad (155)$$

Multiplying by $v_\parallel$ and using the conservation of total (purely kinetic) energy we get

$$\frac{d|\boldsymbol{\mu}|}{dt} = 0 \qquad (156)$$

meaning that the magnetic moment is conserved. It is also called the first adiabatic invariant. It can be shown that there exist two other adiabatic invariants for the movement in a slightly varying magnetic field associated with respective periodic motions. They are best visualized in the classical example of the magnetic bottle (figure 28).

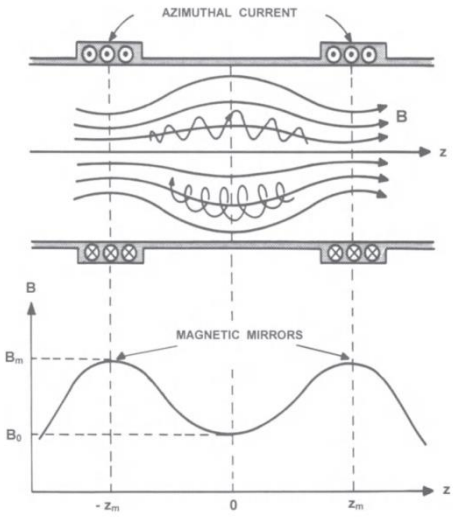

Figure 28. Magnetic bottle, reproduced from [70]

The second adiabatic invariant J, or longitudinal invariant, is associated to the so called bounce movement along a field line, originating from successive reflections in the high field regions, at the points where $v_{\parallel} = 0$ (and change sign), called mirror points.

$$J \coloneqq \oint \boldsymbol{v}.\boldsymbol{dl} \quad \textbf{(157)}$$

The third adiabatic invariant or flux invariant is associated with the azimuthal drift movement around the axis of the magnetic bottle ([71], figure 10.14). It originates from curvature and gradient drifts. It is defined as the magnetic flux through the surface enclosed by that drift trajectory.

$$\phi \coloneqq \frac{1}{2\pi}\iint \boldsymbol{B}.\boldsymbol{dS} \quad \textbf{(158)}$$

The confinement of electrons in a magnetic bottle can be analyzed rigorously in the framework of Hamiltonian adiabatic perturbation theory (RAX, 2005, section 10.3.3 [71]). Canonical transformations enable to change variables from spatial coordinates and associated conjugate momentums to adiabatic invariants and associate angles. Once these variables are identified we can set aside the oscillating variables (angles) and concentrate the analysis on adiabatic invariants. They are constant for the motion in the magnetostatic field but can evolve as a consequence of the interaction with the electromagnetic field or particle collision. The model presented in chapter 7 will draw on this type of approach.

The study of the magnetic bottle is relevant to the ECRT because electrons are confined on the left by a half magnetic bottle (magnetic mirror), and on the right by an electric field parallel to magnetic field lines (electric mirror). In the absence of a detailed analysis we may assume that the electric mirror simply reflect electrons and use the magnetic bottle example to guide our intuition of electron motion in the ECRT.

Estimation of the period of the motions associated with adiabatic invariants (table 5) shows that they develop on well separated time scales (strong ordering). The periodicity associated with the magnetic moment is the well-known cyclotron period already given in table 4. The period of the bounce motion is estimated from equation 155 as $T_B \approx 4\sqrt{\Delta z}\,/\sqrt{(|\boldsymbol{\mu}|/2m)\left|\partial_{\parallel}B\right|}$ and the period of the azimuthal drift motion is estimated as $T_D \approx 2\pi\Delta z/v_{\nabla B\times B}$, where $\Delta z \approx 0{,}1$ m is the scale length of the longitudinal and radial variations of the magnetic field.

Motion	Adiabatic invariant	Period of the motion
Cyclotron	Magnetic moment	$\approx 10^{-10}$ s
Longitudinal bounce	Longitudinal invariant	$\approx 10^{-7}$ s
Azimuthal drift	Flux invariant	$\approx 10^{-5}$ s

Table 5. Oscillating motions in the ECRT

2.3.2.2 Wave absorption

2.3.2.2.1 Cold plasma model

The more common approach to study waves in magnetized plasma is to consider a collisionless, cold, and uniform electron plasma, whose dynamics is described by a linearized fluid equation. Cold plasma means here that the phase velocity of the wave is much larger than the thermal velocity of charged particles. This approach is wide spread and proves very useful even in situations where these rather restrictive assumptions are not fully satisfied. The dielectric tensor is such that the time Fourier transform of the Maxwell-Ampère equation reads

$$\nabla \times \boldsymbol{H} = -j\omega\epsilon_0 \boldsymbol{E} + \boldsymbol{J} = -j\omega\epsilon_0 \bar{\bar{\kappa}} \boldsymbol{E}. \quad (159)$$

The dielectric tensor is a means to describe the response of the plasma to an electromagnetic excitation, that is, to provide an expression for the left-hand side of Maxwell-Ampère equation as a function of the electric field $\boldsymbol{E}$. The dielectric tensor relates to the conductivity tensor ($\bar{\bar{\sigma}}$ such that $\boldsymbol{J} = \bar{\bar{\sigma}}\boldsymbol{E}$) as $\bar{\bar{\sigma}} = j\omega\epsilon_0(\bar{\bar{I}} - \bar{\bar{\kappa}})$. Waves in plasma have been thoroughly studied by STIX (1962, 1992) [72], [73] and the cold plasma dielectric tensor derived from this approach can be found in almost any plasma textbook. It reads

$$\bar{\bar{\kappa}} = \begin{bmatrix} S & -jD & 0 \\ +jD & S & 0 \\ 0 & 0 & P \end{bmatrix} \quad (160)$$

with

$$S = 1 - \frac{\omega_{pe}^2}{\omega^2 - \omega_{ce}^2}, \; D = \frac{\omega_{ce}}{\omega}\frac{\omega_{pe}^2}{\omega^2 - \omega_{ce}^2}, \; P = 1 - \frac{\omega_{pe}^2}{\omega^2}. \quad (161)$$

The combination of Maxwell-Ampère and Maxwell-Faraday equations yields an eigen value problem for $\boldsymbol{E}$. The study of this problem results in a set of wave modes. A wave mode is defined by a dispersion relation (eigen value) and a polarization (eigen vector).

2.3.2.2.2 Cold plasma model with k collinear to B

As a first approach for the analysis of waves in the ECRT we may consider *wave modes whose wave vector is strictly collinear to the magnetic field vector*. The search for eigen values reveals that there are two such modes. They obey the following dispersion relations, with $k = \omega/c$ the wavenumber in vacuum.

$$N_R^2 = \frac{\beta_R^2}{k^2} = 1 - \frac{\frac{\omega_{pe}^2}{\omega^2}}{1 - \frac{\omega_{ce}}{\omega}} \quad (162)$$

$$N_L^2 = \frac{\beta_L^2}{k^2} = 1 - \frac{\frac{\omega_{pe}^2}{\omega^2}}{1 + \frac{\omega_{ce}}{\omega}} \quad (163)$$

The polarization of these modes is defined by the associated eigen vectors, $\boldsymbol{E_r} = \boldsymbol{e_x} + j\boldsymbol{e_y}$ and $\boldsymbol{E_l} = \boldsymbol{e_x} - j\boldsymbol{e_y}$ respectively, indicating circular polarization. When looking towards the direction of propagation, the electric field vector of these modes rotates clockwise (right hand circularly polarized, R) and anti-clockwise (left hand circularly polarized, L) respectively. Let's analyze the propagation of these waves along z, for plasma parameters varying along z only.

R wave

In the ECRT, waves enter the plasma in a monotonically decreasing magnetic field (hence monotonically decreasing ω_{ce}) from a point where $\omega_{ce} > \omega$. At this point $N_R^2 > 0$, indicating propagation. When $\omega_{ce} \to \omega^+$, we have $N_R^2 \to +\infty$, indicating a singularity of the model for $\omega_{ce} = \omega$. This case corresponds to resonant energy transfer from the wave to the electrons, or vice-versa. In the plane perpendicular to propagation where the magnetic field satisfies $\omega_{ce} = \omega$, electrons rotate around the magnetic field lines at the same angular velocity and in the same direction than the electric field vector. It implies that there exists a constant phase between a given electron and the electric field vector,

resulting in a continuous rather than oscillating power transfer (figure 29). We see that for any phase yielding an energy gain, there is an opposite phase (π-shifted) that seems to yield an equal energy loss. Hence we may wonder how net power is transferred to the electrons. This question will be addressed in chapter 7.

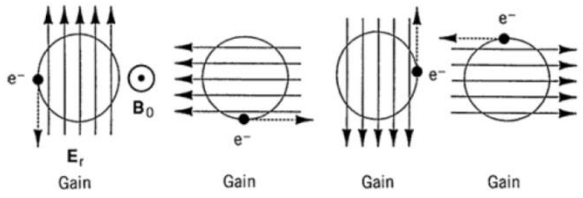

Figure 29. Electron continuously gaining energy from the electromagnetic field through electron-cyclotron resonance (reproduced from [74]). An electron with opposite phase would continuously loose energy.

The possibility of an energy transfer diverging with time can be regularized in the context of the ECRT by including either the effect of collisions or the effect of inhomogeneous magnetic field. Collisions randomly modify the phase of colliding particles with respect to the electric field vector, thus preventing infinite energy transfer. Inhomogeneous magnetic field and non-zero parallel velocity implies that $\omega_{ce} = \omega$ is undergone by particles only during a null duration.

To proceed with the analysis we may then drop the collisionless assumption. It was made for good reasons: the frequency of collisions is three orders of magnitude below the wave frequency (table 4). Yet collisional absorption is usually expected only if $\nu_{col} \approx \omega/2\pi$ and considered negligible if $\nu_{col} \ll \omega/2\pi$. Hence the legitimate collisionless assumption. Nonetheless, collisions do play a role when $\omega_{ce} \cong \omega$. The inclusion of collisions allows for wave absorption calculation through a complex wave number (or more generally a non-Hermitian conductivity tensor). The inclusion of collisions results in the following complex dispersion relation [74] represented in figure 30.

$$N_R^2 = \frac{\beta_R^2}{k^2} = 1 - \frac{\frac{\omega_{pe}^2}{\omega^2}}{1 - \frac{\omega_{ce}}{\omega} - j\frac{\nu_{coll}}{\omega}} \qquad \textbf{(164)}$$

The power absorption of such a R wave in a linearly decreasing magnetic field around $\omega_{ce} = \omega$ has been studied in WILLIAMSON (1992) [75]. They found that the *absorbed power fraction for the R wave is determined mainly by the plasma density and total absorption occurs for relatively small plasma density* ($< 10^{11}$ cm^{-3}). The absorbed power fraction is relatively independent of the collision frequency, from 10^7 (a slight over estimate for the ECRT) to 10^{10} (figure 2b [75]). This indicates that resonant absorption rather than collisional absorption is described by this model. The independence of the absorbed power fraction on collision frequency may be understood by looking at the imaginary part of the wave number, as is done in Appendix A.

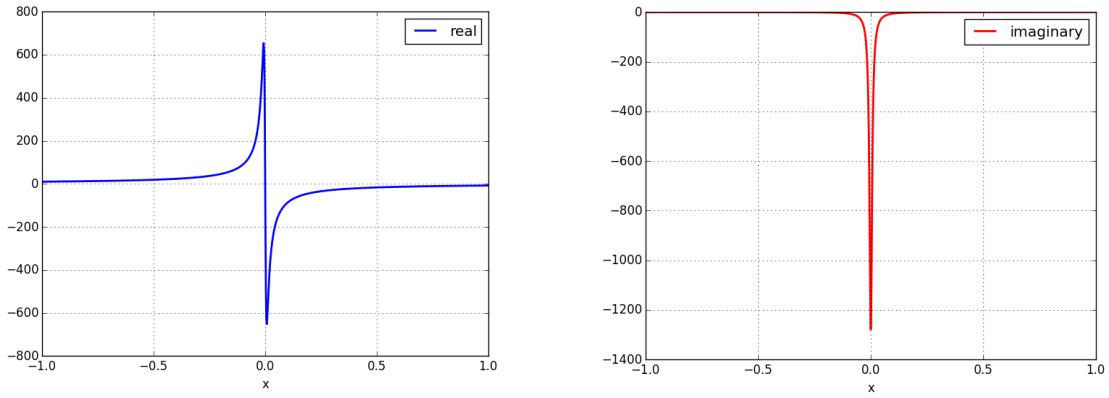

Figure 30. Squared refractive index from relation 164, for constant $\nu_{coll} = 2\pi \times 5.10^6$ s^{-1}, constant plasma frequency $\omega_{pe} = 2\pi \times 4.10^9$ and linearly varying cyclotron frequency $\omega_{pe} = 2\pi \times 2,45.10^9(1 - 0,3x)$. For x in cm, this is the slope in the ECRT.

L wave

The L wave may be transmitted through the plasma of the ECRT if $\beta_r^2 > 0$ for all z locations. Depending on the plasma density profile and magnetic field profile, there may also exists a region where $\omega_{pe}^2/\omega^2 > 1 + \omega_{ce}/\omega$, hence $\beta_r^2 < 0$, indicating that the wave is evanescent, hence reflected at the interface of that region. This may happen in the plasma ($z > 0$) or at the backplate-plasma interface ($z = 0$). In any case, *no absorption of the L wave is predicted by the cold plasma model for propagation strictly parallel to the magnetic field.*

2.3.2.2.3 Coupling of the L wave to the plasma

From the first ECRT experiment, coupling efficiencies (ratio of the absorbed power to the incident power) above *90% were reported for an incident linearly polarized wave* (MILLER AND GIBBONS (1964) [11]). The Vialis prototype operated with linearly polarized wave achieves 96% coupling ([24], table 5). We verified in this study that no power is radiated in the tank. Yet, a linearly polarized wave parallel to the magnetic field is the sum of a R wave and a L wave. Hence the coupling is expected to be 50% at most, corresponding to full absorption of the R wave. This apparent contradiction applies to ECR sources in general and was previously pointed out, for example in GELLER (1996) [76], section 2.4.1.

The generally accepted *explanation for the absorption of the L wave is the conversion into other wave modes that can be absorbed* [75], [76]. Mode conversion is possible under local plasma conditions (ω_{pe}, ω_{ce}) such that distinct wave modes have similar wave number and polarization. Under such conditions, even a small deviation between the real plasma and the modeled plasma may enable "crosstalk" between eigen modes of the model. MUSIL AND ZACEK (1970) [77] studied mode conversion in the framework of the cold magnetized plasma model of section 2.3.2.2.1. In particular, they looked into propagation at a small angle with respect to the magnetic field. This case is relevant for the ECRT, whose magnetic configuration is such that out of axis, field lines quickly form an appreciable angle with the direction of propagation z (figure 22).

The authors showed that the limit of the L mode for $\omega_{pe}^2/\omega^2 \to 1^+$ is the longitudinal plasma wave (dispersion relation: $\omega = \omega_{pe}$) with diverging wave number (hence vanishing phase velocity). No mode conversion argument is required in this case. The case $\omega_{pe}^2/\omega^2 \to 1^-$ may be more relevant for the ECRT. In this case, they proposed that mode conversion from L to longitudinal plasma wave with diverging wave number happens when $\omega_{pe}^2/\omega^2 \to 1^-$. Measurements were presented to support this

analysis. However, these results are limited to $\omega_{ce}/\omega < 1$ whereas the case $\omega_{ce}/\omega > 1$ is also of interest for the ECRT. Besides, similar mode conversion mechanisms exist for the R wave.

The authors also suggest that the longitudinal plasma waves created by mode conversion mechanisms are then absorbed through Landau damping. The diverging wave number when $\omega_{pe}^2/\omega^2 \to 1$ implies that the phase velocity goes from c down to 0 when $\omega_{pe}^2/\omega^2 \to 1$, therefore sweeping through the electron velocity distribution. This may provide Landau damping for all the longitudinal electron distribution.

With such heating mechanism, the electron distribution function may not be as anisotropic as expected at the beginning of ECRT researches when pure ECR heating was assumed (pure ECR heating meaning heating of the perpendicular electron distribution only, by the R wave only). Unfortunately, it seems that no direct electron temperature measurements in the interaction region of a coaxial ECRT are available to contribute to this discussion. Langmuir probe measurements have been tried, but could not be performed in the interaction region. The issue seems to lie in discriminating perpendicular and parallel directions, manage heating due to the plasma conditions in the interaction region, and avoid perturbation of both the plasma and wave propagation while making measurement.

A mode conversion mechanism around $\omega_{pe} = \omega$ may also be the interpretation for an otherwise puzzling observation reported by Cannat ([28], figure 4.3.14). He measured the coupling from the incident (linearly polarized) microwave to the plasma, as a function of magnetic field strength, which was varied using the coil current intensity. In at least one of his ECRT configurations, he observed that the coupling did not show significant variation with respect to the coil current intensity, even when the ECR region was moved out of the coupling structure. It implies that the presence of the ECR condition in the plasma is not critical for wave absorption. This observation was repeated during this study. It stands in clear contradiction with pure ECR heating by the R wave.

With only analytical and experimental results, it is difficult to go beyond speculations on the matter of wave absorption in the ECRT. We may hope that ongoing simulation efforts carried out separately by Sánchez-Villar [66] and Porto [67] shall soon shed clear light on this matter.

A more systematic understanding of wave modes can be developed using the CMA diagram, briefly introduced in Appendix B.

2.3.2.3 Particle-particle interaction

Electron cross sections illustrate one aspect of the complexity of the ECRT (figure 31): at the relevant energy in the interaction region (≈ 50 eV) several processes have cross sections of the same order.

Interestingly, although the electron mean free path is larger than the dimension of the system (table 4), it may not completely preclude collisional effects. Indeed, many authors of modelling work have noted the existence of a trapped population of electrons undergoing oscillations along the magnetic field lines [30], [78], [79]. The amplitude of those oscillations would typically equal the magnetic field variation scale length (≈ 10 cm). As a consequence, the length of the average electron trajectory linearly depends on the number of oscillations it undergoes and may largely exceed the mean free path. We shall elaborate on this oscillating dynamics in chapter 7.

The common approach is followed for the calculation of the Coulomb momentum transfer cross section: to consider cumulative effect of small angle collisions and integration over impact factor limited to Debye length.

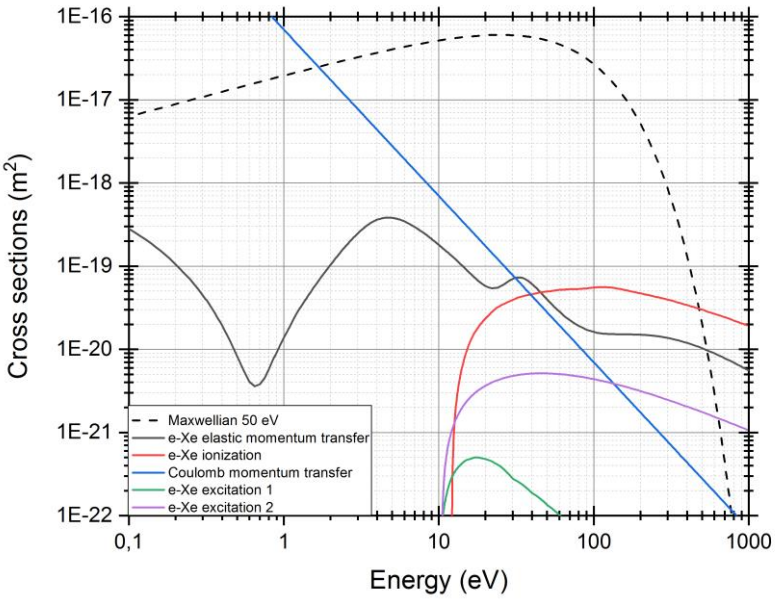

Figure 31. Electron cross sections. Coulomb cross section is estimated from the common approach (see for example [74], section 3.3). Other cross sections are from measurements (LXCat [80]). A 50 eV maxwellian is plotted in arbitrary units.

2.3.2.4 Wall losses

The coupling structure is a metallic coaxial structure, whose surfaces in contact with the plasma are roughly parallel to field lines. The question of wall losses therefore relates to the much debated issue of cross-field diffusion, in particular in fully ionized plasmas. In this case, a rather intuitive classical (or collision induced) diffusion coefficient was originally proposed. It simply describes a random walk process with the Larmor radius as step length and a time scale that is the collision frequency: for each collision event, the guiding center of the particle typically moves of a length r_L in a random direction. This diffusion process scales as $1/B^2$. It was repeatedly shown however since 1946 that this prediction is not verified in a number of experiments. Bohm proposed a semi-empirical formula for the diffusion coefficient scaling as $1/B$ which was obeyed by many experiments. However, the phenomena behind this increased diffusion are unclear (CHEN, 1974 [1]).

As an example, diffusion processes in the Hall effect thruster are still an active area of research. Experiments suggest that the velocity distributions observed with LIF measurements correspond neither to a $1/B^2$ diffusion, nor to a $1/B$ diffusion [81]. "Anomalous" cross-field electron transport is the subject of specific PIC simulations. It seems to originate mainly from $E \times B$ drift instabilities, but also from sheath instabilities in the presence of intense SEE for example [82].

Although the magnetic and electric configuration is different in the ECRT, the cross-field electron diffusion is an issue, a priori. These concerns motivated the use of an empirical radial density profile in the only full global model available for the ECRT [29], [32].

In computational models, frequent assumption of fully magnetized electrons enable to study the dynamic of the nozzle without dealing with cross-field electron transport. Computational models for the plasma in the coupling structure of the ECRT are only preliminary. There is a full-PIC approach [67] and a fluid

electron approach [66] using a turbulent electron transport model initially develop for Hall thrusters [83].

2.3.3 The plasma in the magnetic nozzle

2.3.3.1 "Historical" explanation of the acceleration

From the beginning of ECRT research, magnetic nozzle acceleration is outlined in two key phenomena that are apparent on figure 32, later complemented by a third critical step.

1. Acceleration of electrons through the $-|\mu|\,\nabla_{\parallel}B$ force.
2. Acceleration of ions through charge separation coupling.
3. Detachment of the plasma jet from the magnetic nozzle.

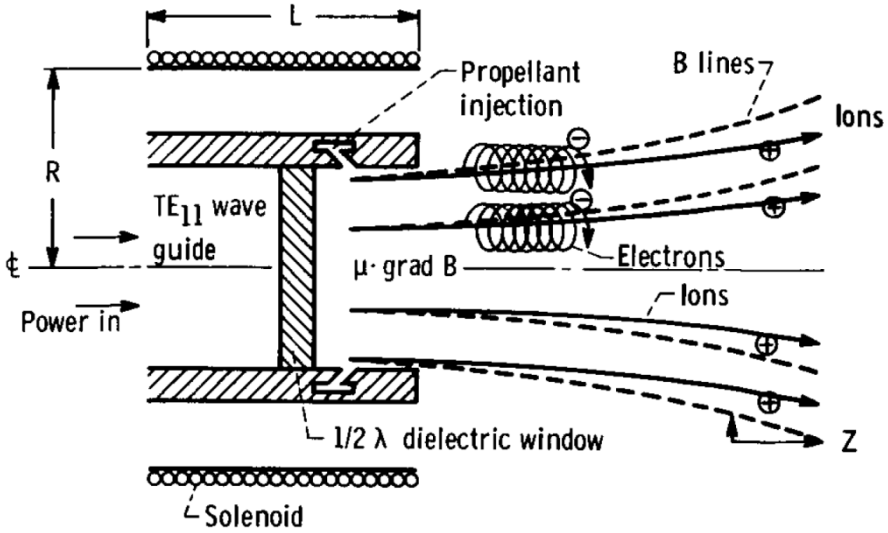

Figure 32. Schematic diagram of ECR accelerator, reproduced from [15], 1967

Each of these phenomena is briefly commented in this section. First, the historical explanation insists on the conversion of perpendicular kinetic energy into parallel kinetic energy performed by the diverging magnetic field [7], [25], [15]. This conversion was all the more required at the beginning of ECRT researches because energy deposition was expected in the perpendicular electron velocity only, as discussed in section 2.3.2.2.3. This conversion mechanism is remarkable because it makes the perpendicular electron temperature available to produce thrust.

Thrust is dominated by the contribution of ion momentum that are accelerated through a mechanism sometimes called "charged separation coupling" [15]. This mechanism is analogous to that of a sheath and can be outlined as follows. Steady state charge conservation applied to a control volume containing the thruster implies equality of ion and electron flux exiting the volume (this volume is taken sufficiently large that no fluxes exist towards the inside). Yet, the electron flux exiting the interaction region to the right is considerably higher than the ion flux because electrons are considerably lighter than ions and have a comparable or higher parallel kinetic energy. Hence the establishment of an electric field accelerating ions. This electric field is often termed "ambipolar electric field" because no net current is drawn from the thruster. However, the plasma is not, a priori, locally ambipolar. Indeed, simulations suggest that local electric current play an important role in the nozzle dynamics [84]. The electric field

accelerating ion and the underlying potential will be simply called accelerating electric field or accelerating potential.

Thrust production requires an additional key mechanism: detachment from the magnetic field. Indeed, if the plasma flow was to follow magnetic field lines it would impart no net force on the thruster. This delicate and still open question has focused dedicated modelling efforts reviewed in AHEDO AND MERINO (2011) [85]. In this paper, they put forward new detachment mechanisms in the context of propulsive magnetic nozzles as alternatives to the already proposed resistive detachment [86], electron inertia detachment [87], and self-field detachment [88]. This question, however fascinating, will be left outside of the scope of this review. Indeed, from a development standpoint, it appears sufficient to know that the plasma jet does detach, since a net thrust is reliably measured [33]. Moreover, it detaches soon enough that beam divergence is not an issue: beam divergence below 20° have always been observed ([14], figure 7), and the Vialis and Cannat prototypes have divergence efficiencies (as defined in section 2.2.3) above 80% ([24], figure 100).

2.3.3.2 Effective role of the magnetic field

The key role of the magnetic field in the acceleration process was clearly demonstrated through separate thrust balance measurement of the force imparted one hand on the magnet ("magnetic thrust") and on the other hand on the coupling structure ("pressure thrust") [34]. The fraction of the total thrust that is imparted on the magnet increases with decreasing mass flow up to 78% at 0.6 sccm Xenon and 40 W. In the 1960's, researchers in fact measured thrust on the magnetic coil only [16], [20], probably for simplicity, but also because they assumed that energy was deposited in the perpendicular electron velocity only and converted into thrust by the diverging magnetic field.

The effect of the magnetic field may be separated into a macroscopic action at the level of the plasma flow (forces applied on the guiding center of electrons) and a microscopic action at the thermodynamics level (conversion between $v_\perp$ and $v_\parallel$ described in flow models as an $n_e(T_{e\perp}, T_{e\parallel})$ relation).

Separate "magnetic thrust" and "pressure thrust" measurements are global measurements integrating all effects, therefore more detailed magnetic nozzle investigations will be reviewed in the next paragraph. Nonetheless, the following sentences are an attempt to speculate on these measurements. Let's assume a uniform flow on a half sphere centered on the thruster to be the "worst realistic" flow distribution in the absence of magnetic nozzle. Indeed, although the divergence of the jet increases with decreasing magnetic field, it seems unlikely that the current density be increasing with angle. Then, imagining an ideal magnetic nozzle, in the sense that it would transform this uniform distribution into a Dirac on axis: the thrust doubles, as can be calculated from relation 169 for example. Therefore, it seems that if the effect of the magnetic field were only to guide the flow, the "magnetic thrust" would be at most equal to the "pressure thrust".

2.3.3.3 Effect of the magnetic field on the plasma flow

There seem to be a consensus that the nozzle dynamics is collissionless. The ion current density circular profile (as defined in section 2.3.4.4) is independent of mass flow rate at least around the nominal mass flow ([24], figure 108). In addition, the divergence efficiency and the ratio E_i/T_e are independent from the mass flow [30]. Hence the systematic collisionless assumption of magnetic nozzle flow models.

Most models are "fluid models". We should however refrain from approaching these models with our intuition of fluid as a continuous medium where the mean free path is much smaller than the fluid parcel, thus ensuring local maxwellian equilibrium. "Fluid model" simply means that averages over the velocity distribution function are considered. In the following we shall term these models "flow models".

In order to estimate thrust, or to study the details of the plasma flow in the magnetic nozzle, two dimensional axis symmetric flow models are implemented. They typically assume collisionless equations, quasi-neutrality, negligible electron inertia, often cold ions and "fully magnetized" electrons.

The assumption of "fully magnetized" electrons means that the streamtubes for electrons are the magnetic streamtubes. The equivalent in a one particle vision seems to be: electron guiding centers follow magnetic field lines. In a three dimensional geometry, this does not preclude however the existence of electrons currents in any direction. They do not stem from guiding center drift but rather from the combination of the cyclotron motion with density or pressure gradients (to visualize this, see for example [89], figure 5.2). In an axis symmetric geometry ($\partial_\theta = 0$), "fully magnetized" electrons implies that the fluid electron velocity reads $\boldsymbol{u_e} = u_{e\parallel}\boldsymbol{B}/B + u_{e\theta}\boldsymbol{e_\theta}$, where $(\boldsymbol{B}/B, \boldsymbol{e}_\perp, \boldsymbol{e_\theta})$ is an orthonormal base attached to the local magnetic field.

The fluid azimuthal electron current $-en_e u_{e\theta}$ (sometimes called Hall current) is central to the flow analysis as already understood by Sercel ([23], section 2.2.1), because the $-eu_{e\theta}\boldsymbol{e_\theta} \times \boldsymbol{B_z}$ Lorentz force balances the radial pressure gradient to provide radial equilibrium of the plasma, while the $-eu_{e\theta}\boldsymbol{e_\theta} \times \boldsymbol{B_r}$ Lorentz force drives the longitudinal plasma acceleration.

Analytical analyses

TAKAHASHI (2011) [90] and FRUCHTMAN (2012) [91] analyzed the flow equations analytically under the additional simplifying assumptions of negligible radial ion inertia and some ambipolarity assumption. They derived an expression for thrust simply depending on the pressures, $p_{e\parallel}(r,z)$ and $p_{e\perp}(r,z)$. Thrust therefore critically depends on the expressions of pressure gradients that are left unspecified by this analysis. It is well known that fluid equations must be closed, typically at the level of the momentum conservation equation, by assigning an expression for the pressure gradient. The simplest possible assumption is the isothermal assumption, implying null pressure gradients. However this assumption is somewhat incoherent in this context because electron thermal energy in fact "fuels" the acceleration. Therefore electrons with constant temperature represent a non-depleted energy reservoir yielding an unbounded accelerating potential, as frequently noted in the literature ([84], among others).

LAFLEUR (2014) [32] proposed and helicon thruster model in this analytical-fluid framework, using an isothermal assumption for simplicity. In order to avoid the unbounded potential issue just discussed, he proposed an order-of-magnitude criterion for detachment that limited the acceleration. This model is associated with a discharge model describing the plasma in the coupling structure. It was adapted to the ECRT configuration of Cannat and compared to experimental results. The integrated ion current seems in good agreement but the model fails to predict thrust ([29], figure 9).

A common way to avoid the isothermal assumption without dealing with all the kinetic complexity is to use a polytropic index γ_e such that

$$\frac{T_e(z)}{T_{e0}} = \left(\frac{n_e(z)}{n_{e0}}\right)^{\gamma_e}. \qquad (165)$$

Such an approach was implemented by Cannat in the context of ECRT. He substituted a polytropic index assumption to the isothermal assumption in the Lafleur model. It still failed to predict thrust ([28], figure 5.1.4).

Computational analyses

Research efforts were directed at the computational treatment of the magnetic nozzle flow. In particular, AHEDO AND MERINO (2010) [92] presented a 2-D axis-symmetric plasma expansion model that is collisionless, electron-magnetized, low-beta, and globally current free. They analyzed the acceleration process in contrast to that of a physical nozzle, and identified that current ambipolarity is not fulfilled everywhere. However, several features of the model preclude the calculation of thrust. First, detachment cannot be simulated mainly because of the fully magnetized assumption but also because plasma-induced magnetic field and electron inertia are neglected. Second, isothermal electrons are assumed for simplicity.

This latter issue is addressed in MERINO AND AHEDO (2015) [84]. The model is adapted to substitute a bi-polytropic index (ions and electrons) to the isothermal assumption. They showed that the characteristics of the flow significantly depend on the thermodynamics of the nozzle and call for more advanced study of kinetic effects.

2.3.3.4 Effect of the magnetic field on the plasma thermodynamics

By using the term "thermodynamics", we temporarily accept the prevailing perspective of a fluid approach, in which the expression of the pressure tensor closing the momentum conservation equation is said to describe the thermodynamics of the plasma.

In order to feed the fluid-based models with a proper thermodynamics closure relation it is interesting to study experimentally the thermodynamics of the magnetic nozzle. Under the assumption of an isotropic maxwellian distribution with temperature T_e, local ambipolarity, and taking into account a presheath, the accelerating potential drop in the absence of magnetic field reads [30]

$$\Delta\phi = \frac{T_e}{2}\left(1 + \ln\left(\frac{M_i}{2\pi m_e}\right)\right) \qquad \textbf{(166)}$$

which is the same relation as for a floating-wall sheath. As explained in section 2.3.3.1, we may expect that a diverging magnetic field increases this potential drop by typically a factor 3 for an isotropic distribution. Indeed, it supposedly extracts the energy contained in the two perpendicular degrees of freedom, for the benefit of the acceleration. The ratio $\Delta\phi/T_e$ can also be related to a polytropic index, which is an input for magnetic nozzle flow simulation [84].

This is the motivation for the work presented in LAFLEUR (2015) [30]. The ratio $\Delta\phi/T_e$ obtained with the Cannat prototype was analyzed in the light these considerations for several mass flows and three magnetic configurations. The magnetic configurations were the following: no magnetic field, or magnetic field produced by a coil, operated either at 130 A or at 160 A. Measurements were made on the thrust axis. Unfortunately, these results seem rather inconclusive because temperature measurements were made 8 cm down the "thruster exit", for reasons relative to Langmuir probe operation. Therefore it was assumed that electron temperature stays constant along the thrust axis, whereas the simple presence of a diverging magnetic field raises concerns about the isothermal assumption. In addition, later temperature measurements made as a function of z on the same prototype showed sharp variations of the $T_e(z)$ around for $z = 8$ cm ([65], figure 6). With that in mind, we may want to compare the ion energy between the three magnetic configurations ([30], figure 6). However, when the magnetic field is reduced or cancelled, wall losses in the coupling structure increase. A common particle balance argument then predicts an increased electron temperature to maintain the plasma. Therefore the sum of several effects is assessed instead of the magnetic nozzle behavior only.

These issues illustrate two important points.

1. The strong coupling between plasma creation processes and plasma acceleration processes is a major difficulty of ECRT physics. In contrast, these phenomena are rather decoupled in other thruster technologies such as GIE.

2. Temperature measurement in the coupling structure (if possible, space resolved) would bring out extremely valuable information, in particular about the nozzle thermodynamics.

CORREYERO (2019) [65] estimated experimentally a polytropic index for the magnetic nozzle electron plasma of the Cannat and Vialis prototypes. The method was a comparison of $T_e(z)$ and $n_e(z)$ measurements, for $z \in [7cm; 25cm]$ the origin being at the "thruster exit". They found a constant polytropic index over the measurement interval for the Vialis prototype and a varying polytropic index for the Cannat prototype. Measured values are around 1,2, in accordance to previous measurements [93], [94], denoting a behavior closer to isothermal ($\gamma_e = 1$) than to isentropic ($\gamma_e = 5/3$). A limitation to this study is that the measured electron temperatures were reportedly to be understood as a total temperature; a refinement of these measurements would need to discriminate between parallel and perpendicular energies.

These experimental results were compared to a model adapted from MARTINEZ-SANCHEZ (2015) [79], which calculates one dimensional steady state transport along z of a maxellian distribution assumed at $z = 0$. (This model is also able to calculate self-consistently a potential drop.) The measured value of the polytropic index is of the same order as the prediction of the model. However the model predicts a dependence on the magnetic field strength that was not observed.

2.3.4 Peculiarities of ECRT testing

2.3.4.1 Established pressure effects

The increase in background pressure was suspected to lower the thruster performance since the 1960s work (mercury was then tried as propellant in order to enable cryogenic pumping [16]). Sercel also identify effects of the background pressure, for example the widening of ion energy distribution function (SERCEL (1993) figure 5.1 [23]). VIALIS (2018) recently studied background pressure effects quantitatively [24]. The decrease of ion energy and the increase of jet divergence with background pressure were measured, as well as the resulting decrease in thrust. Figure 33 reproduces measurements from the literature. Although only three data points are available from Nagatomo, the thruster configuration was different, and the deposited power differs from one point to another, we may speculate that Nagatomo would have measured ion energies similar to Vialis, had he been able to lower the pressure. This substantiates the claim made in the introduction that early researches missed the potential of the technology because of technical reasons.

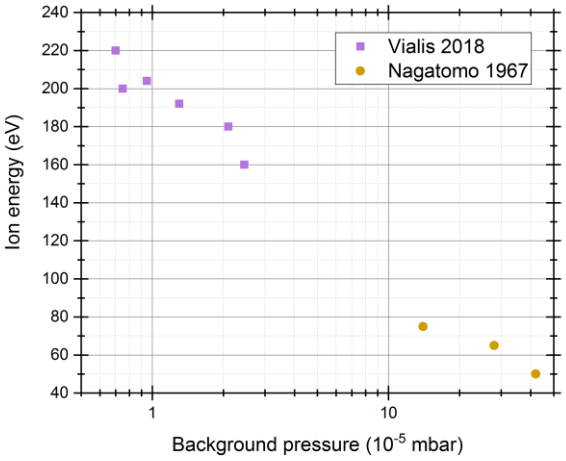

Figure 33. Ion energies measured for coaxial ECRT. For Vialis figure 130 [24] the deposited power is 560 eV per Xenon atom. Pressure is varied with a Xenon leak in the tank, far from the thruster. For Nagatomo [20] the deposited power is 2800, 1100, 700 eV per Argon atom. Pressure varies because the mass flow fed to the thruster varies. The x-axis is in "Nitrogen pressure" (see below).

These results stand in sharp contrast with observations on other thrusters. They likely are a peculiarity associated with the magnetic nozzle. For Hall thrusters for example it seems that no performance variation is observed below 10^{-4} mbar. Above 10^{-4} mbar, performance might on the contrary increase with pressure because of background gas ingestion.

WACHS (2020) [95] furthered these observations using LIF measurement of the ion energy distribution function and proposed and explanation. They observed the formation of a low energy ion population when increasing background pressure. Their analysis, using a discharge model similar to that of LAFLEUR (2014) [32], identifies electron-neutral collisions in the plume as the main mechanism responsible for the pressure effects. Ion neutral charge exchange collisions are ruled out.

2.3.4.2 Speculations on the effect of tank walls

The presence of the tank metallic walls has the effect of short circuiting field lines with one another. This may be seen as a significant perturbation to the nozzle wherein a low conductivity is expected across the field lines. In addition, the walls impose an equipotential grounded surface. Yet, a high conductivity is expected along field lines. Therefore this boundary condition is likely to have an effect on the nozzle dynamics. The value and shape of the plasma potential in space vacuum might be different from that observed in a vacuum tank.

From these considerations stem very practical and open questions for ECRT testing such as: what is the relevant ion velocity? Langmuir probe show a plasma potential over 50 V, on axis 25 cm from the exit plane (figure 34). At this location the potential is getting less and less steep but has not reached an asymptotical value. We may wonder if the potential gradually decreases until 0 V at the wall or if it flattens before undergoing a sharp drop near the wall. In that latter case, what is the potential drop expected in vacuum? It may be the full potential drop down to the walls or the drop from the thruster to the flat region. It seems that Cannat and Vialis ([24], [28]) considered the full ion energy ($E_i = e\phi + \frac{1}{2}Mv_i^2$) as the final kinetic energy and therefore as the relevant energy for thrust estimation.

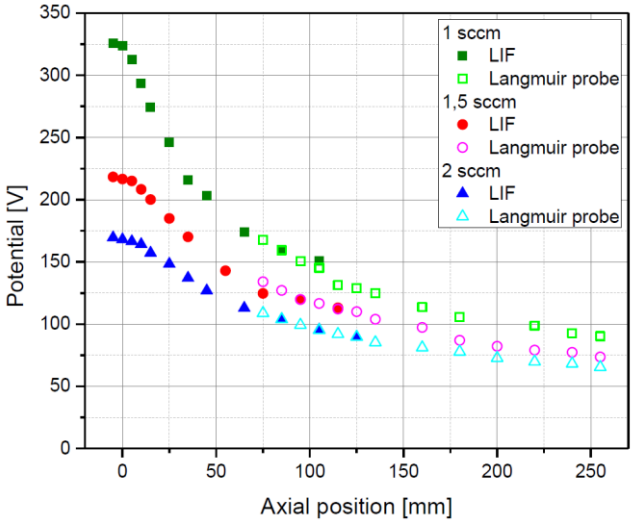

Figure 34. Plasma potential on axis obtained from LIF ion velocity profiles, considering that ions are subjected only to the electrostatic force, $M\partial_t v_i = -e\nabla\phi$. Integration constant is provided by Langmuir probe measurement of the plasma potential. Reproduced from [64].

In the present study, experiments were mainly performed in the B61 facility at ONERA. It is a 4m long and 1m diameter tank with a pumping speed for Xenon around 8000 L/s. The base pressure is around 8.10^{-7} mbar, and working pressure around 9.10^{-6} mbar, for 1 sccm of Xenon fed to the thruster. This facility was described in detail before [24], [28]. The pumping speed V has been frequently verified by reading the "Xenon pressure" P_{Xe} while imposing a certain Xenon leak $\dot{m}$ with a calibrated mass flow meter. The following relation was used.

$$V[L/s] = \frac{\dot{m}[sccm]}{60\ P_{Xe}[mbar]} \qquad (167)$$

The pressure readings are made with a Pfeiffer Penning vacuum gauge which is sensitive to the nature of the gas. Default settings display "Nitrogen pressure" P_{N_2}, which would be the true pressure if nitrogen gas were in the tank. Since the dominating species is Xenon a conversion factor is applied to get the true pressure $P = P_{Xe} = 0{,}4\ P_{N_2}$.

2.3.4.3 Thrust balance measurement

The thrust stand used for this study (figure 35) is one of the outcomes of Vialis's doctoral work [24], [33]. The balance pendulum arm is held into vertical position by a PID controller. The sensor of the PID loop is a capacitive sensor and the actuator is a coil acting on magnets placed on the pendulum arm. Before each test, a calibration procedure determines the relation between the output voltage of the PID and the force exerted on the arm of the balance by calibrated masses. This relation is proportional. For a typical 500 µN thrust measurement the relative uncertainty on the output signal of the balance is estimated to be 4% ([24], figure 93); this uncertainty is mainly systematic for a given thruster configuration.

The ECRT requires a microwave power input. A pair of coaxial-to-waveguide transitions facing each other and separated by a 2 mm gap achieves excellent transmission of the microwave power without any mechanical contact. One is placed on the balance pendulum arm and the other is stationary. Therefore microwave power transmission and free movement of the balance arm are achieved simultaneously.

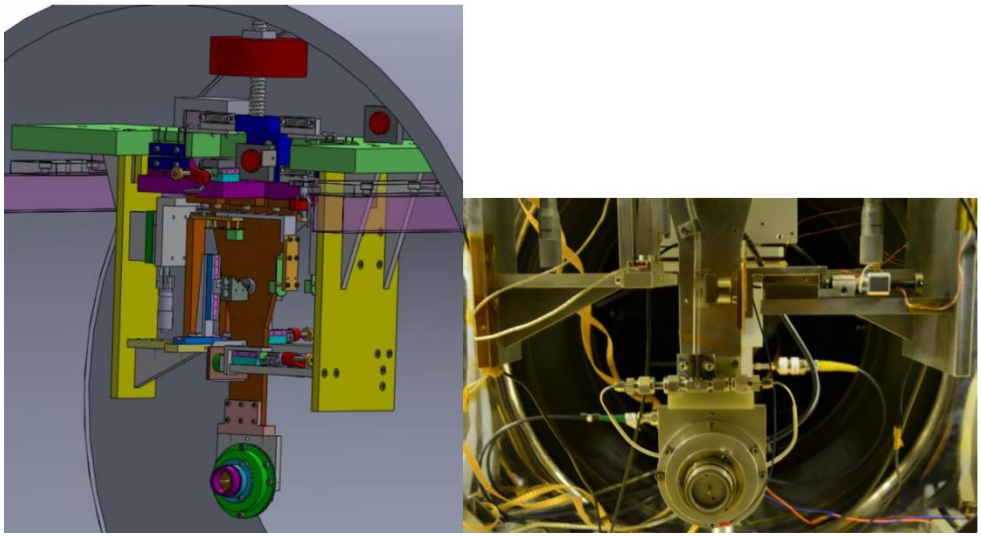

Figure 35. Left: CAD model of the thrust stand in a vacuum tank. Right: photograph in the B61 tank. Reproduced from [24].

2.3.4.4 Ion current and ion energy measurement

Vialis [1] used a gridded Faraday probe that was mounted 26.5 cm from the exit plane of the thruster on a rotating arm (figure 36). Circular rather than linear scan was probably chosen because the ion trajectories can have a significant angle with respect to the thrust axis. The gridded Faraday probe is a simplified retarding potential analyzer consisting of a collector biased at a chosen potential preceded by a grid, usually at a floating potential. This grid is screening the collector voltage to reduce the collected electron current when the collector voltage is swept to highly positive values. This device was used for ion current measurement. The uncertainty on this measurement is believed to be dominated by uncertainty on the grid transparency ([1], table 6).

Ion energy measurement is also possible with the gridded Faraday probe. Since the longitudinal energy distribution of electrons is well separated from that of the ions at most angular locations in the plume, little or no electron current is drawn for bias voltages around the ion most probable energy. Therefore this simple device suffices to provide the ion energy distribution function around the most probable ion energy. It was shown that ion energy does not vary with angle ([1], figure 45).

Figure 36. Measurements with a gridded Faraday probe. Reproduced from [24].

A commercial Hiden mass spectrometer and ion analyzer was also used in this study. It provides a more complete and accurate measurement of the ion energy distribution function on the axis of the thruster as well as a mass spectrum measurement.

A typical ion current density profile for coaxial coupling is shown in figure 37. It is symmetric and strongly dependent on the imposed magnetic field, indicating the critical effect of the magnetic field on

the plasma expanding outside of the material structure of the thruster. In the case of figure 37 it has a half width at half maximum of 17°. The local minimum in the center is interpreted as a decreased plasma flux in the magnetic field tube intercepted by the inner conductor, however smoothed by diffusion across magnetic field lines during expansion in the nozzle.

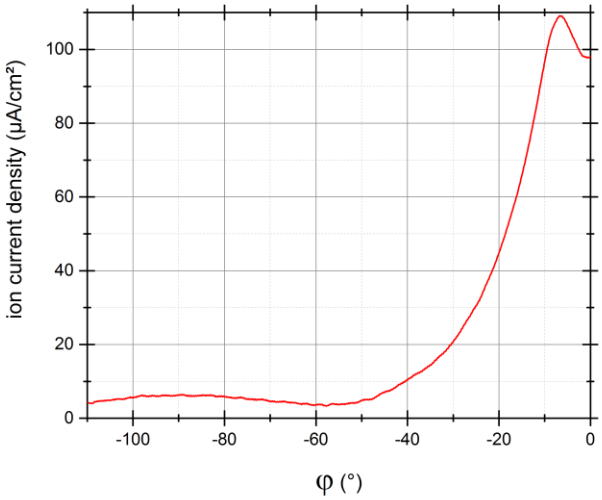

Figure 37. Typical ion current density. φ is defined in figure 36.

2.3.4.5 Estimation of thrust from electrostatic probe measurement

Cannat and Vialis used the following expressions to estimate the total ion current J_{tot} and thrust T from the angular ion current distribution $J(\varphi)$ and from the mean ion velocity v

$$J_{tot} = \pi D^2 \int J(\varphi)|\sin(\varphi)|d\varphi \quad \textbf{(168)}$$

$$T = \pi D^2 \frac{M}{e} \int v\, J(\varphi)\, |\sin(\varphi)| \cos(\varphi)\, d\varphi \quad \textbf{(169)}$$

where M is the ion mass, e is the elementary charge, D is the distance between the probe and the center of rotation of the arm that is moving the probe, φ is the angle of rotation of the probe (figure 36). They performed integration in φ over $[-90°; +90°]$. Vialis reports thrust values in agreement with thrust balance measurement ([1], figure 97) for a few data points. However, as we shall see in section 4.1.1 we found that this integration consistently overestimates thrust with respect to what is measured by the thrust balance and requires a number of strong and unstated assumptions.

2.3.4.6 Repeatability issues

Repeatability issues in recent ECRT development studies are acknowledged ([1], section V - 2.4). Repeatability issues mean that measurements have a significant unexplained dispersion. Vialis distinguished the notion of repeatability from set-up to set-up (that we shall term reproducibility), from the notion of repeatability from run to run (that we shall term repeatability). He showed that the "reproducibility dispersion" is in general dominated by the "repeatability dispersion". The latter is attributed to the following unmonitored effects: temperature variations (affecting thermionic emission and magnetization), background pressure, change in surface condition of the coupling structure in contact with the plasma, unwanted microwave discharges, and random error from the mass flow or

microwave measurement. The dispersion is of the same order than the variations we wish to measure in this study. We shall address this major hurdle to further development in the next chapter.

3. Control of the thruster set-point

Outline of the approach. The goal of this chapter is to accurately control the thruster set-point (i.e. deposited microwave power and neutral gas flow). In a first section we focus on the deposited microwave power, which is not only difficult to measure but also affected by unwanted and often undetected disturbances. In a second section, we identify the possibility of gas leaks and gas discharges occurring before the thruster chamber.

Main results. Gas discharges in connectors of the microwave line are identified as the main cause of random errors on the deposited power and a custom microwave line and thruster connection are designed to eliminate them. On the measurement side, directivity errors of power couplers are identified as a source of significant systematic error on the deposited power. A set-up is proposed to mitigate this error and error bars are calculated as a function of reflected power fraction. Concerning neutral gas injection, changes in thruster design ensure gas tightness and isolate the gas line from the microwave field up to the injection in the thruster chamber.

Content

Definitions. We define the thruster set-point as the deposited microwave power and input neutral gas flow. As in the norm ISO5725 we define accuracy as the combination of precision and trueness (figure 38). A default in trueness implies a difference between the true value and the average over a sufficiently large set of measurements. It originates in systematic errors. In contrast, a default in precision implies dispersion of the measurements and originates in random errors. We shall also distinguish the notion of repeatability from set-up to set-up that we shall term reproducibility, and the notion of repeatability from run to run that we shall simply term repeatability.

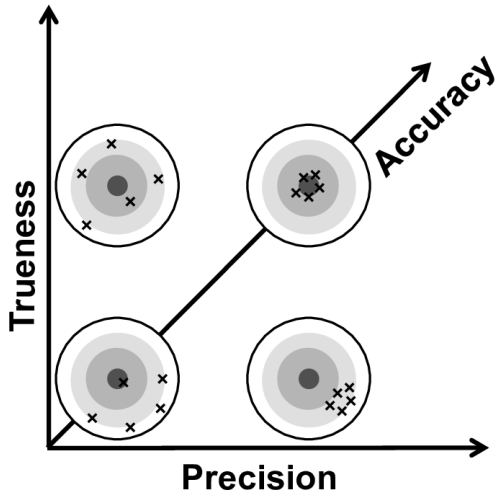

Figure 38. Accuracy, precision and trueness.

3.1 Motivation

Accurate measurement of the microwave power deposited in the thruster is a critical for efficiency estimates. Yet it is a challenging issue at the typical power level used in the experiment. Although accurate microwave measurement devices are available at low power, the measurement of powers of a few tens of watts to a few hundreds of watts is impaired by the strong non-ideality of microwave components in this range of power. In the studies from the 1960's and 1990's no reliable microwave measurement was performed: Crimi [17] is critical about the microwave components used in his experiments, in particular the polarizer, and Sercel [23] acknowledges that the microwave diagnostics were not adequate to measure the thruster coupling (ratio of power deposited in the plasma to incident power at the thruster). Later studies [24], [28] measured the deposited power more accurately using a well-described setup but overlooked the strong non-ideality of bidirectional couplers.

A strong dispersion of measurement was previously reported ([24], section V – 2.4) and extensively observed at the beginning of our study. In figure 39, up to 30% discrepancy is observed for a given power value, hence a 50% discrepancy in total efficiency. The observed dispersion is much larger than the estimated error bars. In addition, such dispersion precludes comparison between the two configurations whereas they might exhibit different behaviors if more precise data were available, thus making the assessment of thruster design evolution nearly impossible.

Preliminary experiments gave reasons to believe that this dispersion may originate not only from the thruster itself, but also from the setup around the thruster. Unwanted discharges occurring in microwave connectors in the vacuum part of the circuit were suspected. Besides, the observation of charred injection lines just upstream the thruster suggested that Xenon discharges were occurring, wasting both power and gas before they reached the thruster chamber.

The motivation for this chapter is to rule out the possibility of random and systematic errors on the thruster set-point in order to later carry out an unperturbed study of the thruster itself. We will identify and mitigate errors that preclude from accurate control of the thruster set-point (that is: microwave power input and neutral gas input).

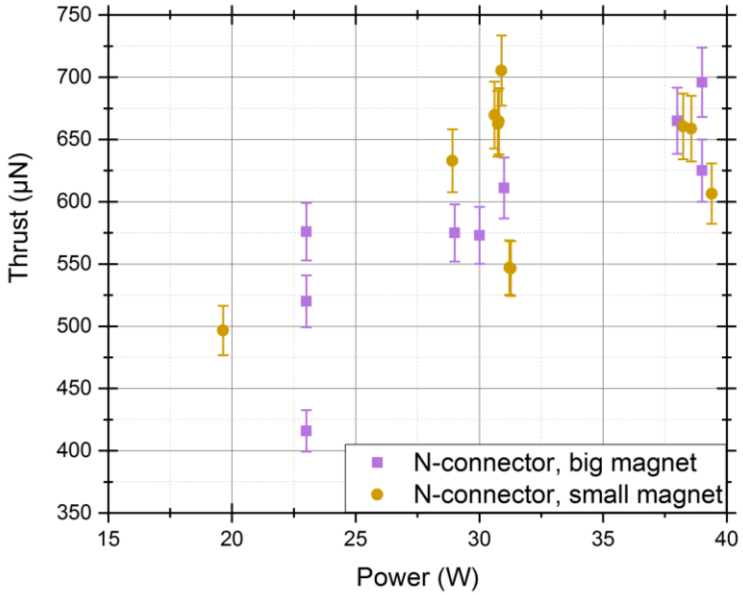

Figure 39. Typical thrust balance measurements at the beginning of the study for 1 sccm Xenon feed. "N-connector" refers to the ECRT configuration presented in [24]. Error bars from ([24], figure 93).

3.2 Control of microwave power

3.2.1 Errors due to the set-up

3.2.1.1 Generator spectrum

The spectrum of the signal generator used in this study has a -12 dB an harmonics which was demonstrated to carry a significant fraction of the power (figure 40). Additional peaks are present at lower frequency. For simplicity of power measurement and interpretation of results it was preferred to have power at 2,45 GHz only. A custom made filter was implemented to obtain a clean spectrum with one frequency only.

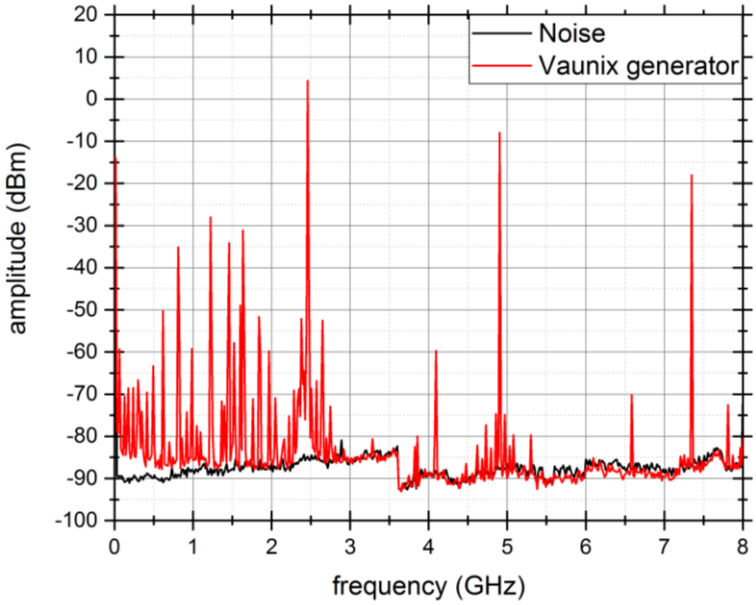

Figure 40. Unfiltered Vaunix generator spectrum set at 2.45 GHz. It includes a -12 dB first harmonics and a set of low frequency peaks.

3.2.1.2 Unwanted plasma discharges in connectors

The implementation of the in-vacuum transmission line available at the beginning of the study featured a number of microwave N or SMA connectors (figure 41). They all house an air volume at an unknown pressure when the tank is pumped down, since connectors are neither airtight nor open. Simple measurements of the temperature of the connectors on the microwave line have shown significant occasional increases interpreted as plasma discharges randomly going off inside. Besides, the connector that is screwed to the thruster is systematically blackened after operation, which is interpreted again as a plasma discharge (figure 42). In addition to this problem, connectors are known to produce a small but significant reflection (see section 2.1.5.1).

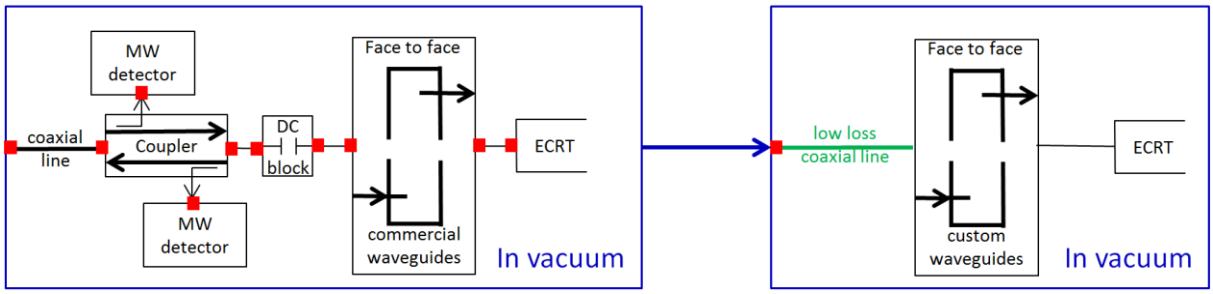

Figure 41. Changes of the in-vacuum microwave transmission line. Red dots are connectors.

Figure 42. N-connector that is screwed to the thruster, after operation.

This is the motivation for the implementation of a completely custom and connectorless microwave line, from the feedthrough to the thruster. Microwave power measurement inside the vacuum tank was considered to have more drawbacks than advantages and eliminated: measurements can be made from the outside, provided that the microwave line is sound and as simple as possible. The DC-block was eliminated because it was considered redundant with regards to the face-to-face waveguides. Their primary role is to mechanically decouple the balance pendulum arm from the microwave line while achieving low loss microwave power transmission ([24], section V – 1.3), but they also do achieve an DC electrical isolation. It was moreover verified that the resulting potential difference between the waveguides (up to 300V, since the thruster and its waveguide are floating electrically) does not create a force on the balance arm. Both electrostatic simulation and experiments where the thruster (not firing) is biased at 300V were used to check this point.

Commercial coaxial-to-waveguide transitions were previously used to transmit the power through waveguides in the particular segment of the line where mechanical decoupling is required, but they were heavy and connectorized. In order eliminate the connectors present on these components custom coaxial-to-waveguide transition were designed, manufactured and implemented. Circular waveguides were chosen to facilitate machining and avoid welding. They excite the TE11 mode of the circular waveguide and were calculated using COMSOL (figure 43). The microwave engineering concepts required for this design are presented in section 0.

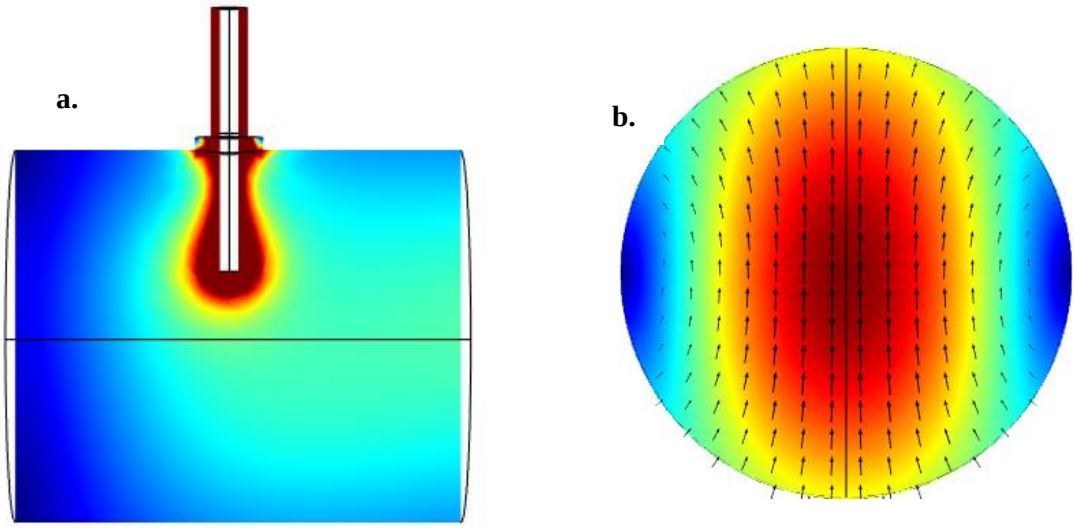

Figure 43. Simulation of the electric field norm (color map) and direction (arrows) inside the custom circular coaxial-to-waveguide transition,

a. sectional view with coaxial input on the top and waveguide open-end on the right,
b. sectional view in the waveguide open-end plane.

Another issue was then addressed. When inspected after the thruster operation, the inside metallic surface of the N-connector at the back of the thruster was systematically blackened. The inside volume of this connector communicated with the plasma chamber through an interstice, thus making it particularly prone to discharges [24]. A custom coaxial microwave line filled with dielectric material was implemented in place of the N-connector to eliminate this discharge volume. It was simulated using COMSOL with the proper dielectric permittivities of the different dielectric materials. The shapes and thicknesses of the different dielectric parts were designed in order to have a $50\,\Omega$ characteristic impedance. However, it appeared that the initial system with N-connector (which was not $50\,\Omega$) was playing an impedance matching role since the reflected power with thruster in operation increased from less than 5% to more than 25% when the first version of the new system was used. Since the microwave

behavior of the plasma is unknown (through an equivalent impedance for example), it was impossible to make the new system achieve impedance matching by design. Several configurations were tested before one was found to achieve less than 10% reflection coefficient. A picture of the in-vacuum microwave line is in figure 44 and a sectional view of the initial and final thruster microwave connection is shown in figure 51.

Figure 44. Thruster connected to custom in-vacuum microwave transmission line used in this study. A corresponding schematic view is in figure 41, right.

The efforts described in this section allowed eliminating all connectors except at the feedthrough. It was found that if an adequate small hole was drilled in the inside connector of the feedthrough, it would allow the escape of the gas from the connector cavity during pump down and therefore would prevent an electric discharge, without perturbing the microwave properties of the connector. Subsequently, temperature measurement of the feedthrough was routinely used to check the absence of discharge. This new in-vacuum microwave setup enabled repeatable microwave measurement. It was also in the perspective of future high power tests of ECRT.

3.2.2 Systematic error due to instruments: directivity error

This section draws on notions of experimental microwave measurement presented in section 2.1.5.2. In particular, we introduced the directivity error which is induced by an unwanted non-zero term in the S-matrix of the coupler. A bidirectional coupler diverts a small known fraction (typically -30 dB) of the incident and reflected power from the main line to the respective coupled ports [38] (in figure 19, 3 is coupled to 1 for the incident power and 4 is coupled to 2 for the reflected power). However, a crosstalk also exists: a fraction of the incident power (typically -50 dB) is coupled to the sampling port for the reflected power and vice versa. Directivity D was defined in section 2.1.5.2 as the ratio between this wanted and unwanted coupling. If the ports are numbered as in figure 19, directivity in dB is defined as $D_I = 20\log|S13/S14|$ for the measurement a wave propagating to the right (incident) and $D_R = 20\log|S24/S23|$ for the measurement a wave propagating to the left (reflected).

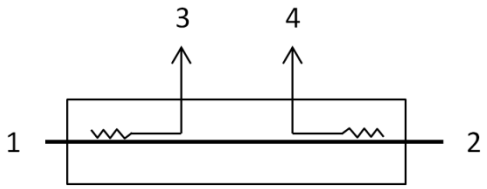

Figure 45. Schematic view of a dual directional coupler. A known fraction (typically -30 dB) of the wave propagating from to the right (resp. left) is measurable at port 3 (resp. 4). Ideally, port 3 (resp. 4) is strictly isolated from the wave propagating from to the left (resp. right). In reality a typical isolation is -50 dB.

The interaction of signals in the coupled lines (due to the directivity defect), results in a perturbed reflected power measurement. The complex amplitudes add, hence

$$P_R^{measured} = P_R^{true} + DP_I^{true} + 2\sqrt{P_R^{true}}\sqrt{DP_I^{true}}\cos(\phi) \quad \textbf{(170)}$$

with $P_R^{measured}$ the measured reflected power, P_R^{true} and P_I^{true} the true reflected and incident powers, D the directivity and ϕ the phase shift between the coupled incident and reflected wave which depends on the location of the reflection on the microwave line and phase difference introduced by the reflection. Here we assumed the different signals are coherent and thus result in constructive or destructive interferences.

It is verified for microwave generators; experimental verification was performed by observing the effect of a changing phase shift ϕ. Phase shift is varied by varying the length of the coaxial cable. Note that when the cable length varies, absorption in the cable also varies, but this is compensated for in the calculations. The reflected power fraction generated by an open coaxial cable is presented in figure 46. This measurement is a means to estimate the directivity because the amplitude of the oscillations is proportional to $\sqrt{D}$ (relation 170). For the example presented, we have $D = 26$ dB.

Note that direct measurement of directivity is not possible. By direct measurement we mean to measure $S14$ with a VNA (Vector Netrwork Analyzer) while having a matched load connected at port 2. The connection of that load would imply a return loss of at least -20 dB at port 2 (1% reflected power), generating an unwanted coupled signal at port 4 commensurate to that we wish to measure.

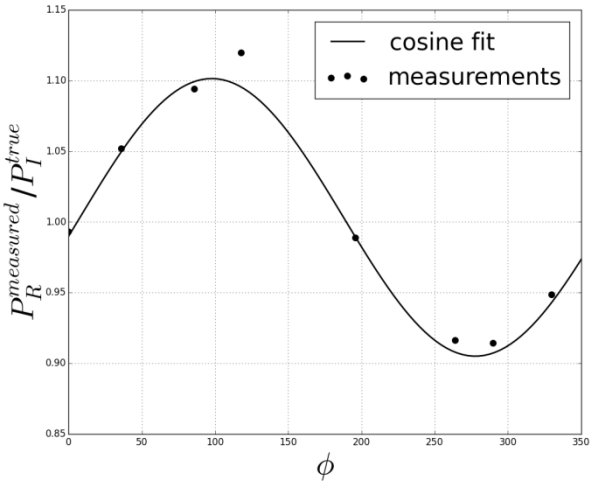

Figure 46. Measurements of interferences on coupler measurement, fitted with relation 170. In this example a directivity.

Let's quantify the error induced by directivity. The absolute error on the reflected power is $P_R^{measured} - P_R^{true}$. Let's define ΔP_R as this difference in the worst cases. By worst cases we mean when the two interfering coupled waves have a phase shift ϕ of 0° or 180°. Then, from relation 170

$$\Delta P_R = \left(P_R^{true} + DP_I^{true} \pm 2\sqrt{P_R^{true}}\sqrt{DP_I^{true}} \right) - P_R^{true} \quad \textbf{(171)}$$

hence

$$\frac{\Delta P_R}{P_R^{true}} = \left(D\frac{P_I^{true}}{P_R^{true}} \pm 2\sqrt{D\frac{P_I^{true}}{P_R^{true}}} \right). \quad \textbf{(172)}$$

Figure 47 is a plot of $\Delta P_R / P_R^{true}$ as a function of P_R^{true}/P_I^{true}. For a given true fraction of reflected power, it represents the interval (relative to P_R^{true}) in which measurements can be found. For example, for a true reflected fraction of 10% (at the measurement device) and directivity of 23 dB, the measured reflected power can be anywhere between -40% and +50% of the actual reflected power, which gives between 6% and 15% of reflected fraction, depending on the phase shift. Such a large effect is counterintuitive, as it seem to stand in stark contrast with the 23 dB (0,5%) directivity defect that it originates from.

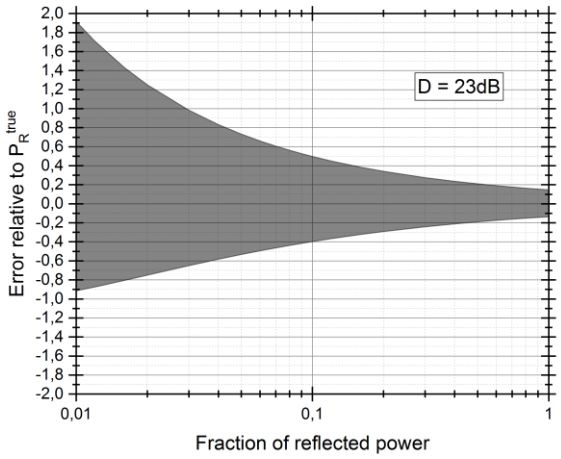

Figure 47. Interval (relative to P_R^{true}) in which P_R measurements with a 23dB directivity bidirectional coupler can be found. The true value of the fraction of reflected power is represented on the horizontal axis

As we will see in details in the next section, such uncertainty largely contributes to uncertainty on the thruster efficiency. In order to decrease these uncertainties, several solutions were considered to increase the directivity. At the power level of interest (≈ 100 W) high directivity (30 to 40 dB) is available on the market only for waveguide couplers. However, they are costly, cumbersome (≈ 1 m in length), and restricted in frequency range. In addition, since the rest of the circuit is made of coaxial line and components, they would require coaxial-to-waveguide transitions that would generate small reflections. Waveguide couplers were therefore deemed a good future option if the microwave circuit were entirely converted into waveguides. This may be required to scale-up the thruster at high power.

For the work described here, we opted for a compromise solution that allowed staying with coaxial components. The directivity on incident power measurement was increased to a level such that incident directivity error is negligible, resulting in a decrease of the uncertainty on the deposited power. This solution is shown on figure 48. It features a pair of couplers and a circulator instead of a single dual

directional coupler as in previous studies [1]. The circulator provides additional isolation of 23dB of the sampled incident power from erroneously coupled reflected power, effectively increasing the directivity to 46 dB. However, no improvement is expected from this setup for reflected power measurement.

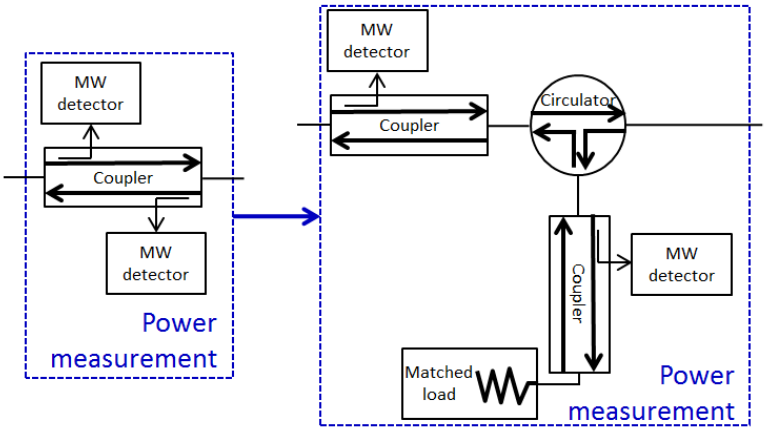

Figure 48. Changes of the power measurement system increasing the trueness of incident power measurement.

3.2.3 Total error on the deposited microwave power

A relative uncertainty on the deposited power induces an equal relative uncertainty on the thruster efficiency, hence the necessity to assess this uncertainty on the deposited power. The power deposited in the thruster is defined as:

$$P_D = \gamma P_I - \frac{P_R}{\gamma} \quad (173)$$

with γ the transmission coefficient of the microwave line (in power) from the output of the measurement system to the thruster, P_I and P_R the incident and reflected power measured at the measurement system. Error on P_D can stem from the three variables of the expression. Let's estimate $\Delta\gamma$, ΔP_I , and ΔP_R the positive worst case absolute error on γ, P_I , and P_R.

The transmission coefficient γ can be subject to random fluctuations due to unwanted discharges appearing in the vacuum part, in particular in N-connectors. We presented in section 3.2.1.2 how this uncertainty was eliminated. Therefore this phenomenon no longer contributes to $\Delta\gamma$. However, the measurement of γ is subject to uncertainties. First, the movement of microwave cables and components occurring between the measurement of γ and the operation of the thruster may induce variations on γ. Second, the VNA used to make measurement has at least a 0,1 dB error bar. Overall the relative uncertainty on γ is estimated to be $\Delta\gamma/\gamma = 5\ \%$.

The dominant source of error on P_R is the directivity error, introducing a possibly large uncertainty, depending on the fraction of reflected power, as exposed in section 3.2.2.

$$\Delta P_R = \left(D P_I^{true} \pm 2\sqrt{D P_I^{true} P_R^{true}} \right) \quad (174)$$

On the contrary, with the use of a circulator, the directivity error on P_I is dominated by uncertainty on the measurement of the coupling of the coupler estimated to be 2.3%, and the uncertainty of the microwave detector given to be 1.95% in the range of power of interest. Thus $\Delta P_I/P_I = 4.25\%$.

Since the errors remaining on γ, P_I, P_R are systematic error (i.e. if the measurement is repeated, the same result is obtained), error on P_D should be written with the following pessimistic form[4]

$$\Delta P_D = \left|\frac{\partial P_D}{\partial \gamma}\right| \Delta\gamma + \left|\frac{\partial P_D}{\partial P_I}\right| \Delta P_I + \left|\frac{\partial P_D}{\partial P_R}\right| \Delta P_R \quad (175)$$

hence

$$\Delta P_D = P_I \left(1 + \frac{1}{\gamma^2}\frac{P_R}{P_I}\right) \Delta\gamma + \gamma\, \Delta P_I + \frac{1}{\gamma}\Delta P_R. \quad (176)$$

Figure 49 is a plot of $\Delta P_D / P_D^{true}$ and of the contributions to $\Delta P_D / P_D^{true}$ from errors on γ, P_I, and P_R. Asymptotic behavior is observed simply because $\lim_{P_R^{true}/P_I^{true} \to \gamma^2} P_D^{true} = 0$. It is apparent that a small fraction of reflected power is preferable to make true measurement of the power deposited in the plasma. The relative error on the deposited power increases as the true reflected power fraction increases, and is about 100% for 50% reflected power in this case. This will be an issue for the waveguide-coupled thruster, which exhibits large reflection factors. It will be addressed in section 6.2.3. Note that for a given microwave line and a given measurement of γ, the total error on the deposited power is a systematic error.

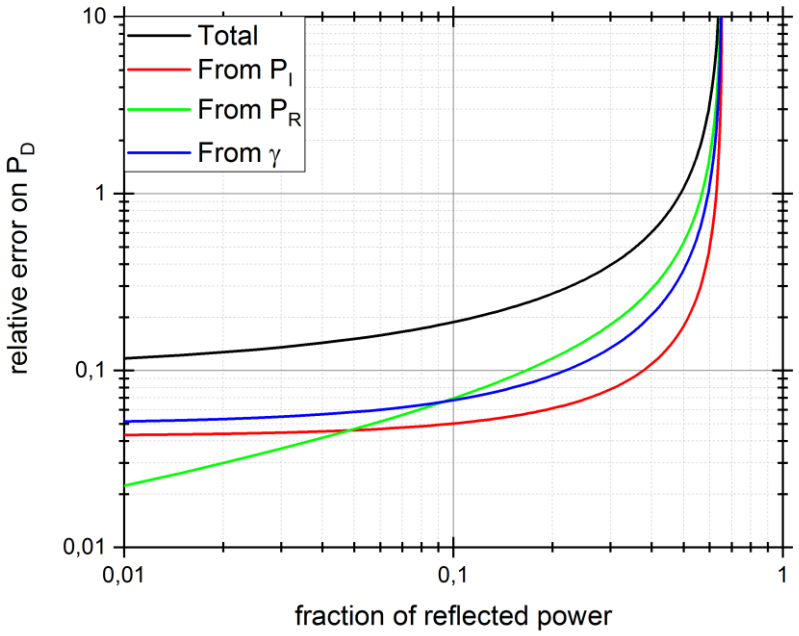

Figure 49. Contributions and total error on P_D for $\gamma = 0.81$ and $D = 25dB$

3.3 Control of neutral gas flow

3.3.1 Errors due to instruments

Most of the times, Xenon flow was measured with a Bronkhorst F-200CV (with 4 sccm full scale), bought for the study. The uncertainty estimated by the manufacturer for 1 sccm is ± 1.6% (0,8% of

[4] By pessimistic we mean that we consider the unlikely worst case scenario where all error terms are maximum in absolute value and have sign such that they add up. An alternative statistical treatment cannot be justified with only three terms [96].

reading plus 0.2% of full scale). Because of circumstantial reasons, two other flow meters were used occasionally: Bronkhorst F-201CV (10 sccm full scale), Brooks 5850E (4 sccm full scale). They were both recalibrated by the manufacturer at the beginning of the study and uncertainties are similar. For each device, the pressure induced by a 1 sccm Xenon flow was measured in the B61 vacuum tank with steady state pumping. This measurement proved that the flow meters were consistent with one another.

3.3.2 Error due to the set-up

In the ECRT prototype available at the beginning of the study, neutral gas was injected through two holes (figure 51a). A pair of gas feed tubes with external diameters (1.7 mm) smaller than those holes (2 mm) were adjusted inside with Teflon tape. This design, although certainly suitable for a preliminary characterization was deemed inadequate for accurate performance measurement, not only because the tightness is questionable but also because discharges were observed in the gas feed lines. They were systematic at start-up and occasional during operation. An example is shown in figure 50 on a thruster configuration where the gas lines are more apparent than they are in the nominal configuration of figure 51a.

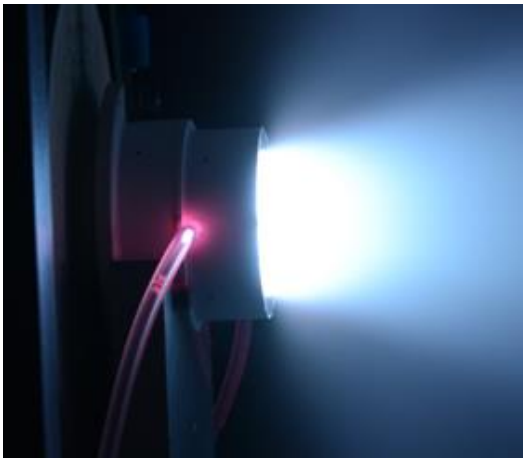

Figure 50. Discharge in the gas feed line of a previous ECRT configuration.

It was supposed that exposition to the microwave field before reaching the coaxial chamber of the thruster was favoring such discharges. Therefore a new gas injection system was designed with the intention to improve gas tightness and to preclude exposition of the neutral gas line to the microwave field. These conditions are conveniently met with the "radial injection" visible in figure 51b. The gas is injected through 6 azimuthally-distributed 0,5 mm square-ducts, going from an annular plenum to the thrust chamber. An o-ring ensures gas tightness (only the groove is represented in the figure). Only slight change in performance was noticed when going from one injection to the other (see section 5.2.1).

3.4 Summary of the results

In this chapter we have implemented a number of improvements on the experimental set-up that aim at accurate control of the thruster set-point (i.e. the deposited microwave power and input neutral gas flow). They are summarized in figure 51 and figure 52. The available experimental set-up was modified to eliminate unwanted discharges that create systematic and random errors on the thruster set-point. Finite directivity of couplers was identified as the source of strong systematic error and reduced by the use of a particular microwave measurement setup.

With the microwave line unperturbed by unwanted discharges and the tight gas line, the uncertainty on the set-point is now determined by instrument uncertainties. Uncertainty on deposited microwave power is estimated to be 20% for 10% of reflected power (which is typical). Since it originates in a systematic error (for a given microwave line and a given measurement of the transmission coefficient), this large uncertainty does not preclude fine comparison between different thruster configurations. Uncertainty on the neutral gas flow as estimated by the flow meter manufacturer is typically $\pm$ 1.6% at 1 sccm.

A schematic view of the improved microwave circuit used in this study can be found in figure 52. It can be broken down into three subsystems: power generation, power measurement, and in-vacuum transmission. It is mainly composed of coaxial components with N connectors.

Equipped with the capacity to control the thruster set-point accurately, we are now able to address plasma measurements. This is the object of the next chapter.

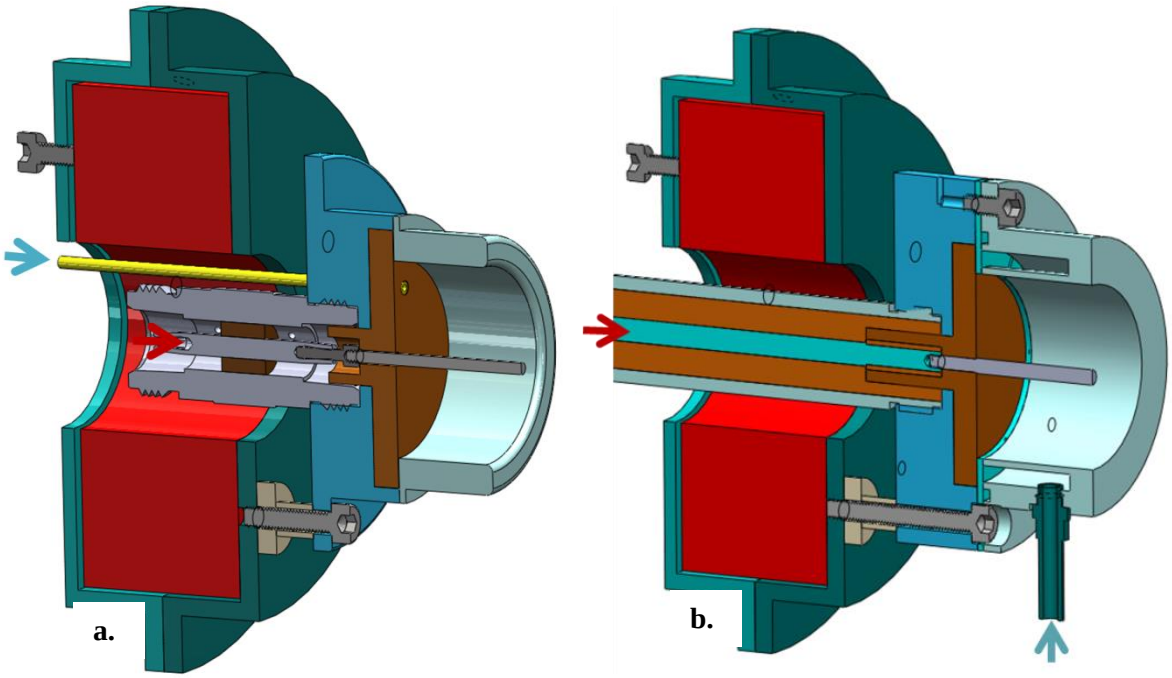

Figure 51. Thruster Solidworks models. Red arrows indicate microwave input. Blue arrows indicate neutral gas input. Blue, green, and gray parts are metallic. The magnet is red. Brown and yellow parts are dielectric.

a. initial design from Vialis available at the beginning of the study [24],

b. improved design developed in this chapter.

3.4 - Summary of the results

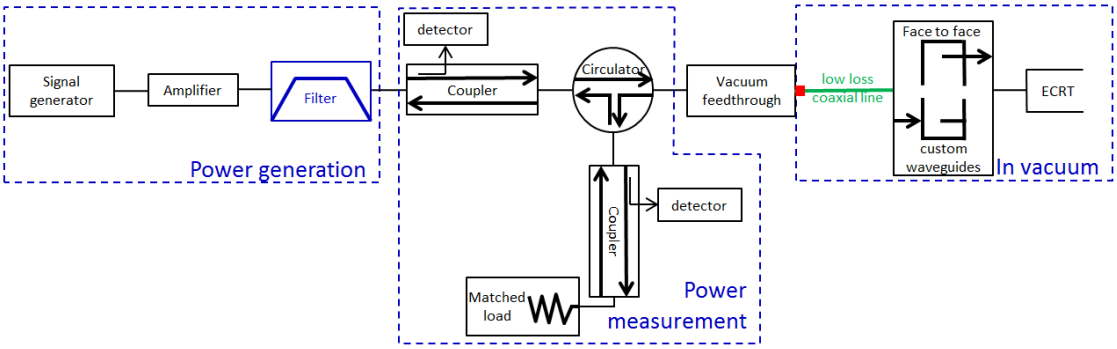

Figure 52. Schematic view of the microwave circuit. From left to right: a Vaunix Labrick LMS402-D signal generator, a Microwave Amps AM3-1-4-50-50R amplifier, a custom-made filter, a pair of ATM CHP274-30F-30R dual directional couplers mounted with Ladybug LB478A Power sensors, an Inmet TN020F-100W 50 ohm load, a RFCR6801 circulator, a Vacom N to N feedthrough, a low loss coaxial line made with a Cable&Connectiques CFP15 cable, and a pair of custom-made waveguides, one of them connected to the thruster by a rigid custom-made coaxial line.

4. Accuracy of the plasma measurements

Outline of the approach. Based on the experimental setup and protocol described in the previous chapter, we are able to operate the thruster in a more repeatable and controlled manner. In this chapter, we assess the trueness and precision of the plasma measurements, in particular the ion current measurement and the thrust balance measurement. The trueness being impossible to establish absolutely, an emphasis is placed on checking the coherence between measurements: first, between diagnostics available at ONERA; second, between measurements made with a slightly different setup in two different vacuum tanks: the B61 facility at ONERA and the Jumbo facility at Justus Liebig University (JLU), Giessen.

We would like to acknowledge the team *Atom, Plasma und Raumfahrtphysik* from JLU for welcoming our experiments in their laboratory.

Main results. Estimates of thrust from the electrostatic probe measurements is often found to disagree with thrust balance measurements. The assumptions underlying this estimate are carefully considered and tests are performed to rule out a number of error causes, whether instrumental or from misinterpretation of the data. In particular, a guard ring Faraday probe is designed to compare with the existing current probe at ONERA. The disagreement in thrust seems to originate from a peculiarity of the ECRT rather than from instrumental error.

The ECRT is also tested at background Xenon pressures as low as 10^{-7} mbar, which is a decade below all previous existing measurements: the results confirm the trend of increased performance when background Xenon pressure is decreased. The thruster potential, which is a sensitive and important parameter is unaffected by the test facility (B61 at ONERA or Jumbo at JLU), validating our ability to control the thruster in a different test environment. With the JLU thrust balance, in the JLU vacuum tank, 825 µN of thrust was measured for 1 sccm Xenon and 24 W of deposited power. The consistency between JLU diagnostics and ONERA diagnostics is examined.

Content

4.1 Consistency between diagnostics

4.1.1 Statement of the problem

As mentioned in section 2.3.4.5, Cannat [28] and Vialis [24] used the following usual expressions to estimate the total ion current J_{tot} and thrust T from the angular ion current distribution $J(\varphi)$ and from the mean ion velocity v (constant with angle)

$$J_{tot} = \pi\, D^2 \int_{-\alpha}^{\alpha} J(\varphi)|\sin(\varphi)|d\varphi \qquad \textbf{(177)}$$

$$T = \pi\, D^2 \frac{M}{e}\, v \int_{-\alpha}^{\alpha} J(\varphi)\, |\sin(\varphi)|\cos(\varphi)\, d\varphi \qquad \textbf{(178)}$$

where M is the ion mass, e is the elementary charge, D is the distance between the probe and the center of rotation of the arm rotating the probe, φ is the angle of rotation of the probe (figure 53). The integrand from expression 178 is plotted in figure 54 for reference, for a current distribution typical of the small magnet thruster. The projection of the ion momentum on the thrust axis brings in a $\cos(\varphi)$ factor and the ring area on the sphere between φ and $\varphi + d\varphi$ brings in a $|\sin(\varphi)|$ factor. Therefore, for the current density, the maximum "weight" toward the thrust, occurs at $\varphi = \pm 45$ ° (maxima of $\varphi \mapsto |\sin(\varphi)|\cos(\varphi)$), and the weight tends to zero when φ approaches ± 90 ° or 0 °.

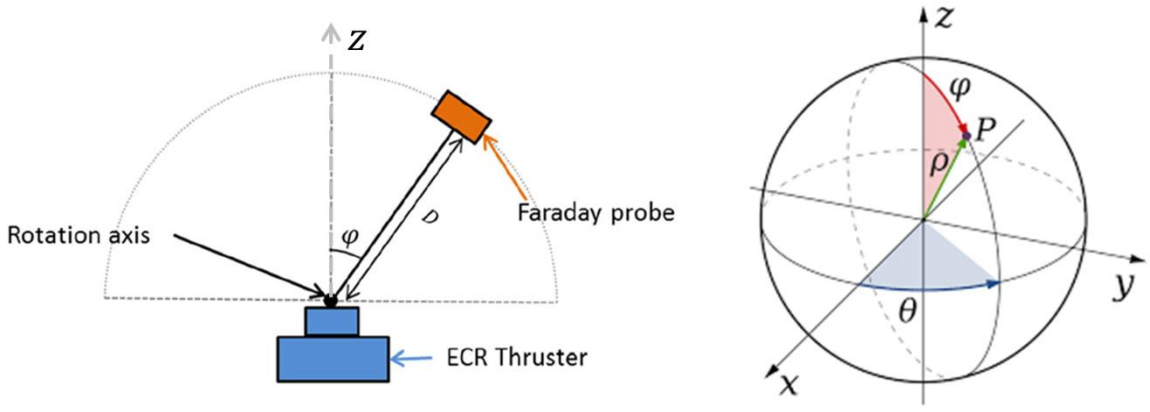

Figure 53. Circular ion current distribution measurement [24].

Cannat and Vialis performed integration in φ over $[-90°; +90°]$. We found that this integration consistently overestimates thrust with respect to what is measured by the thrust balance by a 20% to 80% factor, depending on the thruster configuration. For example, for the profile in figure 37, the estimation yields 820 µN whereas 460 µN is measured with the thrust balance. Such a discrepancy is beyond the customary 10 to 20 % error observed on other type of thrusters between direct thrust measurement and estimation with electrostatic probes [97]. This behavior was verified over the years, by different experimentalists and on different ECRT designs, but was initially attributed to instrumental errors, or was hidden by lack of thruster performance repeatability due to poor set-point control. The later point became moot after the efforts described in the previous chapter.

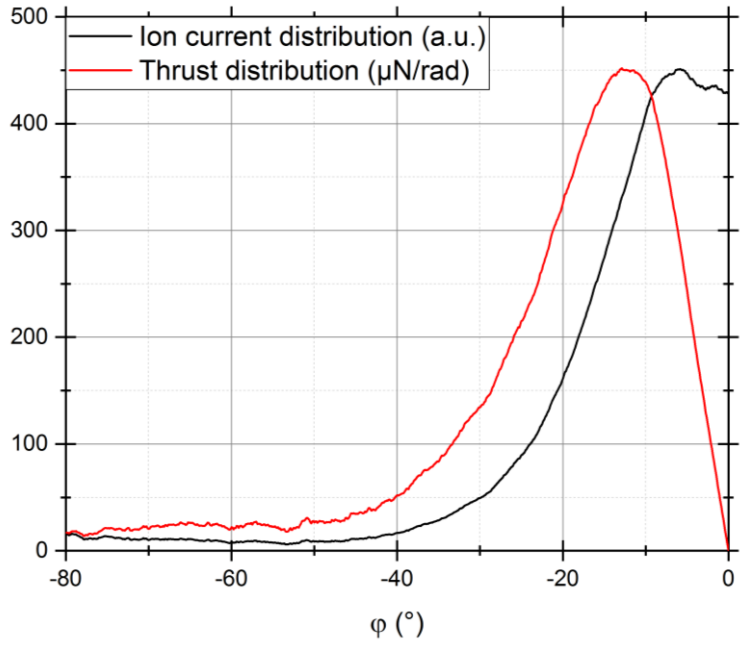

Figure 54. A typical ion current distribution, and thrust distribution according to expression 178.

The former point is ruled out by a number of measurements performed with the same diagnostics in the framework of contractual activities between ONERA and different thruster manufacturers of miniature GIE or HET. For example, the discrepancy does not exceed 5 % for the miniature HET from Exotrail (figure 55), using the same probes, balance and vacuum tank as for ECRT measurements. Such results build confidence in the diagnostics and indicate that the discrepancy does not likely come from

instrumental error but rather comes from a peculiarity of the ECRT, probably linked with the presence of the magnetic nozzle.

The discrepancy can originate in one or both thrust measurement methods (balance or probes). The thrust balance measurement is deemed more robust to the peculiarities of the ECRT and its set-up than the electrostatic probe thrust measurement; however, several simple tests were performed. For example, it was established that the electrostatic force between face to face coaxial-to-waveguide transitions (one at thruster potential and one grounded) does not perturb the measurement. This was done by applying a DC potential on the thruster with the plasma off as well as with electrostatic simulations. Therefore, in the rest of section 4.1, *we are working under the hypothesis that the thrust balance measurement is correct and we are looking for the origin of the error in the determination of thrust from electrostatic probe measurement.*

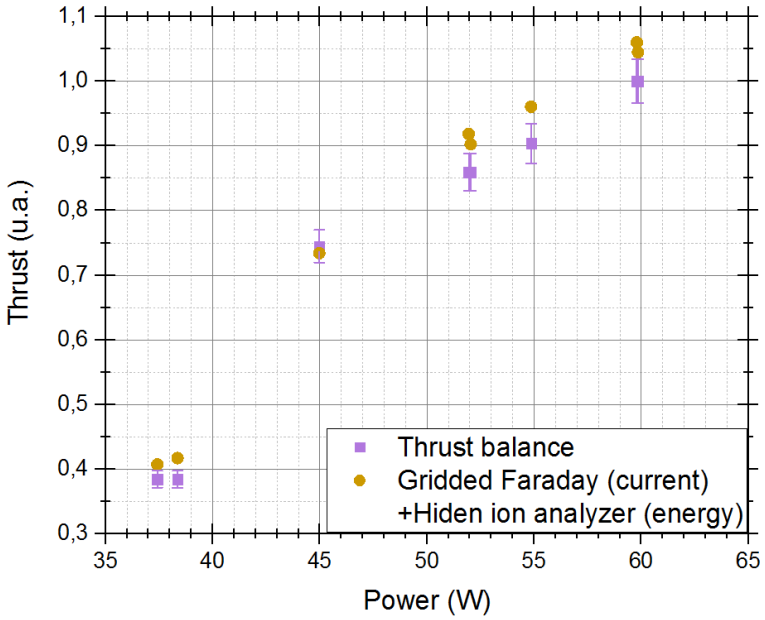

Figure 55. Compared thrust measurement methods at ONERA for the ExoMG™–*nano* thruster (HET) from Exotrail.

4.1.2 Assumptions for thrust estimate from electrostatic measurements

In order to explain the discrepancy between the thrust measured from the balance and that measured from electrostatic measurements, let us examine the assumptions underlying expression 178. In our current understanding of the thruster, the assumptions are as below, presented in increasing order of "validation difficulty".

1. The ion velocity is true and independent of φ.
2. The jet is axis-symmetric.
3. The ion momentum that flows through the dashed horizontal segment in figure 53 is negligible. Integration should be done a priori on any closed surface containing the thruster, so the integration over $\varphi \in [-90^\circ ; +90^\circ]$ in expression 178 supposes that all the ion momentum flows through the front-half sphere only.

4. The probe provides *the true ion current density of the plasma it faces*.
5. This plasma faced by the probe is the same than that in the absence of the probe: *no perturbation of the thruster by the probe*.
6. *The ion current is purely radial*, that is: impacting the probe at normal incidence for every φ angular position of the probe.
7. *The plasma is detached* from the magnetic nozzle at the location of the measurement.

Assumptions 6 and 7 have not been resolved in this thesis. However, preparatory work for assumption 6 was done and will be presented as perspective for future work. Let us examine the validity of the other assumptions.

Assumption 1 is verified according to the following observations. First, the ion velocity is believed to be true because two independent devices yield the same results: the gridded Faraday probe and the Hiden ion analyzer (as we will see later in figure 66 and figure 67). Second, the ion velocity is independent of φ, at least for $\varphi \in [-45\,°; +45\,°]$ ([24], figure 45). Weak signal-to-noise ratio prevented from making the verification for $|\varphi| > 45\,°$, where ion velocity likely keeps constant. In any case, the contribution to thrust for $|\varphi| > 45\,°$ is weak (figure 54).

Assumption 2 was previously verified at ONERA by performing the circular scan for different value of θ (with θ as defined in figure 53), including the θ of the two injection holes (in the axial injection configuration). It seems that the ion current distribution is axis-symmetrical even though neutral gas injection is not.

Assumption 3 is still to be verified in detail. However, this point is unlikely the cause of the discrepancy. The plasma flowing through the dashed horizontal segment in figure 53 likely represents a small fraction of the current and is likely attached to the magnetic field lines. Therefore, either it goes back to the thruster and creates no force, or it encounters an obstacle that creates detachment. In the former case, it does not contribute to thrust. In the latter case, the plasma flux increases thrust if the projection of the ion momentum on the z-axis is positive when impacting the obstacle (maybe half of the cases); otherwise, it decreases thrust. Overall the expected effect is small.

In the following subsections, we will consider assumption 4 (section 4.1.3) and 5 (section 4.1.4).

4.1.3 Trueness of the ion current density measurement

4.1.3.1 Initial gridded Faraday probe

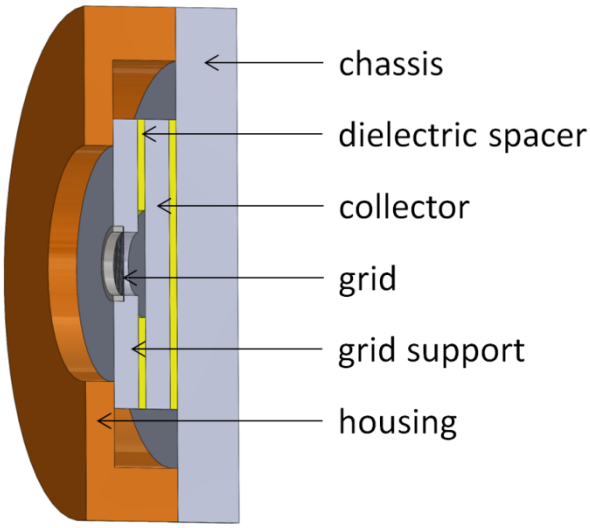

Figure 56. Sectional view of the gridded Faraday probe.

The work started with the probe available in the laboratory (figure 56). First of all, possible current leaks were investigated: the probe parts, as well as cables, were thoroughly isolated to avoid drawing unwanted current.

Effect of the grid. The grid mesh size was initially of the same order as the estimated Debye length (400 µm, see table 4). Yet, a mesh size inferior to the Debye length is required to enforce Laplacian potential in between the grid bars. We suspected that the plasma may significantly curve equipotential lines at the length scale of the mesh, modify the measurement. Therefore, a grid with 40 µm of mesh size was tested. No effect was observed.

However, when considering the effect of the grid, other sources of uncertainty appeared.

1. *Secondary electron emission.* It is possible that secondary electron emission from the grid yields untrue measurement.

2. *Nature of the transparency.* Let's define the relevant grid transparency t as the factor transforming the measured saturation current I into the true ion current density before the grid $J = I/(tS)$, where S is the effective collector surface. In addition, let's define the normal geometrical transparency of a grid to be the fraction of non-opaque area seen when looking at normal incidence, from far away. The issue is that the relevant grid transparency may not be the normal geometrical transparency for at least two reasons. First, the grid has a finite depth that reduces the current in case of non-normal incidence. Second, the ion trajectories may deviate near the grid because the equipotential surfaces are not completely flat ("ion optics" issues).

3. *Uncertainty on the normal geometrical transparency.* The grid transparency provided by the manufacturer sometimes differs from the geometrical transparency measureable on a sharp photograph (such as that in figure 57) by up to 20%.

4. *Dispersion.* It has been observed that two identical pieces of grid can lead to different ion current measurements, all other things being equal (grids in good shape, from the same sample, operated on identical probes, with the same electrical circuit, and on the same ion beam). We suspect the

discrepancy to originate from different surface conditions due to different past usages or non-repeatable grid manufacturing.

Following these considerations, the grid was removed, with the disadvantage that it prevented ion energy measurement on the same probe. Two identical probes then provided equal current measurement whereas with grids they differed significantly. Saturation current was still found when going towards negative collector voltages. The current density was the same than that observed with the grid (divided by grid transparency).

Effect of the collector material. Secondary electron emission (SEE) at the collector surface was also suspected to be a source of error. Indeed, if electrons are emitted by the collector they are expelled towards the plasma, thus creating an unwanted increase of the measured current. In a retarding potential analyzer (RPA), the issue is solved with the collector potential being held slightly above the analyzing grid potential in order for emitted electrons to be recollected. For a gridless probe this technique is not applicable and the collector material should be chosen to reduce SEE. We are interested in SEE by ion impact only, since electrons from the plasma do no reach the collector when ion current is measured. The kinetic energy of these ions is about 500 eV (200 eV initially plus 300 eV for the probe potential drop). SEE yields averaged over the range 100-1000 eV are only a few per cents for impact by singly charged Xenon ions, which is much smaller than SEE yield by electron impact, even at much lower energies. However SEE yields can reach tens of per cents for multiply charged Xenon ions ([98], table 1).

Tungsten is identified as a material with a low SEE yield by ion impact. The stainless steel collector used until then was compared with a Tungsten collector. They were mounted in two identical probes alternatively placed on the axis of the thruster's plasma jet, during the same run (figure 58). The dispersion of the results may originate in variations of the thruster or in variations of the collector surface condition during exposition to the plasma flow. No significant difference is observed between materials thus we concluded that the collector material is not an issue in the current measurement.

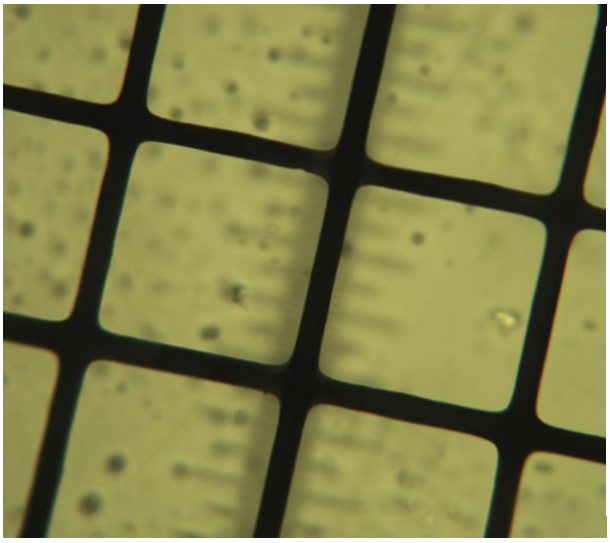

Figure 57. Grid photographed with a Primostar Zeiss microscope.

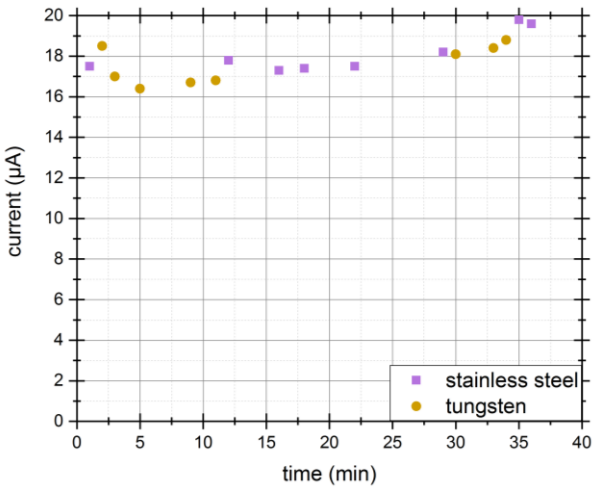

Figure 58. Comparison of collector materials, during the same thruster run, with identical probes.

Effect of the probe geometry. In order to estimate the true ion current density, the current measured by the probe should be divided by the area of collection. The relevant area is that of the collected ion flux tube, measured at the sheath edge (figure 59). In order to make a simple interpretation of the

measurement, probe design should enable a one-dimensional analysis (that is $d \gg s$, figure 59.b). The area of collection should neither depend on the ion velocity nor on the potential of the electrode (figure 59.a).

For densities above 10^{11} cm^{-3} and in a low temperature plasma, ion saturation can be reached for a few tens of volts of negative bias voltage and the sheath around the collector is so thin that the area of the sheath edge is that of the collector [99]. These are condition that lead to a simple interpretation of the ion saturation current. On the contrary, in the thruster jet, the density is only about 3.10^{8} cm^{-3} and ion saturation is reached only below -200 V. In such conditions, a careful interpretation of the measurement is required.

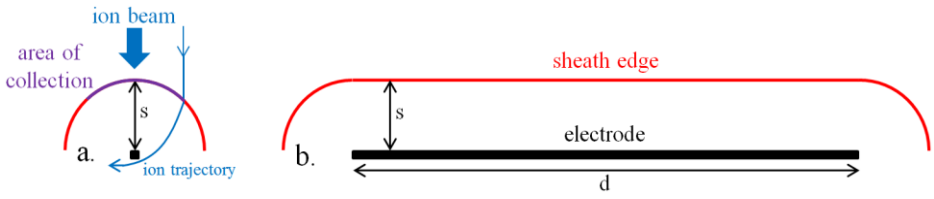

Figure 59. Electrode in a plasma which is (a) small or (b) large compare to the sheath thickness. Red line is an equipotential near plasma potential.

In order to analyze the gridded Faraday probe, *we are interested in the thickness of the sheath it creates*. The sheath that develops in front of the grid is likely not described by the more common sheath models. Let's however briefly review the classical results on collisionless DC sheaths [74]. We are interested in collisionless sheath models since we obviously have a mean free path much larger than the scale length of the sheath (see table 4).

The more simple models are planar models for a cold isotropic plasma. They are planar in the sense that they consider an infinite plane in contact with a plasma filling the half space on one side of the plane. They are applicable to cold isotropic plasmas: electrons are assumed to have a null flow velocity and to be described in the sheath by Boltzmann distribution whereas ions are assumed cold and with a null flow velocity in the bulk plasma. Under these assumptions, using conservation of ion energy and conservation of ion flux, the Poisson equation

$$\frac{d^2\phi}{dx^2} = \frac{e}{\epsilon_0}[n_e - n_i] \qquad \textbf{(179)}$$

can be written as

$$\frac{d^2\phi}{dx^2} = \frac{en_s}{\epsilon_0}\left[\exp\frac{\phi}{T_e} - \left(1 - \frac{\phi}{E_{ci}}\right)^{-1/2}\right] \qquad \textbf{(180)}$$

where ϕ is the electrostatic potential, n_s is the plasma density at the sheath edge, T_e is the electronic temperature in eV, and $E_{ci} = (M/2e)u_s^2$ is the ion energy in eV at the sheath edge. The sheath may be defined as the non-neutral region near a wall (figure 60), hence the electrostatic potential has only little variations outside the sheath. Then, taking the origin of coordinate at the sheath edge, we set $\phi(0) = 0$. Multiplying by $d\phi/dx$ and integrating we get

$$\frac{1}{2}\left(\frac{d\phi}{dx}\right)^2 = \frac{en_0}{\epsilon_0}\left[T_e\left(\exp\frac{\phi}{T_e} - 1\right) + 2E_i\left(\left(1 - \frac{\phi}{E_{ci}}\right)^{1/2} - 1\right)\right]. \qquad \textbf{(181)}$$

where the right hand side should be positive for a solution to exist. We expect this condition not to be met for small ϕ in particular. Therefore, Taylor expansion in ϕ/T_e and ϕ/E_{ci} yields the Bohm sheath criterion.

$$u_s \geq u_B = \left(\frac{eT_e}{M}\right)^{1/2} \quad \textbf{(182)}$$

This condition implies the existence of a region before the sheath that is quasi neutral, although a sufficient potential drop takes place to accelerate ions to the Bohm velocity u_B.

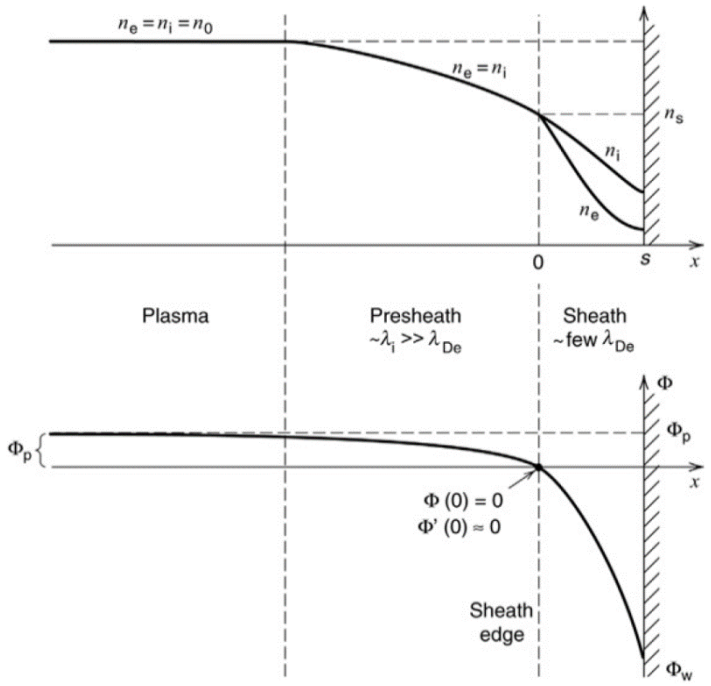

Figure 60. Sheath in a cold isotropic plasma. Reproduced from [74].

The ϕ function in the sheath can be obtained analytically from equation 181 if additional assumptions are made. When the wall is at a fixed potential imposing a large drop from plasma potential (as compared to the electron temperature), we may assume negligible electron density in (most of) the sheath. We may then additionally assume that the ion density is constant. This case is known as the *matrix sheath* ($n_e = 0$ and $n_i = n_s$ in the Poisson equation) and yields a sheath thickness

$$s_{matrix} = \lambda_{Ds}\left(\frac{2V_0}{T_e}\right)^{1/2} \quad \textbf{(183)}$$

for $\phi(s) = -V_0$, with $\lambda_{Ds} = (\epsilon_0 T_e/en_s)^{1/2}$.

A more realistic approach known as the *child law sheath* takes into account ion flux conservation ($n_e = 0$ and $n_i = (J_0/e)(-2e\phi/M)^{-1/2}$ in the Poisson equation). It yields a sheath thickness

$$s_{Child} = \frac{2}{3}\left(\frac{\epsilon_0}{J_0}\right)^{1/2}\left(\frac{2e}{M}\right)^{1/4} V_0^{3/4} \quad \textbf{(184)}$$

Child law is usually put forward in the context of acceleration through grids ([47], chapter 7). For a given potential difference and a given distance between grids, it provides the maximum ion flow that can be drawn, for initially immobile ions (i.e., with kinetic energy negligible as compared to the potential

drop). The maximum ion flow is reached when the density of ions cancels out the electric field at the first grid.

Child law sheath differs from the reality of our experiment where ions have an initial velocity. In such case, numerical integration of equation 180 is required. It is rewritten using $J_0 = en_0u_i$ (measured to be 0,8 A/m^2 with $u_i = 17$ km/s).

$$\frac{d^2\phi}{dx^2} = \frac{J_0}{u_i\epsilon_0}\left[\exp\frac{\phi}{T_e} - \left(1 - \frac{\phi}{E_{ci}}\right)^{-1/2}\right] \quad \textbf{(185)}$$

We take initial conditions representative of the bulk plasma and therefore integrate over the pre-sheath and the sheath. Plasma potential is taken to be 0 ($\phi(0) = 0$), and initial derivative $\phi'(0) = -100$ V/m is estimated from plasma potential measurement in the plume (figure 34). Results are plotted in figure 61. We see that with initial ion velocity of 200 eV, the sheath thickness is increased as compared to the Child case (no initial velocity). In particular, a very small second derivative ϕ'' around $x = 0$ is observed. This is consistent with the existence of an initial velocity: $\phi'' \propto n_i \propto 1/u_i$, yet $du_i \propto d\phi/u_i$, hence for a given ϕ variation, the variation of ϕ''decreases with ion velocity, hence the stagnation of the curve around $x = 0$. In addition, we see as expected that hotter electrons imply a thicker sheath. As a conclusion, we established that *the sheath created by the probe has a thickness of one or a few centimeters.*

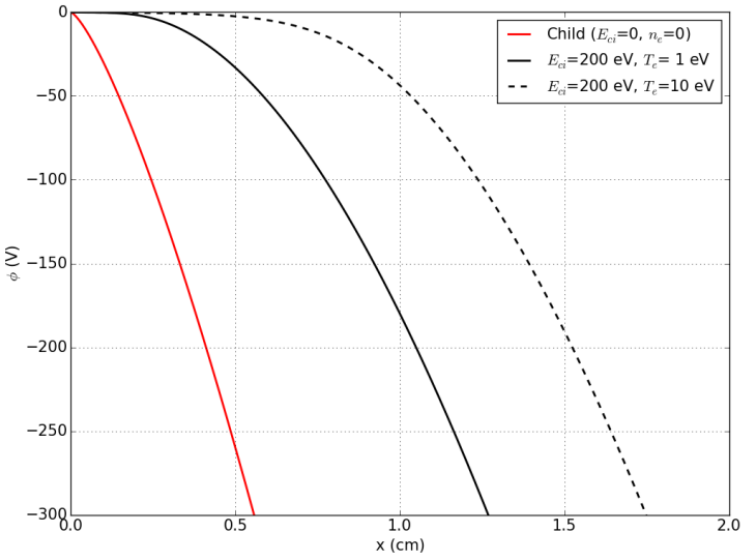

Figure 61. Sheath potential profiles. $J_0 = 0,8$ A/m2. For Child case, $\phi'(0) = 0$. Otherwise $\phi'(0) = -100$ V/m

The discussion about the sheath thickness was needed for the estimate of the area of collection of the probe. From the above calculation it appears that the sheath thickness is superior to or of the order of collector diameter, hence a difficult interpretation of the measured current (figure 59). Moreover, the relevant collector diameter is unknown and the diameter of the opening of the grid support is taken as collector diameter (figure 62). Besides, the grid support is still present although the grid was removed, which complicates the interpretation. Laplacian potential for the gridded Faraday probe without grid is plotted for reference in figure 63.

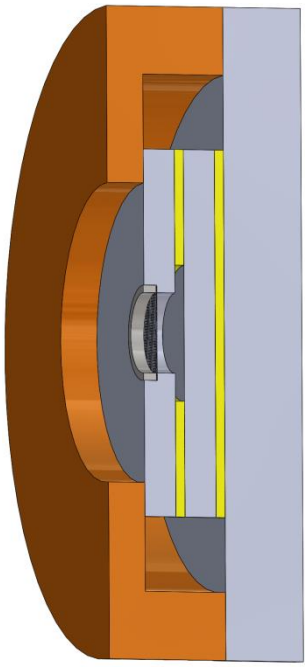

Figure 62. Gridded Faraday, sectional view. Yellow and brown parts are dielectric parts. Gray parts are metallic.

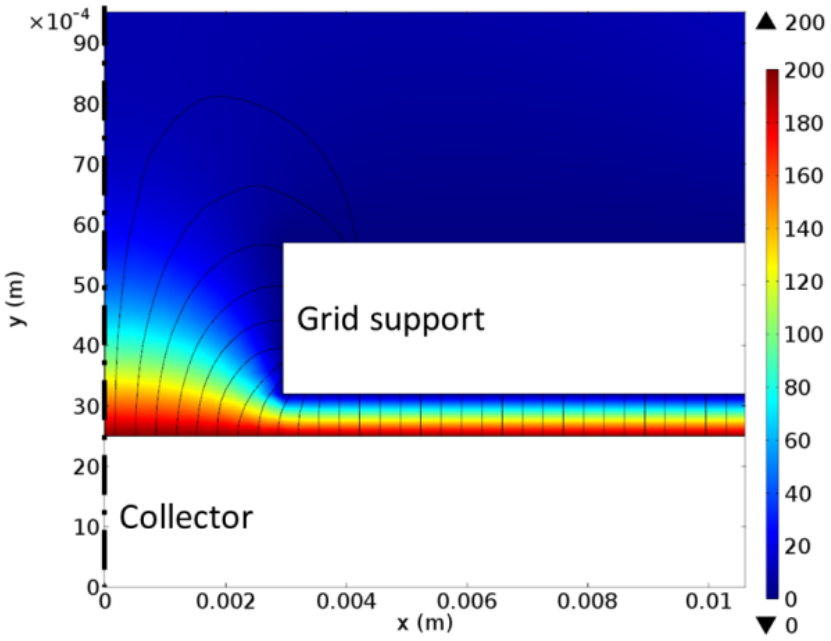

Figure 63. Electrostatic potential in V and electric field lines for the gridded Faraday probe without grid. The opening in the grid support is considered as the collector diameter.

4.1.3.2 Faraday probe with guard ring

In order to ensure simple interpretation of the ion saturation current measurement and to use a proven design, a guard ring Faraday probe was built according to recommendations prevailing in the electric thruster community [98]. The idea behind the guard ring is to impose flat equipotential in the vicinity of the collector so that the area of collection is equal to the geometrical area of the collector (figure 64).

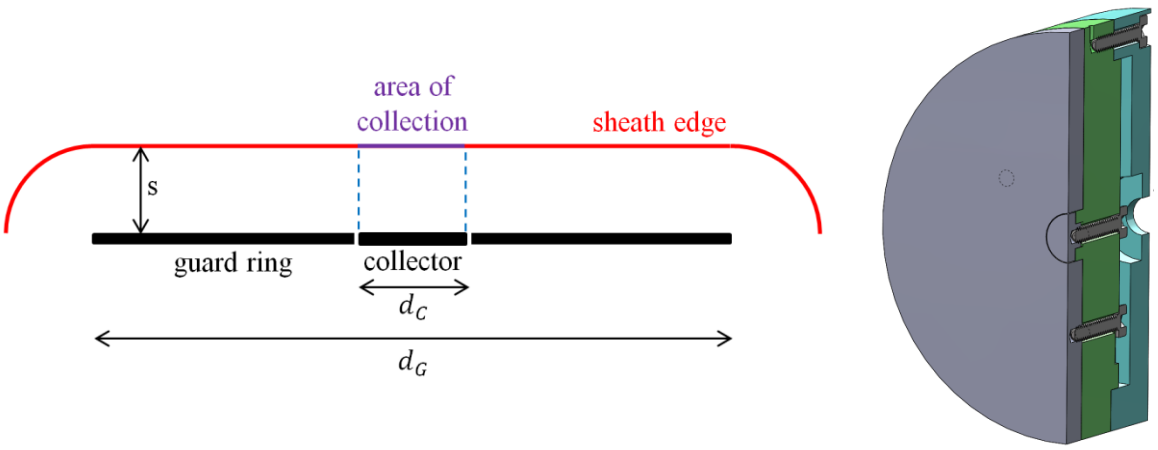

Figure 64. Guard ring Faraday. The collector and guard ring are at the same potential but only the current drawn from the collector is measured.

In order to achieve this, it is recommended that $d_G > 100\,\lambda_D$. Yet we estimate $\lambda_D \approx 0{,}04$ cm (table 4), hence we chose $d_G = 5$ cm, which is coherent with the sheath calculation of the previous section. The collector diameter was taken equal to the grid support opening of the gridded Faraday probe (that is $d_C = 5{,}9$ mm) in order to facilitate comparison. The guard ring and collector are manufactured in Molybdenum in order to limit SEE by ion impact [98]. The gap between the collector and the guard ring

is as low as 100 µm to avoid uncertainty regarding the current flowing in the gap. The collector and guard ring are held by support parts with sufficient accuracy that they are isolated, provided that the gap is clean.

The guard ring Faraday probe was compared with the existing gridded Faraday probe without grid, for several thruster configurations. No significant difference was observed, at least not a difference that would explain the inconsistency with the thrust balance. An example is given in figure 65.

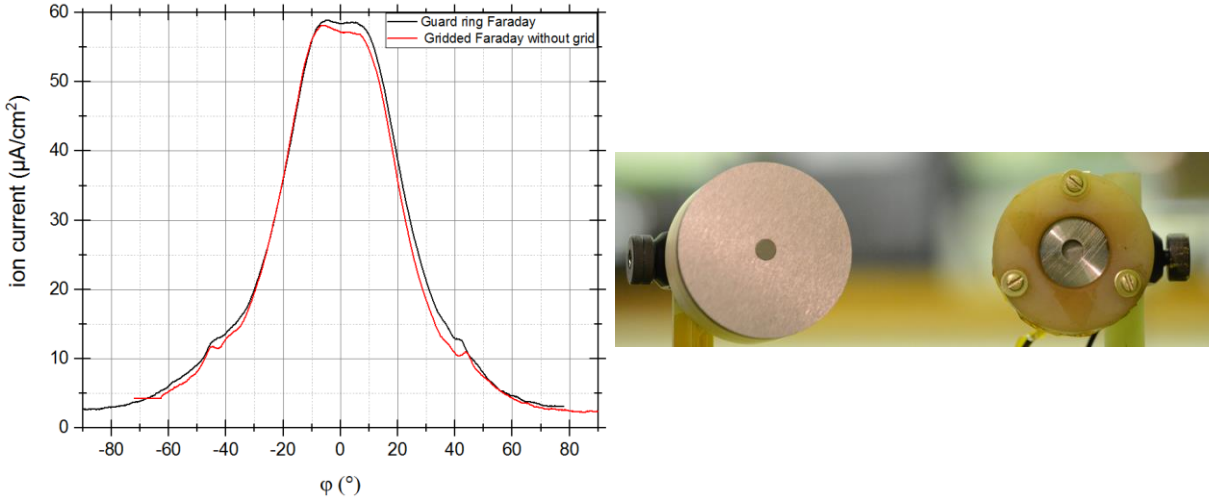

Figure 65. Comparison of probes on a circular scan 26,5 cm from the thruster exit. For the guard ring Faraday (left on the picture): collector and guard ring are at -300 V. For the gridded Faraday (right on the picture): the collector is at -300 V and the grid support left floating. Thruster: axial injection, big magnet, 20 mm outer conductor.

As a conclusion, the Faraday probe with guard ring is a proven diagnostic whose simple geometry allows for simple interpretation of the ion current and yielded the same results as those from the initial gridded Faraday probe. This results gives confidence that *a meaningful ion current density is measured* (assumption 4). This ion current density may not be however the same than in the absence of the probe. The goal of the next section is to assess the perturbation of the probe on the thruster.

4.1.4 Perturbation of the thruster by the probe

In this section we examine assumption 5. As a first step to assess the possible perturbation of the thruster by the probe, the current drawn by the *collector* of the gridded Faraday was measured for several *grid voltages*. The collector voltage is swept from -300 V to +300 V. For a typical scan (figure 66), the so-called "ion saturation current", when all electrons are repelled, is reached around -200 V. When increasing the voltage, the current drop around 0 V is interpreted as the collection of electrons. Increasing again the voltage, we observe again a current drop around 200 V that is interpreted as the repulsion of the main ion beam. The slope between 50 V and 150 V originates in part from the repulsion of slower ions, as indicated by the ion energy distribution measured with Hiden ion analyzer (figure 67). It may also come from an instrumental effect, for example a resolution effect of the probe, that is: particles with non-normal incidence can be collected for bias voltages different from their energy ([100], section 4).

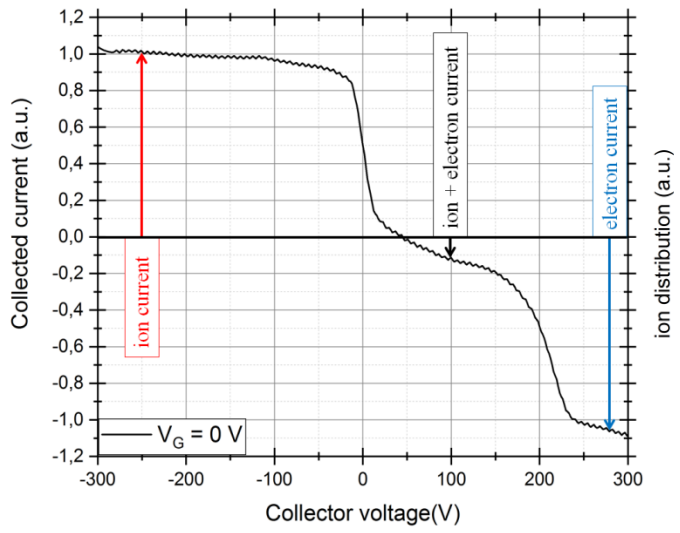

Figure 66. Collector current during a collector voltage sweep. $V_G = 0\ V$ is the grid potential

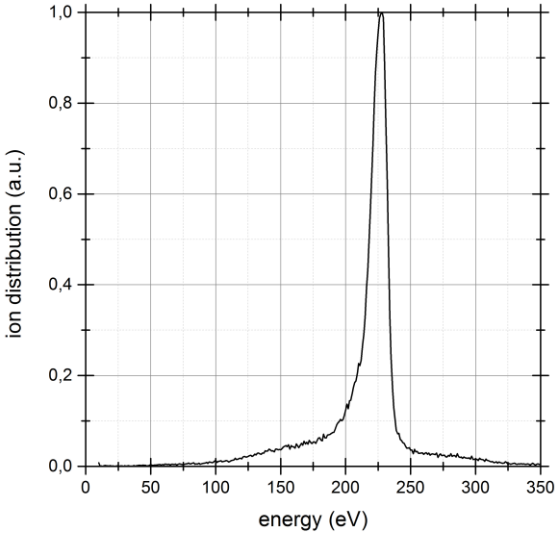

Figure 67. Energy scan with Hiden PSM003.

We look now at the series of curves obtained at different grid voltage. In figure 68, we see that *the value of the ion saturation current is unaffected by the grid voltage.* The dispersion of ion saturation current seen on the zoomed window rather originates in thruster behavior. However, variations of the grid voltage induce variations of the collected electron current. We will focus on this feature in the rest of the section. The main observations are: first, the amplitude of the electron current drop increases with grid potential; second, the drop is centered on the grid potential; third, the width of the drop increases with grid potential.

It is unclear whether the third observation comes from an instrumental effect (for example a resolution effect) so we focus on the first and second observations, which are coherent with the following perspective (developed in more detail in chapter 7). Let us consider the plasma flux tube intercepted by the grid and the grid support of the probe. We assume that it corresponds to a magnetic tube, and that cross field diffusion is low enough that this magnetic tube can be considered to some extent as isolated from the rest of the plasma. For simplicity we will consider a flux tube centered on the z axis. The electron longitudinal equation of motion is

$$\frac{dv_z}{dt} = -\frac{1}{m}\partial_z(-e\phi + |\boldsymbol{\mu}|B), \qquad (186)$$

which is a Hamilton equation describing a movement in the sometimes called "effective potential" $U_{eff} = -e\phi + |\boldsymbol{\mu}|B$. Since this potential is convex, their exist an energy E_0 under which (confined) electrons undergo an oscillatory motion; the abscissa of their right turning point increases with their energy (figure 69); let's ignore the details of the confinement to the left for the moment (this question will be addressed in chapter 7). Electrons above E_0 escape from the potential well.

Above a certain z location no ionization takes place and we have constant ion flux Γ_i in the considered flux tube. This flux is directed to the right and no ion flux exists in the opposite direction. On the contrary there are electrons fluxes Γ_e^+ and Γ_e^- to the right and to the left respectively. The flux to the left is constituted by electrons coming back to the thruster after they are reflected by the increasing potential. Under the assumption of ambipolarity in the flux tube (global ambipolarity is a fact since the thruster is electrically floating and local ambipolarity is a reasonable assumption at most locations), we have $\Gamma_i = \Gamma_e^+ - \Gamma_e^-$. In addition, Γ_e^+ and Γ_e^- decrease with increasing z; for sufficiently large z, $\Gamma_e^- = 0$ and

$\Gamma_i = \Gamma_e^+$. From this perspective, the collector current profiles for different grid voltages can be interpreted as follows.

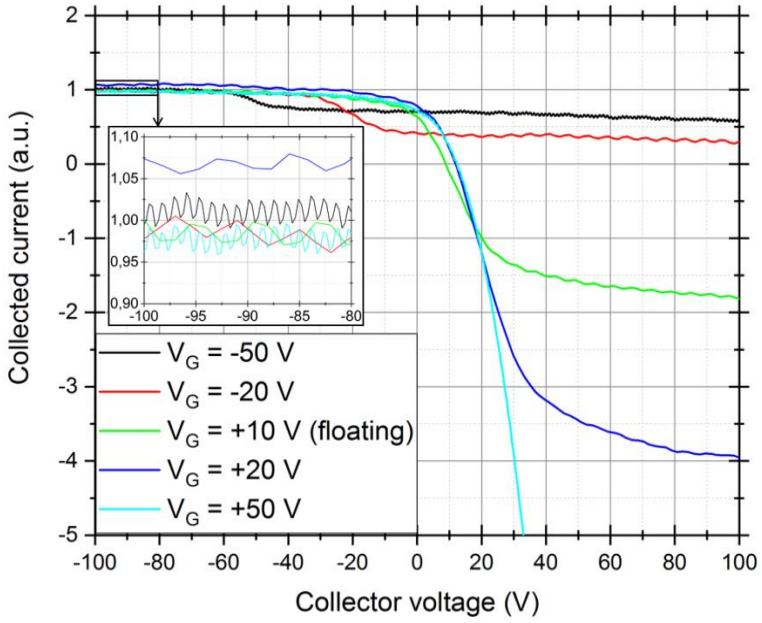

Figure 68. Collector current during a collector voltage sweep. V_G indicates the grid potential

Amplitude of the electron current drop. When the *collector* is placed at a voltage such that it repells all the ions, the unperturbed electron current is that collected when the *grid* is held at the plasma potential, that is $V_G \cong +50$ V for our measurements. In this case we observe $\Gamma_e^+(V_G) \cong 50\Gamma_i$ (cyan curve in figure 68; the y-axis is limited for better reading of other curves). In the absence of the probe, an almost equally large (unmeasured) Γ_e^- ensures that the net electron flux equals the ion flux ($\Gamma_i = \Gamma_e^+ - \Gamma_e^-$). If then a slightly lower grid voltage is applied (for example $V_G = +20$ V, that is $\cong -30$ V from the plasma potential), it screens the low energy part of the electron energy distribution, hence a lower measured Γ_e^+. A particular case is that when $V_G = 0$ V because the grid potential then equals the asymptotic value of the unperturbed potential. In this case, if we assume local ambipolarity, we have $\Gamma_i \cong \Gamma_e^+$, since by holding the grid at 0 V we collect the asymptotic value of the electron current $\Gamma_e^+ = \Gamma_i$. Indeed this is what we observe (figure 66), which seem to confirm both the validity of this approach and the local ambipolarity.

Location of an additional drop around $V_C = V_G$. When we go towards lower grid voltages, an additional phenomenon first overlaps and then becomes dominant: for $V_G = -20$ V and $V_G = -50$ V in figure 68, we observe a drop of collected current (i.e. fewer ions or more electrons) for increasing collector voltage in the curve around $V_C = V_G$, suggesting the collection of electrons with energy around $-eV_G$ which were not present in the unperturbed case ($V_G = +50$ V). For example, the $V_G = -50$ V curve indicates the presence of 50 eV electrons absent in all other cases. This indicates that the electron energy distribution in the plasma flux tube intercepted by the probe is perturbed by the presence of the probe. The presence of electrons with energy as high as the grid voltage can be interpreted as follows. Let's assume that electrons gain energy by small increments (say of order $\Delta E \cong 1 - 5$ eV) when they interact with the electromagnetic field in the ECR region near $z = 0$. They interact with the electromagnetic field once every longitudinal oscillation period in the "effective potential". Yet the effective potential is modified by the grid voltage, increasing electron confinement. Therefore, electrons that would escape to the right in the absence of the probe can gain additional energy up to the grid potential (figure 69). This energy gain is likely achieved through several small ΔE increments since no

electrons are observed for energies larger than $-eV_G + \Delta E$. Indeed, if the interaction with the electromagnetic field provided large energy increments (say, tens of eV), electrons with energies larger than $-eV_G + \Delta E$ eV would be observed by the probe.

Under the assumption of electron fluxes being strongly guided by the magnetic field, the effect of the probe on the electron distribution can be summarized as follows.

1. Let E be the electron energy, for $E < -eV_G$ electrons are repelled by the grid and stay confined in the longitudinal effective potential.

2. For $E > -eV_G$ electrons are collected by the probe, as we will show by considering separately the possible cases. If $-eV_G > -eV_C$, electrons are collected: a fraction $1 - t$ by the grid, and a fraction t by the collector (t being the transparency of the grid). Else if $-eV_G < -eV_C$, we have two cases.

    - If $E > -eV_C$ and electrons are collected: a fraction $1 - t$ by the grid, and a fraction t by the collector
    - Else if $-eV_G < E < -eV_C$ electrons go through the grid and bounce back before they reach the collector, hence a fraction $1 - t^2$ is collected by the grid and a fraction t^2 is sent back to the thruster. Under the assumption made before that the average energy increment for one pass in the ECR region ΔE is small (such that $\Delta E \ll -e(V_C - V_G)$), electrons such that $-eV_G < E < -eV_C$ will undergo a large number of longitudinal oscillations (without significantly changing energy) with a mirror point between the grid an the collector. Thus for every longitudinal oscillation period, a fraction $1 - t^2$ will be collected, leading to complete collection.

A major effect the grid (and grid support) potential V_G is therefore to deplete the electron energy distribution for $E > -eV_G$. Regarding our initial concern of perturbation of the thruster by the probe, we observed that the measured ion current is independent of the grid voltage thus seems independent of the electron energy distribution in the flux tube intercepted by the probe.

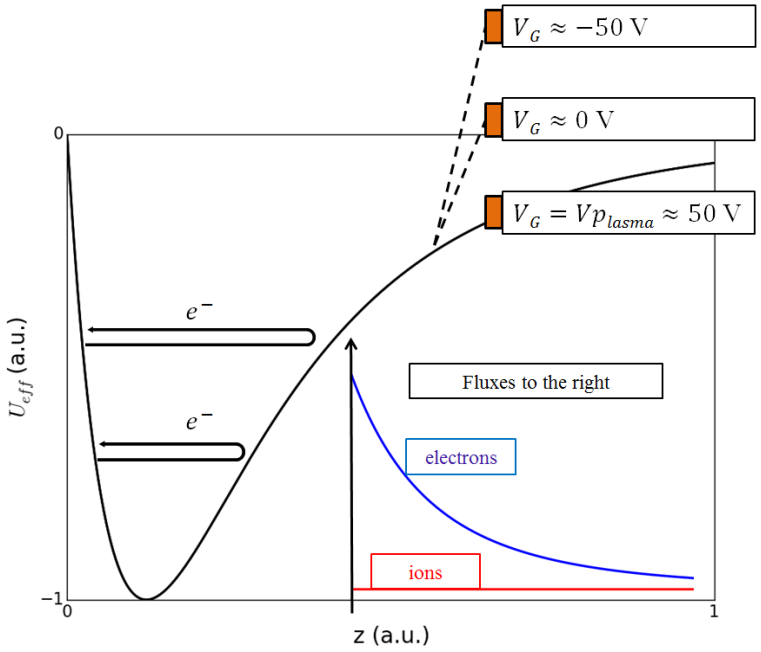

Figure 69. Electron current and effective potential.

Conclusion of section 4.1. Careful measurements with two distinct ion current probes gave confidence that a meaningful ion current density is measured. Concerning the possible perturbation of the thruster by the presence of the probe, we observed that the ion saturation current is unaffected by the grid voltage therefore the electrostatic perturbation induced by the presence of the probe is unlikely the cause of erroneous ion current measurement. Apart from electrostatic perturbation, other sources of perturbation by the probe might however be imagined.

The search of the error cause should address assumption 6 and 7 from section 4.1.2. Methods have been imagined and developed to test these assumptions. They aim at providing information on ion trajectories. A "directional probe" was designed and manufactured with the intention that it collects current only at a small angle with respect to its axis, contrary the guard ring probe which is very "open". It can be operated with two degrees of rotation (figure 70) in order to determine the orientation of the ion current. Preliminary tests were conducted, showing that the maximum ion current does not occur for $\alpha = 0$, but more complete measurements need to be done in the future. Regarding detachment, implementation of a sufficiently powerful laser source would enable to perform LIF measurements in the beginning of the plume, leading to two dimensional ion velocity measurements which could provide extremely valuable information on ion trajectories and detachment.

In the course of our research, *we observed that electron energy distribution is modified by the grid potential*, in coherence with trapped electrons undergoing an oscillatory movement along the magnetic field lines and gaining energy by small increments. Collector current profiles for different grid voltages can be interpreted consistently with the approach that will be developed in chapter 7.

Following our goal of checking the accuracy of plasma measurements, we now turn to verifying consistency between two different facilities.

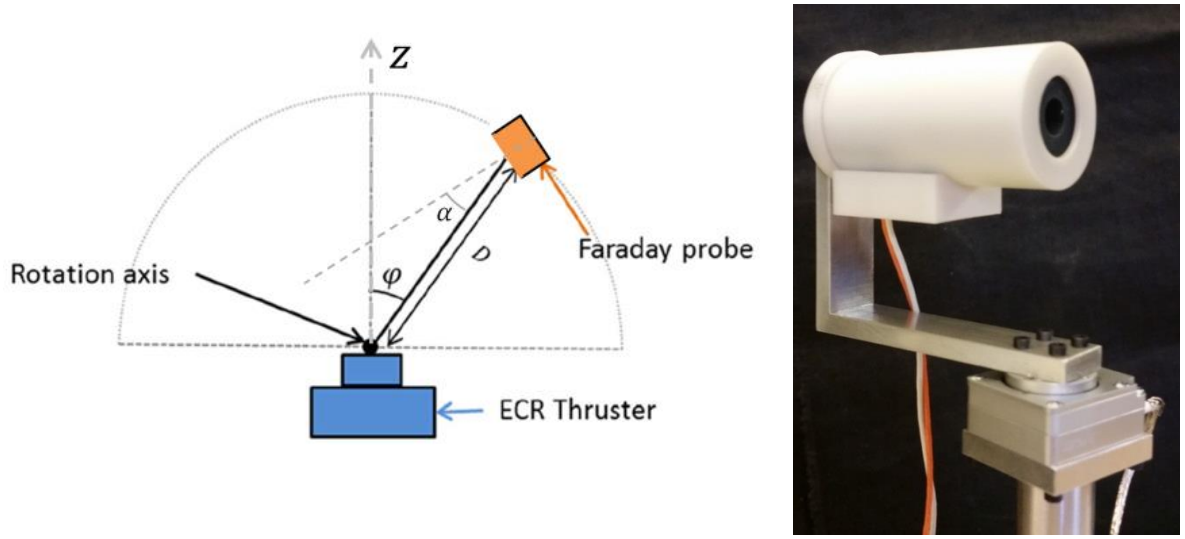

Figure 70. Directional probe with two degrees of rotation.

4.2 Consistency when changing facility

During the course of this study a measurement campaign dedicated to the 30 W ECRT took place in the Jumbo facility at Justus Liebig University (JLU) in Giessen, Germany, from October 9 to October 12, 2018. The Jumbo facility is a 3 m diameter and 6 m long vacuum tank (figure 72) whose Xenon pumping capacity was measured during the campaign to be 166 000 L/s. The goal of this campaign was threefold.

1. To provide new elements regarding the interpretation of ion current measurement in the ECRT. To do so, ONERA probes and JLU probes were used simultaneously (section 0).

2. To check measurement consistency when changing facility and to provide an independent assessment of the thruster performance (which had been measured so far only by ONERA).

3. To test the thruster at lower pressures than at ONERA (and in a larger tank, walls further away), conditions for which more representative performance is expected.

Goal 2 and 3 are addressed in section 4.2.2.

Magnet	**Coupling structure type**	**Outer conductor:** - diameter - length - material	**Inner conductor:** - diameter - length - material	**Injection type**	**Backplate material**	**Other**
Big	Coaxial	- 27,5 mm - 15 mm - Al	- 2,3 mm - 20 mm - Inox	Axial	Boron nitride	Teflon coaxial line just before the ECRT

Table 6. ECRT configuration used at JLU (see Appendix C.)

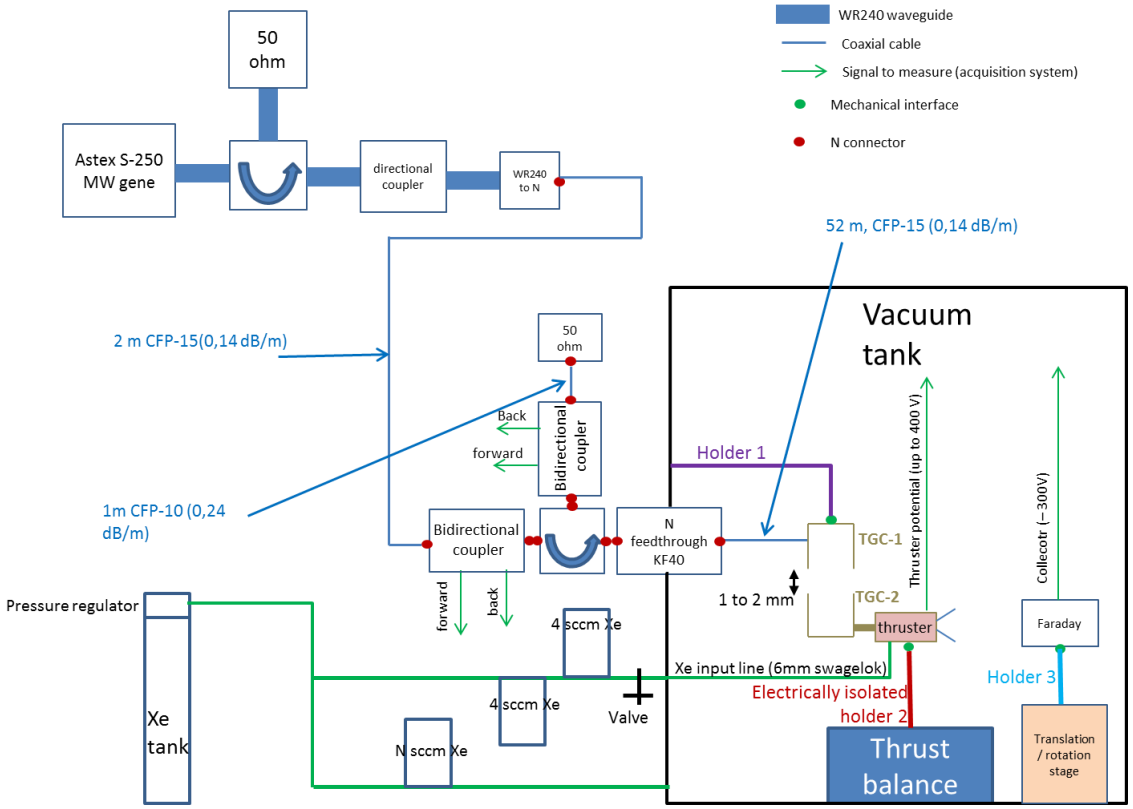

Figure 71. General set-up.

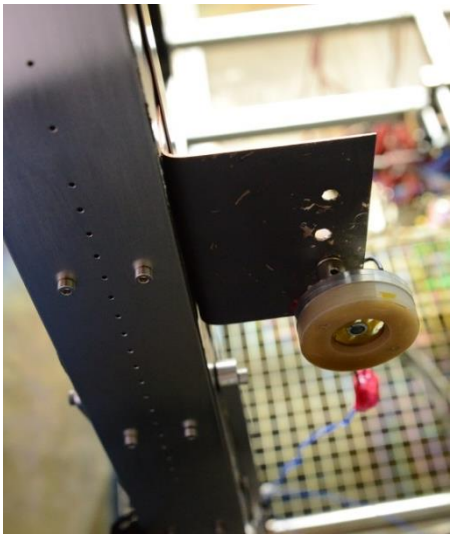

Figure 72. JLU faraday tower and ONERA probe (left), thruster position in the Jumbo tank (right).

The set-up is in figure 71 and the ECRT configuration is that specified in table 3. Unless otherwise indicated the thruster was supplied 1 sccm of Xenon and 24 W of microwave power (at 2.45 GHz) was deposited in the thruster. The diagnostics used during the tests include a gridded Faraday brought by ONERA and a set of Faraday cup from JLU, both performing linear scans perpendicular to the axis of the thruster (figure 72). JLU also provided a new thrust balance (figure 30) adapted for the thrust level of the experiment, and a Parallel Plate Analyzer to measure ion energy. The microwave generator is provided by JLU and has a waveguide output. A waveguide-to-coaxial transition is used, downstream

of which the circuit is the same than that presented in figure 52, except for the absence of the unnecessary filtering system. Mass flow meters from JLU and ONERA were used and compared for coherence. The thruster ignited easily (figure 74) and power coupling was as usual.

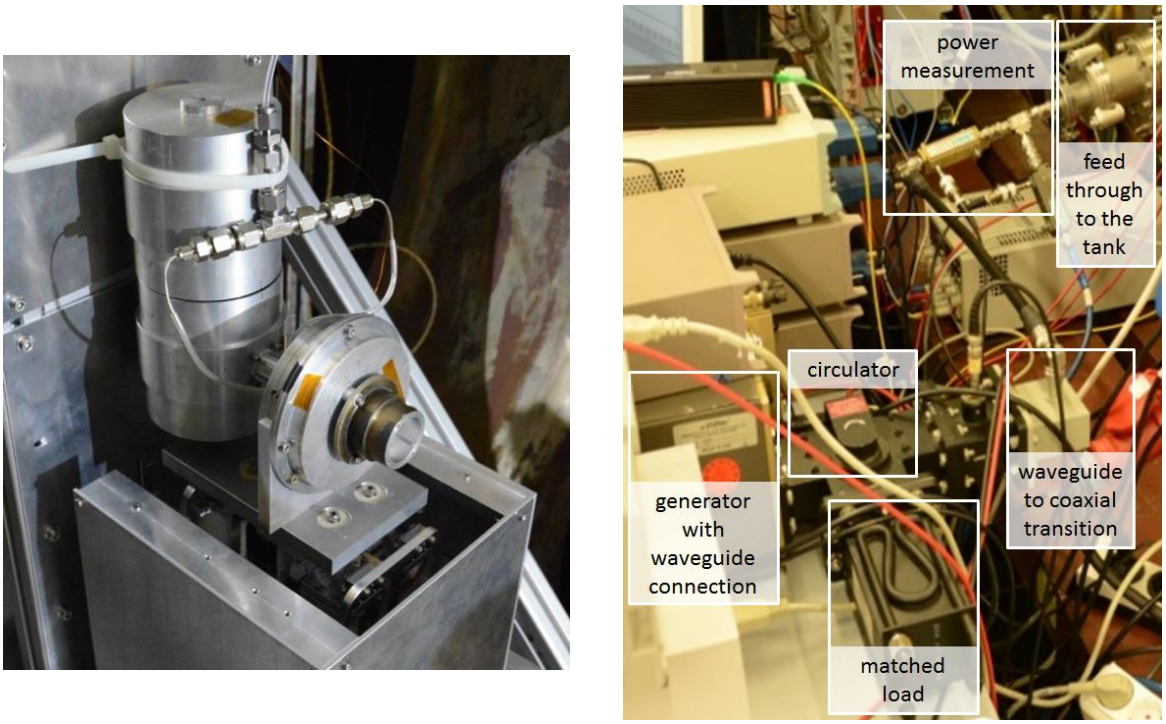

Figure 73. ECRT mounted on the thrust balance (left) and microwave circuit (right).

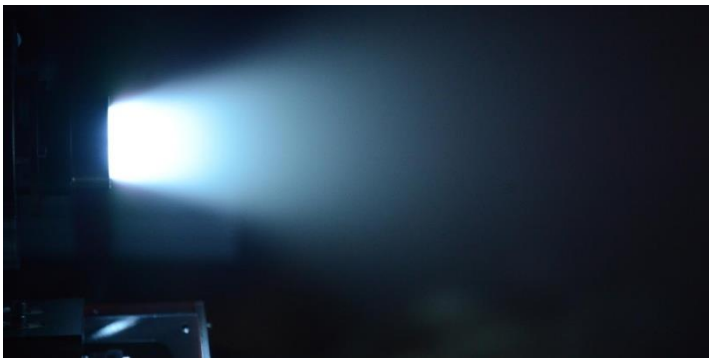

Figure 74. ECRT firing at JLU, mounted on the thrust balance.

4.2.1 Ion current profiles

Overall, the data from the faraday probes proved difficult to interpret due to the reasons that will be exposed, but is nonetheless presented in this section as it is a rare comparison between two facilities and two different probes. As an introduction, figure 75 is an illustrative two dimensional plot of the ion current in arbitrary units measured with the cup tower moving perpendicular to the thruster axis. A large non axis-symmetrical drop near the center was sometimes observed. It could be explained by insufficient repeller potential, overcome in that central region by fast electrons decreasing the measured ion current. Indeed, similar behavior was previously observed on the ECRT ([24], figure 109). However, it did not occur in all measurements. It could also be the shadow of the inner conductor, slightly moving from measurement to measurement.

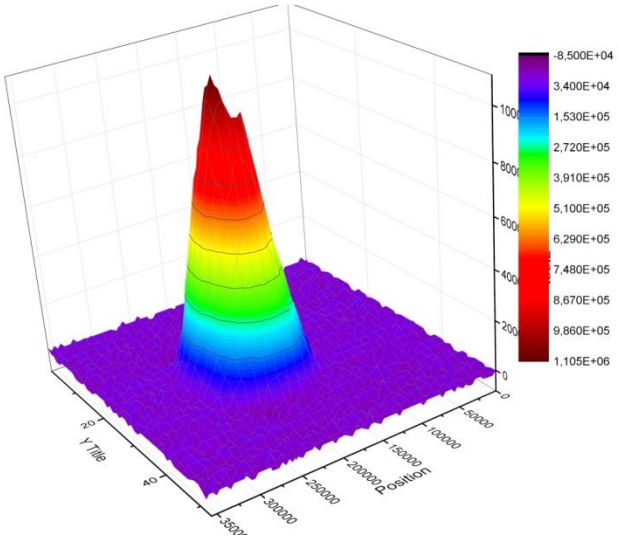

Figure 75. 2D ion current scan performed with the tower of cups.

4.2.1.1 Comparison between probes at Jumbo vacuum facility

Figure 76 is an ion current plot simultaneously measured by the gridded Faraday and by one of the Faraday cups of the tower, moving in the same horizontal plane. The distance $|TD|$ to the thruster (figure 77) differed by 2 cm between the compared probes. In order to make a comparison anyway, (i) we assumed that ions flow along straight lines in the region of the probes and corrected the abscissa by a factor that is the ratio of distances; (ii) we assumed constant current per solid angle (centered on the thruster) and corrected the current by the inversed squared ratio of distances.

In addition to this positioning issue, the probes have different acceptance angles. Indeed, both probes have a cut off lateral position after which no current is measured, attributed to respective acceptance angles. As expected, the narrower JLU Faraday cup displays a smaller cut off distance than the gridded Faraday. Given the opening and the depth of the gridded Faraday and using a purely geometric calculation, we have that it should collect no ion current for any incidence angle above $i' = 72$ °. It is observed that it collects zero ion current for $|x| > 30$ cm. If the acceptance angle calculation is correct, it implies that ions flow at an angle $i' = 72$ ° for $x = 30$ cm. This angle is close to that of the magnetic field lines at this location (estimated to be 65 °). However it is far from a straight line flow from the thruster to the probe which would yield $i' = i = 43$ °. Ion current profile comparison is therefore inconclusive but raises interesting questions regarding acceptance angle and ion trajectories.

These issues a priori vanish for $x = 0$, where the ion flow may reasonably be assumed parallel to the y-axis, that is perpendicular to the opening of the probes. The ion current values at this location show that the gridded Faraday measures a current in excess of 25-30 % as compared to the Faraday cup. Under the assumption that the probe causes a perturbation of the flux tube it intercepts, the difference in ion current might be interpreted as a consequence of different probe sizes: a small probe intercepts a small flux tube that is subject to more diffusion as compared to a larger flux tube. Therefore the perturbation of a small flux tube can be averaged out by diffusion. This is however only a faint hypothesis and the discrepancy is essentially unexplained.

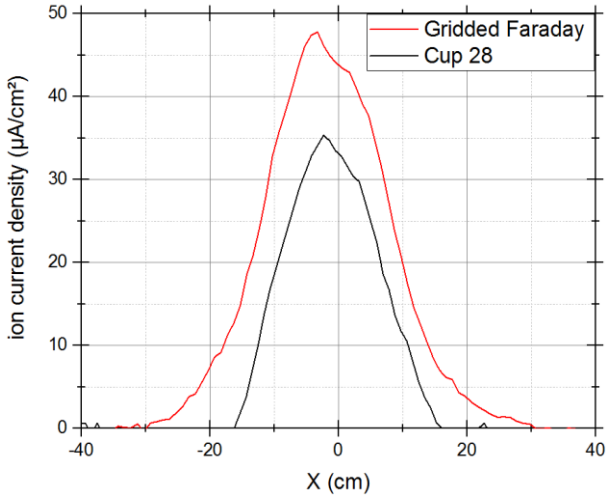

Figure 76. Ion current density at Jumbo facility measured during linear scan 31.5 cm from the thruster. The cup was actually at 34 cm from the thruster and was corrected by a factor (34/31.5)² and its abscissa by a factor (31.5/34). No acceptance angle correction is made.

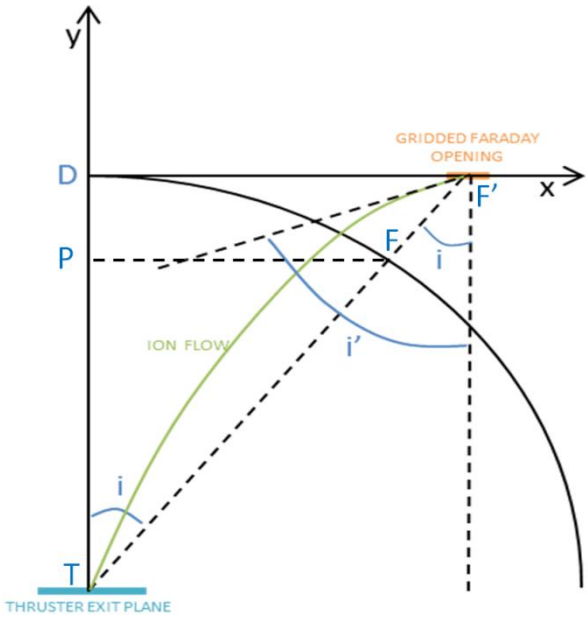

Figure 77. Schematic of the ion current measurement with linear scan.

4.2.1.2 Comparison between vacuum facilities, with the ONERA gridded Faraday probe

Ion current profiles were taken at B61 and Jumbo facility with the same probe: the gridded Faraday from ONERA. However, *circular scans were performed at B61 facility whereas linear scans were performed at Jumbo facility*. This setup is explained by the fact that the facility is mostly used for the study of gridded ion engines, which have a very low divergence and therefore allow the use of linear scans. As a consequence, the data is difficult to interpret because the transformation from a linear scan to what would be obtained in a circular scan for the same thruster (or vice-versa) requires the knowledge of ion trajectories and acceptance angle of the probe.

In order to make a comparison anyway, it can be assumed that the ions flow radially, meaning that, in the case of a circular scan centered on the thruster exit, ions always reach the probe at normal incidence. This is a priori true at least for small angles. Under this assumption and with the additional assumption that all the current flowing through the opening of the cup is collected (no acceptance angle effect, which again is true at least for small angles), the transformation from circular to linear scan ($(i,J) \longmapsto (X,J')$) is the following.

$$\begin{aligned} X(i) &= |TD| \tan(i) \\ J'(X) &= J(i) \cos^3 i \end{aligned} \qquad (187)$$

Variables are defined in figure 77. The transformation $i \longmapsto X$ is straightforward. The transformation of current, is made under the assumption that the current flow per solid angle is conserved. Therefore the difference in distances brings in the squared ratio of distances, which is $\cos^2 i$ (for example using Thales theorem in the TPF and TDF' triangles). The difference in orientation of the opening of the probe brings in a factor $\cos i$.

Ion current profiles taken at B61 and Jumbo facility are compared in figure 78 using transformation 187. Three reasons may be invoked to explain the difference between the two curves. First the assumptions underlying the transformation may not be satisfied. Second there may be a the pressure effect: increased pressure is known to reduce the current on axis while increasing the current for large angles for several type of thruster [98], and this effect was specifically measured on the ECRT ([24], figure 131). Third, the difference in profiles may also originate from a tank effect. From the available information, it seems impossible to discriminate between these possibilities.

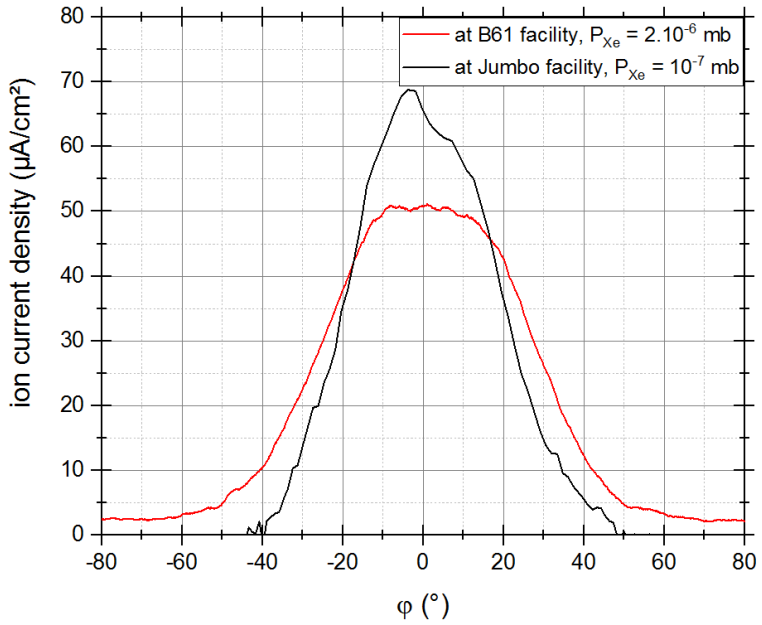

Figure 78. Ion current measurement with the gridded Faraday from ONERA. Transformation 187 was applied to the linear scan in Jumbo facility to provide an estimate of the current that would be measured for a circular scan 26.5 cm from the thruster.

4.2.2 Pressure effects and comparison of thrust balance measurements

Measurements were performed on the newly set parallelogram pendulum thrust balance at JLU Jumbo facility. After tuning of the feedback parameters, the thrust balance behaved well, with little drift. Calibration was performed with masses on a pulley system, down to a few mN. This calibration factor was extrapolated to the $0{,}5 - 1$ mN range, which is the range of interest. For comparison, measurements were also performed with the same thruster and microwave line, and for the same power and gas flow with the ONERA balance in the B61 facility, before and after the JLU campaign. In both facilities, a separate Xenon feed system was used to inject gas in the vacuum tank to change the background pressure.

The background pressure while the thruster is operating at a certain Xenon feed flow is larger than the pressure obtained with the same flow of cold Xenon in the tank, probably due to erosion of the walls by the plasma beam. Most of the “extra” pressure is thus probably due to adsorbed species on the surfaces (H2, H2O, etc.) which, due to their small cross section are expected to have little effect on the thruster behavior compared to that of the background Xenon gas. Therefore the following plots are presented as a function of the background Xenon pressure estimated with the measured Xenon pumping speed and Xenon flow, not the actual total pressure measured.

The thruster potential shows significant increase with decreasing background pressures and no asymptote is clearly reached at low pressures (figure 79). This stands in contrast with the behavior of

other thruster types, particularly Hall effect thruster, for which performance at 10^{-5} mbar are representative of real performance, and that show improved performances when the pressure goes up to 10^{-4} mbar. For ECRT, performances increase down to 10^{-7} mbar, and representative performance may even need better vacuum.

In addition, the data from both facilities join remarkably. This suggests that the size of the facility might only have a minor effect on the thruster since thruster potential measurements are usually rather sensitive to most perturbations. For some set-points, measurements were repeated. The majority of points in the "main curve" were taken just a few minutes after the thruster start-up whereas the points that stand below the "main curve" were taken after longer operation time. It seems that there is a trend towards decreased thruster potential when the operation time is increased. This question will be investigated in the next chapter.

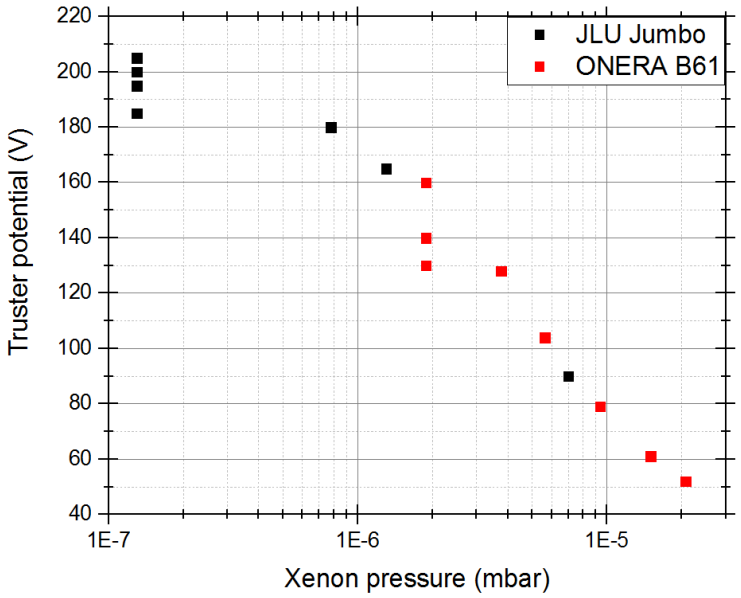

Figure 79. Thruster potential as a function of background Xenon pressure. Black: at Jumbo facility. Red: at B61 facility

The ion energy scan performed with the JLU Parallel Plate Analyzer (PPA) seem to be coherent with thruster potential measurements. Ion energy of 280 eV was measured at Jumbo facility in a regime showing about 200 V of thruster potential (figure 80). This is well above the typical value of about 210 eV measured at B61 facility at a regime showing about 150 V of thruster potential. The same factor of 1,4 is found in both facilities between the thruster potential and the ion energy. These results are also consistent with previous measurement ([24] VI – 5.2.1).

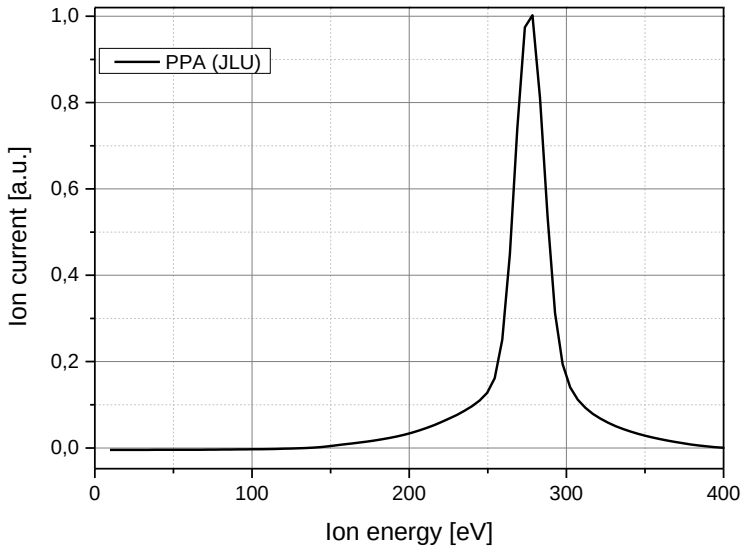

Figure 80. Energy scan with the parallel plate analyzer from JLU.

Ion current and thrust were also measured as function of pressure (figure 81). These curves share common features with the thruster potential curve: increase towards lower pressures, no asymptote clearly reached, and some dispersion of repeated data points. The thrust measured at JLU implies a thruster efficiency at a maximum of 18% at 24 W, 1 sccm. Concerning the comparison of thrust between the two facilities, JLU thrust balance at the Jumbo facility seems to be parallel but $\cong 150$ µN above the data from ONERA balance at B61 facility. Without further measurement it is difficult to say whether this discrepancy should be attributed to:

- one or both of the thrust balances,
- a tank size effect,
- JLU tank gas injection system not reproducing the background density distribution at ONERA,
- an unidentified parameter.

However the good agreement of thruster potential measurements in both facilities (figure 79) does not stand in favor of a facility effect. An issue in one of the thrust measurements seems to be the likelier option. Overall, these measurements confirmed both the performance and behavior of the ECRT. In particular the trend observed at ONERA and elsewhere (for example [95]) that the performance of the ECRT improves when the pressure level decreases is explored a decade lower than existing measurements. Major decrease in performance is confirmed above 10^{-5} mbar.

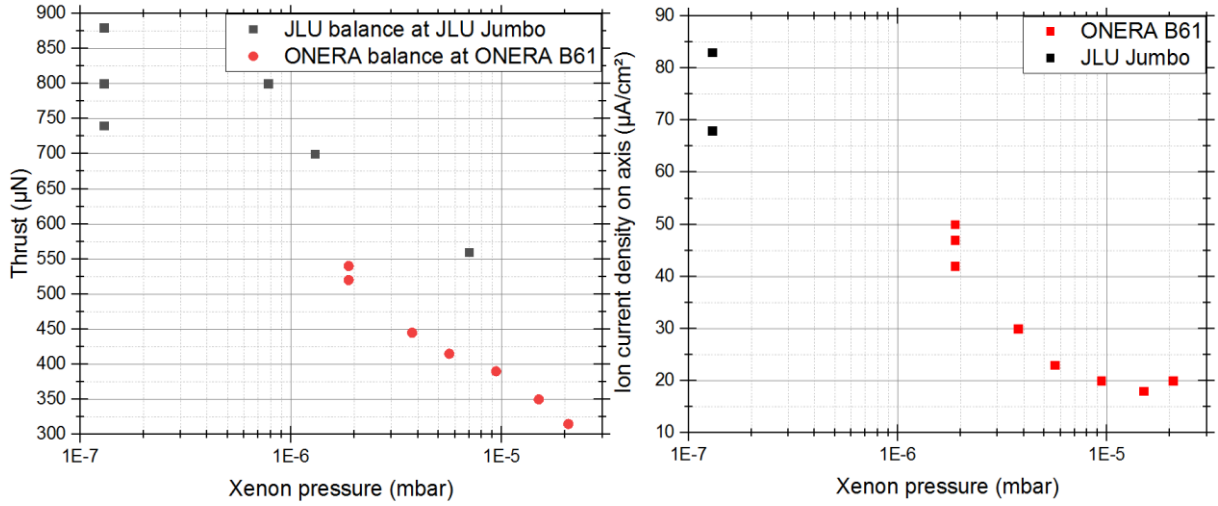

Figure 81. Thrust and ion current density. Estimations of error bars were not available for the JLU balance; ONERA error bars are of the order of the size of the dots ([24], figure 93). Ion current is measured with the gridded Faraday.

4.3 Summary of the results

In this chapter we have assessed the consistency of measurement, first between different diagnostics and second between different test environments. A discrepancy was systematically observed between electrostatic probe thrust measurement and thrust balance measurement. The latter was deemed more trustworthy so we worked under the hypothesis that electrostatic probe thrust measurement is faulty and looked systematically for the source of the error: listing assumptions and checking them one by one. The effect of grids, probe geometry, probe type, and collector material were ruled out. An experiment also concluded that the probe potential does not perturb the thruster's ion current density. In the end, the source of the error was not found and the question of the coherence of thrust measurement methods remains open. The assumptions that are left to check concern the ion trajectories in the nozzle and detachment. To investigate these questions, further work could include measurements with a directional ion current probe and two dimensional LIF measurements.

Experiments carried out at JLU have demonstrated a very encouraging trend of performance increase towards low pressures down to 10^{-7} mbar, where no saturation was clearly reached. This is a peculiarity of the ECRT as compared to other thruster types. The performance measured in vacuum facilities therefore appears as a lower bound for of the performance in space. The thruster potential data from both facilities join remarkably, validating the capacity to control the thruster operation in a different environment. An unexplained discrepancy in thrust was however observed. Besides, dispersion of the data was equally noticed on all diagnostics for a given thruster set-point, indicating a dispersion of the thruster behavior. It is believed that this dispersion is in fact a drift in time towards lower performance. This issue is crucial since stability in time is required, for a good ion accelerator to considered a space thruster. The behavior of the ECRT in time will be investigated in the next chapter.

5. Coaxial ECRT characterization

Outline of the approach. In the previous chapter we have improved our understanding of the diagnostics and of the influence of operating conditions. The goal of this chapter is to further the coaxial ECRT experimental characterization. In section 5.1 we study the thruster behavior in time. First we focus on the transient behavior, in order to explain the time drift of measurement observed in the previous chapter. Second, we tackle the crucial issue of inner conductor erosion, by trying several materials over ~ 20 hours. In section 5.2 we study the effect of the neutral gas injection geometry and the magnetic field topology, as well as the effect of a large metallic or dielectric sheet held in the thruster exit plane. This work paves the way for the design and test of a larger ~ 200 W thruster promising greater efficiencies and whose preliminary results are presented in section 5.3.

Main results. A five hour transient implying variation of plasma quantities by up to 40 % is observed and analyzed. Thruster temperature and tank pressure are identified as main drivers of these variations. Graphite inner conductor is identified as providing relatively high and constant thrust, while limiting erosion as compared to stainless steel and molybdenum inner conductors. The comparison between two different injection geometries reveals only limited differences. On the contrary the comparison between two different magnetic field topologies shows larger differences. The deposition patterns on the backplate are consistent with the existence of an electron bounce movement and low cross field diffusion. A ~ 200 W version of the ECRT is characterized. It is measured, in a preliminary analysis, to consistently provide over 100 hours of operation time, with a constant thrust between 3 and 4.5 mN at the set-point (2 sccm, 105 W).

Content

5.1 Behavior in time

5.1.1 Five hour transient

In order to explain the variation of thrust observed in the previous chapter (figure 81) for a given set-point, the transient behavior of the thruster was investigated; the thruster in table 7 was used for this purpose. The reversible demagnetization of the magnet due to temperature increase was suspected to play a role, therefore a magnetic sensor was designed. It is based on a Hall sensor, whose response is known to vary with temperature, therefore a calibration coil was integrated to provide a reference magnetic field. Before each measurement point, we measure the sensor's response to the magnetic field induced by a 1 A current in the coil in order to calibrate the measurement (figure 82). The temperature is monitored near the sensor but also on the thruster.

Magnet	**Coupling structure type**	**Outer conductor:** - diameter - length - material	**Inner conductor:** - diameter - length - material	**Injection type**	**Backplate material**	**Other**
Small	Coaxial	- 27,5 mm - 20 mm - Al	- 2,3 mm - 20 mm - Stainless steel	Axial	Boron nitride	PTFE coaxial line

Table 7. ECRT configuration used for first magnetic field comparison (see Appendix C.)

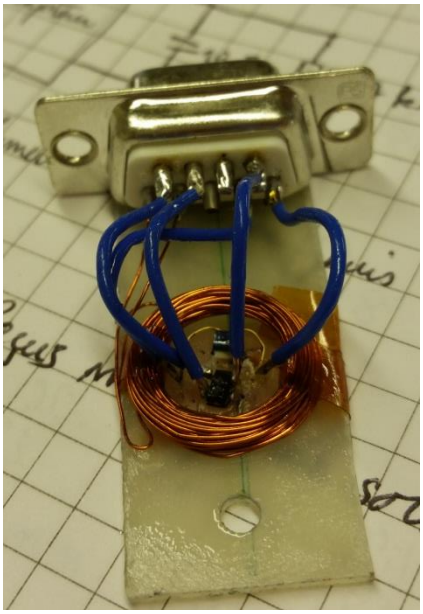

Figure 82. Hall effect sensor AH49F and PT100 temperature sensor at the center of a 50 turn and 1.3 cm diameter calibration coil.

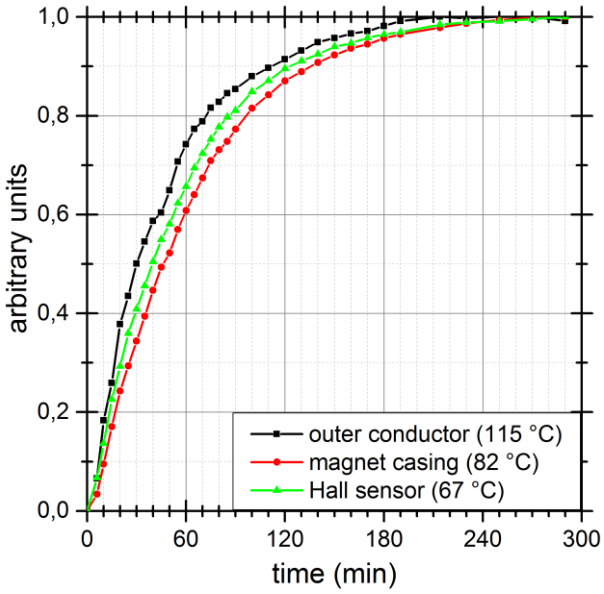

Figure 83. Thermal transients. We plot temperature curves normalized for each part by the difference between the equilibrium temperature and the initial temperature. Equilibrium temperatures are indicated in brackets.

For the outer conductor, 95% of the equilibrium temperature value is reached in 2.5 hours (figure 83). Its equilibrium temperature is higher than that of the magnet casing which is not in direct contact with the heat source (the plasma) and possesses a large radiating surface. Transient profiles show that the Hall sensor temperature and magnet casing temperature have a delay with respect to the outer conductor.

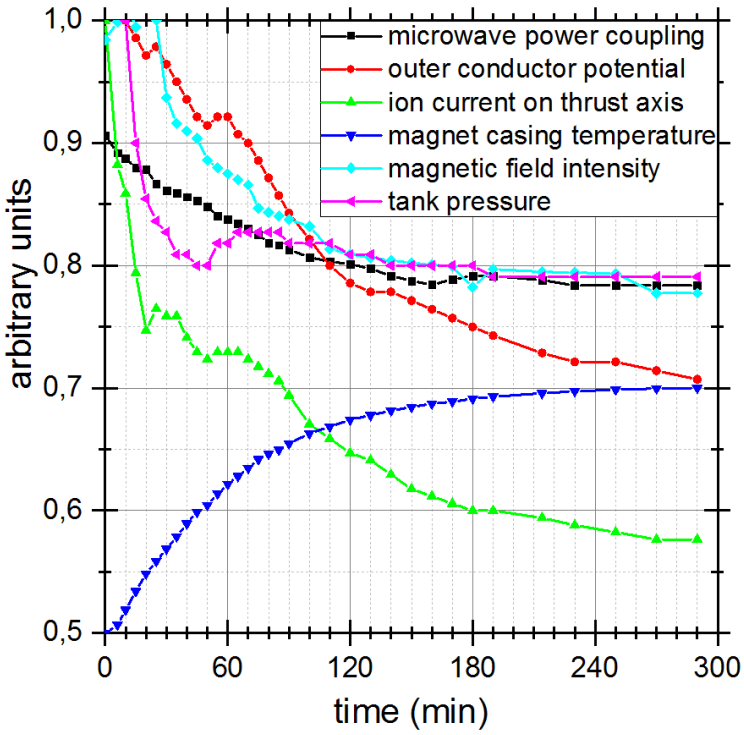

Figure 84. Transient operation of the thruster at 24 W and 1sccm. Microwave power coupling is in real scale. All other curves are arbitrarily normalized.

In figure 84, the thermal transient is seen to correlate with magnetic field intensity and microwave coupling that reach equilibrium values on the same time scale. This is interpreted as temperature demagnetization affecting the plasma-wave interaction in the coaxial coupling structure. The magnet is a sintered Neodymium-Iron-Boron magnet with grade ND35EH. The manufacturer indicates a reversible temperature coefficient of 0.12 %/°C (valid between 20 and 200 °C, with Curie temperature at 310 °C). Hence we expect 7.2% variation of the magnetic field whereas we observe 22%; this discrepancy is unexplained. Whatever the true demagnetization, it implies a very significant change in microwave coupling, from 0.9 at startup to 0.77 in steady state. Future designs could use magnets with lower temperature coefficient (such as Samarium-Cobalt magnets), use a coating (figure 85) to increase emissivity thus decreasing equilibrium operating temperature, and optimize the magnetic field at the this temperature rather that at room temperature. The demagnetization (7.2% to 22%) corresponds to a 3 to 7 mm backward translation of the ECR slab.

Thruster potential and ion current on axis vary by respectively ~ 30% and ~ 40% in the first 5 hours. This observation is consistent with the dispersion of thruster potential observed in the previous chapter for a given set-point (figure 79). These two quantities have a complex behavior since they correlate with tank pressure (and perhaps thruster temperature) but do not reach a steady state, even when pressure and temperature do. Although an instrumental error is possible on ion current measurement, for example due to the probe surface condition, thruster potential measurement is an extremely robust and simple measurement. We are therefore led to believe that thruster steady state is still not completely established even after 5 hours. Progressive material deposition on the backplate (later commented in section 5.2.2) may be responsible. In particular, the metallic deposition obtained for a metallic inner conductor can change significantly the electric boundary condition. No thrust measurements were performed in this experiment because they require shut down of the thruster and subsequent startup, which would likely prevent the observation of a clean transient for thruster temperature and tank pressure.

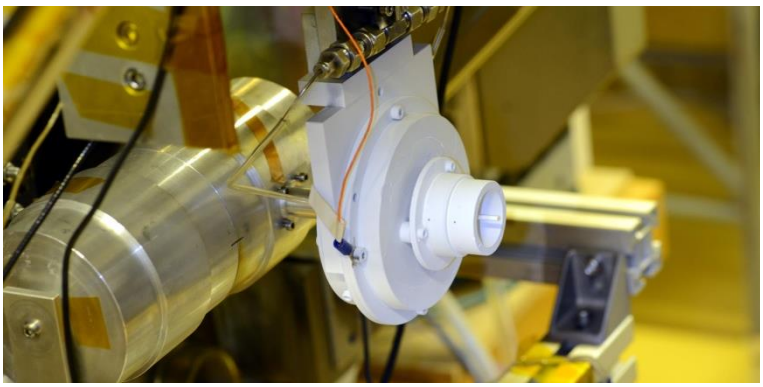

Figure 85. ECRT on the thrust balance fully coated with boron nitride spray.

5.1.2 Lifetime estimate and inner conductor material

Inner conductor erosion was identified in previous work as a challenge for thruster development ([24], section VIII – 2). In this section we vary the inner conductor material of a given thruster (table 7) and measure thrust during 10 to 20 hours of operation-time, without intervention on the thruster. A 50 to 150 µN dispersion is observed. It is unlikely to be related to sources of dispersion previously studied. Indeed, the deposited microwave power and neutral gas flow are adequately controlled and robust to identified perturbations. Besides, the thruster temperature and tank pressure are stable after 5 hours. In spite of this unexplained dispersion, thrust measurements enable to discriminate between inner conductor materials. The material tested are

- stainless-steel,
- Molybdenum,
- graphite,
- BN-sleeved stainless steel,
- BN-sprayed stainless steel,
- BN-coated (pyrolytic) graphite.

Examples of some inner conductor materials, discussed later, are shown in figure 86.

Figure 86. Some of the tested inner conductors. From left to right: boron nitride spray (partly peeled after operation), graphite, pyrolytic boron nitride deposited on graphite. Being translucent but diffusing blue light, this material appears slightly blue on graphite.

Inner conductor erosion was measured by the difference in mass, before and after operation. Since we were concerned about temporary desorption/adsorption perturbing the measurement, we verified that the mass measured just after the experiment was unchanged after a few days at atmospheric pressure. Several materials were tested to design an inner conductor undergoing as limited erosion as possible, while serving its function in the thruster. First, as an element of the electromagnetic coupling structure, it should be a conductor. Second, as an object in contact with the plasma, the surface material is believed to play a critical role, mainly through electron emission and the imposed electric boundary condition (zero local net current for dielectric or zero global net current for a conductor). Indeed, previous experiments led to speculate the existence of a current from the front to the back of a conductive inner conductor. This current would balance a region of dominating electron impact due to ECR heating (the back, see figure 92) to a region of dominating ion impact (the front, where increase erosion was sometimes observed). From the first configuration which was the simple stainless steel inner conductor (used in previous studies), several material were tested.

A pure molybdenum inner conductor was first tested, because it is known as a machinable low erosion metal. The erosion was found to be of the same order as for stainless-steel.

Boron nitride (BN) was also an interesting target for electrode material, because it is well known to undergo relatively low erosion in Hall thrusters and its secondary electrons emission coefficient by electron impact is known to be favorable to plasma sources. However, the core of the inner conductor should be a conductor. To this end, a machined BN sleeve was manufactured; it was adjusted to stainless steel inner conductor, completely covering it with 0.5 mm thickness. The thrust obtained was lower than for the reference stainless-steel conductor. A possible cause was that the intense electric field, likely existing near the inner conductor, was propagating inside the BN sleeve rather than inside the plasma, thus reducing electron heating.

A possible solution would be to reduce the thickness of the wall, but machining is very difficult for a smaller thickness. To obtain a thinner BN wall, two solutions of coating were tested: BN spray and pyrolytic BN coating. At this point, the fact that BN could only be used as a thin layer was already a

drawback compared to a plain inner conductor, since it decreases the lifetime by erosion. However, depending on the erosion rate it could still be a relevant solution. A BN spray was used (Jelt, 5095 – vernis nitrure de bore) to deposit a coating about 100µm thick. It was made of about 10µm BN particles (observed in a binocular microscope) loosely sticking after the solvent has evaporated. The coating was made uniform by continuous rotation of the inner conductor during the deposition and drying process (using a modified drill). Using this inner conductor, no loss of thruster performance was observed proving that a BN coating could potentially reduce sputtering. However two issues were identified. First, the purity of the boron nitride was unknown, along with the possible presence of solvent residue, altering the performances. Second, the BN particles were so loosely attached that it resulted in peeling of the coating during thruster operation (figure 86).

In order to move away from these issues, a real BN coating was desired. After investigation, only pyrolytic deposition of BN (99.9% purity) on graphite was found to be possible, which led to imagine the use of graphite for the inner conductor. Although graphite has very good properties for sputtering [101], as good as BN, it had never been thought of as a proper material for the coupling structure, because it is a resistive material. However, in a parallel study at ONERA [102], a coupling structure made of graphite was utilized in the ECRT for its resistive nature in order to minimize eddy currents for the development of a diamagnetic loop diagnostic. Although performance was not the main focus, it did not seem to decrease, indicating graphite could be used for the thruster.

A pure graphite inner conductor was therefore tested for reference and showed significantly lower erosion than stainless steel while not decreasing performance or coupling. Then, thin boron nitride deposition (50 to 100 µm of pyrolytic BN) on the graphite inner conductor was investigated[5] (figure 86). The thruster performed poorly, which is surprising in comparison with the boron nitride spray. The coated outer conductors were also tested, but did not lead to performance increase. The use of BN coating was dropped. The results concerning inner conductor material are summarized in table 8 and figure 87.

Material	Mass loss for 1 hour (in % of total mass)	Sputter rate (in 10^{15} atom/s)	Extrapolated lifetime (hours)	Thrust (µN)
Graphite	0.11	2.6	≅ 1000	530
Boron nitride spray	not measured			530
Stainless steel	0.73	9.1	≅ 150	470
Boron nitride sleeve	not measured			≅ 400 [6]
Boron nitride coating	0.03	0.88	≅ 800	350
Molybdenum	0.52	5.5	≅ 200	not measured

Table 8. Test of inner conductor material. For mass loss measurement, each configuration was tested about 20 hours except graphite, 60 hours. As a first approximation we estimated life lime as the duration required to consume the entire inner conductor at this constant rate.

[5] The only company that could be found to perform such a coating was Stanford Advanced Ceramics in California, at the expense of a high cost and 5 months lead time. We first had several inner and outer conductors manufactured in S100 graphite and then sent for coating.

[6] Only one measurement was made at this reference set-point instead of several.

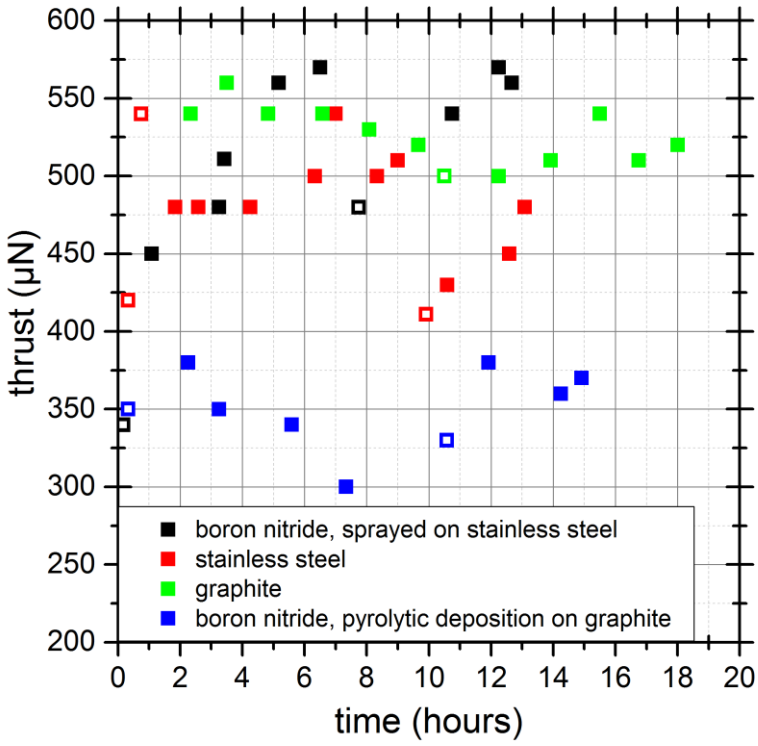

Figure 87. Thrust measurement for several inner conductor material or coatings. Hollow symbols indicate the first measurement point after startup with a cold thruster. The measurements bear a systematic error that may offset all points by up to ± 4%[7].

Overall, the thruster with graphite inner conductor stands out as the best option. It is plain material exhibiting relatively large thrust and low dispersion, in addition to relatively low erosion. Graphite inner conductor was therefore specifically studied for up to 67 hours at 24 W and 1 sccm. Its mass was measured to be linear with operation time and to decrease by 0.11 percent of initial mass per hour (figure 88). Note that Vialis showed that performance is unchanged when the diameter of the inner conductor is increased beyond the 2.3 mm, used in most of this work ([24], figure 116). Thus the lifetimes presented in table 8 likely underestimate the lifetimes obtained with an optimized diameter.

[7] Thrust error bars in this graph and some of the followings are not displayed since the error is constant through tested configurations. The 4% *systematic* error is irrelevant for such a relative comparison.

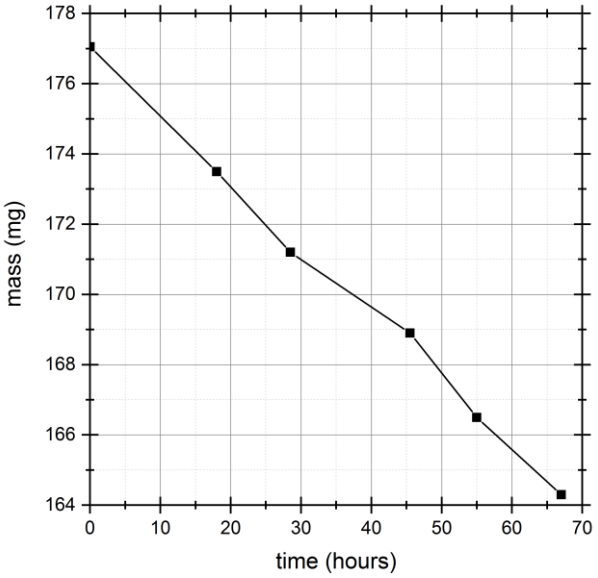

Figure 88. Mass of the graphite inner conductor as a function of operation time typically at 1 sccm and 24 W.

It is difficult to compare these results with existing data in the literature because the sputter yield seems to vary considerably in the energy range of interest. For example the sputter yield (in atom per ion) for Xenon impinging on Molybdenum was measured to vary by a decade between 70 eV and 200 eV. Besides, in this range, the sputter yield on Carbon was measured to have the same shape as a function of energy, however about a decade lower as compared to Molybdenum [101]. We observed instead only a factor two between graphite and Molybdenum (table 8). This discrepancy between our measurement and the cited data is likely explained by a significant influence of the inner conductor material on the plasma as indicated by the difference in thrust observed for several materials. The modification of the plasma by the inner conductor material may modify three factors identified to influence sputter rates: incidence angle, energy and flow. Since incidence angle is unlikely to play a significant role at low energy ([103], figure 22), graphite may undergo lesser plasma flux or lesser ion energy. Although flux seems difficult to measure the energy can be estimated: it is the difference between plasma potential and inner conductor potential. Plasma potential is known already through ion energy measurement in the plume. Therefore we are interested in the inner conductor potential.

In the following section 5.1.3 we present a characterization of the inner conductor and its role. This work has helped us in our search of a better performing inner conductor.

5.1.3 Role of the inner conductor

5.1.3.1 Inner conductor electric potential

The coaxial-to-waveguide transition that is part of the microwave line can provide access to the inner conductor potential. Several solutions were tested to pick up the inner conductor potential while minimizing perturbation on microwave transmission. It appears that a wire placed as in figure 89 only causes 1.5% additional reflection and 2.5% additional dissipation. In addition, an electrical resistance of 300 kΩ is found to limit the wire heating. Indeed if too conductive, the wire was found to melt.

It is observed with this setup that the inner conductor potential is lower than the outer conductor potential (simply called thruster potential in this text, except in this section) (figure 90). In addition, the bulk plasma potential estimated with ion energy is above both wall potentials, hence a non-monotonous radial profile of the electrical potential, with sheathes at the walls (figure 91). Although their thickness was

not measured, the constant mean ion energy observed in the plume suggests that they are thin compared to the distance between walls.

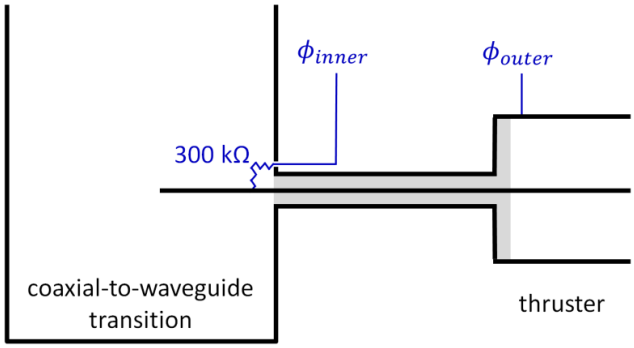

Figure 89. Inner conductor potential measurement setup.

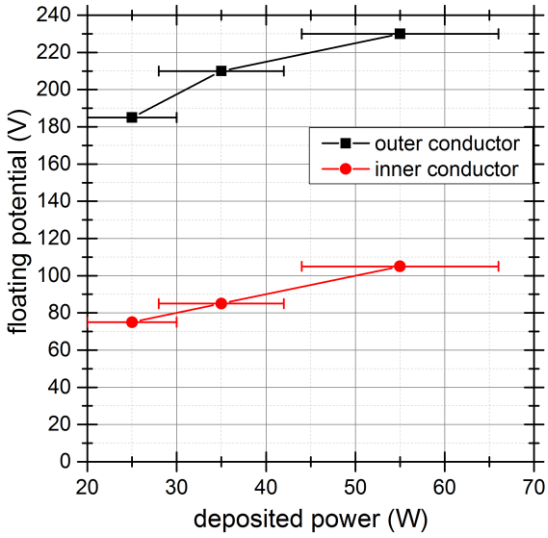

Figure 90. Electrostatic potential at the walls

When operating at high microwave deposited power relative to neutral gas flow, the inner conductor is sometimes observed to glow (figure 92). This observation raised the question whether sublimation is of importance in mass loss. The possibility of sublimation was ruled out because of very close stainless steel and Molybdenum mass losses (table 8) whereas they have very distinct melting points (resp. 1500 and 2600° C) and boiling points (resp. 2900 and 4600 ° C). The inner conductor variation in brightness suggests that the heat flux reaches a maximum 5 to 10 mm from the backplate. This is consistent with the microwave absorption taking place quite locally in the rear half of the coupling structure.

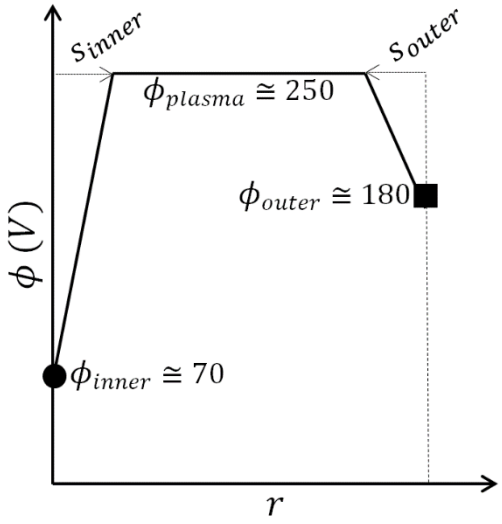

Figure 91. Sketched radial potential profile in the coaxial structure for a typical test condition.

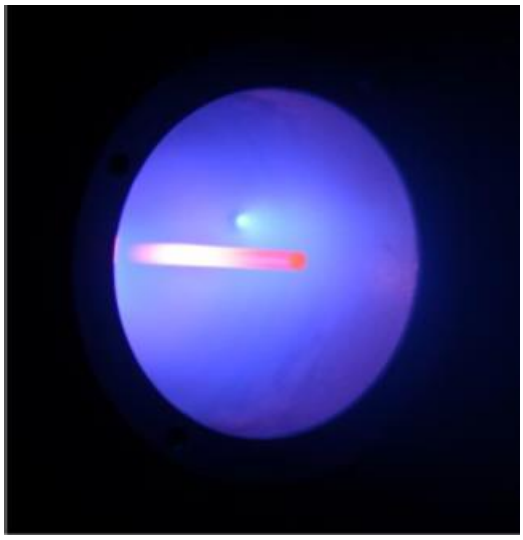

Figure 92. Inner conductor glowing with a gradient in temperature along its main axis.

5.1.3.2 Inner conductor length

The microwave coupling was measured for several inner conductor lengths, for a stainless-steel inner conductor. The results support the idea that coupling takes place in the first few millimeters at the rear of the coaxial structure. If coupling were the only requirement, the inner conductor length could be

below 10 mm (table 9). However, faster heating (glowing) is observed in the case of the 10 mm inner conductor. A possible explanation is that lengthening the inner conductor provides increased radiating surface thus facilitating thermal management.

Length (mm)	20	10	1
Coupling	0.70	0.70	0.05

Table 9. Effect of inner conductor length on microwave coupling. Outer conductor length: 15 mm. Non-ideal conditions are used: coupling is usually close to 90% with 20 mm inner conductor.

Concerning outer conductor length, an optimum for outer conductor length was previously found at 20 mm [24] which is the length used in most experiments of this study. In addition to electromagnetic coupling, the outer conductor is confining plasma and neutral gas. The optimum length was interpreted as a tradeoff between neutral gas confinement and plasma losses.

5.1.3.3 Thruster electromagnetic emission

In order to justify the calculation of deposited microwave power as $P_D = \gamma P_I - P_R/\gamma$ (section 3.2.3) we verified that no power is radiated in the tank by the coaxial structure. Analytical calculation of the power radiated by the open end of the thruster in the absence of plasma and with inner and outer conductor cut in the same plane yields a value below 1% ([104], equation 15). This result is in agreement with COMSOL simulation of the electromagnetic field radiated by the thruster in a half sphere in front of the thruster, covered with a perfectly matched layer[8]. These calculations hold only in the absence of plasma, thus experimental measurements are required to make sure that the presence of plasma in the coaxial structure does not enable radiation.

These measurements were conducted with a ~ 5 mm diameter loop antenna that was built at the end of a SMA coaxial cable (figure 93) placed inside the vacuum tank and connected to a spectrum analyzer. Note that placing the antenna outside the tank in front of a viewport, or changing the antenna orientation, gave the same results. For this measurement, we could not use coaxial-to-waveguide DC isolation because the ~ 1% power radiated by the two faced waveguides would interfere with the measurements. A closed coaxial DC block was used instead.

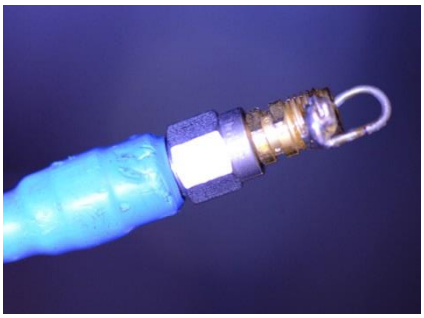

Figure 93. Small antenna used for measuring the electromagnetic environment near the thruster.

Measurements were performed in three cases. First, with the microwave power fed to the thruster, but no plasma. Second, with the microwave power and plasma. Third, without plasma or microwave power, to have the response of the spectrum analyzer in ambient electromagnetic signal.

With the thruster turned on (microwave and plasma), no signal was observed in the range 30 kHz – 3 GHz, except for the signal from the microwave generator (figure 94). We did observe broad emission

[8] For some thruster configurations the inner and outer conductors are not cut in the same plane but rather the inner conductor extends 5 mm longer. In this case the radiated power fraction simulated with COMSOL is larger but less than 10%, thus the conclusion of this subsection still holds in this case.

between 2.4 to 2.46 GHz (red curve), probably by the plasma, but at a negligible level (50 dB below the peak). We also noted a jitter of the microwave frequency during measurements, due to the generator. The main peak with plasma was about - 20 dB with respect to the peak observed in the absence of plasma, this peak itself being known to be -20 dB of the incident power, through analytical calculation and simulation[9]. It is therefore concluded that the radiated power fraction in the presence of plasma is of order - 40 dB (or 10^{-4}) hence it is justified to neglect radiation in the power deposition calculation.

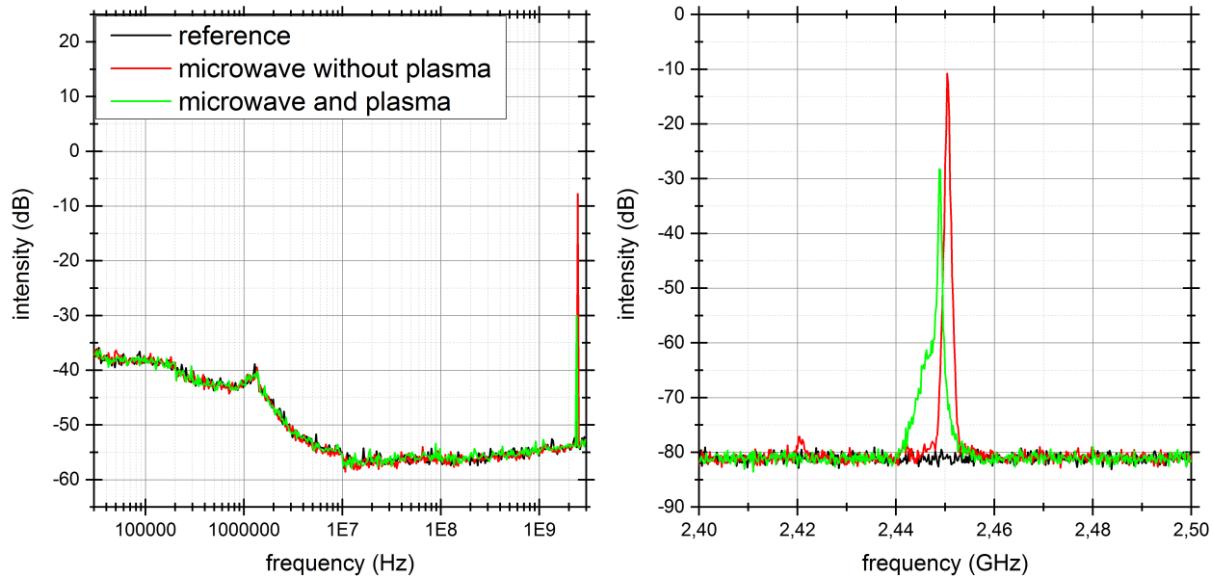

Figure 94. Radiated power in the tank.

5.2 Design optimization

5.2.1 Injection

Gas injection was suggested as an area for improvement in previous development work [24]. A different injection was designed with the intention that gas be tightly conducted up to the plasma and that no discharge would occur in the gas line (section 3.3). A radial injection instead of axial injection (initial velocity of neutral gas along $\boldsymbol{e_r}$ instead of $\boldsymbol{e_z}$) was more practical to satisfy these constraints. The gas is injected through 6 azimuthally-distributed 0,5 mm square-ducts instead of two circular tubes with 1 mm diameter. The total "injection area" is thus approximately conserved. The compared thrusters are identical except of the injection and the thruster with radial injection is that of figure 51b. Injection locations are schematically recalled in figure 95.

[9] As demonstrated in section 3.2.3, measurement with directional couplers would be irrelevant here: with such reflected power fraction, the uncertainty is prohibitively large.

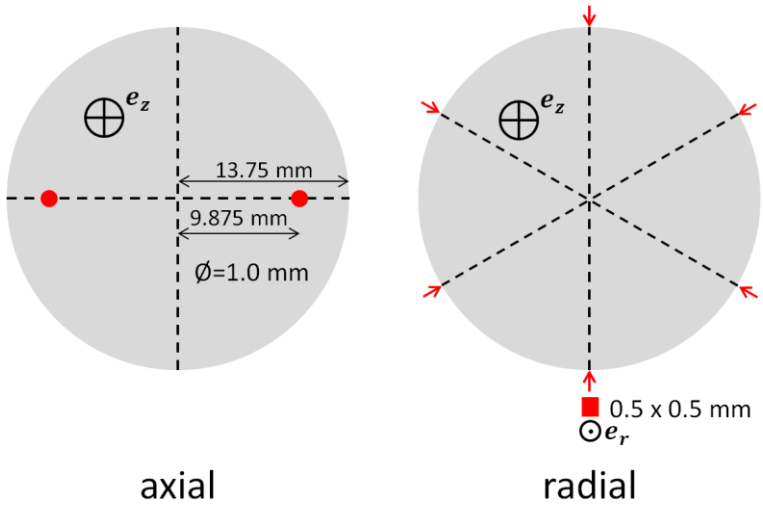

Figure 95. Schematics of tested injections. The grey disk is the surface of the backplate. Radial injections are in a plane parallel to this surface and distant of 1 mm.

Both injections yield similar ion current profiles and slightly different thrust levels (Figure 96, Figure 97). The axial injection provides about 50 µN more thrust, corresponding to 10% relative difference. This difference may come in part from the cold gas thrust, estimated by thrust balance measurement to be 40 µN in the case of axial injection and about 15 µN in the case of radial injection. Measurements performed with other thruster configurations, such as with the big magnet, gave similar results.

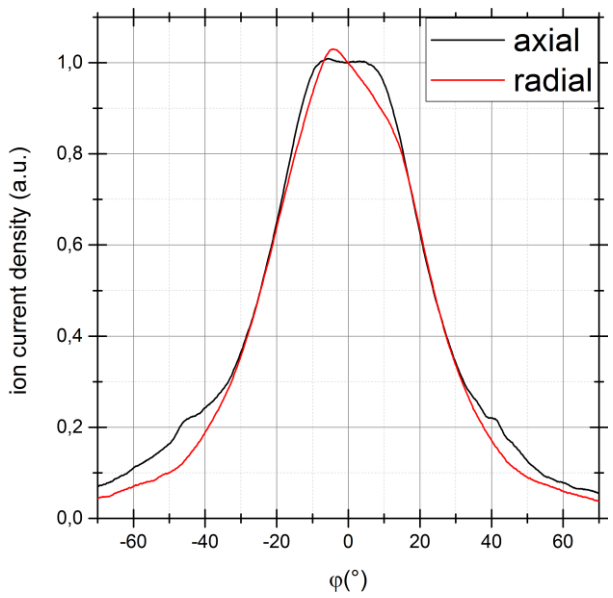

Figure 96. Angular profiles (thruster configuration in table 7, except for big magnet instead of small magnet).

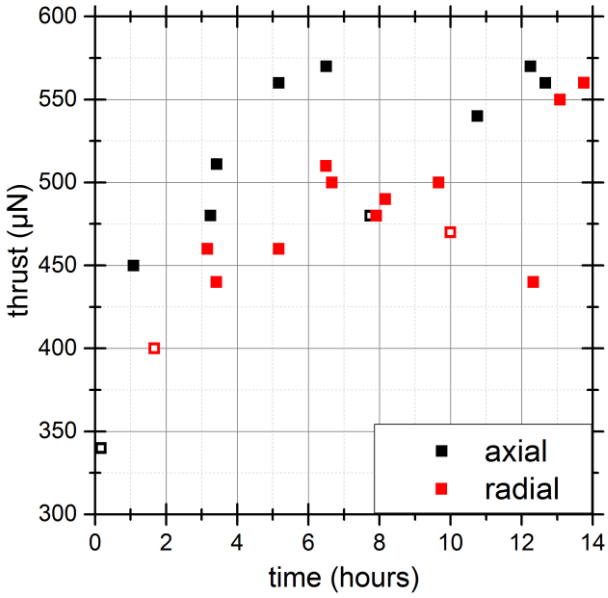

Figure 97. Thrust (thruster configuration form table 7 except for the inner conductor being covered with boron nitride spray). Hollow symbols indicate the first measurement point after startup with a cold thruster.

5.2.2 Imposed magnetic field topology

Magnetic field was suspected in previous work to have significant effect on thrust [24]. However, in the tests that were conducted either several parameters were changed in addition to the magnetic field, or one magnetic configuration could not be tested on a thrust balance (because it was a coil generated

magnetic field requiring large cable and water cooling). That coil thruster seemed to perform very well therefore a permanent magnet was designed to reproduce the magnetic field of the coil.

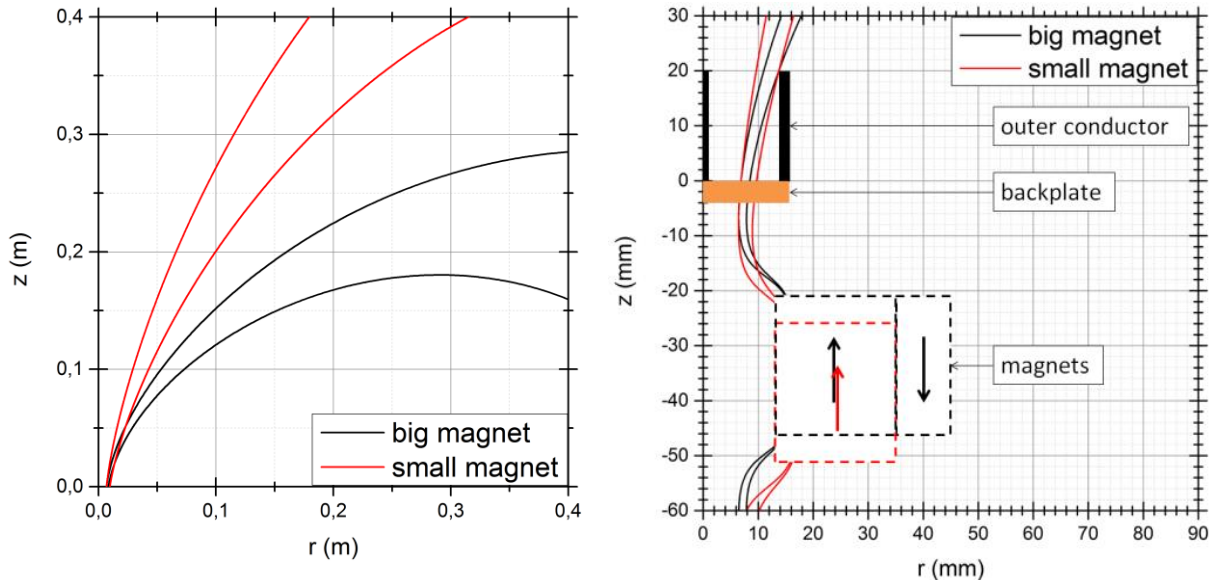

Figure 98. Magnetic field lines. For each magnet, we plot the field line going through the middle of the backplate radius ($r = 6,875$; $z = 0$) mm and that going through the tip of the outer conductor ($r = 13,75$; $z = 20$) mm. Arrows represent magnetization.

Several solutions were considered and simulated using COMSOL software with either radial or axial magnetization. The main constraints of the magnet design were to conserve a central hole for the microwave cable going to the thruster and to optimize the weight. The chosen solution for the more divergent, "coil-like" magnet, also called "big magnet", features two ring magnets with rectangular section and reversed axial magnetization of 955 kA/m (grade ND35EH). The reversed magnetization of the outer magnet encourages divergence of the magnetic field. This two-magnet system is called the "big magnet" in the rest of the text. It will be compared with the so called "small magnet", which was the standard available magnet at the beginning of this study (figure 98, figure 99). Note that the inner magnet of the big magnet is actually the small magnet. The magnets were manufactured on-demand for size and magnetization. Assembly of the two magnets proved challenging given the force and torque between them. A special casing helping assembly was designed, and after several tries the operation was done in water: the small clearance between the magnets and the casing provided underwater a damping force which allowed controlled and smooth assembly.

The thruster configuration used here is that of table 7 except for an outer conductor of 15 mm in length, and small or big magnet.

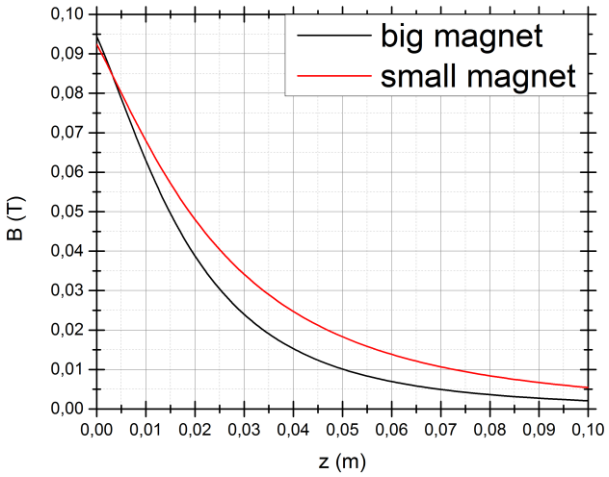

Figure 99. On-axis magnetic field norm.

Thrust measurements performed with the two configurations showed about 100 µN difference in thrust, representing about 20%, which leads to about 44% difference in total efficiency: the big magnet significantly outperform the small magnet (figure 100). It should be noted that the 20% found here contrasts with the 40% difference between the small magnet and the coil, measured using electrostatic probe estimates ([24], figure 98). This discrepancy is now thought to come primarily from overestimate of probe measurements (section 4.1.1).

The comparison was also performed with a different thruster configuration described in table 10. It confirmed the difference between magnets, with 410 µN and 500µN for the small and big magnet respectively. These figures are averages, at 24 W of deposited power and 1 sccm Xenon.

Magnet	**Coupling structure type**	**Outer conductor:** - diameter - length - material	**Inner conductor:** - diameter - length - material	**Injection type**	**Backplate material**	**Other**
Small or Big	Coaxial	- 27,5 mm - 20 mm - Al	- 2,3 mm - 20 mm - Stainless steel with boron nitride spray	Radial	Boron nitride	

Table 10. ECRT configuration used for second magnetic field comparison (see Appendix C.)

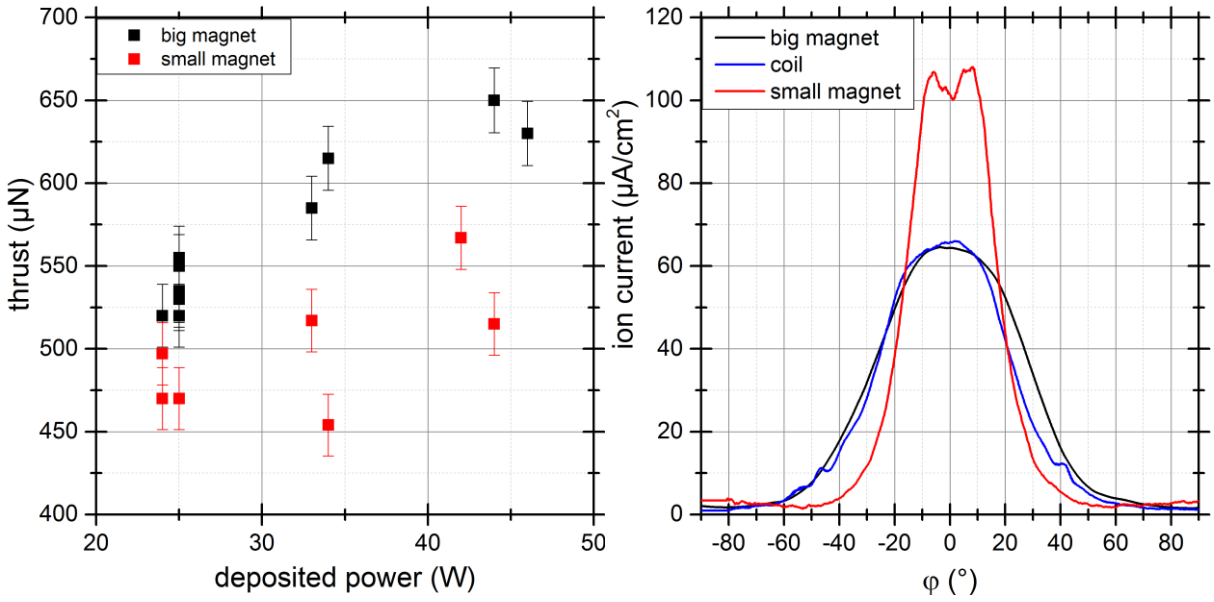

Figure 100. Comparison of magnetic field topology at 1 sccm[10]. Right: ≅ 30 W.

We observe that the ion current density angular profiles are strongly affected by the magnetic field divergence, and that the big magnet profile is similar the coil profile, as was sought. The local minimum in the center of the small magnet profile may be interpreted as the shadow of the inner conductor smoothed by diffusion. This local minimum is absent in the big magnet profile, maybe because of increased diffusion in this case.

Material deposition on the backplate also illustrates the crucial influence of the magnetic field, and more specifically that the plasma is strongly tied to the magnetic field, at least for z locations where the field is intense enough. Figure 101 is a picture of a thruster configuration with two forward gas injection holes facing backward, that was used for gas injections studies not presented in this work. It was run for several hours, with the backplate exhibiting a pattern of three concentric rings. The main white area looks as it was before performing the test, whereas some brownish material seems to be deposited in a peripheral ring and in a fainter central ring surrounding the inner conductor. A reasonable explanation for this observation is the following. While the thruster is running, material sputtered from the inner conductor is uniformly deposited on the backplate. This deposition is simultaneously eroded by the plasma. In the main white ring, the erosion rate is greater than the deposition rate because dense plasma is present, whereas near the walls the deposition rate is greater than the erosion rate. Two factors may contribute to this phenomenon. First, the presence wall sheathes implies lesser plasma density, hence a lesser eroding flux. Second, the magnetic field topology implies plasma depletion in the peripheral region because magnetic field lines from this region intercept the outer wall. Measurement of the outer radius of the main white ring shows that it is a section of the magnetic tube that goes through the exit section of the thruster. The fortunate presence of two ergots on the exit section and their associated "shadows" contribute to support this interpretation. *This observed deposition receives a coherent explanation if we suppose that the plasma is strongly guided by the magnetic field lines and electrons undergo a bounce movement.*

[10] Power error bars are not mentioned because the microwave line is identical in both cases thus the 20% *systematic* error is irrelevant for such a relative comparison. Thrust error bars are mentioned however, since by changing the magnet we change the pendulum equilibrium position, thus generating an uncertainty on the calibration (section 2.3.4.3).

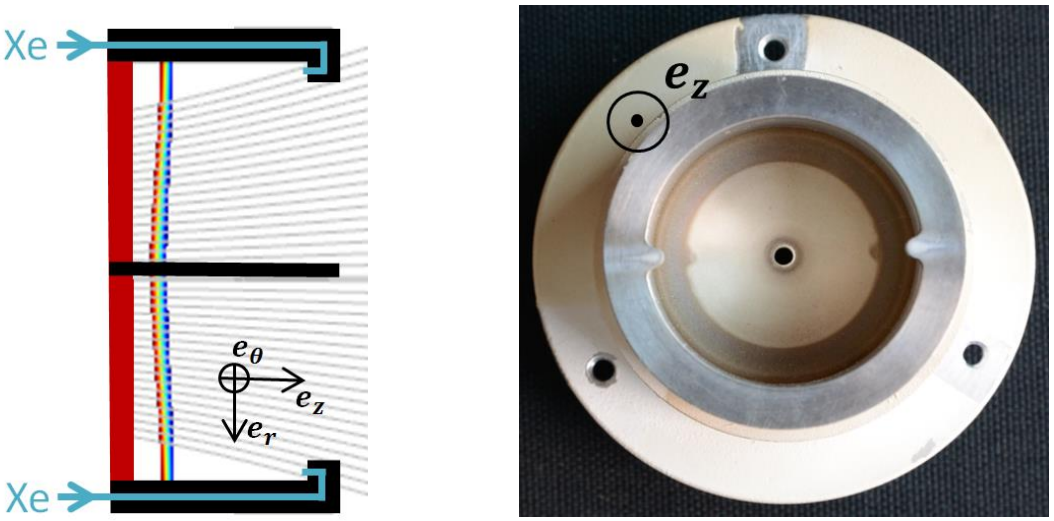

Figure 101. Deposition on the backplate in the shadow of the front section of the thruster structure. Big magnet. Inner conductor material: boron nitride on stainless steel.

The material deposition on the backplate was proved to come mainly from the inner conductor by electron X-ray fluorescence on the backplate deposition by a laboratory at ONERA. For this a specific ECR test was performed, using a stainless steel inner conductor and an aluminum outer conductor to identify the source of the deposit.

In figure 101, the brownish color is likely the sign of a boron deposition; a boron nitride sprayed inner conductor was indeed used in this case. For comparison, several other typical sputter deposition patterns for axial or radial gas injection are shown in Figure 102. When comparing figure 101 with figure 102a we see that these patterns are to some extent independent from the injection; however not completely: we observe in figure 102b the appearance of two additional deposited areas with a crescent shape, in comparison with figure 102c. A possible interpretation is the following. The graphite inner conductor implies moderate sputtering rates (table 8) hence the plasma density in the main white ring is sufficient to erode the deposited material (figure 102c). On the contrary, the stainless steel inner conductor implies enhanced sputtering rates that reveal two areas of intermediate plasma density that are able to wipe out carbon deposit but not iron deposit (figure 102b). The shape and position of those areas suggest the existence of slightly higher plasma density in the vicinity of the injection holes.

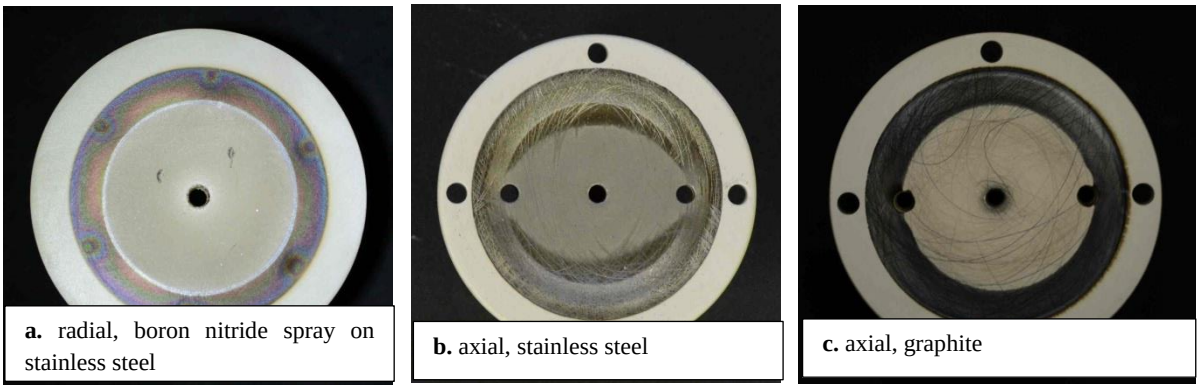

a. radial, boron nitride spray on stainless steel

b. axial, stainless steel

c. axial, graphite

Figure 102. Backplate depositions. Big magnet. Labels indicate injection type and inner conductor material.

5.2.3 Plate in the exit plane

In the course of our investigation regarding the comparison between thrust balance measurement and electrostatic probe measurements (section 4.1) we carried out the experiment with a dielectric or metallic plate mounted in the thruster exit plane, with electrical and mechanical contact with the thruster (figure 103). It was performed with the thruster specified in table 11 and measurements are presented in table 12.

Magnet	**Coupling structure type**	**Outer conductor:** - diameter - length - material	**Inner conductor:** - diameter - length - material	**Injection type**	**Backplate material**	**Other**
Big	Coaxial	- 27,5 mm - 15 mm - Al	- 2,3 mm - 20 mm - Stainless steel	Axial	Boron nitride	Boron nitride coaxial line just before the ECRT

Table 11. ECRT configuration used for the measurement with a plate (see Appendix C.)

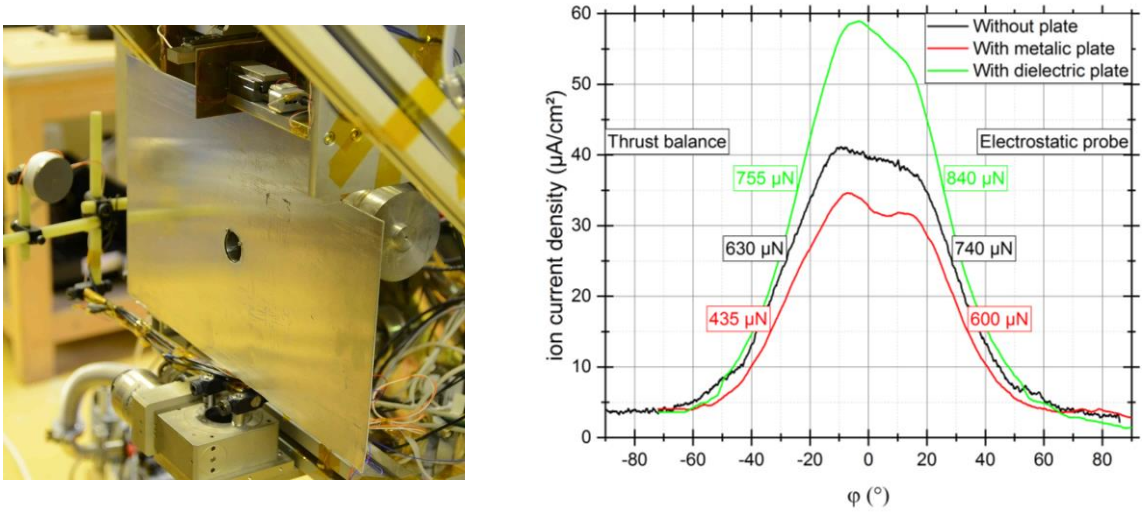

Figure 103. Measurement with a metallic plate in the thruster exit plane.

In table 12 we observe that the ion energy keeps constant in all cases, indicating constant plasma potential in the coupling structure, where ions are mostly created. We also observe that the thruster and plume (figure 103) are perturbed as a whole. In particular, when we go through tested configurations in the table we observe an increasing total ion current correlated with an increasing thruster potential. The interpretation for the correlation between those quantities could be the following. With constant plasma potential and increasing thruster potential, we have a decreasing sheath potential drop (to the outer conductor wall) which may be the reason for decreased ion losses, hence increased ion current in the jet when we go through the tested configurations in table 12.

Plate	**Total ion current (mA)**	**Thruster potential i.e., of the outer conductor (V)**	**Ion energy (eV)**	**Thrust from electro-static probe (µN)**	**Thrust from thrust balance (µN)**	**Ensuing total efficiency (%)**	**Discrepancy in thrust (%)**
Metallic	34	65	250	600 (-19%)	435 (-31%)	4	28
Without	42	150	N.A.	740	630	8	15
Dielectric	48	210	240	840 (+13.5%)	755 (+20%)	12	10

Table 12. Measurements with a plate mounted in the thruster exit plane. The ion energy without plate was not measured.

Regarding the variation of thruster potential in these experiments, a possible interpretation is the following. There exists a small plasma flow that goes around the thruster because it is attached to the magnetic field. In the absence of a plate, part of this flow encounters obstacles from the set-up, and part of this flow impacts the thruster from the rear side (slight erosion marks on the rear side of the magnet casing are consistent with this claim). When a metallic plate is present, the thruster collects all this plasma flow instead of just the latter part, thus lowering the thruster potential. Indeed, a few tens of centimeters away from the thruster, the plasma potential is only of a few tens of volts. On the contrary, when a dielectric plate is present, the plate collects this plasma flow thus isolating the thruster from the fraction that would impact it in the absence of the plate.

This interpretation would imply that for a dielectric plate the same result is obtain whether the plate be in mechanical contact with the thruster or not. On the contrary, a rival interpretation based on ion momentum flow impacting the plate predicts a difference between these cases. This test should be made in the future. Let's note for the moment that the presence of a dielectric plate in the exit plane significantly improves performances.

5.3 Towards higher efficiency and higher power

The work reported up to this point in this dissertation was the basis for the design of the thrusters thereafter presented and the author was involved in design choices. However, Victor Désangles is acknowledged as the main contributor and the results presented in this specific section are the product of team work. Experiments were performed in July 2020 by Victor Désangles, Patrick Dietz, Julien Jarrige, Denis Packan, Simon Peterschmitt Steffen Scharman, and Jana Zorn, under the framework of the H2020 "MINOTOR" project.

From the measurements that will be presented, it is apparent that efficiencies are much higher than for the previous versions tested at ONERA, and erosion of the inner conductor is significantly lower. However, the results available to date are preliminary and will require further measurements in order to increase confidence in the numbers and to identify the respective contribution of the several design changes to the overall increase of performance. Measurements were performed in the JLU Jumbo facility, already presented in section 4.2. Several ~ 30 W and ~ 200 W thruster configurations were tested.

5.3.1 Improved ~ 30 W thruster

The ~ 30 W thruster design whose performance is partially presented here, combines several features that were shown in this chapter to improve performance. It features a coupling structure entirely made of graphite, a plate in the exit plane, a radial injection and an advantageous magnetic field topology. The thrust obtained is mapped in figure 104. The thrust is up to 2.2 mN and is quite independent of mass flow rate thus the thruster efficiency is higher at low mass flow rates: a maximum of about 0.50 for the thruster efficiency is measured at 0.8 sccm and 35 W. For the specific impulse, a maximum of about 2600 s is obtained at 0.6 sccm and 45 W.

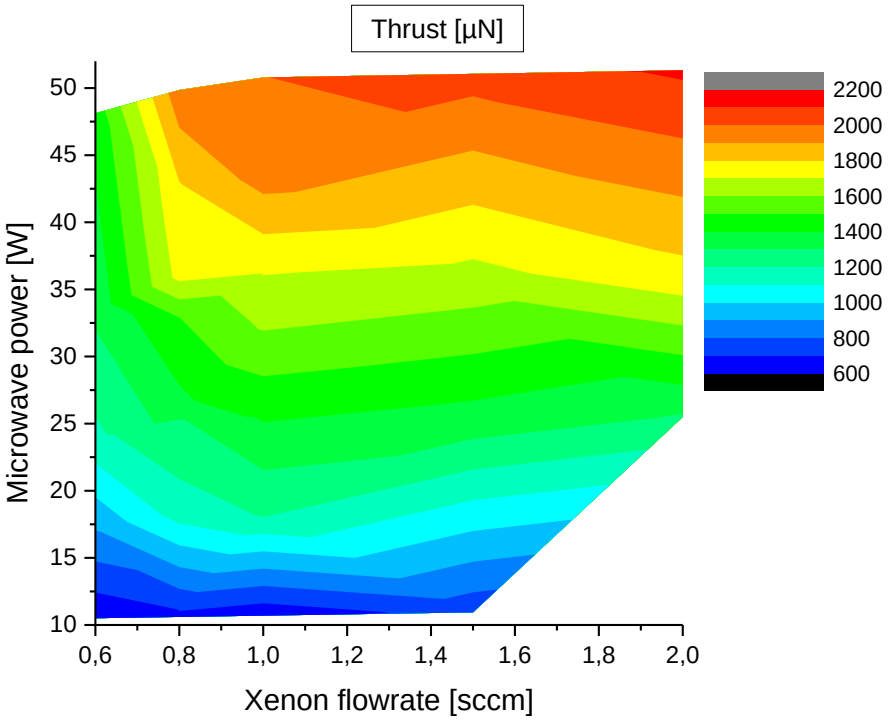

Figure 104. Thrust as a function of set-point for the best performing ~ 30 W thruster at JLU Jumbo facility.

5.3.2 Exploration of a ~ 200 W thruster

5.3.2.1 Presentation of the thruster

The design and test of the high power version of the thruster was in fact an initial goal of this thesis; it benefits from the improvements presented in the different chapters, in particular removal of nearly all connectors from the vacuum microwave line to prevent arcing and material analysis (magnet, inner conductor, plate). Several thrusters were designed for ~ 200 W (instead of 30 W), as a first step to explore higher powers. The interest is at least twofold: to compare the performance of the ECRT to the clear tendency of EP devices of increased efficiencies when scaling up; and to provide insight on the general behavior of the thruster.

The design of the ~ 200 W version (figure 105) is based on that of the ~ 30 W version, keeping constant the microwave power per unit area. The ~ 30 W ECRT is 27.5 mm in diameter, (i.e. an open end area of 5.94 cm^2) corresponding to a power per unit area around 5 W/cm^2, with a Xenon flowrate between 0.6 and 1 sccm. The so-called ECR-200-PM5 version are 70 mm in diameter, with an expected operating flow rate in the range [3.5 ; 6] sccm. The gas is injected radially through several holes close to the backplate. For reasons specific to mechanical design the backplate is in fact made of two parts, appropriately adjusted. The microwave connection on the thruster is similar to that presented in figure 51. A new Samarium-Cobalt permanent magnet (PM5) was designed with an axial magnetization and annular shape (98 mm outer diameter, 18 mm inner diameter, 17 mm width). As previously mentioned a Samarium-Cobalt magnet reduces temperature demagnetization as compared to Neodymium magnet. Its weight is less than 1kg, thus it is not significantly more than the 30W thruster. A specificity as compared to ~ 30 W version is that the outer conductor can be easily extended with a cylindrical or

connical part. Several ~ 200 W configurations were tested where the inner conductor, outer conductor, and extension varied in shape or material.

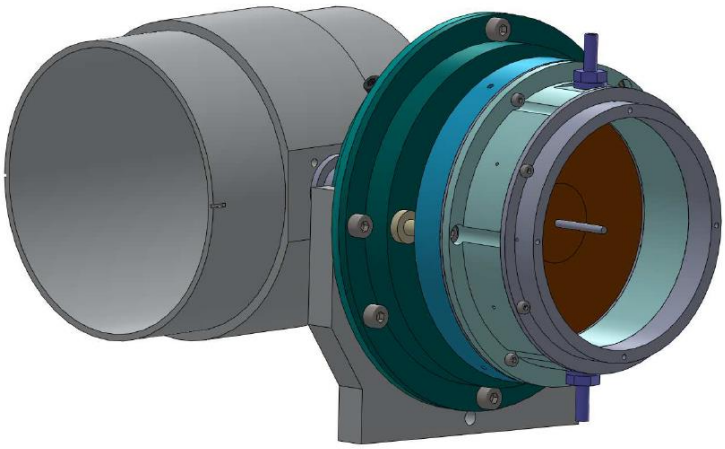

Figure 105. ECR-200-PM5 thruster (with a cylindrical outer conductor and extension) connected to a coaxial-to-waveguide transition.

In the rest of the section we will focus on the best performing configuration, the so-called ECR-200-PM5-V4 benefiting from the developments described in previous sections: it is equipped with a coupling structure entirely made of graphite and a dielectric FR4 plate extending in the exit plane. Besides, in the wake of previous developments [24], the outer conductor is extended with the intention to increase neutral gas confinement. It is conical to avoid intercepting magnetic field lines thus limiting additional losses. In order not to disclose the details of the ECR-200-PM5-V4, we show a slightly different configuration in figure 106.

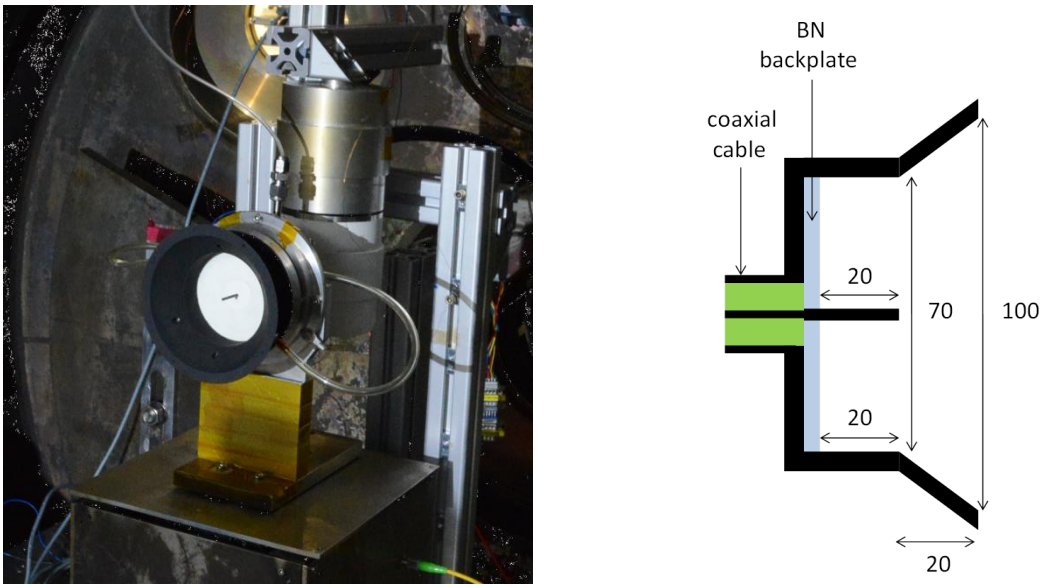

Figure 106. ECR-200-PM5-V3.

5.3.2.2 Overall behavior

The thruster ignited easily, showed a good microwave coupling and was stable (figure 107). At 2 sccm and 138 W the pressure in the tank is $2.2\ 10^{-7}$ mbar with a thruster potential of 315 V and 82 % microwave coupling. The measurements share common features with the ~ 30 W thruster. First, the

performance increased with decreasing Xenon pressure. Second, thrust is quite independent from mass flow rate (figure 108).

A maximum of about 2900 s of specific impulse is measured around 2.5 sccm and 250 W and a maximum total efficiency of about 0.50 is measured at 2 sccm and 80 W. Microwave coupling is bewteen 80 and 85 % at this most efficient set-point. This value is slightly below the minimum of 90 % observed on the 30 W version. However, as previously done for the 30 W version, the microwave design can be modified to improve coupling (impedance matching).

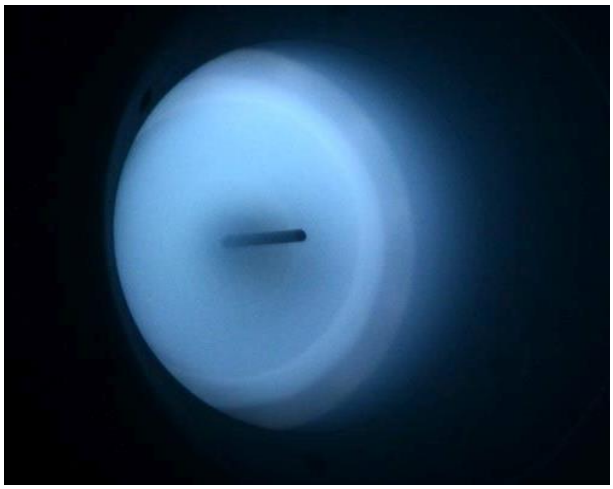

Figure 107. ECR-200-PM5 in operation at JLU Jumbo facility.

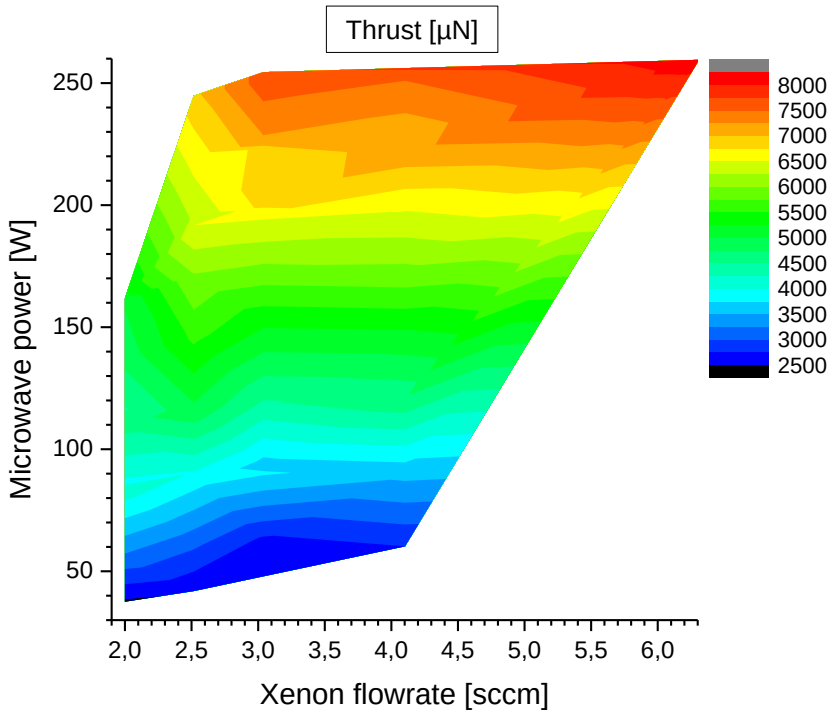

Figure 108. Thrust as a function of set-point for ECR-200-PM5-V4 at JLU Jumbo facility.

5.3.2.3 Behavior in time

In order to check the stability of the thruster and measure the inner conductor erosion, the ECR-200-PM5-V4 was operated for 100 hours distributed over 8 periods of continuous operation. Note that the duration of this test was limited only by the availability of the vacuum facility; the thruster was perfectly functional at the end of the test. The set-point (2 sccm, 100 W) was chosen to achieve very good total efficiency while limiting the steady state temperature of the microwave feedthrough to an acceptable level. Indeed, during preliminary tests, feedthroughs were damaged by unwanted discharges likely triggered by overheating of the dielectric filling. This is a minor technical problem that will be addressed before future tests.

At the chosen set-point the following values were consistently measured: 85° C of magnet casing temperature, 85 % of coupling, and 4500 µN of thrust (figure 109). Thrust exhibits some dispersion, in particular at the beginning but it reduces to about 5 % after 50 hours.

The mass loss of the inner conductor during this test suggests a lifetime of about 3300 hours, extrapolated with the same simple method in table 9. It seems reasonable to expect that, within a certain limit, an increase in inner conductor diameter will increase life time while maintaining the efficiency ([24], figure 116).

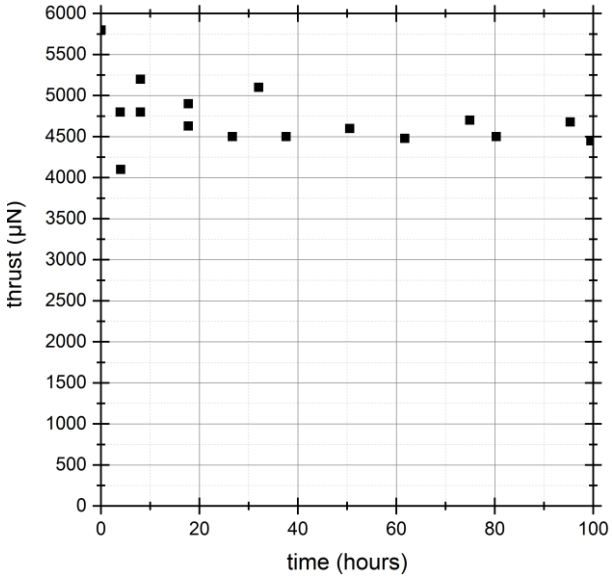

Figure 109. Thrust during operation at 2sccm and 100 W. There was no intervention on the thruster during the 100 hours of this test.

5.4 Summary of the results

In this chapter we furthered the coaxial ECRT experimental characterization. We first studied the thruster behavior in time. We pointed out one more source causing the dispersion of previous measurements: the existence of a transient regime spanning over more than 5 hours, driven by the pressure in the tank and the thruster temperature, as well as other unidentified parameters. The large variation observed on critical quantities requires that the measurements be done in steady state or at least at the same time since startup. The 30 W ECRT was also studied on longer time scales (67 hours) focusing on thrust and erosion. Among several inner conductor materials, graphite stood out as exhibiting relatively large thrust and low dispersion, in addition to relatively low erosion, possibly allowing a life time of 1000 hours. Strong erosion is likely related with low inner conductor potential.

Therefore inner conductor polarization could mitigate this effect although this solution is opposed to the goal of simplicity driving the development. Other materials may still be tested such as tungsten or diamond deposition. However a more radical solution is sought in the next chapter: to remove inner conductor by the use of waveguide coupling.

Second, the effect of magnetic field and gas injection was investigated. We showed that the ion current density angular profile is largely affected by the magnetic field but unaffected by injection. Although the two tested injections were very different, the thrust varied only by 10%, a difference that is of the order of the difference in cold gas thrust. Therefore we recommend that the more reliable radial injection design be used (as discussed in chapter 3), although slightly less performant. From the results obtained in this chapter, injection optimization appears as matter of fine tuning to be tackled later in the development. In contrast, optimization of the magnetic field topology seems to bear more potential for increasing thrust. Analysis of the material deposition on the backplate seems to indicate that the plasma is strongly tied to the magnetic field, at least for z locations where the field is intense enough. The observed deposition patterns are also consistent with the existence of a bounce movement. These elements will support the modelling approach followed in chapter 7. It was incidentally discovered that the presence of a dielectric plate, attached to the thruster in the thruster exit plane significantly improves performance.

Third, a ~ 30 W version and a larger ~ 200 W versions were designed and built, benefiting from the observations and developments to date. Impressive increase in efficiency, to up to 0.50, were measured in the Jumbo facility with the JLU thrust balance. One of the ~ 200 W versions was tested for100 hours. It proved stable and the erosion rate of the inner conductor allows to expect a life time of the order of 3300 hours. Given the experimental difficulties previously encountered with the ECRT, these results are to be confirmed and developed by measurements in another large facility.

6. Comparison between waveguide and coaxial coupling structures

Outline of the approach. The aim of this chapter is to study waveguide coupling as a solution to the erosion issue of the coaxial-coupled thruster. To this end, the first step was to design and manufacture a waveguide-coupled thruster. The goal was to obtain two identical thrusters, except for the coupling, in order to make a reliable comparison involving a change in coupling structure only. The second step was to make the experimental comparison, including ion current angular density, ion energy and thrust balance measurement.

Main results. A circular waveguide-coupled ECRT with 27.5mm diameter operated at ~ 2.45 GHz is designed and a procedure is proposed to make accurate microwave measurement for this thruster having a reflected power fraction of ~ 0.4. Microwave and thermal engineering issues are tackled. Thrust balance measurements report 500 µN for the coaxial-coupled thruster and 240 µN for the waveguide-coupled thruster, both operated at 25 W of deposited microwave power and a mass flow rate of 0.1mg/s of Xenon. These are the first published thrust balance measurement on a waveguide-coupled ECRT. Ion energy measurements reveal that this difference can be almost entirely explained by a difference in ion energy. The measured ion energies for the waveguide coupled thruster are in line with the available data in the literature, supporting the claim that the difference in ion energy is an intrinsic feature of the coupling.

From section 6.2.3 onwards, the content of this chapter is extracted from a submitted paper.

Content

6.1 Motivation

The erosion of the inner conductor of the coaxial-coupled thruster was quantified in section 0 in order to estimate the lifetime of such a thruster. It is possible that the use of adequate geometry and adequate material reduces erosion to an acceptable level. However, a more disruptive solution to this problem is sought. A waveguide coupling structure appears has a possible way to circumvent the erosion issue since no inner conductor is required in this case.

Waveguide coupling for ECRTs has been studied in the past as described in chapter 0, although the measured performance was quite poor. However, with the recent expertise acquired on the coaxial ECRT [24], [28], [29], [33], [95], [102], it seems relevant to investigate again the waveguide-coupled ECRT, for at least four reasons.

1. In previous waveguide coupled ECRT studies [11], [15]–[17], [23], thrust balance measurements were deemed unsuccessful (hence unpublished) because of a number of practical issues. For example: drift due to heating of the balance arm and difficulty in transmitting microwave power to the balance arm without mechanical coupling. Yet it is now well known, as illustrated in section 4.1.1, that the estimate of thrust from electrostatic probe measurements bears large uncertainty in particular for magnetic nozzle thrusters and that a specific measurement procedure and data analysis is to be developed for each thruster type [98].

2. A critical lack of accuracy of several key measurements including the deposited microwave power and the input gas flow rate blurred the assessment of the performance. Indeed, CRIMI, in his PhD dissertation section 3.2 [17], casts doubts on the polarizer that he used, and SERCEL, in the conclusion of his PhD dissertation [23] is critical about the microwave diagnostics he used: *"we suggested (Chapter 2) that coupling efficiency can be expected to be very high (>0.95) for ECR plasma propulsion devices. Unfortunately, our microwave diagnostics were not adequate to confidently confirm this assumption and the coupling losses may be much larger than we assumed".*

3. It was shown repeatedly that a high facility pressure decreases the ECRT performance [35], [105],[95]. The background pressure achievable in the facility used in this work is one order of magnitude below the background pressure reported by SERCEL for example [23], thus more representative performance is expected in the present work.

4. To our knowledge, in all previous waveguide-coupled ECRT studies, Argon was used as propulsive gas penalizing the performance in comparison with Xenon, in particular mass utilization efficiency, as demonstrated by CANNAT for a coaxial ECRT (PhD dissertation, table 4.1 [28])

6.2 Design

The waveguide and coaxial thrusters to be compared were designed with the intention that they would differ only by the coupling, other things being equal. It should be noted that the design compromises of the coaxial-coupled thruster imposed non-optimal features as far as performance is concerned, leading to efficiencies lower than that presented in section 4.2 and published by HOLSTE [105]. In order to benefit from the already existing coaxial design, the same outer conductor size is used: the waveguide thruster characterized in this work consists of a 27.5 mm diameter and 20 mm long waveguide coupling structure. In addition, in order to take advantage from data available in the literature for the coaxial configuration, microwave frequency should be around 2.45 GHz.

6.2.1 Microwave design

The combination of a 27.5 mm-diameter structure and the use of a 2.45 GHz microwave is a strong constraint. Indeed, as exposed in section 2.1.2.3 the cut-off frequency of an empty circular waveguide of such diameter is 6.39 GHz (i.e. the boundary conditions imposed by the metallic structure do not allow propagating modes below that frequency). Additionally, to avoid high metallic losses, the working frequency should be ~ 15 % above the cutoff frequency. As a consequence, the relative permittivity of the dielectric inside the waveguide should be at least $\epsilon_r \sim 9$. For this reason, alumina was chosen.

6.2.1.1 Simulation of several microwave transition solutions

Several solutions are considered to excite a TE11 mode at 2.45 GHz in a 27.5 mm-diameter circular waveguide : quarter-wave transformer or smooth transition from an empty circular waveguide propagating at 2.45 GHz, or direct coaxial-to-waveguide transition (see section 0). These technical solutions are sketched in figure 110.

The level of coupling achievable by a coupling structure is obviously strongly dependent on electromagnetic behavior of the plasma. However, self-consistent electromagnetic calculation in a magnetized plasma is a difficult problem which would by itself require a thesis (this is the main issue the ongoing doctoral simulation work of PORTO [67] and SANCHEZ-VILLAR [66]). To simplify this complicated issue, the following heuristic approach was chosen: make a microwave design such that propagation without reflection occurs up to the surface where the wave encounters the plasma. In practice we aimed at keeping reflected power before that surface below 1%.

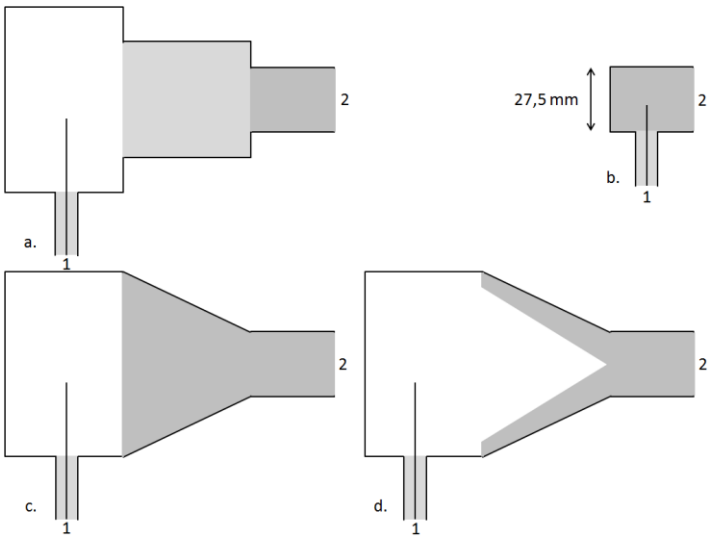

Figure 110. Sectional schematic views of transitions that are considered. Black lines are metallic surfaces and grey areas are ceramic volumes. Light grey is ϵ_r~4 and dark grey is ϵ_r~9. The ports are numbered.

Microwave engineering guidelines and analytical electromagnetic calculation provide useful rules of thumb regarding the design of such transitions. However, in order to achieve a reflected power below 1% either empirical tuning or electromagnetic simulation is necessary. Simulation and parametric optimization is performed using the finite element software COMSOL®. The conductivity of aluminum $\sigma = 3{,}77.10^7 S/m$ is used for the metallic walls, and loss tangent $\tan\delta = 2.10^{-3}$ is used for ceramics, which appears as a conservative estimate [38], [106]–[108]. The loss tangent is the ratio of imaginary part to real part of the permittivity.

Name of the transition solution	Reference on figure 110	Reflected power ($\|S11\|^2$)	Dielectric losses	Metallic losses	Size	Machining
Quarter-wave	a	1.6%	8.5%	0.7%	cumbersome	very easy
Coaxial-to-waveguide	b	0.3%	2.4%	0.3%	compact	easy
Smooth 1	c	4%	8.2%	0.8%	cumbersome	difficult
Smooth 2	d	2%	8.2%	0.7%	cumbersome	very difficult

Table 13. Summary of the features of the microwave transitions considered to excite the TE11 mode at 2.45 GHz in a 27.5 mm-diameter circular waveguide. From COMSOL simulations.

The respective merits of the solutions are summarized on table 1. From this analysis, the coaxial to waveguide transition appeared as the best solution according to all criterions, except machining. It turned out that the manufacturing of this part is possible although requiring a long lead time (12 weeks for the ceramics that was used in the end for plasma experiment). In order to maintain reflected power below 1%, it is necessary to manufacture the parts with geometrical lengths within $\pm$ 0.5 mm from the optimal value, which is standard, even for alumina ceramics manufacturing. It is also verified that a value of the relative permittivity between 9 and 10 ensures to stay below 1% of reflected power. Relative permittivity of alumina ceramics is expected to be in this interval. Unfortunately, ceramics manufacturers do not guarantee better accuracy on the value of this parameter.

6.2.1.2 Experimental measurement on the chosen solution

In order to verify the achievement of our goal (reflected power below 1% up to the ceramics-plasma interface), N-connector inputs as well as a second coaxial-to-waveguide transition were manufactured in order to make measurements with a vector network analyzer (figure 111 and figure 112).

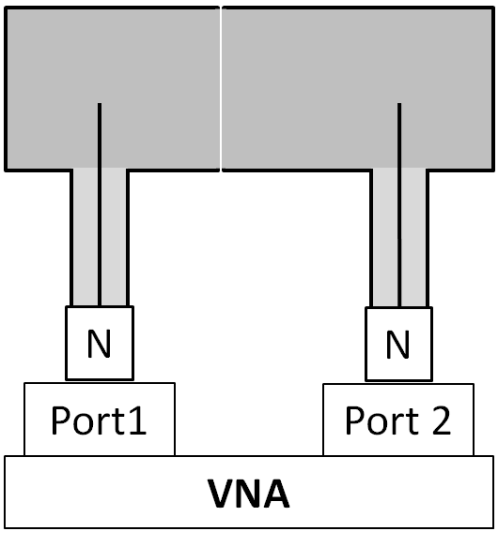

Figure 111. Test setup connected to a VNA through N connectors. On the schematic view, a gap enables to visualize the two distinct parts. In reality the ceramics are in contact and the metallic walls are tightly screwed to each other.

Figure 112. Picture of the microwave test setup. On the left is the coaxial-to-waveguide transition used in the thruster. On the right are test parts.

Three distinct alumina ceramics from two manufacturers were tested before finding a ceramics with sufficiently low $\tan\delta$. The first alumina ceramics (thereafter named "pressed ceramics" in reference to the manufacturing process) was successfully characterized at room temperature with the setup shown in figure 111. The reflected power was 1% and the absorbed power was 2%. However, during the in-vacuum test, we realized, using a thermal camera pointed at the visible part of the ceramics through a germanium window, that the temperature was diverging, up to several hundred degrees Celsius, to the point that the ceramic appeared to visually glow from heat after several minutes. The plasma was not ignited during these experiments (i.e. no gas was injected), only the microwave power was on. This observation is interpreted as the combination of two features. First, the absorption of the alumina ceramics is increasing with temperature, as confirmed by additional measurement presented on figure 113. Second, the alumina ceramics is thermally isolated for all three heat-transfer processes: no conduction is possible since the fitting with the surrounding part is loose, no air convection is possible in vacuum, and the radiating surface is small. Using a water cooling circuit, plasma measurement were performed and were the subject of an article and presentation at the Space Propulsion Conference 2018 [109].

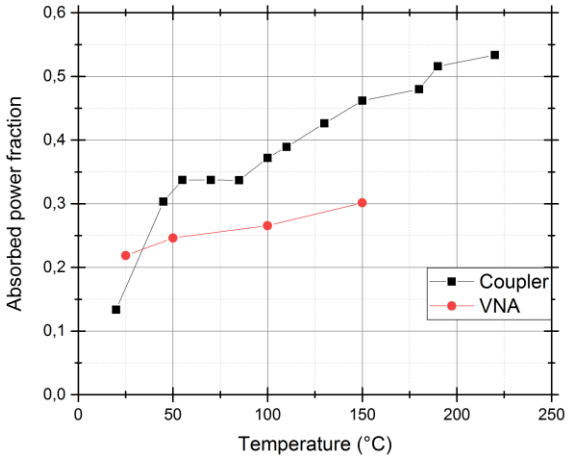

Figure 113. Estimated power fraction absorbed by the pressed alumina ceramics. The value of the absorption at 20 °C is much higher than measured upon receipt of the parts (2% at room temperature). It is assumed that exposure to high temperature permanently altered the absorption[11].

However, water cooling prevents from mounting the thruster on the thrust balance and the varying temperature of the ceramics generates uncertainty on the estimate of the power deposited in the plasma. In order to tackle this issue,

1. other alumina ceramics were used, referred to as "molded ceramics", in reference to the manufacturing process and

2. thermal design was improved as described in the next section.

Regarding the improvement on the ceramics, molded ceramics from Final Materials were used for the final thruster measurements. At the expense of a long delay (4 months) and high cost, a custom-shaped molded alumina insert was ordered. Table 14 shows the results for these ceramics of the test sketched in figure 111. Both the real and imaginary part of the permittivity seem to vary with temperature, since both reflected power and absorbed power vary with temperature.

This setup can also be simulated. Parametric analysis of the simulation enables to determine the relative permittivity that would result in the measured S parameters. The relative permittivity is estimated to be $\epsilon_r = 8.7 - 0.07j$ at the working temperature of the thruster which is around 110°C. At this temperature, the real part of the permittivity is lower than the value assumed for the design. However, this ceramics achieves major improvement regarding absorption at 110 °C with respect to the first ceramics that was tested (figure 113).

	$\|S11\|^2$	$\|S12\|^2$	$\|S21\|^2$	$\|S22\|^2$	to be considered absorbed for future plasma measurement
25 °C	0.8%	92.9%	92.9%	0.7%	2.5%
110 °C	8.9%	82.6%	82.6%	7.9%	3.4%

Table 14. Values of S-parameters for the test sketched in figure 111, for the molded ceramics used in the experiments presented in section 6.3. The last column is $(2/5)(1 - |S11|^2 - |S21|^2)$ because the absorbing waveguide length present in the thruster is $2/5$ of the measured length present in the test.

[11] This phenomenon seems to be known as dielectric thermal aging. Considerable permanent variation of the absorption is observed for some material ([110], figure 8). However no data was found for alumina.

6.2.2 Mechanical and thermal design

A sectional view of the thruster is presented on figure 114. It is similar to the thruster presented previously (figure 51b) except for microwave coupling. Given the significant absorption, and thus heat production, implied by the imaginary part of the permittivity, it is necessary to allow for heat dissipation. A tight fastening of the dielectric material ensures appropriate thermal conduction to the rest of the mechanical structure, acting as a radiator. The thruster external surfaces are covered with an emissivity-enhancing coating.

The tight fastening is obtained with thermal shrink-fitting of the ceramics cylinder into the surrounding metallic part. The inner ceramics part is machined ~0.4% wider in diameter than the outer metallic part housing it. Therefore, the ceramics cylinder does not fit inside the metallic housing when both parts are at room temperature, but can be inserted if the housing is at ~ 200 °C. This operation is performed by heating the housing with a stove heater in the laboratory and by subsequent fast insertion of the ceramic cylinder. It is both critical and risky since it is irreversible: good thermal contact would then make it difficult to obtain a difference in temperature between the parts. It was nonetheless successfully done, both regarding the operation of the mounting and the thermal results obtained.

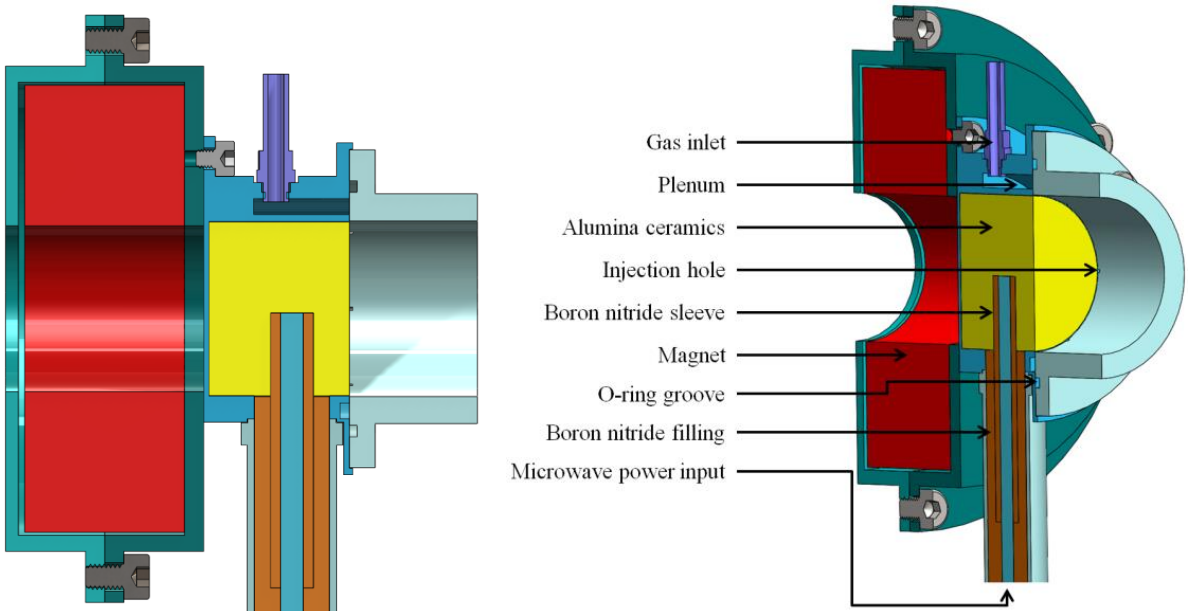

Figure 114. Sectional Solidworks view of the waveguide coupled thruster.

Boron nitride is used as dielectric for the coaxial line immediately before the thruster because its dielectric properties are assumed robust to temperature swings well above 100 °C (contrary to PTFE which was used before). In addition, unwanted discharges were observed in the development process between the inner and outer conductor, just at the interface with the waveguide structure. They are prevented by a boron nitride sleeve covering the inner conductor around that location (figure 114).

6.2.3 A procedure for microwave measurement in case of high reflection

Since no significant reflection is observed when calibrating the microwave line, the fraction of reflected power at the thruster is:

$$R = \frac{1}{\gamma^2}\frac{P_R}{P_I} \qquad (188)$$

where P_I , and P_R are measured at the couplers. With the waveguide-coupled thruster, R = 0.4 is observed at typical set-points. It is likely that the relatively poor thruster coupling results from the dimension of the waveguide coupling structure imposed in this comparison work (see section 6.2.1) and is not a general feature of waveguide coupling.

$R = 0.4$ results in an unacceptably high uncertainty on the power deposited in the plasma (figure 49). However, a large fraction of this uncertainty originates from a systematic directivity error on P_R that can be eliminated provided that the phase shift ϕ from the interference term from equation 170 is known.

Yet, since the microwave line has been shown to produce only small reflection without plasma, the reflection while the thruster is operating does not takes place before the backplate-plasma interface. In addition, the bulk plasma created in the coupling structure is a priori a continuously and slowly varying medium, therefore reflection is unlikely to happen after backplate-plasma interface. Thus it assumed that the reflection take place at this interface. We are aware however that the wavelength on the plasma side is quickly decreasing as the wave approaches resonance (see section 2.3.2.2.2), which is a limitation to the accuracy of this assumption.

Using a dedicated test set-up it is possible to impose R = 1 at backplate-plasma interface by short-circuiting the microwave circuit with a metallic plate. The reflected power is then measured both at operating power with the coupler setup and at low power with a vector network analyzer (VNA), a device for which directivity errors can be neglected (figure 115). Neglecting also the directivity error on the incident power (see section 3.2.3) and under the customary assumption that the behavior of the microwave line is unaffected by the level of power, $\cos(\phi)$ is retrieved using the following relation, derived from equation 170. Power fractions P_R/P_I are provided by the coupler setup for the left-hand side and by the VNA for the right hand side.

$$\frac{P_R^{measured}}{P_I^{true}} = \frac{P_R^{true}}{P_I^{true}} + D + 2\sqrt{D\frac{P_R^{true}}{P_I^{true}}}\cos(\phi) \qquad (189)$$

The knowledge of $\cos(\phi)$ enables to debias reflection measurements with plasma, thus making more accurate measurements with smaller uncertainty.

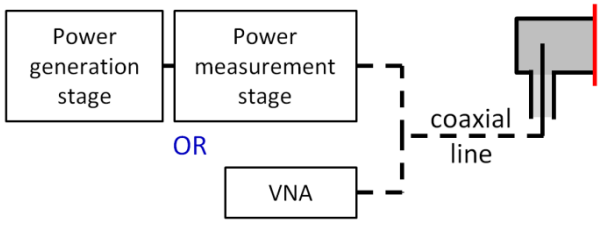

Figure 115. Schematic of the test setup. A metallic plate in red is placed at the interface between the microwave circuit and the plasma. Reflection measurement made with the power generation and power measurement stages from figure 52 is compared with measurement made with a VNA.

6.3 Experimental comparison

The two thrusters compared in this section are identical except for the use of circular-waveguide or coaxial coupling structures, excited with TE11 mode and TEM mode respectively (table 11, figure 116, figure 117, figure 118). Consequently, the material of the backplate is alumina in the case of waveguide coupling (imposed by the coupling structure) and boron nitride in the case of coaxial coupling. All other features are identical, in particular: the magnetic field, the gas injection, the geometry and material of the coupling structure in contact with the plasma.

Magnet	**Coupling structure type**	**Outer conductor:** - diameter - length - material	**Inner conductor:** - diameter - length - material	**Injection type**	**Backplate material**	**Other**
Small	Coaxial or waveguide	- 27,5 mm - 20 mm - Al	For coaxial coupled: - 2,3 mm - 20 mm - Stainless steel covered with boron nitride spray	Radial	Boron nitride or alumina	

Table 15. ECRT configuration used for coupling comparison (see Appendix A.)

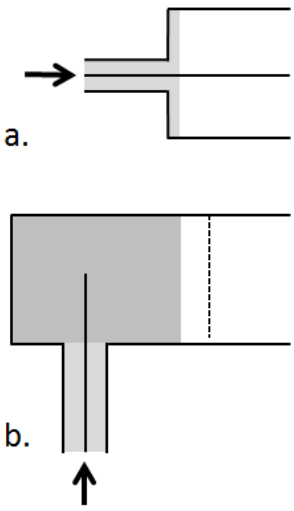

Figure 116. Sectional schematic view of (a) the coaxial coupling structure and (b) the waveguide coupling structure. Black lines are metallic surfaces and grey areas are ceramic volumes. Light grey is boron nitride and dark grey is alumina. The arrows indicate microwave power feed. The electric field in the dashed cut plane is in figure 118.

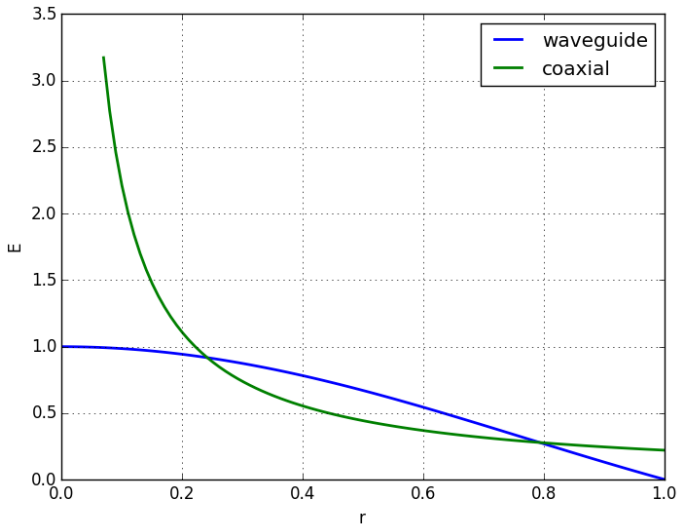

Figure 117. Electric field norm in arbitrary units, along a radial cutline, for a given power flow. For the waveguide, the TE11 mode is represented and the cutline is perpendicular to the electric field main axis (TE11 is not axis-symmetric).

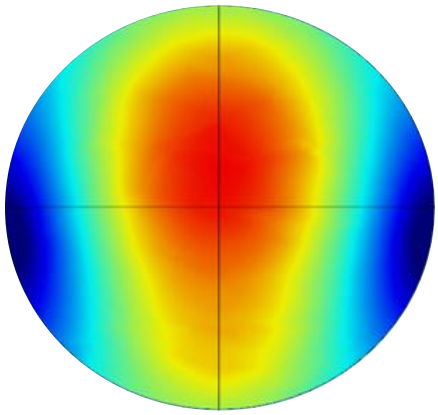

Figure 118. Microwave field norm in the absence of plasma for the waveguide-coupled thruster (COMSOL). It is plotted in the plane 3 mm from the close-end (dashed line in figure 116).

The microwave power is fed through a rigid coaxial line. Careful microwave design enables transmission up to the back end of the plasma volume with little wave reflection. The inserted alumina ceramics material has been characterized using a dedicated test setup to have a relative permittivity $\epsilon_r = 8.7 - 0.07j$ at the working temperature of the thruster which is around 110°C.

Xenon gas is collected in a plenum from the gas feed tube and injected through six injection holes distributed radially at the back end of the plasma volume. Gaskets ensure gas tightness.

Figure 119 is a picture of the waveguide thruster mounted on the thrust balance and equipped with a coaxial-to-waveguide transition. The thruster is equipped with temperature probes and a measurement of its floating potential. Experiments are performed in the B61 facility at ONERA. It is a 4m long and 1m in diameter tank with a pumping speed for Xenon around 8000 L/s. The base pressure is around 8.10^{-7} mbar, and working pressure around 9.10^{-6} mbar.

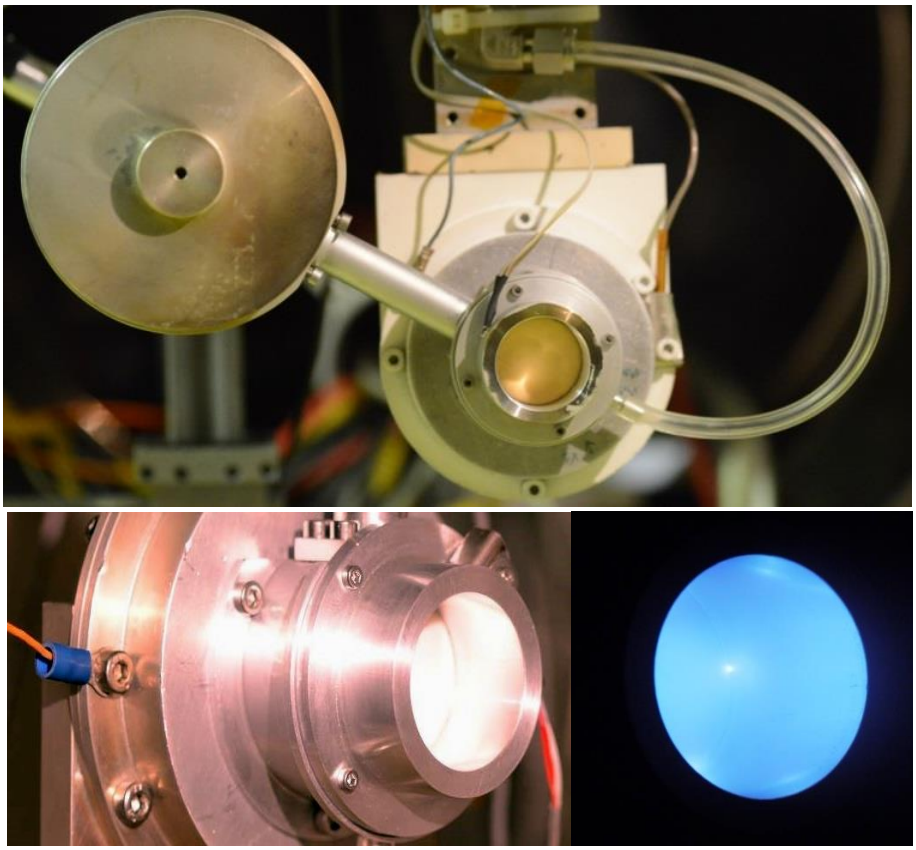

Figure 119. Top: Waveguide thruster on the thrust balance. The wide cylinder on the left is a coaxial-to-waveguide transition designed for testing on the thrust balance. It enables microwave feeding without mechanical coupling of the balance arm. Bottom: side view, and thruster in operation.

Both thrusters ignite easily under the condition that a puff of gas if provided at start up. For the waveguide-coupled thruster, temperature equilibrium around 110° C is reached in about one hour and a half under operation at 1 sccm and 52 W of power deposited in the plasma. The frequency of the microwave power is experimentally tuned to 2.25 GHz in order to minimize reflected power. During operation of the thruster the pressure in the vacuum tank is about 6.10^{-6} mbar.

For the coaxial-coupled thruster the fraction of reflected power at the thruster is below R = 0.1 whereas for the waveguide-coupled thruster it can be up to 0.4. Therefore, for the latter, the procedure described in section 6.2.3 was used to calculate the power deposited in the plasma and the error bars.

6.3.1 Comparison of the performance using thrust balance measurement and ion energy measurement

The thrust obtained by thrust balance measurement is shown in figure 120. The two types of coupling seem to be associated with distinct slopes in this graph. At 25 W and 1 sccm of Xenon the coaxial-coupled system provides 500 µN of thrust whereas the waveguide-coupled system provides 240 µN of thrust corresponding to respective total efficiencies of 5% and 1%. Since thrust is expected to scale as the square root of mean ion energy, this difference is almost fully explained by the difference in mean ion energy: 190 eV and 65 eV respectively, as can be interpolated from the data presented in figure 121. Examples of ion energy distribution function are in figure 122.

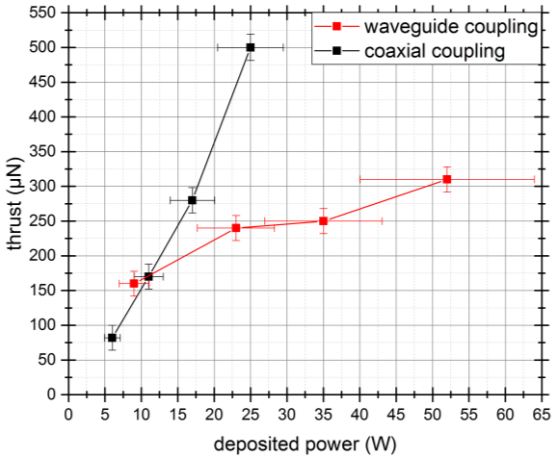

Figure 120. Thrust balance measurement as a function of deposited power at 1 sccm of Xenon. For both series of data the last point is mean of three or more measurements.

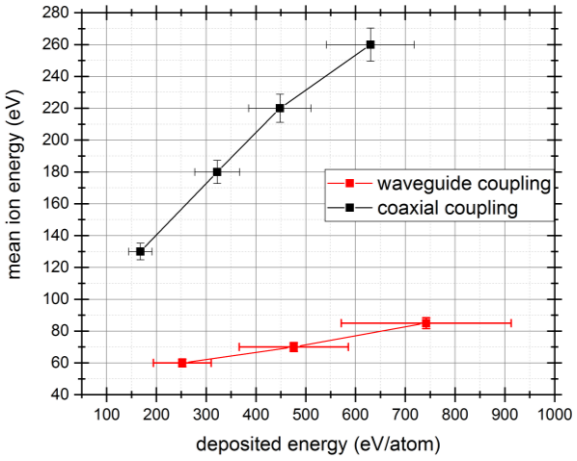

Figure 121. Mean ion energy measured with a Hiden ion analyzer as a function of deposited energy in electron-volt per atom of injected Xenon. The flow rate is 1sccm.

Although no previous direct thrust measurement data is available in the literature, several experiments previously measured mean ion energies. Figure 123 displays data from the literature as well as measurements from this study. The set of data taken from coaxial thrusters (all from ONERA studies since 2010) exhibits a linear increase in energy with a slope that is higher than that sketched by the data points from the waveguide thrusters. This plot suggests an intrinsic difference between waveguide-coupled and coaxial-coupled thrusters, regardless of the details of the design. The measurement of mean ion energy is a basic measurement that appears as quite robust to experimental perturbation. However, interpretation of this data should be tempered by the fact that the background pressure has certainly lowered the ion energies measured by Sercel (1993) who reports a background pressure of 6.10^{-5} mbar. The experiment of Crimi (1967) on the other hand was reportedly run at a background pressure of 5.10^{-6}, the same as for coaxial coupling experiments.

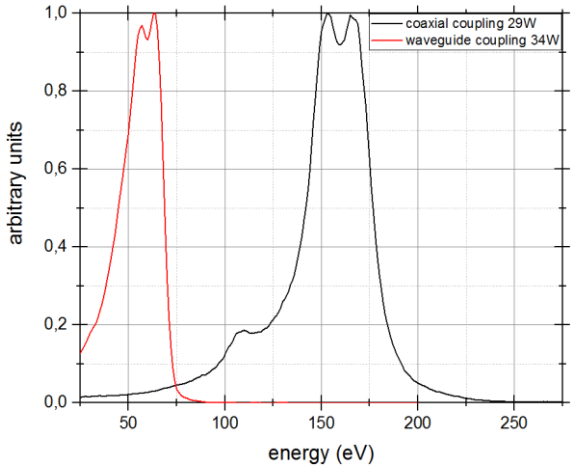

Figure 122. Ion energy distribution function measured with a Hiden ion analyzer. The Xenon flow rate is 1sccm.

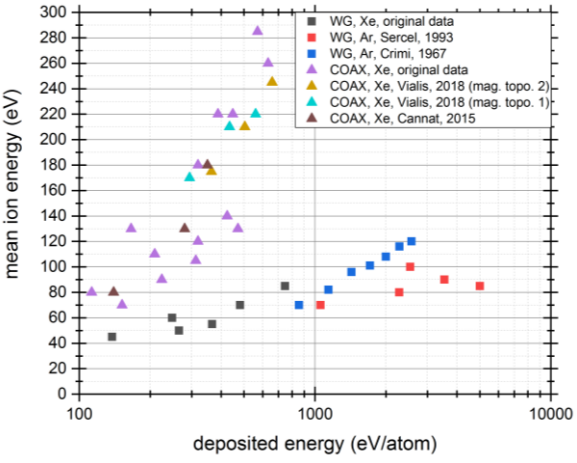

Figure 123. Mean ion energy as a function of deposited energy in electron-volt per atom of injected neutral gas. The legend specifies the type of coupling and the propulsive gas. Vialis [24] published data from 2 distinct magnetic field topologies.

6.3.2 Compared characteristics of the plume using angular Faraday probe scans

To further the analysis beyond the scalar integrated quantity that is thrust, the distribution of ion current density in the plume can be analyzed. Figure 124 is a plot of ion current density measured on the waveguide-coupled thruster. The total integrated current is monotonically increasing with flow rate. Nevertheless the ion current density on axis is not. It is quite remarkable that a variety of profiles are observed depending on the flow rate contrary to the coaxial-coupled thruster for which the profiles at different set points are proportional (i.e. can be superposed by applying a multiplying factor on the y axis) as is apparent in figure 125 for a variety of relevant set points. The change in the angular position of the central depression of the profiles may simply be a consequence of small movement of the inner conductor. This variety of profiles observed for the waveguide coupling may be correlated to the variety of electromagnetic modes that can be accommodated by waveguides whereas the coaxial structure, which imposes more constraining boundary conditions, only have propagating solutions for the TEM mode, unless excited at very high frequencies [38].

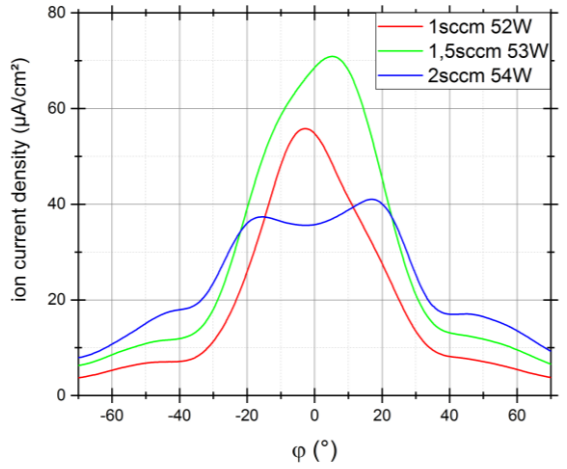

Figure 124. Angular profiles of ion current density for the waveguide-coupled thruster measured with a guard ring Faraday probe at 26.5 cm from the thruster exit plane. The legend specifies the set point.

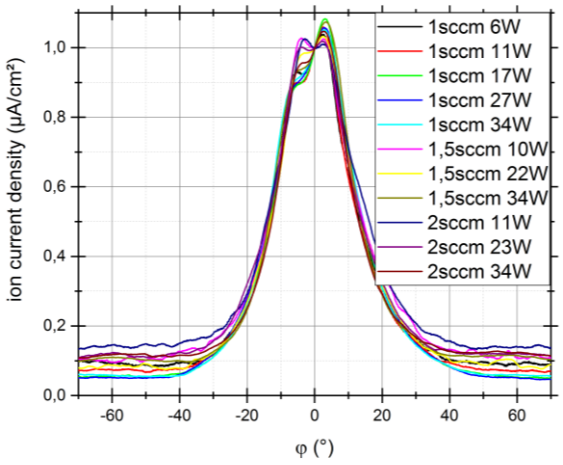

Figure 125. Normalized angular profiles of ion current density for the coaxial-coupled thruster measured with a guard ring Faraday probe at 26.5 cm from the thruster exit plane. The legend specifies the set point.

The measured angular profiles are significantly more spread for the waveguide-coupled system. The calculation of integrated quantities such as the divergence efficiency or the mass efficiency would be interesting to quantify the consequences of increased spread of the current on performance. Yet it would probably be inaccurate due to issues related to ion current measurement pointed out in section 4.1.1. In particular, faulty ion current measurement at large angle could induce large error on these integrated quantities. Thus the analysis is restricted to the thrust angular density, that is the contribution to thrust from the current in the portion of the sphere included between φ and $\varphi + d\varphi$. This quantity is plotted in figure 126. It is proportional to $v(\varphi)\, J(\varphi)\, |\sin(\varphi)| \cos(\varphi)$. In the case of the waveguide-coupled thruster, thrust receives more contribution from large angles. For both thrusters the maximum is between 10° and 15°.

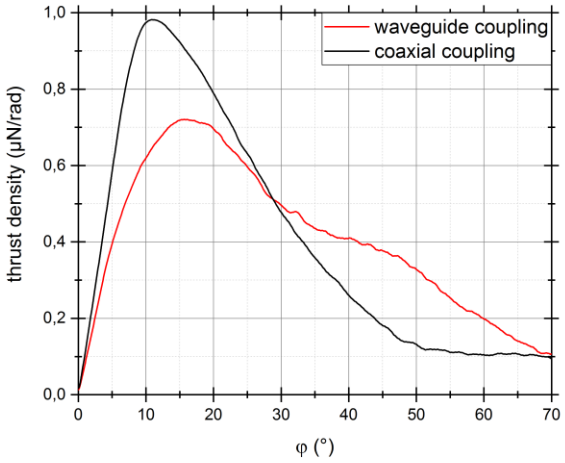

Figure 126. Thrust angular density normalized by total thrust (i. e. contribution to thrust from ion current flowing between φ and $\varphi + d\varphi$). Flow rate: 1 sccm

For the coaxial-coupled thruster, when the bias voltage of the probe is increased, local minima appear in the angular current density scan about $\varphi = \pm 5$ ° (figure 126). This is interpreted as a high energy conical electron beam partially canceling out the ion current. Under the assumption that diffusion across magnetic field lines is sufficiently low, this population originates from the periphery of the inner conductor and appears because of locally intense heating, as indicated by self-consistent electromagnetic simulation of this system [66]. The electrostatic sheath potential in the vicinity of the (floating) inner conductor and secondary electron emission at the surface may also play a role in this phenomenon. This high energy electron beam is specific to the coaxial coupling and no local minimum is observed for the waveguide-coupled thruster when increasing bias voltage of the probe up to - 25 V. This phenomenon may be part of the explanation for the aforementioned discrepancy in mean ion energy, and also thruster potential: 15 V and 130 V for the waveguide and coaxial coupling respectively, at 1 sccm and 25 W. It is hypothesized that these high energy electrons are responsible for building up the plasma potential in the coupling structure (and consequently thruster potential) in a similar way as high energy electrons would build up a high sheath potential drop. Ions therefore have higher energy because they are created in a higher plasma potential.

Unfortunately, no self-consistent heating simulation is known to the authors in the case of waveguide coupling. However, such simulation for the coaxial system has shown that the electromagnetic profile share common features with that in the absence of plasma [66]. For the sake of argument, we may therefore assume the same for the waveguide system. Vacuum circular waveguide modes are proportional to first kind Bessel functions, instead of reciprocal multiplicative function for coaxial geometry (figure 117) [38]. Hence waveguide modes are more spatially homogeneous, without strong local maximum. This may result in an electron energy distribution function having the same mean energy than that created by coaxial coupling (since the same power is deposited), but deprived from the high energy part, only created in the presence of intense electric field. This distribution then only builds up a significantly smaller accelerating potential. Electron energy distributions for both systems could still achieve similar ion flow, since ionization cross section varies only moderately between 30 and 120 eV.

The difference of thrust between both thrusters can also be interpreted from the fluid point of view developed in TAKAHASHI (2011) [90] where the magnetic thrust is calculated to be proportional to $\partial p_{e\perp} / \partial r$. When the microwave heating is radially uniform, only the radial density profile due to the

presence of boundaries contributes to $\partial p_{e\perp}/\partial r$. On the contrary, when the microwave heating is decreasing with radius, the temperature profile and the density profile both contribute to $\partial p_{e\perp}/\partial r$. Besides, the density may exhibit a faster radial decrease because of ionization decreasing with radius. From this point of view the more the radial profile is peaked, the more thrust is obtained, which is coherent with the observation made with the coaxial-coupled and waveguide-coupled thrusters.

The results presented in this chapter question the global understanding of the thruster, which until now may have overlooked the role of the coupling structure. For example, in the only comprehensive analytical model of the thruster known to the author [29] (derived from [32]) the coupling structure is not considered. A maxwellian electron distribution is assumed and the power transfer is entirely described by the amount of deposited power, prescribing the electron temperature. From such perspective, the two thrusters described in this paper cannot be discriminated whereas experimental measurements reveal considerable differences. These measurements therefore point out microwave coupling as an area for improvement for future ECRT models.

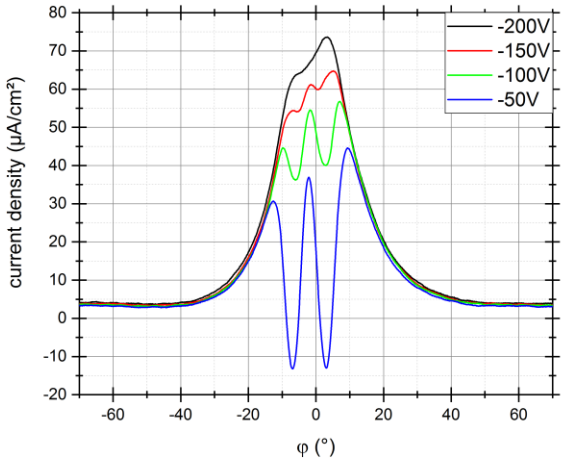

Figure 127. Guard ring Faraday probe current density profile for the coaxial-coupled thruster at 26.5 cm from the thruster exit plane. The legend specifies the bias voltage of the probe.

6.4 Summary of the results

The first thrust balance measurements of an ECRT using a waveguide coupling structure were performed and compared with measurements on an identical thruster except for the use of a coaxial coupling structure and consequently a boron nitride backplate, instead of alumina. Several microwave engineering solutions were considered for the waveguide-coupled thruster. A ceramics-filled coaxial-to-waveguide transition was chosen to feed the microwave power and manufactured. Given the significant and unexpected absorption, and thus heat production, implied by the imaginary part of the permittivity of the ceramics, a tight fastening was implemented to ensure appropriate thermal conduction to the rest of the mechanical structure, acting as a radiator. The waveguide-coupled thruster exhibits a reflected power fraction of ~ 0.4 which implies very large uncertainties on the deposited microwave power because of directivity errors. A procedure to eliminate systematic directivity error in the case of low thruster coupling was proposed and used in the analysis of the waveguide-coupled thruster performance.

Several distinct angular ion current density profiles were observed for the waveguide-coupled thruster whereas for the coaxial thruster they are proportional for all the tested set-points. At 25 W and 1 sccm of Xenon the coaxial-coupled system provides 500 µN of thrust whereas the waveguide-coupled system provides 240 µN of thrust. It is shown that this discrepancy can be almost fully explained by a discrepancy in ion energy and that lower ion energy seems to be an intrinsic feature of the waveguide-coupled thruster. Besides, for the coaxial-coupled thruster, a population of high energy electrons that seem to originate from the periphery of the inner conductor are observed in the plume. It is hypothesized that this population, unobserved in the case of the waveguide-coupled thruster, plays a key role in establishing a high accelerating potential.

Future work could include space resolved spectroscopy measurement in both thrusters to further investigate the link between the electron energy distribution function at several locations in the coupling structure and the establishment of the accelerating potential in the plume. Besides, directional ion current density measurements in the plume would provide valuable information about the dynamics of the nozzle and bring in new elements regarding the interpretation of angular ion current density profile.

The difference in ion energy induced by the coupling structure is quite unexpected. Indeed, the global models availabl use only the spatially integrated deposited power to characterize the heating [32]. Therefore they are unable to distinguish between a waveguide-coupled and a coaxial coupled thruster. Nevertheless, the experimental investigation reported in this chapter, exhibits major differences between those two systems. This situation calls for a new modeling of the ECRT, using input parameters that would vary from coaxial coupling to waveguide coupling structures, in order to model appropriately both cases.

7. Heating model

Outline of the approach. We saw in the previous chapter that two thrusters differing only by the type of electromagnetic coupling, can yield very different performance. This observation frustrates our current intuition which is based on global maxwellian models. For these models, the (scalar) deposited power completely describes electron heating through the prescription of a global electronic temperature, and the type of electromagnetic coupling is ignored. To explain the observations of the previous chapter it seems that the radial electromagnetic profile should be taken into account, as well as the likely non-maxwellian electron velocity distribution. In this chapter we make a first step towards addressing the latter issue: we propose a kinetic approach to calculate the formation of the electron distribution function in the ECRT, from which we derive ion energy and ion flux in the jet.

Main results. The electron motion and electron confinement are studied in static fields representative of those in the ECRT. From this analysis, a Fokker-Planck equation is used to describe the heating of the distribution through a diffusion term in perpendicular electron velocity; a loss term in this equation account for collisions with neutrals. In addition, we provide boundary conditions, and provide additional energy balance and neutral gas balance equation. A parametric study of the model analyses the effect of electron emission, power deposition, neutral gas flow, and diffusion coefficient. The results are also compared with measurements.

Paul-Quentin Elias is acknowledged for initiating this approach and for fruitful discussions, fueled by the results of a one-dimensional electromagnetic PIC model of the ECRT that he is developing [67].

Content

Nomenclature.

μ = Magnetic moment

ϕ = Electrostatic potential

B = Static magnetic field

τ_B = Bounce period

D = Diffusion coefficient in perpendicular velocity

P = Distribution function in perpendicular velocity in the interaction region

$v_{\perp 0}$ = Perpendicular velocity in the interaction region

F_0 = Electron flux entering the system at low energy

F_* = Electron flux in the jet, exiting the system at high energy

v_0 = Velocity of low energy electrons entering the system

v_* = Velocity of electrons in the jet, exiting the system at high energy

L_{el} = Integrated number of elastic collisions per unit time

σ_{el} = Elastic collision cross section

L_i = Integrated number of ionizing collisions per unit time

σ_i = Ionization collision cross section

K = Integrated power loss due to collisions

ψ_g = Neutral gas flow

P_{in} = Microwave input power

$\bar{\sigma}$ = Electron emission coefficient at the “backplate”

$E_{\mu\lambda}$ = Intensity of the microwave field

ω = Radian frequency of the microwave

m_e = Electron mass

M_i = Ion mass

7.1 Motivation

The presentation of ECRT modelling made in section 2.3 described two distinct regions: the plasma in the coupling structure (or "interaction region") on the one hand, and the magnetic nozzle plasma on the other hand. This structure reflects the organization of the literature on the subject and models usually focus on either region. However, although the dominant physical processes differ between regions, this separation does not seem to lie on a fundamental decoupling between the two regions. On the contrary, the study of particle trajectories (section 2.3.2.1) show that electrons under a certain energy level bounce back and forth between the nozzle and the coupling structure, at a velocity ($\approx 10^7$ m/s) considerably higher that the ion flow velocity ($\approx 10^4$ m/s). They are these often mentioned "trapped electrons" or "reflected electrons" [30], [78], [79]. They probably acquire their "exiting" energy not only in their first pass in the coupling structure, but rather through several passes. This mechanism is described in the non-propulsion oriented literature on ECR heating, for example JAEGER (1972) [111]. The electron bounce movement is likely responsible for the energy flow that is accounted for by an ad-hoc polytropic law in the fluid approach. We saw that measured polytropic indices are closer to isothermal than to isentropic (section 2.3.3.4), which indicates a substantial energy flux, consistent with a fast electron bounce movement. *These arguments and observations invite to also consider the problem from a langrangian standpoint (focusing on particle trajectories) rather than exclusively from a eulerian standpoint (focusing on local averages).*

In addition, it seems that the systematic assumption of a maxwellian electron distribution function is only a convenient working hypothesis. Even the kinetic model described in MARTINEZ-SANCHEZ (2015) [79] a maxwellian distribution function is assumed at "the nozzle throat" and transported into the nozzle. However, the maxwellian assumption may preclude the prediction of effects arising from the complexity of the real distributions, and non-maxwellian energy distributions were measured in the plume ([30], figure 3). We can identify at least two processes responsible for non-maxwellian distribution functions. First, the resonant ECR heating has no reason a priori to generate a maxwellian distribution. Second, the confinement of the electron population implies a distribution function depleted from "unconfined regions" of velocity space. Both these processes take place at the bounce frequency ($\approx 10^7$ s^{-1}) thus collisions cannot a priori provide relaxation towards a maxwellian distribution because they are estimated to be less frequent ($\lesssim 5\ 10^6$ s^{-1} in the coupling structure, $\approx 3\ 10^3$ s^{-1} in the nozzle). *These arguments invite to look into the formation of the electron distribution function.*

These two considerations are the basis for the approach presented in this chapter. We are looking for a kinetic equation able to describe the microwave heating process. We will consider a one particle electron distribution function and neglect all interactions between electrons; static fields will be imposed. The electromagnetic field will be imposed as well. A Fokker-Planck equation will be the basis for the model; it will describe diffusion in perpendicular velocity due to microwave heating. This equation will arise by considering the heating process as a Markov process. The model is integrated in space over a given magnetic field tube.

7.2 Presentation of the model

7.2.1 Introduction: adiabatic motion and perturbation of the motion

The electron adiabatic motion in the ECRT features oscillations on several time scales, similar to a magnetic bottle (section 2.3.2.1).

Cyclotron motion. In the presence of a strong static magnetic field, the smaller relevant dynamic time scale is that of the cyclotron motion, which has a typical period of 10^{-10} s. Provided that the spatial variation of the magnetic field B inside the electron orbit is small compared to its magnitude [70], this motion is associated to an adiabatic invariant: the magnetic moment $\mu = mv_\perp^2/(2B)$.

Bounce motion. The magnetostatic field in the ECRT is imposed by the magnet and the electrostatic field on axis is known through LIF measurement [64]; typical fields are represented in figure 128. Given those fields, there exists an oscillation motion often called bounce motion along magnetic field lines. In particular, on the axis of symmetry, the equation of motion is

$$m\frac{dv_z}{dt} = -\mu\frac{\partial B_z}{\partial z} + e\frac{\partial \phi}{\partial z} \qquad (190)$$

where m is the electron mass, μ is the magnetic moment, e is the absolute value of the elementary charge and ϕ the electrostatic potential. For certain initial conditions in μ and v_z (that will be spelled out later), this equation describes an oscillating motion for electrons in the concave "effective potential" $U_{eff} = \mu B - e\phi$ with a period referred to as the bounce time τ_B. If B is linearized as $B = B_0(1 - \alpha z)$ and ϕ is assumed to have a concave quadratic shape $\phi = -\phi_0 z^2$ then equation 190 is the equation for a harmonic oscillator. In this case, the magnetic field simply contributes as a constant force, and does not affect the bounce period (of the harmonic oscillator) $\tau_B = 2\pi/\sqrt{2e\phi_0/m_e} \approx 10^{-7}$ s ($\phi_0 \approx 10^{-4}$ to have a ≈ 100 V potential drop over ≈ 10 cm).

Perturbation of adiabatic motion. An Hamiltonian analysis of the system would enable to identify the full angle-action variables, providing the adiabatic invariant associated with the bounce motion as well as a rotation around the axis of symmetry of the system (at a larger time scale), itself associated with a third adiabatic invariant [71]. However, identification of all adiabatic invariants is unnecessary because the adiabatic motion is perturbed at the time scale of the bounce motion. Indeed, every bounce period, electron may undergo interaction with the electromagnetic field. Therefore only the cyclotron adiabatic motion is able to develop (i.e. to display oscillations with constant μ for a certain number of periods) in between two interactions with the electromagnetic field. Two separate idealized regions are considered. The first region, thereafter named the interaction region, is a section of the coaxial chamber containing the ECR slab near the closed end of the source. There, electrons interact both with relatively dense neutral gas able to randomize their velocity vector and with intense microwave field (figure 129) able to change their magnetic moment. In a second region extending to the right (the plume), the electron motion is considered adiabatic. *The approach described in this chapter focuses on the distribution in magnetic moment of confined electrons.*

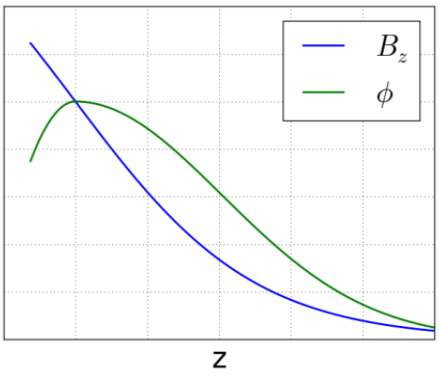

Figure 128. Normalized typical shape of magnetic field and electrostatic potential[12].

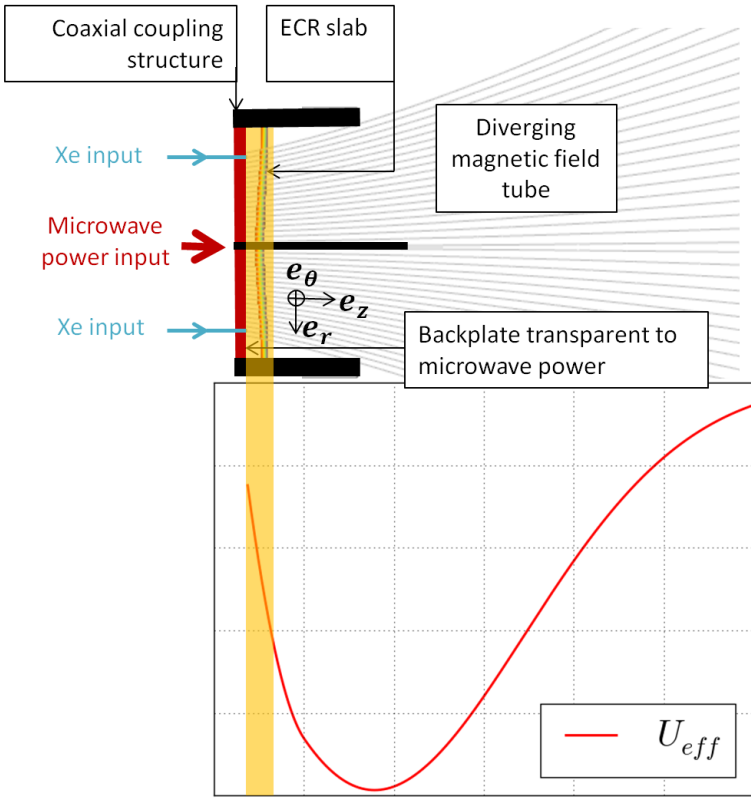

Figure 129. Interaction region (orange slab) and effective potential calculated from the fields in figure 128.

7.2.2 Confinement and deconfinement

The longitudinal confinement is achieved on the left by the converging magnetic field lines as well as the electrostatic potential drop of the sheath formed at the backplate, and on the right by the electrostatic field only. When the electron energy increases through an increase in magnetic moment, the confinement provided to the left by the magnetic field also increases because the repelling force is proportional to μ. Since the microwave power is assumed to be deposited in μ, interaction with the microwave field does not affect the confinement to the left. On the contrary, the electrostatic confinement to the right keeps constant when increasing μ because the repelling force is only proportional to the charge. As a consequence, there exists a certain magnetic moment for which the electron can get out of the potential well to the right, meaning that it exits the thruster in the jet (figure 122).

[12] The shape and thickness of the backplate-sheath were not resolved by the cited LIF measurements. It is represented quite thick for simplicity; the exact shapes of the fields only have little influence in the following.

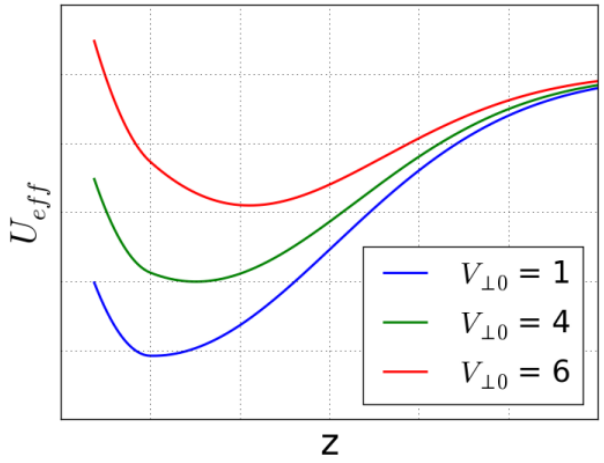

Figure 130. Confining potentials corresponding to the fields of figure 128 for several perpendicular velocities in the interaction region. A velocity in the interaction region corresponds to a magnetic moment.

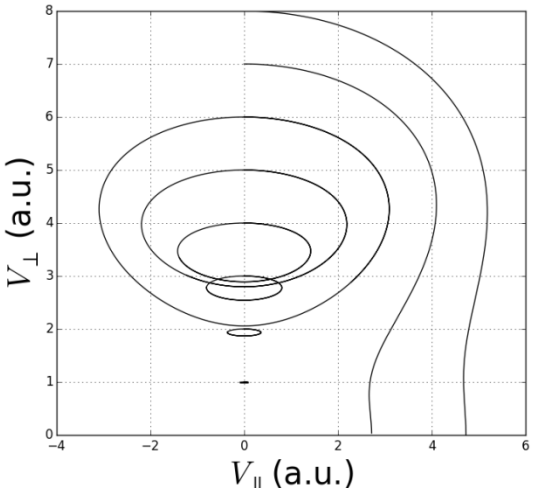

Figure 131. Orbits for $v_{\perp 0} = 1, 2, 3, 4, 5, 6, 7, 8$ and $v_{\parallel 0} = 0$ in the fields of figure 128.

Confinement can also be analysed in velocity space, where closed and open orbits can be plotted by solving the equation of motion for different initial conditions (figure 123). Similarly to the loss cone for a magnetic bottle, there is for our configuration a certain shape of confinement in the $(v_\parallel, v_\perp)$ plane. An example is given in figure 132 for an arbitrary axial location. The shape is delimited by a side boundary and an upper boundary. The side boundary is the result of both electric and magnetic confinement. In our configuration, the magnetic loss cone is the limit for large $v_\perp/v_\parallel$ of a loss hyperboloid. Indeed for large $v_\perp/v_\parallel$ the magnetic confinement is dominant, whereas for small $v_\perp/v_\parallel$ the electric confinement is dominant. The upper boundary is the result of electric confinement. Crossing the upper boundary means exiting in the jet and crossing the side boundary means impacting the backplate.

Collisions may deconfine electrons when their velocity vector after the collision is outside the confinement shape. A collision implies a scattering of the electron velocity vector. For elastic collisions, where the kinetic energy is conserved ($v_\perp^2 + v_\parallel^2 = v_\perp'^2 + v_\parallel'^2$) the electron stays in the same circle centred on zero in the $(v_\parallel, v_\perp)$ plane. The confinement shape, the nature of the collision and the incident velocity, together determine a probably to deconfine the incident electron. As a first approach, only the elastic and ionizing collisions with neutrals are considered. Yet, in the thruster, the gas is injected at the backplate; due to the rapid gas expansion in vacuum and depletion by ionization, electrons are assumed to interact with neutrals only in the interaction region, close to the backplate. In this region, the confinement surface is quite narrow (figure 133) thus we will consider that the deconfinement probability due to a collision is 1. *Therefore, as a first approach, any collision is considered as deconfining the incident electron, resulting in an impact on the backplate and possibly electron emission.*

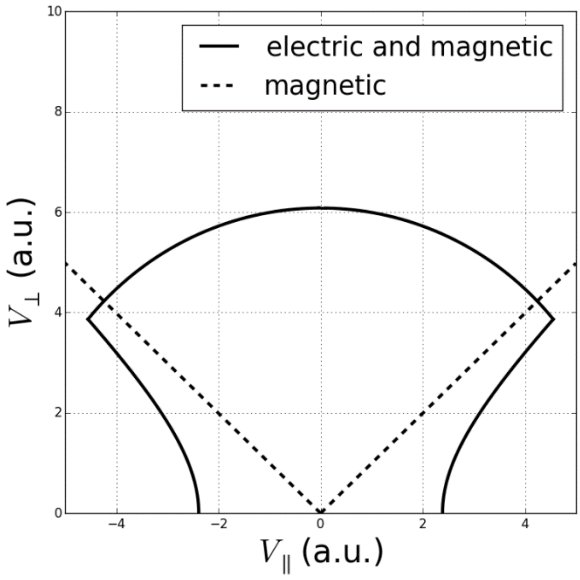

Figure 132. Confinement shape at an arbitrary axial location for the purely divergent magnetic field and convex electric potential of figure 128.

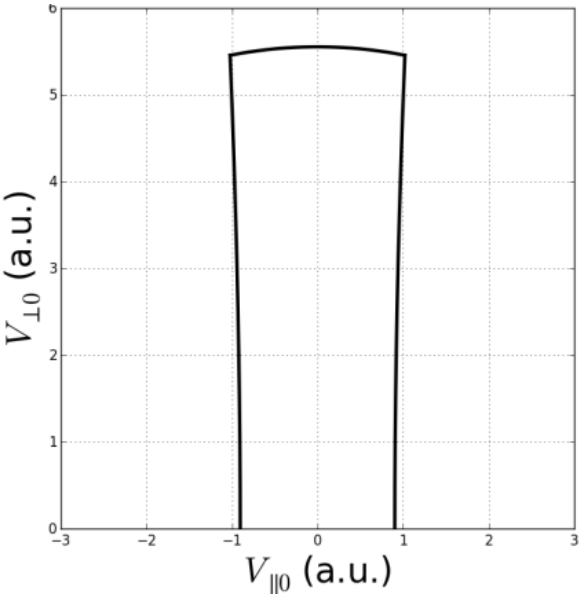

Figure 133. Confinement shape at the axial location of the interaction region for the field of figure 128.

Other deconfinement mechanisms are neglected. Collective effects that may create turbulence or space charge electric field contributing to deconfinement are not considered. Besides, the electron self-induced magnetic field is arguably too weak to cause demagnetization. Coulomb collisions should a priori be considered: as can be seen from figure 31, Coulomb collisions have a relatively large cross-section at low energies (until ~ 50 eV); they comprise electron-ion and electron-electron collisions. The count of electron-electron collisions a priori requires the two particle distribution function which is non-trivial, and all the more that the trajectories are strongly guided by the magnetic field. In general the count of electron-electron collisions requires sophisticated approaches (GOLDSTON section 11.2 [68], DELCROIX section 13 [69]). In contrast, electron-ion collisions could be counted more easily by considering a flux of electrons impinging on fixed ion targets with a certain density. In a first approach however, Coulomb collisions as a whole are not considered.

7.2.3 Heating

7.2.3.1 Derivation of a Fokker-Planck equation

To model the heating process, the Boltzmann integral equation is considered as in RAX (2005) [71]. In addition, it is assumed that the only relevant kinetic parameter for heating is the perpendicular velocity in the interaction region $v_{\perp 0}$ and that the phase difference between the cyclotron motion and the microwave electric field at resonance bears no correlation between two successive passes. If $P(v_{\perp 0}, t)$ is a distribution function and $w(v_1 \leftarrow v_2)$ is a transition rate between v_2 and v_1, modelling the change in velocity for a single pass in the resonant region

$$\frac{\partial P(v_{\perp 0}, t)}{\partial t} = \int [w(v_{\perp 0} \leftarrow v_{\perp 0} + \widetilde{v_{\perp 0}})\, P(v_{\perp 0} + \widetilde{v_{\perp 0}}, t) - w(v_{\perp 0} + \widetilde{v_{\perp 0}} \leftarrow v_{\perp 0})\, P(v_{\perp 0}, t)]\, d\widetilde{v_{\perp 0}}. \quad \textbf{(191)}$$

Under the assumption that the velocity increment is small, that is $\widetilde{v_{\perp 0}} \longmapsto w(v_{\perp 0} \leftarrow v_{\perp 0} + \widetilde{v_{\perp 0}})$ *is a narrow function compared to the distribution function*, a Fokker-Planck equation can be derived from equation 191

$$\frac{\partial P(v_{\perp 0}, t)}{\partial t} = -\frac{\partial}{\partial v_{\perp 0}}\left[\frac{\langle \delta \widetilde{v_{\perp 0}} \rangle}{\delta t} P(v_{\perp 0}, t) - \frac{\partial}{\partial v_{\perp 0}}\left(\frac{\langle \delta \widetilde{v_{\perp 0}} \delta \widetilde{v_{\perp 0}} \rangle}{2\delta t} P(v_{\perp 0}, t)\right)\right] \quad \textbf{(192)}$$

where $\langle \delta \widetilde{v_{\perp 0}} \rangle / \delta t$ and $\langle \delta \widetilde{v_{\perp 0}} \delta \widetilde{v_{\perp 0}} \rangle / \delta t$ are first and second order moments of the transition rate. Because of the micro-reversibility of the short time electron-electromagnetic field interaction, we have $w(v_{\perp 0} + \widetilde{v_{\perp 0}} \leftarrow v_{\perp 0}) = w(v_{\perp 0} \leftarrow v_{\perp 0} + \widetilde{v_{\perp 0}})$ and equation 192 can take the so called quasi-linear form [71]

$$\frac{\partial P(v_{\perp 0}, t)}{\partial t} = \frac{\partial}{\partial v_{\perp 0}}\left[\frac{\langle \delta \widetilde{v_{\perp 0}} \delta \widetilde{v_{\perp 0}} \rangle}{2\delta t} \frac{\partial P(v_{\perp 0}, t)}{\partial v_{\perp 0}}\right]. \quad \textbf{(193)}$$

An additional loss term is inserted in this equation to account for collisions. Collisions are modelled in an idealized way previously discussed: any collision is assumed to deconfine the particle therefore collisions are treated as a plain loss. Moreover $\langle \delta \widetilde{v_{\perp 0}} \delta \widetilde{v_{\perp 0}} \rangle / (2\delta t)$ is thereafter noted as a diffusion coefficient $D(v_{\perp 0})$ for simplification, and also to emphasize that the heating process can be understood as a diffusion in velocity space. Equation 193 can then be recast as

$$\frac{\partial P(v_{\perp 0}, t)}{\partial t} = \frac{\partial}{\partial v_{\perp 0}}\left[D(v_{\perp 0}) \frac{\partial P(v_{\perp 0}, t)}{\partial v_{\perp 0}}\right] - \left(\frac{1}{\tau_{el}} + \frac{1}{\tau_i}\right) P(v_{\perp 0}, t) \quad \textbf{(194)}$$

with

$$\frac{1}{\tau_{el}} = \sigma_{el} k n_g v_{\perp 0}$$
$$\frac{1}{\tau_i} = \sigma_i k n_g v_{\perp 0} \quad \textbf{(195)}$$

where σ_{el} and σ_i are the elastic and ionization cross sections, and k [13] measures the fraction of bounce period spent in the interaction region where the neutral gas density is n_g. It is assumed that the neutral gas density is negligible along the rest of the trajectory.

7.2.3.2 Intuitive stochastic approach

A more "bottom-up" derivation is the following. Let $P(v_{\perp 0}, t)$ be the distribution function such that the number of electrons having their perpendicular velocity in the interaction region in $[v_{\perp 0}, v_{\perp 0} + dv_{\perp 0}]$ is $P(v_{\perp 0}, t) dv_{\perp 0}$. Given this distribution at a time t, let us calculate it at time $t + dt$. We assume that the duration between two successive interactions with the electromagnetic field is τ_B, hence during dt, the fraction of electrons interacting is dt/τ_B. We model the interaction process as a probability $1/2$ to gain a *small* perpendicular velocity increment $\Delta V(v_{\perp 0})$ and a probability $1/2$ to lose $\Delta V(v_{\perp 0})$. Collisions, occurring with period τ_{coll} are modeled as a loss term. This modelling is described by the following relation.

[13] With the shape of the static fields and a certain width where neutral gas is present, k can be quite easily calculated. However, changing k has the same effect as changing n_g so we will first set $k = 1$ and assess the effect of n_g on the model.

$$
\begin{aligned}
&P(v_{\perp 0}, t+dt)dv_{\perp 0} \\
&= +\left(1-\frac{dt}{\tau_B}\right)P(v_{\perp 0}, t)dv_{\perp 0} \\
&+\frac{dt}{\tau_B}\left(\frac{1}{2}P(v_{\perp 0}+\Delta V, t)d(v_{\perp 0}+\Delta V)\right. \\
&\left.+\frac{1}{2}P(v_{\perp 0}-\Delta V, t)d(v_{\perp 0}-\Delta V)\right) \\
&-\frac{dt}{\tau_{coll}}P(v_{\perp 0}, t)dv_{\perp 0}
\end{aligned}
\qquad \textbf{(196)}
$$

Dividing by dt, rearranging, and having $dt \to 0$ we get

$$
\begin{aligned}
\frac{\partial P(v_{\perp 0}, t)}{\partial t}dv_{\perp 0} = &+\frac{1}{\tau_B}\left(\frac{1}{2}P(v_{\perp 0}+\Delta V, t)d(v_{\perp 0}+\Delta V) - P(v_{\perp 0}, t)dv_{\perp 0}\right. \\
&\left.+\frac{1}{2}P(v_{\perp 0}-\Delta V, t)d(v_{\perp 0}-\Delta V)\right) - \frac{1}{\tau_{coll}}P(v_{\perp 0}, t)dv_{\perp 0},
\end{aligned}
\qquad \textbf{(197)}
$$

then, expanding as $d(v_{\perp 0}+\Delta V) = dv_{\perp 0} + (\partial \Delta V/\partial v_{\perp 0})dv_{\perp 0}$ and dividing by $dv_{\perp 0}$

$$
\begin{aligned}
\frac{\partial P(v_{\perp 0}, t)}{\partial t} = &+\frac{\Delta V^2}{2\tau_B}\ \frac{P(v_{\perp 0}+\Delta V, t) - 2P(v_{\perp 0}, t) + P(v_{\perp 0}-\Delta V, t)}{\Delta V^2} \\
&+\frac{1}{2\tau_B}2\Delta V\frac{\partial \Delta V}{\partial v_{\perp 0}}\ \frac{P(v_{\perp 0}+\Delta V, t) - P(v_{\perp 0}-\Delta V, t)}{2\Delta V} - \frac{1}{\tau_{coll}}P(v_{\perp 0}, t).
\end{aligned}
\qquad \textbf{(198)}
$$

By having $\Delta V \to 0$ we get

$$
\frac{\partial P(v_{\perp 0}, t)}{\partial t} = +\frac{\Delta V^2}{2\tau_B}\ \frac{\partial^2 P(v_{\perp 0}, t)}{\partial v_{\perp 0}^2} + \frac{1}{2\tau_B}\frac{\partial \Delta V^2}{\partial v_{\perp 0}}\ \frac{\partial P(v_{\perp 0}, t)}{\partial v_{\perp 0}} - \frac{1}{\tau_{coll}}P(v_{\perp 0}, t)
\qquad \textbf{(199)}
$$

and

$$
\frac{\partial P(v_{\perp 0}, t)}{\partial t} = \frac{\partial}{\partial v_{\perp 0}}\left[\frac{\Delta V^2}{2\tau_B}\frac{\partial P(v_{\perp 0}, t)}{\partial v_{\perp 0}}\right] - \frac{1}{\tau_{coll}}P(v_{\perp 0}, t)
\qquad \textbf{(200)}
$$

which is equivalent to equation 194.

Key assumptions. This derivation makes concrete and apparent two key assumptions already used in the more formal previous derivation.

1. *The random phase assumption* [112] that is used when we suppose that ΔV is independent of the phase of the cyclotron motion or state that the phase "bears no correlation between two successive passes". This assumption supposes the existence of perturbations to the adiabatic motion such that the phase is randomized between two interactions with the electromagnetic field. Under this assumption, the heating is a Markov process, in the sense that the future $v_{\perp 0}$ only depend on the present $v_{\perp 0}$, and that the memory of initial conditions is lost because of randomization of the phase. Whether this widely used random phase assumption (for example [113]) is indeed verified in our device remains, in our understanding, an open question.

2. *The assumption that* ΔV *must be small* in comparison with the scale of the variations of $v_{\perp 0} \mapsto P(v_{\perp 0}, t)$ in order to write a differential equation; this assumption corresponds to "$\widetilde{v_{\perp 0}} \mapsto w(v_{\perp 0} \leftarrow v_{\perp 0} + \widetilde{v_{\perp 0}})$ is a narrow function compared to the distribution function" used in the

more formal derivation. Without this assumption, we are to solve the integral equation 191. Whether this assumption is indeed verified in our device also remains an open question[14].

7.2.3.3 Diffusion coefficient

The calculation of diffusion coefficients in Fokker-Planck models is known to be a delicate issue. As a first step, it is written as

$$D(v_{\perp 0}) = \frac{\Delta V^2}{2\tau_B} \quad (201)$$

where ΔV represents the root mean square of the statistical change in velocity for one pass in the resonant region. ΔV is taken from [114] as

$$\Delta V = 0.71 \frac{e}{m_e} E \, \omega^{-1} \left(\frac{2\omega}{\alpha v_{\perp 0}}\right)^{2/3} \quad (202)$$

where E is the norm of the electric field in the interaction region, α the scale length of variation of B, and ω the frequency of the wave. The derivation of this ΔV supposes that electrons have their mirror point in the interaction region, which is reasonable in our configuration for the following reasons. Let's assume the interaction region lies in the interval $[B_{res}^-; B_{res}^+]$ centered on B_{res}. If $B_{mirror} < B_{res}^-$, then the electron is not heated and is outside the scope of the modelling. If $B_{res}^- < B_{mirror} < B_{res}^+$, then the electron has its mirror point in the interaction region. If $B_{mirror} > B_{res}^+$, it will have its mirror point in the interaction region after a few bounces. Indeed conservation of energy and magnetic moment yield $\mu B_{mirror} = \mu B_{res} + (1/2) m v_{\parallel res}^2$ hence

$$B_{mirror} = \frac{\mu B_{res} + (1/2) m_e v_{\parallel res}^2}{\mu} \quad (203)$$

and $\lim_{\mu \to \infty} B_{mirror} = B_{res}$, assuming that the energy is deposited in the perpendicular direction, hence $v_{\parallel res}$ does not vary. In practice, given the width of the interaction region, a moderate increment in μ is sufficient to bring B_{mirror} in $[B_{res}^-; B_{res}^+]$. It seems to happen in typically one or a few bounces as was observed by solving numerically the electron equation of motion.

7.2.4 Boundary conditions

7.2.4.1 Particle balance equation

The velocity spread of the distribution function P is bounded at low energy by v_0 which is the mean energy of the electrons produced by secondary electron emission and ionization events in the interaction region. These electrons are supposed to have a velocity of a few eV [115], [116]. It was verified that the results of the model do not depend on the exact value of v_0. Electrons which have gained enough kinetic energy will leave the potential well when $v_{\perp 0} \geq v_*$. Above that value P is zero.

[14] Regarding this assumption we observe conflicting hints. The relatively narrow electron distribution function observed for low grid potential, suggests an energy gain taking place by small increments as commented in section 4.1.4, and thus supports the assumption. We also solved numerically the full equations of motion for static fields representing those in the ECRT and in the presence of an electromagnetic field with an ECR resonance. The results feature sometimes large energy gains, in particular for small initial magnetic moment thus refuting the assumption.

The total number of electrons is $N = \int_{v_0}^{v_*} P(v_{\perp 0}, t) dv_{\perp 0}$ thus equation 194 can be integrated to get the particle balance

$$\frac{dN}{dt} = -F_* + F_0 - L_{el} - L_i \quad \textbf{(204)}$$

where all terms are positive. F_* is the particle flux lost in the jet, F_0 is a source term, L_{el} and L_i are the loss terms due to elastic collisions and ionization.

$$L_i \coloneqq \int \frac{P(v_{\perp 0}, t)}{\tau_i(v_{\perp 0})} dv_{\perp 0}$$
$$L_{el} \coloneqq \int \frac{P(v_{\perp 0}, t)}{\tau_{el}(v_{\perp 0})} dv_{\perp 0} \quad \textbf{(205)}$$

If the only creation term of low energy electrons is the ionization, then $F_0 = L_i$ and the balance equation is $dN/dt < 0$, meaning that no steady state can be reached. We see that an additional electron creation mechanism is required to sustain a steady regime. Accounting for electron induced[15] electron emission at the backplate, we consider that

$$F_0 = L_i + \bar{\sigma}(L_i + L_{el}), \quad \textbf{(206)}$$

where $\bar{\sigma}$ is the emission coefficient, defined as a ratio of emitted to incident electron fluxes. Under this condition, a steady regime is possible

$$F_* = (\bar{\sigma} - 1)L_{el} + \bar{\sigma} L_i \quad \textbf{(207)}$$

provided that $L_{el}/L_i \leq \bar{\sigma}/(1 - \bar{\sigma})$. This inequality is not very constraining since $\bar{\sigma}$ is likely very close to 1. The flux of electrons in the jet is related to electron emission at the backplate by equation 207.

7.2.4.2 Emission coefficient

For a floating wall at steady state, charge conservation implies

$$\Gamma_e^+ - \Gamma_e^- = \Gamma_i^+ - \Gamma_i^- \quad \textbf{(208)}$$

where the terms account for incoming and emitted fluxes at the wall, + indicating a flux pointing to the wall. Assuming that all incoming ions are neutralized at the wall we have $\Gamma_i^- = 0$. Then, since ion induced electron emission is negligible [117] we may write the emitted electron flux as $\Gamma_e^- = \bar{\sigma}\Gamma_e^+$ and

$$\Gamma_e^+(1 - \bar{\sigma}) = \Gamma_i^+ \quad \textbf{(209)}$$

with

$$\bar{\sigma} = \frac{\int_{v_x=-\infty}^{+\infty} \int_{v_y=-\infty}^{+\infty} \int_{v_z=0}^{+\infty} \sigma(\boldsymbol{v}) v_z f(\boldsymbol{v}) dv_x dv_y dv_z}{\int_{v_x=-\infty}^{+\infty} \int_{v_y=-\infty}^{+\infty} \int_{v_z=0}^{+\infty} v_z f(\boldsymbol{v}) dv_x dv_y dv_z} \quad \textbf{(210)}$$

[15] It seems that ion induced electron emission is negligible compared with electron induced electron emission at the energy of interest (10-200 eV) [117]. The emission seems to be decreasing with ion mass. For Xenon impact on MgO (a good emitter) the yield is below 0.02 [118], however that value may differ for boron nitride.

where f is the electron energy distribution function at the wall. The z-axis is normal to the wall and oriented towards the wall. The function $\sigma(\boldsymbol{v})$ is the electron emission yield measured by shooting single electrons on the surface. In this context its angular dependence is not considered so it is written as a function of energy $\sigma(\epsilon)$. It is independent of plasma conditions, contrary to $\bar{\sigma}$. Assuming a monotonous sheath potential and no collisions in the sheath, $\bar{\sigma}$ can be calculated from $\sigma(\epsilon)$ and the electron distribution function at the sheath edge. Furthermore, if the distribution is maxwellian, and $\sigma(\epsilon)$ is linear, the calculation is straightforward and $\bar{\sigma}$ is linear with electron temperature. HOBBS AND WESSON (1967) [119] calculated the sheath potential drop under these assumptions as

$$\Delta\phi = T_e \ln\left((1-\bar{\sigma})\sqrt{M_i/2\pi m_e}\right). \quad (211)$$

The derivation of this relation is valid for $\Delta\phi \geq 0$ only, yielding an upper limit for $\bar{\sigma}$, depending on ion mass. It is $\bar{\sigma}_{max} = 0.985$ for Xenon. When $\bar{\sigma}$ approaches $\bar{\sigma}_{max}$, a non-monotonous potential forms near the wall that traps a fraction of the emitted electrons [116], [120]–[122]. This regime is called space charge saturation or space charge limited regime; the transition between this regime and the monotonous regime can give rise to an oscillating regime. In any case it is clear already from equation 209 that $\bar{\sigma} \leq 1$. *In our modelling, we will take* $\bar{\sigma} \lesssim 1$. *The precise value of* $\bar{\sigma}$ *is not critical since we do not solve for the sheath.*

Three processes of electron emission are generally distinguished: true secondary emission of an electron initially present in the material (emission at a few eV), elastic backscattering of the incident electron (emission at the energy of the incident electron), and inelastic backscattering of the incident electron (emission at a fraction of the energy of the incident electron). It appears that the first process is dominant above a few tens of eV [115] so we may neglect backscattering processes.

7.2.5 Energy balance equation

An energy balance equation is derived from equation 194. Multiplying by the kinetic energy and integrating by parts yields

$$\begin{aligned}
&\int \frac{\partial P(v_{\perp 0},t)}{\partial t}\frac{1}{2}m_e\, {v_{\perp 0}}^2\, dv_{\perp 0} \\
&= \left[D(v_{\perp 0})\frac{\partial P(v_{\perp 0},t)}{\partial v_{\perp 0}}\frac{1}{2}m_e\, {v_{\perp 0}}^2\right]_{v_0}^{v_*} \\
&- \int_{v_0}^{v_*} D(v_{\perp 0})\frac{\partial P(v_{\perp 0},t)}{\partial v_{\perp 0}} m_e\, v_{\perp 0} dv_{\perp 0} \\
&- \int_{v_0}^{v_*} \left(\frac{1}{\tau_{el}}+\frac{1}{\tau_i}\right) P(v_{\perp 0},t)\frac{1}{2}m_e\, {v_{\perp 0}}^2\, dv_{\perp 0}
\end{aligned} \quad (212)$$

where v_* is the velocity above which electrons are lost in the jet and v_0 is the mean velocity of electrons created at low energy by ionization and electron emission at walls. The first term on the right hand side accounts for the energy flux related to those electrons. The second term is a heating term that is identified as the microwave power input in the system

$$P_{in} = -\int_{v_0}^{v_*} D(v_{\perp 0})\frac{\partial P(v_{\perp 0},t)}{\partial v_{\perp 0}} m_e\, v_{\perp 0} dv_{\perp 0}. \quad (213)$$

The third term accounts for the power lost because of collisions. Under the assumptions of this model, this power is deposited at the backplate. Let us define

$$K \coloneqq \int_{v_0}^{v_*} \left(\frac{1}{\tau_{el}} + \frac{1}{\tau_i}\right) P(v_{\perp 0}, t) \frac{1}{2} m_e \, {v_{\perp 0}}^2 \, dv_{\perp 0}. \quad (214)$$

7.2.6 Neutral gas depletion

A balance equation for neutral gas density n_g is considered, including a source term for the gas inlet ψ_g, two integral loss terms accounting for collisions, and a loss term $V_{th} \, S \, n_g$ which is the flux of gas escaping to the right from the interaction region. V_{th} is the gas velocity which is typically the thermal velocity, and S is the area where the gas escapes which is typically the thruster section. The density of gas is assumed to be zero outside of the interaction region and have a constant value inside

$$\frac{\partial n_g}{\partial t} = \psi_g - V_{th} \, S \, n_g - \bar{\sigma} \, L_i + (1 - \bar{\sigma}) L_{el}. \quad (215)$$

The coefficients multiplying L_i and L_{el} are decided as follows. An ionizing collision implies not only the immediate the loss of a neutral (-1) but also the impact of the colliding electron on the backplate (see section 7.2.4.2) hence the recombination of $1 - \bar{\sigma}$ ions at the backplate (relation 209), hence the creation of $1 - \bar{\sigma}$ neutrals. An elastic collision implies the impact of the colliding electron on the backplate hence the creation of $1 - \bar{\sigma}$ neutrals, for the same reason.

7.2.7 Equations to be solved

The steady state equations 194, 206, 212, and 215 are to be solved. They are recast as the following system 216-219, where 216 is an ordinary differential equation for $P(v_{\perp 0})$ associated with the initial condition (P_0, F_0), and the following are integral equations.

$$\frac{\partial}{\partial v_{\perp 0}} \left[D(v_{\perp 0}) \, \frac{\partial P(v_{\perp 0})}{\partial v_{\perp 0}} \right] - \left(\frac{1}{\tau_{el}} + \frac{1}{\tau_i}\right) P(v_{\perp 0}) = 0 \quad (216)$$

$$F_0 = -D(v_{\perp 0}) \frac{\partial P(v_{\perp 0})}{\partial v_{\perp 0}}\bigg|_{v_0} = (1 + \bar{\sigma}) \, L_i + \bar{\sigma} \, L_{el} \quad (217)$$

$$\psi_g = V_{th} \, S \, n_g + \bar{\sigma} \, L_i - (1 - \bar{\sigma}) L_{el} \quad (218)$$

$$P_{in} = K + F_* \frac{1}{2} m_e \, {v_*}^2 - F_0 \frac{1}{2} m_e \, {v_0}^2 \quad (219)$$

We solve an optimization problem for (P'_0, F'_0), of the function

$$\begin{aligned} H(P'_0, F'_0) \coloneqq & \left(\frac{[(1 + \bar{\sigma}) \, L_i + \bar{\sigma} \, L_{el}]}{F_0} - 1 \right)^2 \\ & + \left(\frac{\left[V_{th} \, S \, n_g + \bar{\sigma} \, L_i - (1 - \bar{\sigma}) L_{el}\right]}{\psi_g} - 1 \right)^2 \\ & + \left(\frac{\left[K - F_* \frac{1}{2} m_e \, {v_*}^2 - F_0 \frac{1}{2} m_e \, {v_0}^2\right]}{P_{in}} - 1 \right)^2 \end{aligned} \quad (220)$$

under the constraint of equation 216.

In practice, we start with a guess on (P'_0, F'_0) and run a loop wherein

1. the ordinary differential equation 27 is solved with initial condition (P'_0, F'_0),
2. function H is evaluated using the obtained $P'(v_{\perp 0})$, and
3. (P'_0, F'_0) is updated by the optimization solver.

The loop is run until H is sufficiently small. The input parameters to be set are S, V_{th}, P_{in} , ψ_g, $\bar{\sigma}$, the function $D(v_{\perp 0})$, and the functions $\sigma_{el}(v)$ and $\sigma_i(v)$. The code is written in Python, scipy.integrate.odeint is used as ODE solver for step 1, and scipy.optimize.fmin is used as optimization solver for step 3. All quantities are normalized by typical values.

7.3 Results

7.3.1 Choice of input parameters and interpretation of the results

The main parameters to be set for each run of the model are the area of the exit section S, the velocity of neutral gas V_{th}, the input power P_{in}, the Xenon flow rate ψ_g, and the electron emission coefficient at the backplate $\bar{\sigma}$, which is a supposed average value over incident energy. We will take $S = 5.9\ 10^{-4}$ m and $V_{th} = 236$ m/s. The input power typically ranges between 10 and 50 W and the xenon mass flow rate is typically between 0.04 and 0.4 mg/s, and the emission coefficient $\bar{\sigma} \lesssim 1$. In addition, ionization and elastic cross section for Xenon are taken from [123].

Besides, in order to set the diffusion coefficient $D(v_{\perp 0}) = \left(\Delta V(v_{\perp 0}, E_{\mu\lambda})\right)^2 / 2\tau_B$, an estimate of the norm of the microwave electric field E in the interaction region has to be assumed, as well as a value for the bounce period τ_B. The bounce period τ_B is taken as in section 7.2.1. As a first guess, the norm of the microwave electric field is taken to be the average value $\overline{E_{\mu\lambda}}$ over the section of the coaxial coupling structure of the thruster, of the TEM mode of the coaxial line. If R_1 and R_2 are the diameters of the inner conductor and outer conductor respectively, straightforward analytical calculation provides a relation between $\overline{E_{\mu\lambda}}$ and the power flowing in the coaxial line, identified to P_{in},

$$\mathrm{P}_{in} = \frac{1}{4}\sqrt{\frac{\epsilon_0}{\mu_0}}\pi \ln\left(\frac{R_2}{R_1}\right)(R_2 + R_1)^2 \overline{E_{\mu\lambda}}^2 = 1.14\ 10^{-6}\ \overline{E_{\mu\lambda}}^2. \qquad (221)$$

For reference, we want to compare the result of the model with a maxwellian distribution. Starting with a maxwellian in Cartesian coordinates $f_M^{Ca}(v_x, v_y, v_z) = (m/2\pi kT)^{3/2}\ exp(-m\boldsymbol{v}^2/2kT)$, we transform to cylindrical coordinates $f_M^{Cy}(v_\perp, \theta, v_\parallel) = (m/2\pi kT)^{3/2}\ v_\perp exp\left(-m(v_\perp^2 + v_\parallel^2)/2kT\right)$ and integrate over θ and $v_\parallel$ to obtain the relevant function to compare with, $P_M(v_\perp) = (m\ v_\perp / kT)\ exp(-mv_\perp^2/2kT)$. We will plot it with the same mean energy as the result function from the model.

A typical curve of $P(v_{\perp 0})$ is shown in figure 134, having a mean electron kinetic energy (temperature) of 95 eV. This curve is the electron distribution function in perpendicular-velocity-in-the-interaction-region, spatially integrated over the full thruster. For convenience, the *same* function is plotted as a function of kinetic energy in figure 135 (i.e. it is *not* a distribution function in energy). In comparison with the maxwellian, the distribution appears truncated at high energy. Besides, the distribution is monotonically decreasing whereas the maxwellian is increasing at low energy. The diffusion coefficient used for this calculation is presented in figure 136. The local particle balance is illustrated in figure 137: the net incoming flux in $[E; E + dE]$ due to diffusive transport (heating) is balanced by losses due to collisions.

The zero of $P(v_{\perp 0})$ *is interpreted as the confinement threshold, thus as the ion energy.* The interpretation *is as follows.* Since electron energy is gained by small increments, the confinement threshold is the energy of electrons exiting the thruster through the jet. Far enough from the thruster, where the magnetic and electrostatic field reach their zero asymptotic value, conservation of magnetic moment and energy for electrons implies that the energy is fully contained in parallel kinetic energy. If we equate the energy of an electron-ion pair, first in the interaction region and then far from the thruster we get

$$\frac{1}{2}m_e {v_*}^2 = \frac{1}{2}m_e {v_\parallel}^2 + \frac{1}{2}M_i {V_i}^2 \qquad \textbf{(222)}$$

where m_e and M_i, $v_\parallel$ and V_i , are the mass and average parallel velocity in the jet for electrons and ions respectively. Since the thruster is electrically isolated, the ion flux (mainly constituted of singly charged ions) equals the electron flux in permanent regime. Besides, where the fields reach their asymptotic values, the plasma is still at a density where quasi neutrality is required, implying that the average electron and ion velocities are the same: $v_\parallel = V_i$. Since $m_e \ll M_i$, we get that far enough from the thruster ions carry all the kinetic energy. The energy transfer from electrons to ions is achieved through the establishment of an electrostatic potential (cancelled out in relation 222 by considering an electron-ion pair).

The slope of the curve at its zero is interpreted as the flux of electrons exiting the thruster through the jet, hence the ion flux, since the thruster is electrically isolated. The model therefore provides a value for ion energy and ion flow. In the case represented in figure 134 and figure 135 the ion energy is 431 eV and the ion flow is 0.48 of the input neutral gas flow, which are values in the range of what can be measured experimentally for the ECRT. Note that no tuning of the model was performed; we just set the input parameters to what we deemed the best available estimate. The dynamics in the magnetic nozzle being at least a 2 dimensional problem in space, this model cannot provide an angular ion flow profile. Therefore, thrust can be estimated only if we provide an ion flow profile (or divergence efficiency).

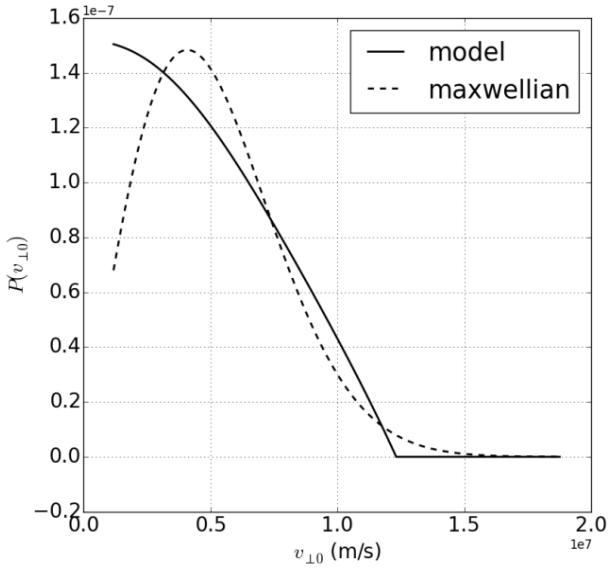

Figure 134. $P(v_{\perp 0})$ for P_{in} = 20 W, ψ_g= 96 µg/s, $E_{\mu\lambda}$ = 4200 V/m, $\bar{\sigma}$ = 1.0. The integral is normalized to 1.

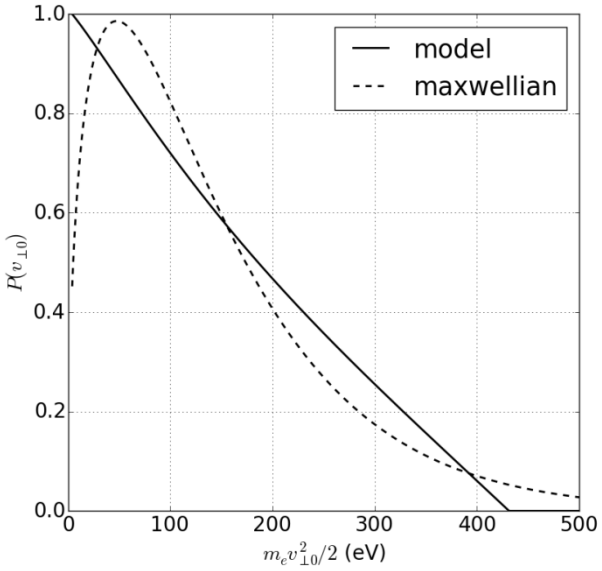

Figure 135. $P(v_{\perp 0})$ plotted as a function of kinetic energy for P_{in} = 20 W, ψ_g= 96 µg/s, $E_{\mu\lambda}$ = 4200 V/m, $\bar{\sigma}$ = 1.0. The initial value is normalized to 1.

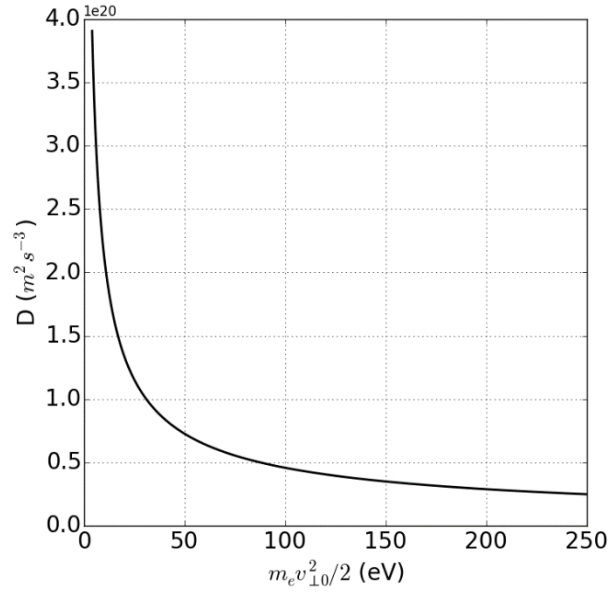

Figure 136. Diffusion coefficient.

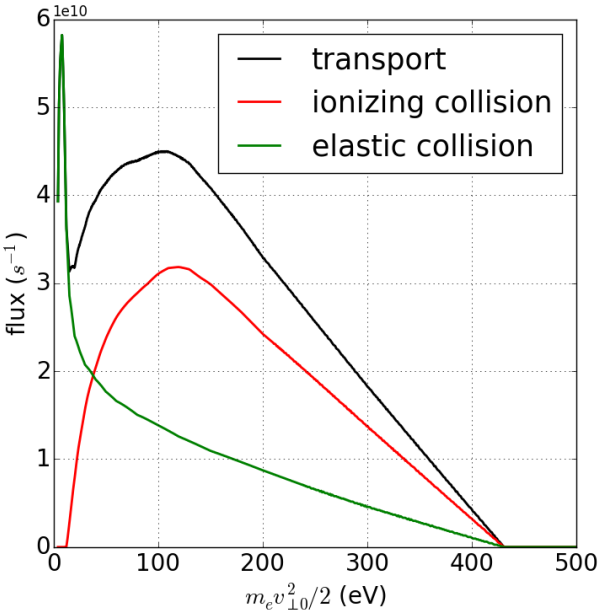

Figure 137. Particle balance in $[E; E + dE]$. The peak of elastic collisions at low energy is due to a peak in the cross section.

7.3.2 Parametric analysis

A parametric analysis helps to get familiar with the content of the model. To analyze the results, we plot the mass efficiency $\eta_m = F_*/\psi_g$, the power efficiency $\eta_E = (F_* m_e v_*^2/2)/P_{in}$, the thrust $T = F_* M v_*$ (using Xenon and neglecting all divergence effect) and the neutral gas density n_g. The distributions are

plotted as a function of energy because electron-volts are more practical. However, it makes the particle balance less apparent because PdE is *not* a number of particles.

Deposited power. When the deposited power is increased, the number of particle is increased and the outgoing ion and electron flow, as well as the outgoing energy, are increased (figure 94). These variations derive from the energy balance: an increase of the deposited power is balanced first, by an increase of both the outgoing flow (or mass efficiency) and the outgoing energy, and second, by an increase of the number of electrons (responsible for increased losses). This latter phenomenon becomes less and less efficient as the neutral gas is depleted (since losses are proportional to n_g), yielding a relatively constant power efficiency.

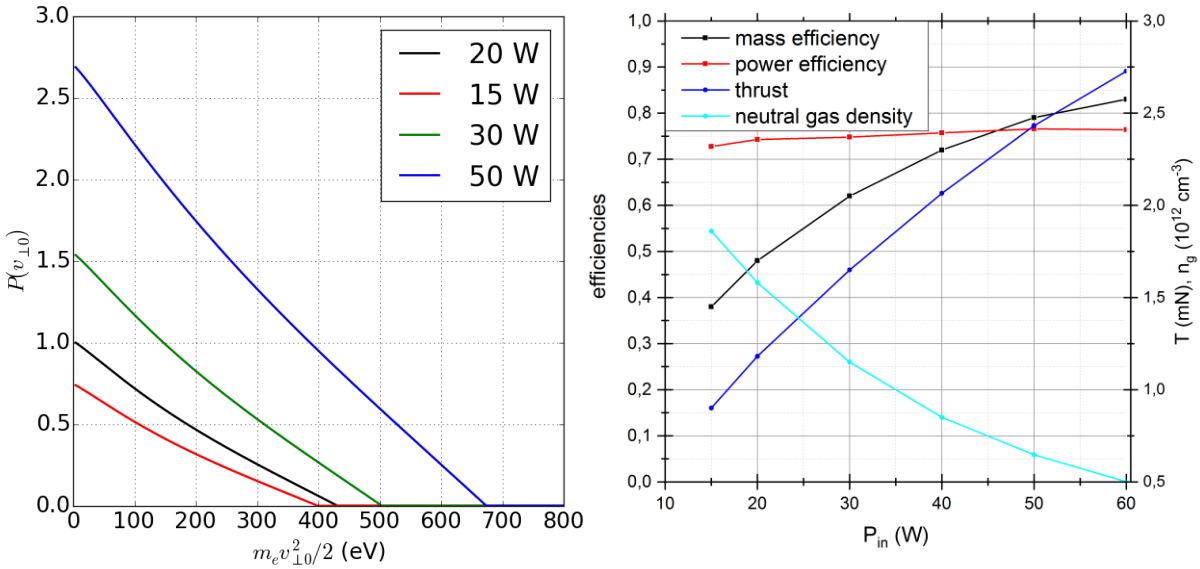

Figure 138. Parametric sweep in deposited power P_{in}, for ψ_g= 96 µg/s, $E_{\mu\lambda}$ = 4200 V/m, $\bar{\sigma}$ = 1.0. Left: electron distribution; right: other model outputs.

Neutral gas flow. When neutral gas flow is increased (figure 139), losses due to collisions are increased. The energy balance is ensured by a significant decrease of the number of electrons and a slight decrease of the outgoing power flow as indicated by the power efficiency. Besides, we observe that the outgoing flow is decreasing when the number of electrons in the system increases, which may appear counterintuitive (as we may think the flux is proportional to the density of electrons). The relative increase of thrust, say when flow rate is doubled, is small as compared to that when the power is doubled. The general slope of the graph of P can be understood as a competition between losses which tend to steepen the curve and diffusion which tends to stretch out the distribution towards high energy.

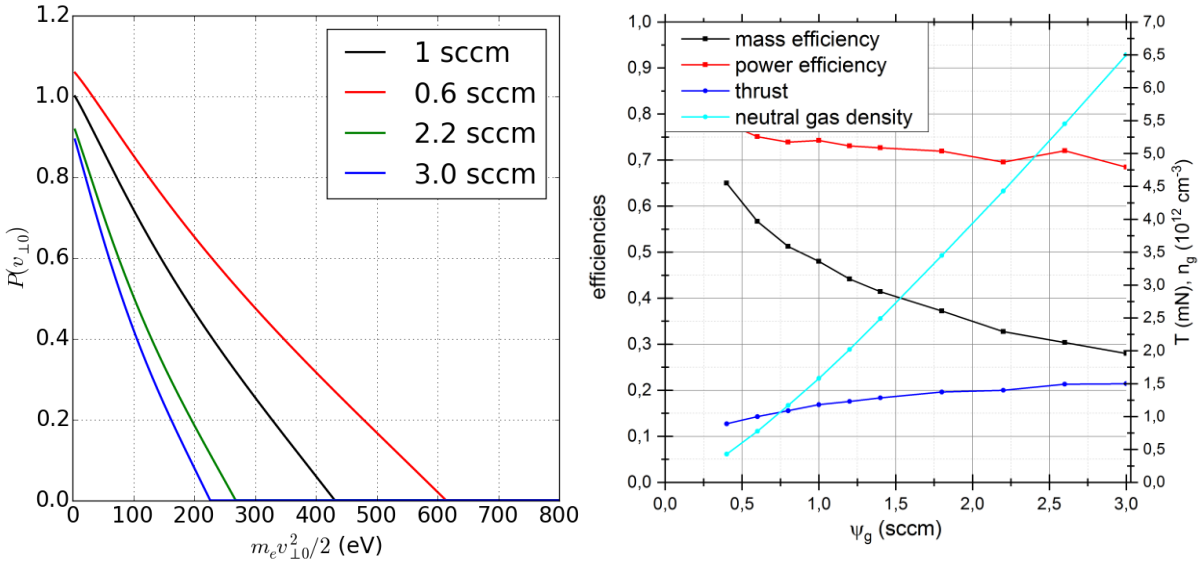

Figure 139. Parametric sweep in neutral gas flow ψ_g, for $E_{\mu\lambda}$ = 4200 V/m, $\bar{\sigma}$ = 1.0, P_{in} = 20 W. Left: electron distribution; right: other model outputs.

Diffusion coefficient. When the diffusion coefficient is increased, the outgoing electron and ion flux decreases and the outgoing power flux increases; overall, thrust decreases (figure 140). The number of particles also decreases while the neutral gas density increases; overall, the power losses decrease as indicated by an increase of the power efficiency. The effect of the diffusion coefficient can also be understood by focusing on a single electron: a higher coefficient will transport electrons more quickly towards high energies, hence limiting their residence time in the thruster and their interaction with neutral gas. As consequence, the higher the coefficient, the lesser the total number of electrons, and the higher the neutral gas density.

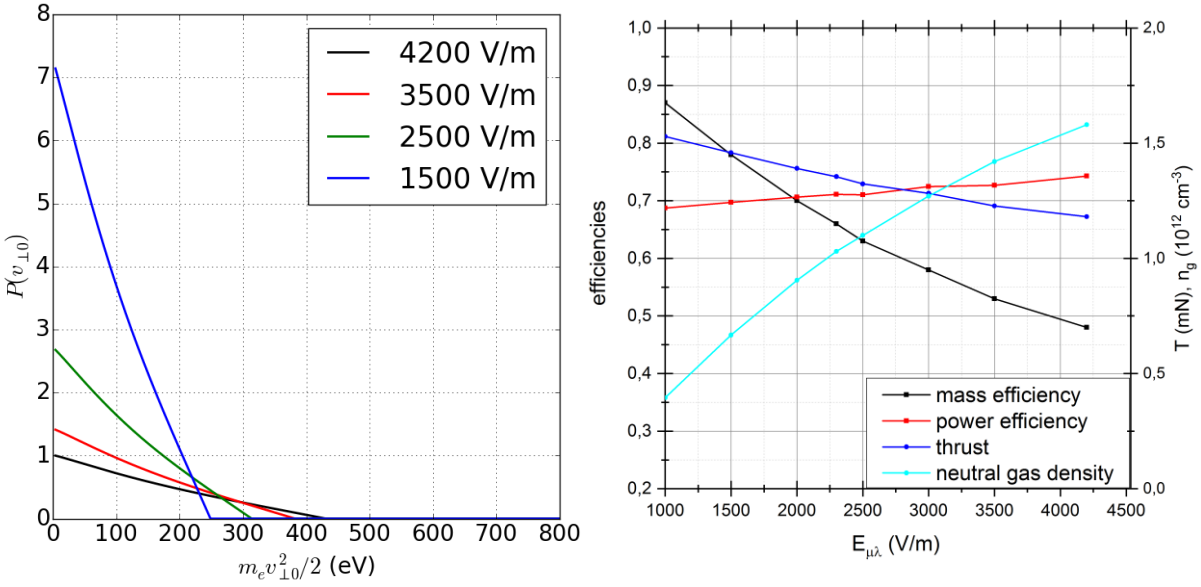

Figure 140. Parametric sweep in diffusion coefficient (varied using $E_{\mu\lambda}$), for $\bar{\sigma}$ = 1.0, P_{in} = 20 W, ψ_g = 96 µg/s, Left: electron distribution; right: other model outputs.

Emission coefficient. The emission coefficient influences the shape of the curve, instead of just its slope or magnitude, as for the previous parameters. This likely originates in the fact that the emission coefficient influences the particle balance equation without significantly influencing the energy balance

equation. Indeed, when an electron undergoes a collision its energy is lost and the fact that it causes an emission has only little effect on the energy balance because the emission energy is very small as compared to the average energy of the distribution. The total number of electrons is almost constant over all tested emission coefficients (which is not apparent in figure 141 because the distribution is plotted versus energy). When decreasing the emission coefficient, the power efficiency decreases dramatically, because of higher power losses related to an increase in neutral gas density and a stretch of the distribution towards higher energies.

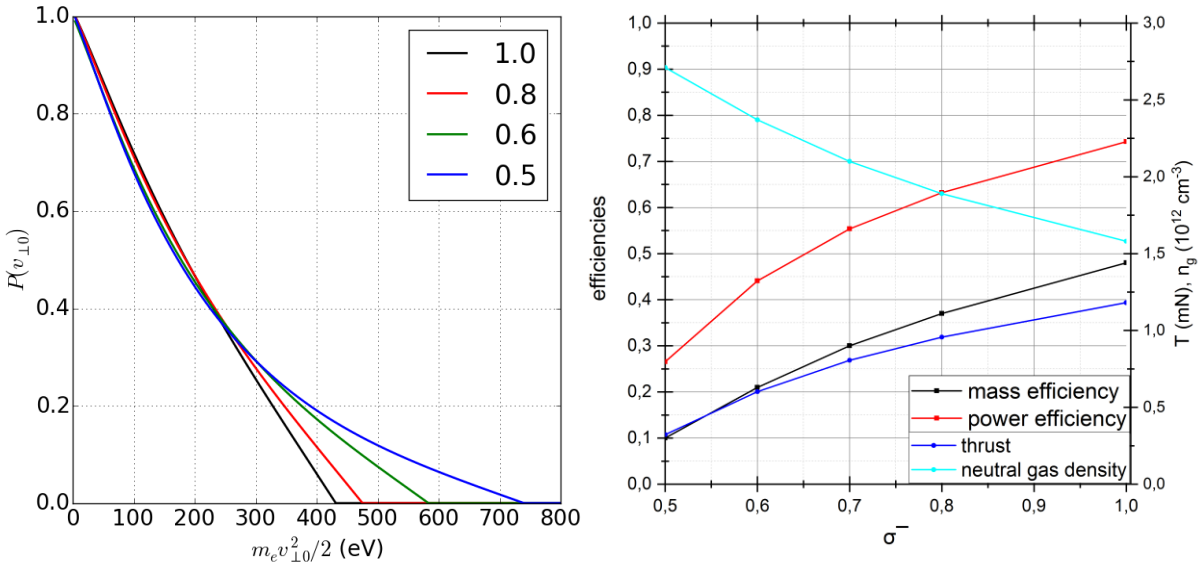

Figure 141. Parametric sweep in emission coefficient $\bar{\sigma}$, P_{in} = 20 W, ψ_g= 96 µg/s, $E_{\mu\lambda}$ = 4200 V/m. Left: electron distribution; right: other model outputs.

The results of the model exhibit the main expected tendencies in regard of our intuition of the system based on experiments: increase of the ion energy and the outgoing ion flow when increasing the deposited power, decrease of the ion energy and increase of the outgoing ion flow when increasing the neutral gas flow. A remarkable feature is the very high power efficiency of the system which is related to the treatment of power losses. They are roughly proportional to $n_g n_e$, because they originate only in electron-neutral collisions. As a consequence, since the increase of the number of electrons is associated with neutral gas depletion, power losses keep relatively constant even though the number of electrons is increased considerably. This observation may invite to a more careful modelling of losses; as suggested earlier, a model of anomalous cross filed diffusion (likely proportional to n_e^2) is a perspective for future development.

7.3.3 Preliminary comparison with experimental data

Comparison with experimental data is tempting to check rough quantitative agreement and tendencies. However, given the simplicity of the model and the measurement difficulties, quantitative agreement is not expected. On the one hand, measurements based on ion current measurement suffer very large uncertainties and on the other hand thrust is reliably measured, but can only be compared to results of the model if we suppose a divergence of the jet. Ion energy is perhaps the best quantity for making a comparison. More importantly, all measured quantities dramatically depends on vacuum tank pressure (section 4.2), a parameter that is ignored in the model. In addition, experiments have also shown that the nature of the materials in contact with the plasma (almost ignored in the model) can have a considerable and unexplained effect, questioning the relevance of a comparison with experiments at this stage. In particular we will not attempt to tune the model parameters in order to obtain matching with

experimental data. This could be done at a later stage; in particular the diffusion coefficient could be reconsidered in regards of experimental results.

In spite of these considerations a preliminary comparison with experimental data is presented in figure 142 and figure 143. Both experimental and calculated ion energies exhibit a linear increase with a similar slope with respect to power; the calculated data has a 250 eV off-set with respect to measurements. As for thrust, both experimental and calculated data exhibit a linear increase with respect to power, although with a different slope. A decrease in tank pressure would bring the experimental considerably closer to the model. However, the available data to date at $\sim 10^{-7}$ mbar is insufficient to look at trends as a function of power or flow rate. If the discrepancy is confirmed for measurements performed at lower pressure, it would again suggest the necessity of an additional loss mechanism in the model.

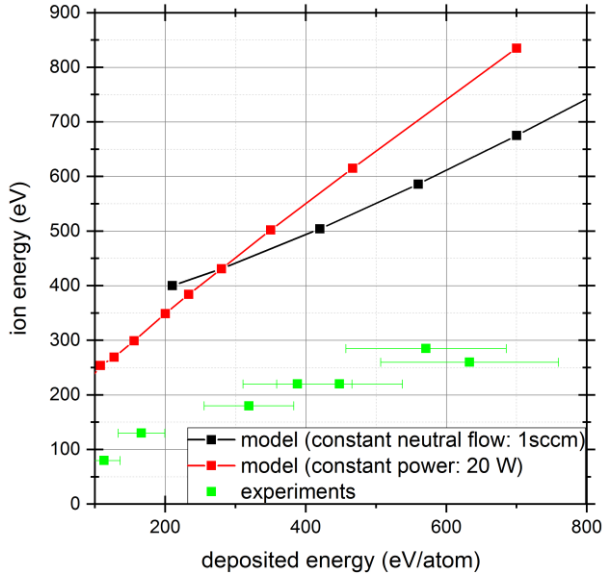

Figure 142. Ion energy as a function of deposited electron-volt per injected neutral atom. The model results are those from figure 94 (supposing $\eta_D = 1$). Experimental data is from chapter 6.

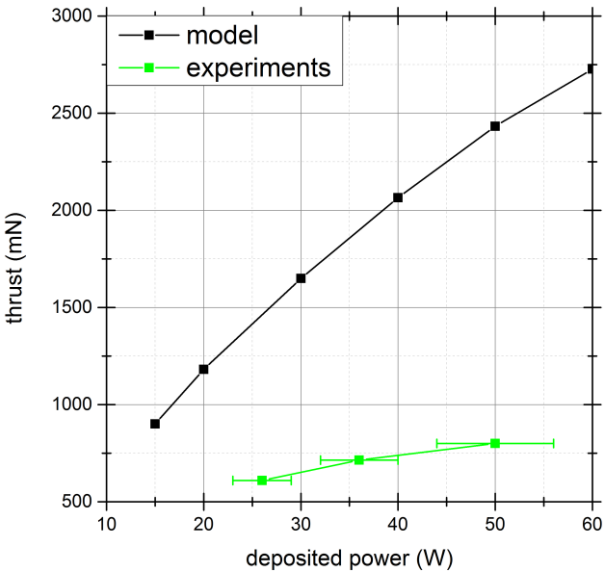

Figure 143. Thrust as a function of deposited power. The model results are those from figure 94 (supposing $\eta_D = 1$). Experimental data taken from ([24], figure 102).

7.4 Summary

A novel approach to model the ECRT was presented. It is based a Fokker-Planck equation modelling electron heating as a Markov system evolving by small increments in perpendicular velocity. Electron trajectories were studied in the specific static fields and geometry of the ECRT. From this analysis, a diffusion coefficient in perpendicular velocity is proposed as well as a way to model losses. Additional equations are considered: an energy balance equation and a neutral gas balance equation. The main output of the model is the distribution function in magnetic moment of the confined electron population. From this function we deduce the ion flux and the ion energy. Orders of magnitude are coherent with experimental measurement however quantitative comparison reveals that the calculated ion energy and thrust are in excess as compared to experiments. This comparison is made for reference but was not expected to yield good quantitative agreement for all parameters since measurements are very sensitive to phenomena ignored by the model. In particular, a decrease in tank pressure would bring the experimental data much closer to experiments. This model can be thought of as “an instructive model”

as defined by Peierls (1980) [124], in the sense that it provides insight although it does not receives quantitative justification.

Having the intensity of the microwave field (appearing in the diffusion coefficient) as an input parameter and having mass efficiency as an output parameter is an improvement as compared to the available ECRT model [29], [32]. The intensity of the microwave field, decoupled from the deposited power, may enable to discriminate between the waveguide-coupled thruster and the coaxial-coupled thruster. For example the diffusion coefficient could depend on the radial coordinate, to represent the distinct radial dependences of the intensity of the microwave field. Besides, future development could look at different ways to calculate the diffusion coefficient. It could also be fitted in a particular experimental configuration to test the validly of the rest of model against experimental data. Additional loss mechanisms such as anomalous cross-field mobility and Coulomb collisions could also be implemented. With the static field and the distribution function provided by the model, the distribution in space along the axis of the thruster could be deduced.

8. Conclusion

The work presented in this document obtained eight main results, thereafter stated along with suggested future work.

(1) The control of the thruster set-point was improved, both by modification of the thruster design, as well as by modification of the experimental set-up and procedures. These vital improvements successfully addressed the main issues previously impeding repeatable measurements for the ~ 30 W thruster. With an updated solution for the microwave feedthrough, the design proved to be successful for the operation of a ~ 200 W thruster in steady state.

(2) The discrepancy between thrust balance measurements and electrostatic probe measurements was investigated systematically, ruling out several possible error causes. This investigation is necessary to understand the thruster; it brought insight on the plasma dynamics in the thruster. The cause of the discrepancy however was not yet found; we suggested the investigation of the real direction of ion current in the nozzle as the next step, and we built an electrostatic diagnostic for this purpose. The investigation of the location of detachment is also an area for future research.

(3) The performance of the ONERA prototype was confirmed for the first time in a different test environment and a different laboratory (than ONERA), thus increasing our confidence in the measured performance. Some discrepancies were however observed and several different causes are possible; it is difficult to discriminate between them based on the available data. Futures tests campaign will certainly shed light on this matter.

(4) The marked tendency to improved thruster performance when decreasing background pressure was explored down to ~ 10^{-7} mbar Xenon. Introducing background gas in the numerical models will certainly help understanding the detailed physics at play in this effect.

(5) The thruster design was improved to obtain not only better repeatability but also improved performance and improved lifetime, thus achieving the goal set in the introduction. From several coupling structure materials that were tested, graphite was chosen because it yields very good thruster performance and lifetime likely over 1000 hours (for the ~ 30 W thruster). Change of the magnetic field topology and the nozzle boundary conditions were shown to have a strong potential for future performance improvement. Optimization of these parameters as a first priority, and gas injection as a second priority, is recommended for future work.

(6) A ~ 30 W and a ~ 200 W thruster were designed and tested, benefiting from all the development work that we described. The stability of the thruster that was observed over 100 hours of operation is considered as a major achievement of this work. In addition, very significant performance improvement was measured, with a total efficiency up to 0.50 at both power level. These results are to be confirmed by additional measurements in another facility. Further characterization will be required to identify the respective contributions of the several design changes to the overall performance increase.

(7) It was shown that the performance of the thruster depends not only on previously studied parameters but also on the microwave coupling structure. Two thrusters differing only by the coupling structure (coaxial or circular waveguide) were designed and characterized. For the same set-point the waveguide coupling structure exhibited half the thrust, a difference that seemed to originate in ion energy. Waveguide coupling does not appear as a promising solution but the origin of the poor performance is still to be understood in detail.

(8) We proposed a heating model to describe the formation of the electron energy distribution function. To develop this model, we studied the confined electron trajectories in the static fields of the thruster. Some qualitative experimental observations could be interpreted with these trajectories. The heating model does not however pretend to make quantitative predictions since it ignores parameters that experiments proved critical: in particular the thruster material and the vacuum tank background pressure. The model could be augmented by including an appropriate loss term for cross-field diffusion.

With the sum of these results the ECRT seems to be heading toward clear skies: the thruster consists of a simple design, can be operated in a repeatable manner with state-of-the-art performance as compared to other technologies, and exhibits a sufficient estimated lifetime. Although performance and lifetime are already satisfactory, improvements are expected in the future since many design features are still to be optimized.

Apart from further thruster development, future work could address issues at system level such as the design and integration of a dedicated microwave generator, whose efficiency is not included in the efficiency calculation at the moment. This aspect is already investigated in the framework of the "MINOTOR" project.

Given the number of unanswered questions raised by this work, it seems clear that the technological development is running ahead of the physical understanding of the system. The approach of the last chapter however appears to be a fertile point of view that can help interpret some of the experimental results, although quantitative predictions are not expected. On the experimental side, several measurements would be extremely insightful. In particular, the space-resolved measurement of electron temperature in the coupling structure, as well as the measurement of ion trajectories in the nozzle. Besides, the understanding of the thruster as a whole is expected to strongly improve in future years with detailed simulation codes. In particular, the current development of a hybrid code at the University Carlos III de Madrid, and of a full electromagnetic PIC code at ONERA, both dedicated to the ECRT, will undoubtedly accelerate the progress of this technology.

References

[1] Francis F. Chen, *Introduction to Plasma Physics and Controlled Fusion*. .

[2] K. S. Packard, "The Origin of Waveguides: A Case of Multiple Rediscovery," *IEEE Trans. Microw. Theory Tech.*, vol. 32, no. 9, pp. 961–969, Sep. 1984, doi: 10.1109/TMTT.1984.1132809.

[3] E. V. Appleton, "Wireless Studies of the Ionosphere," *Inst. Electr. Eng. - Proc. Wirel. Sect. Inst.*, vol. 7, no. 21, pp. 257–265, Sep. 1932, doi: 10.1049/pws.1932.0027.

[4] Nagatomo M., "A microwave plasma accelerator for space propulsion," presented at the The Third International Symposium on Rockets and Astronautics, Tokyo, 1961.

[5] T. Consoli and R. B. Hall, "Plasma acceleration by electromagnetic and magnetostatic field gradients," *Nucl. Fusion*, vol. 3, no. 4, p. 237, 1963, doi: 10.1088/0029-5515/3/4/001.

[6] T. Ziemba, J. Carscadden, J. Slough, J. Prager, and R. Winglee, "High Power Helicon Thruster," Jul. 2005, doi: 10.2514/6.2005-4119.

[7] David B. Miller, Per Gloersen, Edward F. Gibbons, and D J. BenDaniel, "Cyclotron Resonance Propulsion System," presented at the Third Annual Symposium on the Engineering Aspects of Magnetohydrodynamics, University of Rochester, Mar. 1962.

[8] P. Gloersen, D. Miller, and E. Gibbons, "Microwave Driven Magnetic Plasma Accelerator 'Cyclops,'" Contract No. NAS5-1046, Feb. 1962.

[9] DavidB. Miller, Edward F. Gibbons, Per Gloersen, "Cyclotron resonance propulsion system," Colorado Springs, 1963.

[10] D. Miller, E. Gibbons, and P. Gloersen, "CYCLOTRON RESONANCE PROPULSION SYSTEM," presented at the Electric Propulsion Conference, Colorado Springs,CO,U.S.A., Mar. 1963, doi: 10.2514/6.1963-2.

[11] E. F. Gibbons and D. B. Miller, "Experiments with an electron cyclotron resonance plasma accelerator," *AIAA J.*, vol. 2, no. 1, pp. 35–41, Jan. 1964, doi: 10.2514/3.2210.

[12] G. W. BETHKE and D. B. MILLER, "Cyclotron resonance thruster design techniques," *AIAA J.*, vol. 4, no. 5, pp. 835–840, 1966, doi: 10.2514/3.3554.

[13] David B. Miller, Goerge W. Bethke, and Giles F. Crimi, "Investigation of Plasma Accelerator (Cyclotron Resonance Propulsion System), CYCLOPS," Contract NAS3-6266, Nov. 1965.

[14] Kosmahl, H. G., "Three Dimensional Plasma Acceleration Through Axisymmetric DivergingMagnetic Fields Based on Dipole Moment Approximation," Cleaveland, Ohio, NASA TN D-3782, 1967.

[15] H. G. Kosmahl, D. B. Miller, and G. W. Bethke, "Plasma Acceleration with Microwaves near Cyclotron Resonance," *J. Appl. Phys.*, vol. 38, no. 12, pp. 4576–4582, Nov. 1967, doi: 10.1063/1.1709188.

[16] G. F. Crimi, A. C. Eckert, and D. B. Miller, "Microwave Driven Magnetic Plasma Accelerator Studies (CYCLOPS)," Contract NAS3-8903, Mar. 1967. Accessed: Jun. 12, 2018. [Online]. Available: https://ntrs.nasa.gov/search.jsp?R=19670018272.

[17] G. F. Crimi, "Investigation of a Microwave Generated Plasma in a Non-Uniform Magnetic Field .," Ph. D. Dissertation, University of Pennsylvania, 1967.

[18] H. W. Hendel and T Todd Reboul, "Continuous plasma acceleration at electron cyclotron resonance," Colorado Springs, 1963.

[19] S. AHMED and H. HENDEL, "Space charge acceleration of ions at electron cyclotron resonance," doi: 10.2514/6.1964-24.

[20] Nagatomo M., "Plasma acceleration by high frequency electromagnetic wave in staticmagnetic field gradient," presented at the Electric Porpulsion and Plasma Dynamics Conference, Colorado Springs, Sep. 1967.

[21] M. Nagatomo, "Plasma Acceleration by Microwave Discharge in Magnetic Field Gradient," presented at the Sixth International Symposium on Space Technology and Science, Tokyo, 1965.

[22] Nagatomo M., "Plasma Acceleration by High Frequency ElectromagneticWave in Static Magnetic Field Gradient," Tokyo, May 1967.

[23] J. C. Sercel, “An experimental and theoretical study of the ECR plasma engine,” Ph. D. Dissertation, California Institute of Technology, 1993.
[24] T. Vialis, “Développement d’un propulseur plasma à résonance cyclotron électronique pour les satellites,” Ph. D. Dissertation, Sorbonne Université, 2018.
[25] Sercel, J. C., “Electron Cyclontron Resonance Ploasma Acceleration,” presented at the AIAA 19th Fluid Dynamics, Plasma Dynamics and Lasers Conference, Honolulu, 1987.
[26] F. E. C. Culick and J. C. Sercel, “Electron-Cyclotron-Resonance Plasma Thruster Research,” California Institute of Technology, Final Report for the Air Force Office of Scientific Research AFOSR-TR-910809, Aug. 1990.
[27] S. Larigaldie, “Plasma thruster and method for generating a plasma propulsion thrust,” US20150020502A1, Jan. 22, 2015.
[28] F. Cannat, “Caractérisation et modélisation d’un propulseur plasma à résonance cyclotronique des électrons,” Ph. D. Dissertation, Ecole Polytechnique, 2015.
[29] F. Cannat, T. Lafleur, J. Jarrige, P. Chabert, P.-Q. Elias, and D. Packan, “Optimization of a coaxial electron cyclotron resonance plasma thruster with an analytical model,” *Phys. Plasmas*, vol. 22, no. 5, p. 053503, May 2015, doi: 10.1063/1.4920966.
[30] T. Lafleur, F. Cannat, J. Jarrige, P. Q. Elias, and D. Packan, “Electron dynamics and ion acceleration in expanding-plasma thrusters,” *Plasma Sources Sci. Technol.*, vol. 24, no. 6, p. 065013, 2015, doi: 10.1088/0963-0252/24/6/065013.
[31] J. Jarrige, P.-Q. Elias, D. Packan, and F. Cannat, “Characterization of a coaxial ECR plasma thruster,” doi: 10.2514/6.2013-2628.
[32] T. Lafleur, “Helicon plasma thruster discharge model,” *Phys. Plasmas*, vol. 21, no. 4, p. 043507, Apr. 2014, doi: 10.1063/1.4871727.
[33] T. Vialis, J. Jarrige, A. Aanesland, and D. Packan, “Direct Thrust Measurement of an Electron Cyclotron Resonance Plasma Thruster,” *J. Propuls. Power*, vol. 34, no. 5, pp. 1323–1333, 2018, doi: 10.2514/1.B37036.
[34] T. Vialis, J. Jarrige, and D. Packan, “Separate measurements of magnetic and pressure thrust contributions in a magnetic nozzle electron cyclotron resonance plasma thruster,” SEVILLE, Spain, May 2018, Accessed: Mar. 06, 2019. [Online]. Available: https://hal.archives-ouvertes.fr/hal-01961041.
[35] T. Vialis, J. Jarrige, and D. Packan, “Geometry optimization and effect of gas propellant in an electron cyclotron resonance plasma thruster,” in *Proc. 35th Int. Electr. Propuls. Conf*, Atlanta, 2017, pp. 1–12.
[36] D. Packan *et al.*, “The MINOTOR H2020 project for ECR thruster development,” presented at the Presented at the 35th International Electric Propulsion Conference, Atlanta, 2017.
[37] J. D. Jackson, *Classical Electrodynamics, third edition.*, 3rd Edition. New York: John Wiley & Sons, Inc., 1998.
[38] D. M. Pozar, *Microwave Engineering*, 4th Edition. Hoboken, NJ: John Wiley & Sons, 2011.
[39] Simon Ramo, John R. Whinnery, and Theodore Van Duzer, *Fields and Waves in Communication Electronics*, Wiley. 1965.
[40] George L. Ragan, *Microwave Transmission Circuits*. .
[41] P. A. Rizzi, *Microwave engineering: passive circuits*. Prentice Hall, 1988.
[42] CEPADUES, *CIRCUITS PASSIFS Tome 1, Thourel Léo, Editions Cépaduès*. .
[43] R. Dey, S. B. Chakrabarty, and R. Jyoti, “Analysis of a coaxial probe-fed circular waveguide,” *Microw. Opt. Technol. Lett.*, vol. 55, no. 11, pp. 2652–2656, Nov. 2013, doi: 10.1002/mop.27841.
[44] W. W. S. Lee and E. K. N. Yung, “The input impedance of a coaxial line fed probe in a cylindrical waveguide,” *IEEE Trans. Microw. Theory Tech.*, vol. 42, no. 8, pp. 1468–1473, Aug. 1994, doi: 10.1109/22.297808.
[45] J.-M. Rax, *Electromagnétisme : Milieux, structures & énergie*. DE BOECK UNIVERSITE, 2017.
[46] Paul-François COMBES, Raymond CRAMPAGNE, “Circuits passifs hyperfréquences - Éléments passifs réciproques,” *Techniques de l’ingénieur*. Accessed: Sep. 04, 2017. [Online]. Available: https://www.techniques-ingenieur.fr/base-documentaire/electronique-photonique-th13/hyperfrequences-circuits-et-emetteurs-de-puissance-42281210/circuits-passifs-hyperfrequences-e1403/.
[47] Robert G. Jahn, *Physics of Electric Propulsion*. McGRAW-HILL, 1968.

[48] D. M. Goebel and I. Kartz, *Fundamentals of Electric Propulsion, Ion and Hall Thrusters*. .
[49] E. Ahedo, "Plasmas for space propulsion," *Plasma Phys. Control. Fusion*, vol. 53, no. 12, p. 124037, 2011, doi: 10.1088/0741-3335/53/12/124037.
[50] G. P. Sutton and O. Biblarz, *Rocket Propulsion Elements*. John Wiley & Sons, 2010.
[51] H. Luebberstedt *et al.*, "Electra - Full Electric PropulsionSatellite Platform for GEO Missions." Jan. 2018.
[52] D. Packan, N. Berend, J.-C. Mateo Velez, J.-P. David, and D. Lazaro, "Rapport Final ARF ELECTRA," Apr. 2017.
[53] Dan Lev et al., "The Technological and Commercial Expansion of Electric Propulsion in the Past 24 Years," presented at the International Electric Propulsion Conference, Atlanta, Oct. 2017.
[54] "List of spacecraft with electric propulsion," *Wikipedia*. Feb. 27, 2020, Accessed: Apr. 03, 2020. [Online]. Available: https://en.wikipedia.org/w/index.php?title=List_of_spacecraft_with_electric_propulsion&oldid=942841395.
[55] R. Joseph Cassady, Timothy Kokan, Claude Joyner-II, James Horton, and Jerry Jackson, "The Importance of Electric Propulsion to Future Exploration of the Solar System," presented at the International Electric Propulsion Conferernce, Vienna, Sep. 2019.
[56] ASD-EUROSPACE, "Space Trends 2015," 2015.
[57] T. Wekerle *et al.*, "Status and Trends of Smallsats and Their Launch Vehicles — An Up-to-date Review," *J. Aerosp. Technol. Manag.*, vol. 9, no. 3, pp. 269–286, Sep. 2017, doi: 10.5028/jatm.v9i3.853.
[58] "Les méga-constellations de satellites : un tournant pour l'Internet de demain ?," *Digital Corner*, Sep. 16, 2019. https://www.digitalcorner-wavestone.com/2019/09/les-mega-constellations-de-satellites-un-tournant-pour-linternet-de-demain/ (accessed Apr. 02, 2020).
[59] "Why Space Propulsion - ThrustMe." https://www.thrustme.fr/why-space-propulsion (accessed Apr. 18, 2020).
[60] D. Packan *et al.*, "H2020 MINOTOR: Magnetic Nozzle Electron Cyclotron Resonance Thruster," presented at the Presented at the 36th International Electric Propulsion Conference, Vienna, 2019.
[61] Peter Erichsen, "Perfromance Evaluation of Spacraft Propulsion Systems in Relation to Mission Impulse Requirements," presented at the Second European Spacecraft Propulsion Conference, 1997.
[62] D. Rafalskyi and A. Aanesland, "Neutralizer-free gridded ion thruster," doi: 10.2514/6.2014-3423.
[63] Jarrige J, Elias P Q, Cannat F, and Packan D, "Characterization of a coaxial ECR plasma thruster," Diego, USA, Jun. 2013.
[64] J. Jarrige, S. Correyero Plaza, P.-Q. Elias, and D. Packan, "Investigation on the ion velocity distribution in the magnetic nozzle of an ECR plasma thruster using LIF measurements," presented at the IEPC, 2017, Accessed: Feb. 26, 2019. [Online]. Available: https://e-archivo.uc3m.es/handle/10016/27690.
[65] S. Correyero, J. Jarrige, D. Packan, and E. Ahedo, "Plasma beam characterization along the magnetic nozzle of an ECR thruster," *Plasma Sources Sci. Technol.*, 2019, doi: 10.1088/1361-6595/ab38e1.
[66] A. Sanchez-Villar, J. Zhou, M. Merino, and E. Ahedo, "PIC/fuid/wave Simulation of the Plasma Discharge in an ECR Plasma Thruster," presented at the 36th International Electric Propulsion Conference, Vienna, Sep. 2019, Accessed: Jan. 24, 2020. [Online]. Available: https://planner.smart-abstract.com/uploads/IEPC19/abstracts/pdf/A-633-Paper-List-15d89f7dc8d02f.pdf.
[67] J. C. Porto and P.-Q. Elias, "Full-PIC Simulation of an ECR Plasma Thruster with Magnetic Nozzle," presented at the 36th International Electric Propulsion Conference, Vienna, Sep. 2019.
[68] R. J. Goldston and P. H. Rutherford, *Introduction to Plasma Physics*, Pap/Dskt. Bristol, UK ; Philadelphia: Routledge, 1995.
[69] J.-L. Delcroix and A. Bers, *Physique des plasmas, volume 2*. EDP Sciences, 1994.
[70] J. A. Bittencourt, *Fundamentals of Plasma Physics*. Springer Science & Business Media, 2004.
[71] J.-M. Rax, *Physique des plasmas - Cours et applications*. Paris: Dunod, 2005.
[72] T. H. Stix and W. a Nierenberg, *The Theory Of Plasma Waves*. Literary Licensing, LLC, 1962.
[73] Stix, *Waves in Plasmas*. 1992.

[74] M. A. Lieberman and A. J. Lichtenberg, *Principles of Plasma Discharges and Materials Processing*. John Wiley & Sons, 2005.
[75] M. C. Williamson, A. J. Lichtenberg, and M. A. Lieberman, "Self-consistent electron cyclotron resonance absorption in a plasma with varying parameters," *J. Appl. Phys.*, vol. 72, no. 9, pp. 3924–3933, Nov. 1992, doi: 10.1063/1.352244.
[76] R. Geller, *Electron Cyclotron Resonance Ion Sources and ECR Plasmas*. CRC Press, 1996.
[77] J. Musil and F. Zacek, "Linear transformation of waves in a magnetoactive plasma generated by a strong microwave signal," *Plasma Phys.*, vol. 12, no. 1, pp. 17–22, Jan. 1970, doi: 10.1088/0032-1028/12/1/002.
[78] A. V. Arefiev and B. N. Breizman, "Ambipolar acceleration of ions in a magnetic nozzle," *Phys. Plasmas*, vol. 15, no. 4, p. 042109, Apr. 2008, doi: 10.1063/1.2907786.
[79] M. Martinez-Sanchez, J. Navarro-Cavallé, and E. Ahedo, "Electron cooling and finite potential drop in a magnetized plasma expansion," *Phys. Plasmas*, vol. 22, no. 5, p. 053501, May 2015, doi: 10.1063/1.4919627.
[80] "lxcat." https://fr.lxcat.net/ (accessed Jun. 19, 2019).
[81] L. Garrigues, J. Pérez-Luna, J. Lo, G. J. M. Hagelaar, J. P. Boeuf, and S. Mazouffre, "Empirical electron cross-field mobility in a Hall effect thruster," *Appl. Phys. Lett.*, vol. 95, no. 14, p. 141501, Oct. 2009, doi: 10.1063/1.3242336.
[82] A. Tavant, V. Croes, R. Lucken, T. Lafleur, A. Bourdon, and P. Chabert, "The effects of secondary electron emission on plasma sheath characteristics and electron transport in an ${\bf{E}}\times {\bf{B}}$ discharge via kinetic simulations," *Plasma Sources Sci. Technol.*, vol. 27, no. 12, p. 124001, Dec. 2018, doi: 10.1088/1361-6595/aaeccd.
[83] A Domınguez-Vázquez, J Zhou, P Fajardo, and E Ahedo, "Analysis of the plasma discharge in a Hall thruster via a hybrid 2D code," presented at the IEPC, Vienna, Sep. 2019.
[84] M. Merino and E. Ahedo, "Influence of Electron and Ion Thermodynamics on the Magnetic Nozzle Plasma Expansion," *IEEE Trans. Plasma Sci.*, vol. 43, no. 1, pp. 244–251, Jan. 2015, doi: 10.1109/TPS.2014.2316020.
[85] E. Ahedo and M. Merino, "On plasma detachment in propulsive magnetic nozzles," *Phys. Plasmas*, vol. 18, no. 5, p. 053504, May 2011, doi: 10.1063/1.3589268.
[86] R. W. Moses, R. A. Gerwin, and K. F. Schoenberg, "Resistive plasma detachment in nozzle based coaxial thrusters," *AIP Conf. Proc.*, vol. 246, no. 1, pp. 1293–1303, Jan. 1992, doi: 10.1063/1.41752.
[87] E. B. Hooper, "Plasma detachment from a magnetic nozzle," *J. Propuls. Power*, vol. 9, no. 5, pp. 757–763, 1993, doi: 10.2514/3.23686.
[88] R. Winglee, T. Ziemba, L. Giersch, J. Prager, J. Carscadden, and B. R. Roberson, "Simulation and laboratory validation of magnetic nozzle effects for the high power helicon thruster," *Phys. Plasmas*, vol. 14, no. 6, p. 063501, Jun. 2007, doi: 10.1063/1.2734184.
[89] Savoini, "Cours d'introduction à la physique des plasmas."
[90] K. Takahashi, T. Lafleur, C. Charles, P. Alexander, and R. W. Boswell, "Electron Diamagnetic Effect on Axial Force in an Expanding Plasma: Experiments and Theory," *Phys. Rev. Lett.*, vol. 107, no. 23, p. 235001, Nov. 2011, doi: 10.1103/PhysRevLett.107.235001.
[91] A. Fruchtman, K. Takahashi, C. Charles, and R. W. Boswell, "A magnetic nozzle calculation of the force on a plasma," *Phys. Plasmas*, vol. 19, no. 3, p. 033507, Mar. 2012, doi: 10.1063/1.3691650.
[92] E. Ahedo and M. Merino, "Two-dimensional supersonic plasma acceleration in a magnetic nozzle," *Phys. Plasmas*, vol. 17, no. 7, p. 073501, Jul. 2010, doi: 10.1063/1.3442736.
[93] J. M. Little and E. Y. Choueiri, "Electron Cooling in a Magnetically Expanding Plasma," *Phys. Rev. Lett.*, vol. 117, no. 22, p. 225003, Nov. 2016, doi: 10.1103/PhysRevLett.117.225003.
[94] Y. Zhang, C. Charles, and R. Boswell, "Thermodynamic Study on Plasma Expansion along a Divergent Magnetic Field," *Phys. Rev. Lett.*, vol. 116, no. 2, p. 025001, Jan. 2016, doi: 10.1103/PhysRevLett.116.025001.
[95] B. Wachs and B. A. Jorns, "Background pressure effects on ion dynamics in a low-power magnetic nozzle thruster," *Plasma Sources Sci. Technol.*, 2020, doi: 10.1088/1361-6595/ab74b6.
[96] D. C. Baird, *Experimentation: An Introduction to Measurement Theory and Experiment Design*, 3rd ed. Englewood Cliffs, N.J: Pearson, 1994.

[97] S. Mazouffre, T. Hallouin, M. Inchingolo, A. Gurciullo, P. Lascombes, and J.-L. Maria, “Charaterization of Miniature Hall Thurster Plume in the 50 - 200 W Power Range,” presented at the Presented at the 36th International Electric Propulsion Conference, Vienna, 2019.
[98] D. L. Brown, M. L. R. Walker, J. Szabo, W. Huang, and J. E. Foster, “Recommended Practice for Use of Faraday Probes in Electric Propulsion Testing,” *J. Propuls. Power*, vol. 33, no. 3, pp. 582–613, Sep. 2016, doi: 10.2514/1.B35696.
[99] Francis F. Chen, *Plasma Diagnostic Techniques*. New-York: Academic Press, 1965.
[100] C. Böhm and J. Perrin, “Retarding-field analyzer for measurements of ion energy distributions and secondary electron emission coefficients in low-pressure radio frequency discharges,” *Rev. Sci. Instrum.*, vol. 64, no. 1, pp. 31–44, Jan. 1993, doi: 10.1063/1.1144398.
[101] R. P. Doerner, D. G. Whyte, and D. M. Goebel, “Sputtering yield measurements during low energy xenon plasma bombardment,” *J. Appl. Phys.*, Feb. 2003.
[102] S. Correyero, M. Merino, P.-Q. Elias, J. Jarrige, D. Packan, and E. Ahedo, “Characterization of diamagnetism inside an ECR thruster with a diamagnetic loop,” *Phys. Plasmas*, vol. 26, no. 5, p. 053511, May 2019, doi: 10.1063/1.5093980.
[103] J. Williams, M. Johnson, and D. Williams, “Differential Sputtering Behavior of Pyrolytic Graphite and Carbon-Carbon Composite Under Xenon Bombardment,” in *40th AIAA/ASME/SAE/ASEE Joint Propulsion Conference and Exhibit*, 2004, p. 3788.
[104] K. T. McDonald, “Radiation from the Open End of a Coaxial Cable.”
[105] K. Holste, P. Dietz, S. Scharmann, K. Keil, D. Zschätzsch, F. Becker, M. Reitemeyer, B. Nauschütt, F. Kiefer, J. Zorn, N. Kleinmichel, H. Leiter, K. T. Brinkmann, C. Heiliger, N. Joshi, R. Henrich, U., and Probst, R. Thüringer, A. Reeh, T. Sommavilla, C. Volkmar, D. Packan, S. Peterschmitt, and P. J. Klar, “Ion Thrusters and Electric Propulsion Developments.”
[106] K. Z. Rajab *et al.*, “Broadband Dielectric Characterization of Aluminum Oxide (Al_2O_3),” *J. Microelectron. Electron. Packag.*, vol. 5, no. 1, pp. 2–7, Jan. 2008, doi: 10.4071/1551-4897-5.1.1.
[107] “Alumine usinable 960.” https://www.final-materials.com/fr/60-alumine-usinable-960 (accessed Mar. 09, 2020).
[108] “ALUMINE C799,” *Céramique technique*, Aug. 28, 2017. https://www.sceram.com/alumine-c799/ (accessed Mar. 09, 2020).
[109] S. Peterschmitt, D. Packan, and J. Jarrige, “Waveguide microwave coupling to a magnetic nozzle ECR thruster,” presented at the Space Propulsion 2018, Seville, May 2018.
[110] L. Harvanek, V. Mentlik, P. Trnka, and J. Hornak, “Effect of electrical/thermal aging on dielectric properties of polymer/SiO2 nanocomposites,” in *2016 IEEE International Conference on Dielectrics (ICD)*, Jul. 2016, vol. 2, pp. 92–95, doi: 10.1109/ICD.2016.7547720.
[111] F. Jaeger, A. J. Lichtenberg, and M. A. Lieberman, “Theory of electron cyclotron resonance heating. I. Short time and adiabatic effects,” *Plasma Phys.*, vol. 14, no. 12, p. 1073, 1972, doi: 10.1088/0032-1028/14/12/002.
[112] A. J. Lichtenberg and M. A. Lieberman, *Regular and Stochastic Motion*. New York: Springer-Verlag, 1983.
[113] A. F. Kuckes, “Resonant absorption of electromagnetic waves in a non-uniformly magnetized plasma,” *Plasma Phys.*, vol. 10, no. 4, pp. 367–380, Jan. 1968, doi: 10.1088/0032-1028/10/4/304.
[114] M. A. Lieberman and A. J. Lichtenberg, “Theory of electron cyclotron resonance heating. II. Long time and stochastic effects,” *Plasma Phys.*, vol. 15, no. 2, pp. 125–150, Feb. 1973, doi: 10.1088/0032-1028/15/2/006.
[115] Marc Villemant, “Modélisation et caractérisation expérimentale de l’influence de l’emission électronique sur le fonctionnement des propulseurs à courant de Hall,” ISAE, 2018.
[116] S. Barral, K. Makowski, Z. Peradzyński, N. Gascon, and M. Dudeck, “Wall material effects in stationary plasma thrusters. II. Near-wall and in-wall conductivity,” *Phys. Plasmas*, vol. 10, no. 10, pp. 4137–4152, Sep. 2003, doi: 10.1063/1.1611881.
[117] F. Taccogna, S. Longo, M. Capitelli, and R. Schneider, “Surface-Driven Asymmetry and Instability in the Acceleration Region of Hall Thruster,” *Contrib. Plasma Phys.*, vol. 48, no. 4, pp. 375–386, 2008, doi: 10.1002/ctpp.200810061.
[118] K. S. Moon, J. Lee, and K.-W. Whang, “Electron ejection from MgO thin films by low energy noble gas ions: Energy dependence and initial instability of the secondary electron emission coefficient,” *J. Appl. Phys.*, vol. 86, no. 7, pp. 4049–4051, Sep. 1999, doi: 10.1063/1.371328.

[119] G. D. Hobbs and J. A. Wesson, “Heat flow through a Langmuir sheath in the presence of electron emission,” *Plasma Phys.*, vol. 9, no. 1, pp. 85–87, Jan. 1967, doi: 10.1088/0032-1028/9/1/410.
[120] A. Smirnov, Y. Raitses, and N. J. Fisch, “Electron cross-field transport in a low power cylindrical Hall thruster,” *Phys. Plasmas*, vol. 11, no. 11, pp. 4922–4933, Oct. 2004, doi: 10.1063/1.1791639.
[121] D. Sydorenko, I. Kaganovich, Y. Raitses, and A. Smolyakov, “Breakdown of a Space Charge Limited Regime of a Sheath in a Weakly Collisional Plasma Bounded by Walls with Secondary Electron Emission,” *Phys. Rev. Lett.*, vol. 103, no. 14, p. 145004, Oct. 2009, doi: 10.1103/PhysRevLett.103.145004.
[122] A. Tavant, “Plasma-wall interaction and electron transport in Hall Effect Thrusters,” Université Paris Saclay, 2019.
[123] J. Meunier, Ph. Belenguer, and J. P. Boeuf, “Numerical model of an ac plasma display panel cell in neon-xenon mixtures,” *J. Appl. Phys.*, vol. 78, no. 2, pp. 731–745, Jul. 1995, doi: 10.1063/1.360684.
[124] Rudolf Peierls, “Model-Making in Physics,” *Contemp Phys*, vol. 21, no. 1, pp. 3–17, 1980.
[125] V. L. Ginzburg, *Propagation of Electromagnetic Waves in Plasma*. Gordon & Breach Science Publishers Ltd, 1962.

Appendix A. Comments on the collisional wave number of the R wave

The independence of the absorbed power fraction on collision frequency may be understood by looking at the imaginary part of the wave number. Let's write the square of the wave number as $\beta_R^2 = k^2\epsilon$, where $\epsilon = \epsilon_r + j\epsilon_i$ is a complex number. Then the wave number writes

$$\beta_R = \pm\frac{k}{\sqrt{2}}\left(\sqrt{\epsilon_r + |\epsilon|} + j\frac{\epsilon_i}{\sqrt{\epsilon_r + |\epsilon|}}\right). \quad \textbf{(223)}$$

From 164 we have

$$\epsilon_i = -\frac{\frac{\omega_{pe}^2}{\omega\nu_{coll}}}{1+\left(\frac{\omega-\omega_{ce}}{\nu_{coll}}\right)^2}, \epsilon_r = 1 - \frac{\frac{(\omega-\omega_{ce})\omega_{pe}^2}{\omega\nu_{coll}^2}}{1+\left(\frac{\omega-\omega_{ce}}{\nu_{coll}}\right)^2} \quad \textbf{(224)}$$

With $\omega_{ce} \approx \omega_{pe} \approx \omega \gg \nu_{coll}$, $\epsilon_r \approx 1$. However, far from $\omega_{ce} = \omega$ we have $\epsilon_i \approx \left(\frac{\omega}{\nu_{coll}}\right)^{-1}$ whereas near $\omega_{ce} = \omega$, $\epsilon_i \approx \frac{\omega}{\nu_{coll}}$. Hence the imaginary part of the wavenumber is vanishingly small far from resonance whereas in the vicinity of resonance for propagation in positive direction (upper sign in relation 223). It is represented in figure 30 and reads

$$\Im(\beta_R) = -\frac{k}{\sqrt{2}}\sqrt{\frac{\frac{\omega_{pe}^2}{\omega\nu_{coll}}}{1+\left(\frac{\omega-\omega_{ce}}{\nu_{coll}}\right)^2}}. \quad \textbf{(225)}$$

For ω_{ce} linearly varying with spatial coordinate z, this is the square root of a Cauchy distribution with a width proportional to ν_{coll} and a height inversely proportional to ν_{coll}. Hence it is no surprise that the power absorption, which is proportional to $\exp(\int \Im(\beta_R)(z)dz)$, is independent of ν_{coll}.

This fact may also be understood from a one particle point of view. The energy transfer from one electron to the plasma is proportional to ν_{coll} times the energy transfer between the electron and the wave in between two collisions, which is proportional to time and thus to ν_{coll}^{-1}.

Appendix B. The CMA diagram

A systematic analysis of wave modes in a cold magnetized plasma is beyond the scope of this document and the reader is referred to dedicated books or book chapters [70], [73], [125]. However a few elements are given here, based on the Clemow-Mullaly-Allis (CMA) diagram. The CMA diagram remarkably unfolds in a readable form the information encapsulated in the cold magnetized plasma dielectric tensor. It usually includes the dynamics of ion species. However, in the case of a Xenon plasma excited at microwave frequency, it appears unnecessary to complicate the presentation with ion dynamics. A CMA diagram for electrons is presented in figure 144.

The first layer of information contained in this diagram is a plot in the ($X = \frac{\omega_{pe}^2}{\omega^2}$, $Y = \frac{\omega_{ce}}{\omega}$) plane. For a given frequency, plasma density is increased towards increasing X and magnetic field is increased towards increasing Y. In this plane, the dashed lines indicate the loci of the reflection points; the solid and dotted lines indicate the loci of resonance points. The letters S, P, R, L refer to definition 161, with $R = S + D$ and $L = S - D$. These plots divide the plane into regions characterized by a given set of propagative modes, and labeled by Roman numerals.

The second layer of information contained in this diagram is a polar plot of the phase velocity of the waves, for each region. The angle of the polar plot with respect to the vertical axis indicates the propagation angle with respect to the magnetic field vector. A dashed circle corresponding to a wave in vacuum (phase velocity c) is plotted for reference.

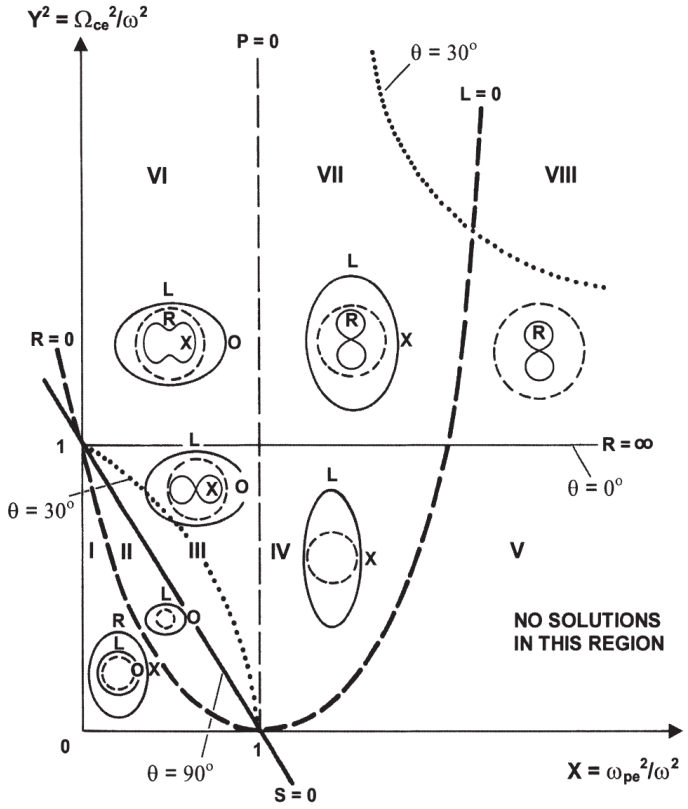

Figure 144. Clemow-Mullaly-Allis (CMA) diagram for a cold electron plasma (reproduced from [70])

As can be noted from the polar plots, there exist at most two propagating modes for each region (two polar plot curves) whose dispersion relation is function the angle with respect to the magnetic field vector (the polar plot curves are not circles). An analysis of the eigen value problem for arbitrary angle shows that three type of waves can exist in a magnetized plasma. The first is the plasma oscillation for $\omega = \omega_{pe}$, which is propagative only in hot plasma. The other two are the extraordinary wave labelled X and the ordinary wave labelled O. From GINZBURG (1962) [125] we have the following dispersion relation.

$$N_{\substack{X \\ O}}^2 = 1 - \frac{2\frac{\omega_{pe}^2}{\omega^2}\left(1 - \frac{\omega_{pe}^2}{\omega^2}\right)}{2\left(1 - \frac{\omega_{pe}^2}{\omega^2}\right) - \frac{\omega_{ce}^2}{\omega^2}\sin^2\alpha \mp \sqrt{\frac{\omega_{ce}^4}{\omega^4}\sin^4\alpha + 4\frac{\omega_{ce}^2}{\omega^2}\left(1 - \frac{\omega_{pe}^2}{\omega^2}\right)^2\cos^2\alpha}} \quad \textbf{(226)}$$

Note that depending on the context the term "extraordinary wave" may refer to the wave having the refractive index N_X^2 above for any angle, or specifically the wave propagating perpendicular to the magnetic field with refractive index $N_X^2(\alpha = \pi/2)$. The same applies for the term "ordinary wave".

A comprehensive understanding would require more development. However, let's point out a few features of the cold magnetized plasma electron waves that are apparent on the CMA diagram.

- For $\omega > \omega_{pe}$, the R wave discussed in section 0 is the extraordinary wave for $\alpha = 0$ and the L wave is the ordinary wave for $\alpha = 0$. On the contrary, for $\omega > \omega_{pe}$, the R wave is the ordinary wave for $\alpha = 0$ and the L wave is the extraordinary wave for $\alpha = 0$. It is only for $\alpha = 0$ that the R wave appears as a single mode across the frontier $\omega = \omega_{pe}$ (see for example [77], figure 1). The same applies for the L wave, hence the argument exposed in section 2.3.2.2.3 about the absorption of the L wave.
- In most regions there exist a wave slower than the speed of light and a wave faster than the speed of light referred to as slow wave and fast wave.
- The ordinary wave propagating strictly perpendicular to the magnetic field is a wave that ignores the magnetic field. As a consequence, similarly to the wave in an unmagnetized plasma, it propagates only for $\omega > \omega_{pe}$.
- For the ECRT, assuming variation along z only, the parametric curve $(X = \frac{\omega_{pe}^2}{\omega^2}(z), Y = \frac{\omega_{ce}}{\omega}(z))$ may be plotted to visualize the successive regions encountered by the wave.

Appendix C. Thruster configurations

For the lower power thruster (~ 30 W) a number of different configurations were used depending on what we wanted to test and depending of the gradual development of the thruster that took place throughout the study. This appendix aims at defining the terms that are used to describe a given configuration. A typical configuration is in figure 145.

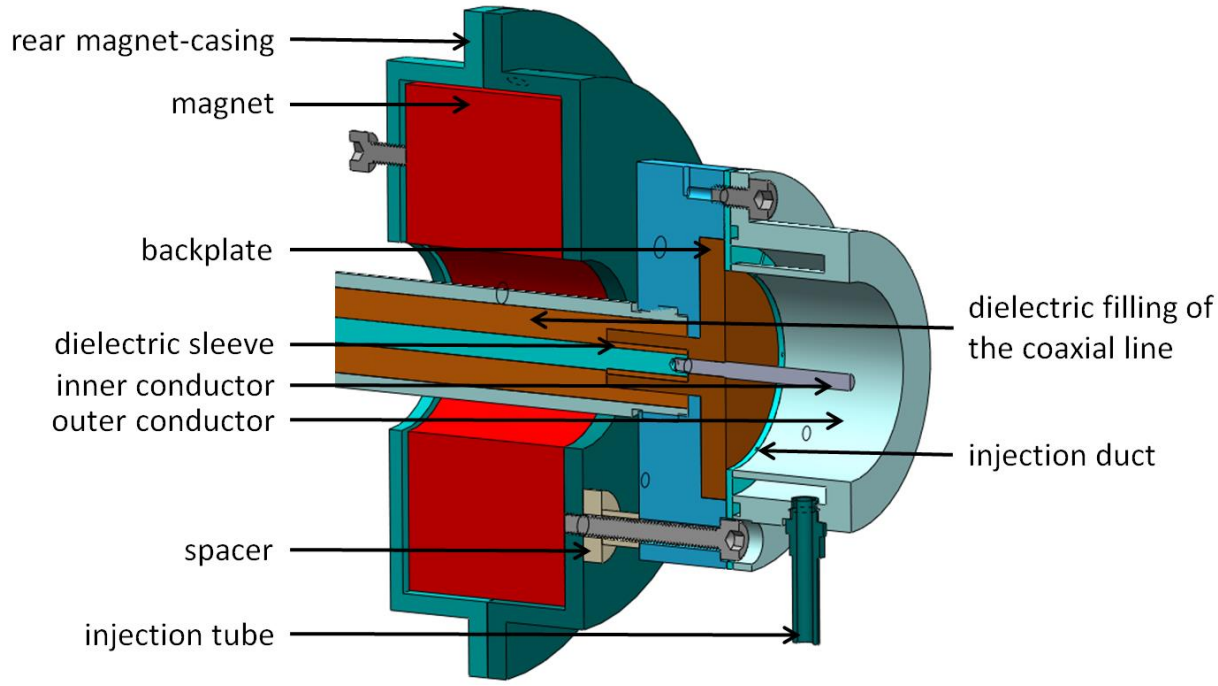

Figure 145. Typical configuration of the thruster: small magnet, coaxial coupling structure, 20 mm outer conductor, 2.3x20 mm inner conductor, radial injection, boron nitride backplate, PTFE coaxial line before the coupling structure. Blue, green, and gray parts are metallic. Brown parts are dielectric.

Magnet.

At the beginning of the study we used the small magnet also described in ([24] IV – 2.1.2). We then built the big magnet, which is in fact composed of two magnets with reversed magnetization. Both magnets are made with sintered Neodymium-Iron-Boron with grade ND35EH. Both are axis-symmetric (in z), have magnetization along z, and their sections are represented to scale in figure 98. In both cases the thruster is mounted so that a relatively flat surface of constant $B = 875$ G is located at $z = +2$ mm (with $z = 0$ at the backplate-plasma interface). This requires that the distance between the backplate and magnet is specific to the magnet.

Coupling structure.

The two types of coupling structure are described in detail in chapter 6.

Outer conductor.

The given outer conductor diameter is the diameter of the wall in contact with the plasma. The material of the outer conductor is always aluminum and its diameter changes only in chapter 5 for the 200 W

thruster. Else, only the length may vary: either 15 mm or 20 mm. The length indicate the extension towards positive z from $z = 0$ (backplate-plasma interface).

Inner conductor.

The length is defined as for the outer conductor.

Injection type.

Two injection types were used in this study, referred to as axial or radial. Details of the design can be found in figure 51 and figure 95.

Backplate material.

The backplate material is in fact always boron nitride. Tests of other material were performed but were considered inconclusive.

Other.

This column indicates the dielectric material filling the 50 Ω coaxial line just before the thruster. It can be PTFE ($\epsilon_r = 2.1$) or boron nitride ($\epsilon_r = 4.3$). Boron nitride may be useful in some instances to work under higher temperatures. It requires modification of the microwave design, in particular: inner conductor diameter of the coaxial line, length and diameter of the extension into the coaxial-to-waveguide transition. The details of the microwave line just before the thruster (mounting of the backplate inside the coaxial line dielectric) should also be reconsidered. We believe that the microwave design in this region (which does not continuously have 50 Ω of characteristic impedance) performs an impedance matching of the thruster and plasma.